University of Calgary

PRISM Repository **https://prism.ucalgary.ca**

The Vault Open Theses and Dissertations

2014-01-07

Soil Moisture Estimation with Polarimetric SAR Data

Mazaheri Tehrani, Habib

Mazaheri Tehrani, H. (2014). Soil Moisture Estimation with Polarimetric SAR Data (Doctoral thesis, University of Calgary, Calgary, Canada). Retrieved from https://prism.ucalgary.ca. doi:10.11575/PRISM/27821 http://hdl.handle.net/11023/1238

Downloaded from PRISM Repository, University of Calgary

UNIVERSITY OF CALGARY

Soil Moisture Estimation with Polarimetric SAR Data

by

Habib Mazaheri Tehrani

A THESIS

SUBMITTED TO THE FACULTY OF GRADUATE STUDIES

IN PARTIAL FULFILLMENT OF THE REQUIREMENTS FOR THE

DEGREE OF DOCTOR OF PHILOSOPHY

DEPARTMENT OF GEOMATICS ENGINEERING

CALGARY, ALBERTA

January, 2014

© Habib Mazaheri Tehrani 2014

Abstract

Soil moisture (SM) is widely used in analyzing the interaction of ground and atmosphere. It has applications in many disciplines including but not limited to weather forecasting and hydrological modeling. Measuring SM is difficult. It has been traditionally carried out by time-consuming field work consisting of direct ground-based soil sampling. Remote sensing seems promising for estimation of SM, because of its unique data gathering specifications. Among different sensors in remote sensing, synthetic aperture radar (SAR) sensors have attracted considerable attention for SM estimation because of their high resolution, independence from weather conditions, and sensitivity to changes in soil dielectric constant, which can be used to quantify SM.

The relationship between the observations of a SAR system and the dielectric constant of soil is usually described using a mathematical model known as surface scattering model. A class of information which can be utilized in post-processing the outputs of these models to improve their performance include the information about the spatial variability of SM. Analyzing the spatial variability of SM can help in calibrating the results of the scattering models. A model may be established for predicting the difference between the outputs of a scattering model and the field-measured SM using a set of concurrent SAR data and ground measurements, which may be generalized to SAR data acquired on other dates.

In this thesis, the spatial variability of SM estimated by the Integral Equation Model (IEM) is analyzed by the STRAIN multifractal model which is a multi-resolution tool. The IEM is selected because of its superior inversion pattern which is necessary for multifractal analysis. We propose a simple calibration model for improving the quality of the results of the IEM based on the relationship between the parameters of the multifractal model and ground measurements of SM.

The results of the experiments in this study show that, the proposed calibration model

is, to some extent, robust when considering SAR images acquired on different dates, and can usually improve the agreement between ground measurements of SM and SM estimated by the IEM.

Acknowledgments

First and foremost, I would like to thank God for giving me the strength to complete this thesis and sustaining me through these tough years.

I express my sincere gratitude to my advisor Dr. Michael Collins for the continuous support of my PhD study, and his patience. Being his student was a great experience. I would also like to thank my advisory committee members Professor Larry Bentley and Dr. Alain Pietroniro for their comments. Dr. Pietroniro also provided early funding for the project through the Drought Research Initiative (DRI).

My gratitude goes to my external examiner Professor Joseph Buckley for his careful reading of the thesis and his valuable comments which were very helpful in revising the thesis.

Dr. Heather McNairn and Dr. Amine Merzouki, of Agriculture and Agri-Food Canada, provided us with both the field data and the Radarsat-2 scenes used in this study.

Thanks to Dr. Andrew Hunter and Professor Rod Blais for our talks on statistical modeling, model evaluation and fractal analysis.

Through the years of completing this research many friends have helped me. If I had to mention just a few I would name Dr. Sina Taghvakish, Dr. Yasser Maghsoudi, Babak Amjadiparvar, Ehsan Mohammadi, Majeed Pouyandeh, Babak Farjad and Ali Moussavi.

My special thanks go to Professor Danielle Marceau for offering me a job when I needed it the most. Without her help I could not complete my research work in time.

Finally, and most importantly, I would like to thank my wife, Fatemeh. Her support, understanding, encouragement and quiet patience were definitely the foundation upon which this thesis has been built. I owe her for accepting to live with me in Calgary far away from her parents. My deepest gratitude also goes to her parents for providing me with endless encouragement, and my parents for years of support and dedication.

To my wife, Fatemeh,

for her endless support

Table of Contents

List of Tables

List of Figures and Illustrations

List of Symbols, Abbreviations, Nomenclatures

A	Scattering anisotropy
ϵ_r	Dielectric constant (Relative permittivity)
H	Scattering entropy
IEM	Integral Equation Model
k	Wavenumber
$\mathcal{L}$	Lagrangian function
l	Surface roughness correlation length
λ	Wavelength
m_v	Volumetric soil moisture
∇	Gradient operator
p	Power index
QP	Quadratic programming
R_h	Horizontal Fresnel reflection coefficient
R_v	Vertical Fresnel reflection coefficient
$[S]$	Scattering matrix
σ°	Backscattering coefficient
σ	Surface roughness RMS height
SQP	Sequential quadratic programming

$[T]$	Coherency matrix
τ	Mass exponent
θ	Incidence angle
$W^{(n)}$	n^{th} power of surface power spectrum

Epigraph

There is always enough light for one who wants to see.

-Ali bin Abu-Talib, 7^{th} century

Chapter 1

Introduction

1.1 Background

Agricultural productivity plays a significant role in the economic development of most countries, and is highly dependent on availability of water. Thus, management of water resources at the farm and regional level is a global issue that needs to be addressed. Acquiring precise information about soil moisture (SM) is a main factor affecting preparation of a suitable water resource management scheme (Heathman et al., 2003). Soil moisture, also known as soil water content, is usually defined as the amount of water contained between soil particles. It is a quantity widely used in analyzing the interaction of ground and atmosphere (Shang et al., 2007). SM, at different spatial and temporal scales, has applications in many disciplines (Quattrochi et al., 2004), including but not limited to climate prediction (e.g., (Ni-Meister et al., 2005)), weather forecasting (e.g., (Anantharaj et al., 2008)) and hydrological modeling (e.g., (Houser et al., 1998)). Especially, estimating SM accurately and producing maps of its spatial and temporal changes and anomalies can improve the quality of monitoring drought (Shao-E et al., 2010) and flood risk (Jeyaseelan, 2003) which are serious problems in many regions of the world.

SM estimation is difficult. It has been traditionally carried out by field work consisting of direct ground-based soil sampling and water content quantification. This type of measurement is time consuming and expensive. Although modern probes now facilitate the process, measuring SM using these probes is still time consuming and costly, and still needs calibration by the direct gravimetric method. Installing permanent probes can help in reducing the effort needed to collect SM information, but this cannot be a practical method for large areas. Furthermore, an intrinsic weakness is associated with ground measurement of SM:

each measurement can represent the status of SM for only a small area, probably a few centimeters, about the measurement location. Therefore, it is difficult to create a SM map using ground measurements.

Given the difficulties involved in traditional measurements of SM, the scientific community has shown a lot of enthusiasm for using remote sensing (RS) in estimation of surface SM (Wang et al., 2009). RS seems promising for estimation of surface SM, because of its unique data gathering specifications. The advantages of using RS for the estimation of SM content (namely speed, regular revision, wide-area coverage and being cost-effective) over traditional field-based methods of measurement have been a motivation for extensive research (Baghdadi et al., 2006b). RS measurements are also non-destructive, in that we do not need to touch the soil to assess it spatially (Anderson et al., 2009). Research on SM using remotely sensed images started in the 1970s (Laymon et al., 2001)(Schmugge et al., 1974) and it is still an active field of research.

Estimation of SM using RS data has been made possible through a number of models, which connect the observations of RS sensors to SM. The main problems with establishing a connection between RS observations and SM is that (Goward et al., 2002):

1. Many objects, for example soil, vegetation cover and woods, contribute to the final response from every single ground pixel received by the sensor. Thus, the contribution of soil to what sensor has detected is not clear.

2. Many factors, including SM, soil roughness and slope, may affect the condition of the wave which transmits back to the sensor. Therefore the effect of each one must be analyzed separately in order to accurately estimate SM.

3. In many cases, electromagnetic radiation is changed during its travel from data collection platform or sun to ground surface and/or from ground surface to platform. Therefore, atmospheric corrections, which usually need theoretical

models and considerable amount of ground-based measurements (Katra et al., 2006), may be necessary while estimating soil surface parameters.

Consequently, there are usually more unknowns than known parameters when we intend to use RS data for SM estimation, and some simplifying assumptions have to be made during the modeling.

1.2 Motivation

Different regions of the electromagnetic spectrum have been studied for the purpose of SM estimation by remotely sensed data. Because of the sensitivity of microwave sensors to changes in SM content, these sensors are more suitable for estimation of SM. Thus, synthetic aperture radar (SAR) sensors which work in the microwave region of electromagnetic spectrum, are less affected by weather conditions, and can produce high-resolution images seem suitable in monitoring SM for agricultural purposes. These sensors are able to generate SM information at field scale (about 500-800 m) which is the target scale in this study.

SAR based models usually estimate a physical property of soil called the *dielectric constant*, and then, another model is used to convert the dielectric constant of soil to SM. In the case of SAR, the relationship between the observations of the system and the dielectric constant of soil is usually described using a mathematical model known as *surface backscattering model*. As is the case with every model describing a natural phenomenon, SAR backscattering models are not perfect, i.e. they are subject to errors while converting SAR observations to soil dielectric constant. This can be the result of the interference of the effect of soil surface roughness and the vegetation covering the soil surface. In order to improve the accuracy of the results of the models, researchers have usually tried to either remove the approximations and simplifying assumptions from the model (Fung et al., 2002)(Wu et al., 2001)(Oh, 2004b), or improve the way roughness and vegetation parameters are handled in the model (Baghdadi et al., 2006a)(Sikdar et al., 2004).

Another approach, which has attracted less attention in the SM estimation literature, is to leave the models as is and try to improve the performance by incorporating ancillary information in the process of the inversion of the model or as a post-processing step. This information can include some SM or roughness parameters from ground measurements or coarse hydrological models (Mattia et al., 2006), or images from optical or passive microwave sensors (Prakash et al., 2012)(Notarnicola et al., 2001). There are other sources of information which can be imagined as constraints in the inversion process. Multi-temporal images are an example of such sources, which result in construction of *temporal constraints*, and have already been successfully used (Mattia et al., 2009). These constraints are based on the assumption that soil surface roughness does not change much between consecutive image acquisitions, and thus, the parameters of soil surface roughness can be assumed constant in the inversion process. This approach can also be seen in recent papers like (Kim et al., 2012), which uses Maxwell 3D model with simulated and truck-mounted radar data to evaluate a multi-temporal method.

Another class of information which can be utilized in post processing the outputs of SAR backscattering models include the information about the spatial variability of SM. SM is highly variable in space and time. Analyzing the spatial variability of SM and its changes over a range of scales can help in calibrating the results of the backscattering models, as we will see in the results of the experiments performed in this study. A model may be established for predicting the difference between the outputs of a backscattering model and the field-measured SM using a set of concurrent SAR data and ground measurements, which can be, to some degree, generalized to SAR data acquired on other dates. This is the core approach to improve the quality of SM estimated using SAR backscattering models in this thesis. To the best knowledge of the author, analyzing the spatial variability of SM has never been utilized for this purpose in any study before. Our objectives in this research have been:

- to analyze the spatial variability of ground-measured and model-estimated SM

values by the models commonly used for this purpose

- to investigate the feasibility of using the information obtained from the analysis of the spatial variability of SM to improve the quality of SM estimation using SAR backscattering models

1.3 Organization of the Thesis

This thesis is organized as follows: In Chapter 2 we cover the physical properties of soil and the methods used for measurement and estimation of SM. In Chapter 3 we review the methods for estimating SM by SAR images, which are the images used in this research, in detail. Chapter 4 contains a description of the spatial variability of SM and the models proposed in the literature for explaining this variability in a region. In Chapter 5 Radarsat-2 satellite images and the field measurements of SM we have used to carry out our tests and analyses will be explained. It also includes a description of the processing steps for preparing the images, the parameters selected, and the measures used for evaluation of the performance of implemented models and algorithms. Chapter 6 contains the results of SM estimation using the models explained in Chapter 3 and analysis of the spatial variability of SM using the models introduced in Chapter 4. Finally, in Chapter 7 conclusions from running the experiments and some suggestions for future research will be presented.

Chapter 2

Soil Moisture and Its Estimation

In this chapter we introduce the physical properties of soil related to estimation of SM, and briefly review the methods used for measurement and estimation of SM.

2.1 Soil Mixture Components

Soil can be considered as a collection of natural layers made from a mixture of solid particles (minerals and organic matter), air and water (Figure 2.1). These components are mixed in a state that their quantitative separation is difficult (Behari, 2005). SM is defined as the ratio of the volume (or mass) of the water in soil to the total volume (or mass) of soil. Thus, volumetric SM is defined as

$$m_v = \frac{V_W}{V_T} \tag{2.1}$$

where V_W is the volume of water in soil and V_T is the total volume of soil. Usually the number obtained from this equation is multiplied by 100 and is stated in units of *volumetric percent* (vol.%).

Solid particles can be classified using their size (diameter) into sand, silt and clay. Traditionally, three quantitative ranges have been used to determine the type of soil particles:

- Sand: $d > 0.05$ mm
- Silt: 0.002 mm $< d < 0.05$ mm
- Clay: $d < 0.002$ mm

where d is the particle size. These three types of particles can be evenly distributed in soil, or the soil may be composed of a high dominance of one particle type and small percentages

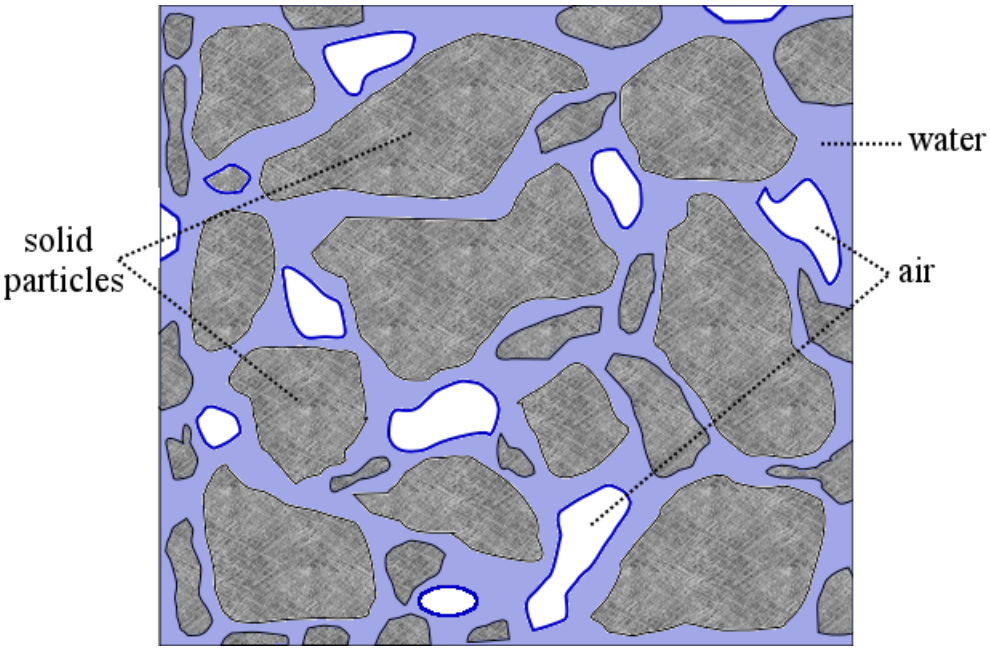

Figure 2.1: Schematic cross section of soil

of others. The texture of soil is classified based on the ratio of these three particle types. The soil classification triangle depicted in Figure 2.2 can be used to determine the class of soil texture according to a method devised by United States Department of Agriculture (Behari, 2005). Soil texture can affect the dielectric constant of soil (see section 2.2) and hence the RS observations of soil. Soils with equal dielectric constant values but different relative amounts of sand, silt and clay can have different moisture values (Wang et al., 1980). But, when accurate texture information is not available for the soil under study (as is the case with our data set) its effect is neglected.

2.2 Dielectric Constant of Soil

Electric dipole moment vector for two electric charges $+q$ and $-q$ is defined as (Atkins et al., 2006)

$$\boldsymbol{\mu} = q\mathbf{R} \tag{2.2}$$

where $\mathbf{R}$ is the vector of distance between the charges, pointing toward the positive charge. Molecules with separated centers of positive and negative charges have an electric dipole

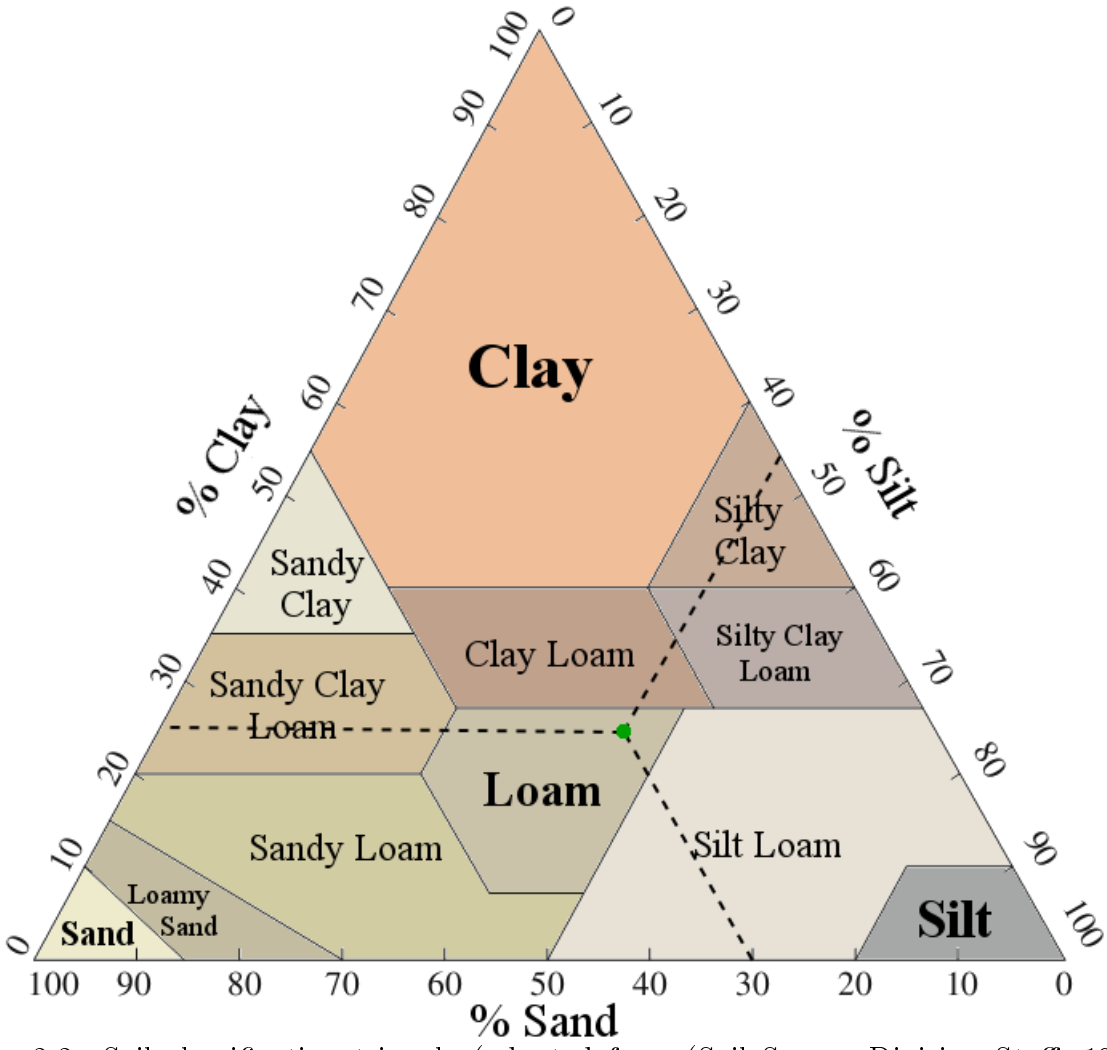

Figure 2.2: Soil classification triangle (adapted from (Soil Survey Division Staff, 1993)): Decision about the name of a given soil with known sand, silt and clay percentages can be made by finding the location of soil in the triangle. For a given percentage of sand, silt and clay, first, the point corresponding to the percentages should be found on sand, silt and clay axes. Then, the points are projected inward parallel to silt, clay and sand axes, respectively. Location of the given soil will be the intersection point of the three projection lines, and class name is determined from the partition that the intersection point lies. Location of an example soil with 30% sand, 45% silt and 25% clay is shown in the graph (green point). The soil is determined as being Loam according to its location.

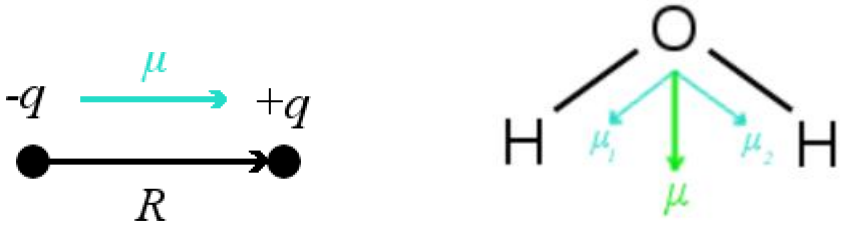

(a) Separate charges (b) Molecule of water

Figure 2.3: Electric dipole moment: Figure (a) shows the electric dipole moment vector $\boldsymbol{\mu}$ for two charges $+q$ and $-q$ separated by distance vector $\mathbf{R}$. In figure (b), direction of dipole moments $\boldsymbol{\mu}_1$ and $\boldsymbol{\mu}_2$ for oxygen and hydrogen atoms in a molecule of water is shown. The overall dipole moment for the molecule, $\boldsymbol{\mu}$, is the result of vector addition of $\boldsymbol{\mu}_1$ and $\boldsymbol{\mu}_2$.

moment, and those with permanent dipole moments are called *polar molecules*. If there are more than one dipole moment in a molecule, the total moment is calculated by adding the vectors of all dipole moments (Figure 2.3) (Atkins et al., 2006).

When an electric field is applied to a material with polar molecules, the dipole moments of its molecules tend to align with the electric field. *Dielectric constant* or *relative permittivity* of a medium shows the ability of its molecules to align their dipole moments along an applied electric field (Behari, 2005). In other words, the dielectric constant shows the ability of the material in getting polarized when exposed to an electric field (Chudinova, 2009). When time elapses, the electric field changes and the dipole moment must align with the electric field again. However, loss of energy in the material causes a phase difference between the applied field and the dipole. In other words, the polarization does not happen immediately. In general, the dielectric constant is treated as a complex number

$$\epsilon_r = \epsilon' - j\epsilon'' \tag{2.3}$$

to allow representing a phase difference. Because, a complex number can be used to show both an amplitude and a phase. The real part of the dielectric constant, ϵ', reflects the stored energy in the medium, and the imaginary part, ϵ'', is related to the amount of energy loss (Fannin et al., 2002). Estimation of SM when illuminated by synthetic aperture radar (the type of sensor we have used in this study; see section 3.1) signals often becomes possible

via estimation of the soil dielectric constant. Indeed, the quantity obtainable by surface scattering models (see section 3.2) is the dielectric constant of the soil, which can be later converted to a volumetric SM value using dielectric mixing models (see section 3.3).

Several studies have shown that the sensitivity of the real part of the dielectric constant to changes in SM is much higher than the imaginary part (Schmugge, 1985)(Hallikainen et al., 1985)(Ulaby et al., 1986) (as cited in (Altese et al., 1996)). Thus, for the purpose of estimation of SM, it can be assumed that the dielectric constant of the soil is a real number. This assumption will hold throughout this thesis for simplifying the process of inversion of the backscattering models.

For microwave frequencies dielectric constant of free water is high (about 80) comparing to the water in soil. The reason is that dipole moments of water molecules can freely align with an applied electric field. Thus, any thing that can restrict the molecule rotation of molecules of water can decrease the dielectric constant of water. For example, freezing can reduce the dielectric constant of soil. The water molecules inside a body of soil can also be bound to soil particles, and may not align with an applied field as easily as free water molecules outside. Thus, the water in soil has a lower dielectric constant.

When soil starts absorbing water, the molecules that first enter the soil cannot increase the dielectric constant of soil much. Because, these molecules are tightly bound to the surface of solid particles of the soil, and their dipole moments cannot be adjusted to the direction of an applied field unrestrictedly. Thus, the increase in the dielectric constant of soil remains slow below a *transition point*. As more water is added to soil, new water molecules become more distant from the surface of particles, and the binding forces become weaker. Consequently, water molecules can rotate with less difficulty, and the dielectric constant of the soil increases. The behavior of soil in response to precipitation can be affected by this process.

Binding forces are stronger in clay for which the size of solid particles are smaller, and hence, the area of their surfaces are larger. In this case, more water needs to penetrate the

soil before water molecules start to move freely and contribute more in dielectric constant of soil. This results in a higher transition point for clay than silt and sand (Behari, 2005).

2.3 Soil Surface Roughness

As we will see in section 3.1, in addition to the properties of the wave transmitter and the dielectric properties of the object, the properties of the wave backscattered from an object depends on the geometry of the object. In surface backscattering models, geometry of the object is described using the parameters of the roughness of the soil surface. Therefore, characterization of the roughness is an important factor in modeling the backscattered wave from the soil. Soil surface roughness also affects the estimation of SM by passive microwave sensors.

Soil roughness is usually described by three parameters: RMS height, correlation length, and auto-correlation (correlation) function. These are usually determined by analyzing the distribution of soil heights (with respect to a known reference) along horizontal soil profiles (Verhoest et al., 2008).

The surface correlation function plays a key role in determination of the response of soil to the SAR signal. Indeed, different correlation functions may result in very different outputs in models such as the Integral Equation Model (see section 3.2.2.1) which need the correlation function. Usually the surface is assumed to be isotropic, causing a one-dimensional correlation function, which can be calculated as (Verhoest et al., 2008)

$$C(\rho) = \frac{\sum_{i=1}^{N-\frac{\rho}{\Delta x}} z_i z_{i+\frac{\rho}{\Delta x}}}{\sum_{i=1}^{N} z_i^2} \tag{2.4}$$

where z_i is the i^{th} height observation, N is the number of observations, and Δx is the resolution of profile. The function can be defined using height measurements in the field,

but usually a well-known function is used as the correlation function. The most common correlation functions in literature are (Verhoest et al., 2008)

- exponential correlation function: $C(\rho) = \sigma^2 e^{-(\frac{\rho}{l})}$
- Gaussian correlation function: $C(\rho) = \sigma^2 e^{-(\frac{\rho}{l})^2}$

where σ is the RMS height and l is the correlation length. A fractal correlation function

$$C(\rho) = \sigma^2 e^{-(\frac{\rho}{l})^\tau} \tag{2.5}$$

has also been used for describing the relation of surface heights (Baghdadi et al., 2004). Here, $\tau = -1.67D + 3.67$ and D is the fractal dimension assumed to be approximately 1.4 for agricultural lands. Indeed, the fractal correlation function has been applied because natural surfaces are often more complicated than what exponential and Gaussian functions describe, and they are special cases of fractal function for $\tau = 1$ and $\tau = 2$, respectively. It has been shown that fractal correlation functions have always generated better or about the same quality results compared to Gaussian and exponential correlation functions (Li et al., 2002).

RMS height describes the vertical variations of soil surface heights and can be obtained from field observations along a profile by (Verhoest et al., 2008)

$$\sigma = \sqrt{\frac{1}{N}\left[\left(\sum_{i=1}^{N} z_i^2\right) - N\bar{z}^2\right]} \tag{2.6}$$

where $\bar{z}$ is the mean height

$$\bar{z} = \frac{1}{N}\sum_{i=1}^{N} z_i \tag{2.7}$$

The correlation length describes the horizontal variations of the surface heights, and is defined as the horizontal distance over which the correlation of the surface heights is more than $1/e = 0.368$. Unlike its simple definition, measuring the correlation length is complicated (Verhoest et al., 2008). It has been shown that, in order to gain a 10% precision

in measurement of the correlation length, the length of the profile should be at least 200 times the mean correlation length (Oh et al., 1998).

The degree of roughness or smoothness of soil surface depends on wavelength of the wave which is used to sense the soil and on incidence angle (see section 3.1). A surface can be rough for a wavelength and smooth for another. Rayleigh's criterion for surface roughness states that, a surface can be considered as smooth if

$$\sigma < \frac{\lambda}{8\,cos\theta} \tag{2.8}$$

where λ is the wavelength and θ is the incidence angle (Reddy, 2008). There is also a stricter criterion called Fraunhofer criterion which is stated as (Ulaby et al., 1982) (as cited in (Pinel et al., 2010))

$$\sigma < \frac{\lambda}{32\,cos\theta} \tag{2.9}$$

According to these criteria, waves with longer wavelengths are more tolerant of changes in surface heights, i.e. sensors using such waves can see surfaces with larger RMS heights as smooth. Since roughness is a disturbing factor in estimation of SM, microwave sensors with longer wavelengths, such as L-band sensors, are more suitable for SM estimation. Because of the dependence of the degree of roughness on wavelength, RMS height and correlation length are usually scaled by wavenumber (see section 3.1) and expressed as $k\sigma$ and kl, respectively.

2.4 Penetration Depth

The depth to which an electromagnetic wave can penetrate into soil depends highly on dielectric constant of the soil and wavelength of the electromagnetic wave. As an electromagnetic wave penetrates into a soil profile it attenuates, i.e. its power decreases. *Penetration depth*, P_d, is usually defined as the depth at which the power of the wave reduces to $1/e$ of its power before entering the soil, and can be approximately calculated by (Rees, 2001)

$$P_d = \frac{\lambda\sqrt{\epsilon'}}{2\pi\epsilon''} \tag{2.10}$$

Since the dielectric constant is unitless, P_d and λ have the same units in this equation. According to this equation, waves with longer wavelengths (lower frequencies) can penetrate into soil profile more, and thus, microwave sensors working in lower frequencies can get information from deeper layers of soil. Figure 2.4 shows the penetration depth of waves with frequencies from 1.4 GHz to 18 GHz for a sandy-loam soil (65% sand, 5% clay and 30% silt) for four different moisture levels (5%, 10%, 15% and 20%). Obviously, penetration depth decreases as soil becomes wetter, or frequency becomes higher. The blue (dash-dot) line shows the Radarsat-2 data acquisition frequency. In this frequency the wave can penetrate into a low moisture soil about 7 cm before its power reduces to $1/e$ of its original value.

Penetration depth values in Figure 2.4 have been calculated using equation (2.10). An empirical model[1] proposed by Hallikainen et al. (1985) has been used to convert soil moisture level, m_v, to real and imaginary parts of the dielectric constant, ϵ' and ϵ'':

$$\epsilon' \, or \, \epsilon'' = (a_0 + a_1 \times S + a_2 \times C) + (b_0 + b_1 \times S + b_2 \times C) m_v + (c_0 + c_1 \times S + c_2 \times C) m_v^2 \quad (2.11)$$

In this equation, S and C are percentage of sand and clay in soil mixture, respectively. a_0, a_1, a_2, b_0, b_1, b_2, c_0, c_1 and c_2 are constant coefficients which depend on frequency, and are presented in Table 2.1 and Table 2.2. Separate sets of coefficients are used for calculating ϵ' and ϵ''.

At the wavelengths used in remote sensing, the physical interaction of an electromagnetic wave with soil is complex to model, and the penetration depth is usually estimated to be in the 0-5 cm range (Adams et al., 2013). If the dielectric constant of soil changes smoothly with depth, the backscattering of an illuminating electromagnetic wave can be assumed to occur completely at the soil surface. However, discontinuities in the dielectric properties of soil may result in backscattering within the volume of the soil (Walker, 1999). The scattering models used for estimation of SM using SAR which will be introduced in section 3.2 assume that SM is uniformly distributed down to the depth that the sensor can receive signals from.

[1]This type of model is called *dielectric mixing model* as explained in section 3.3

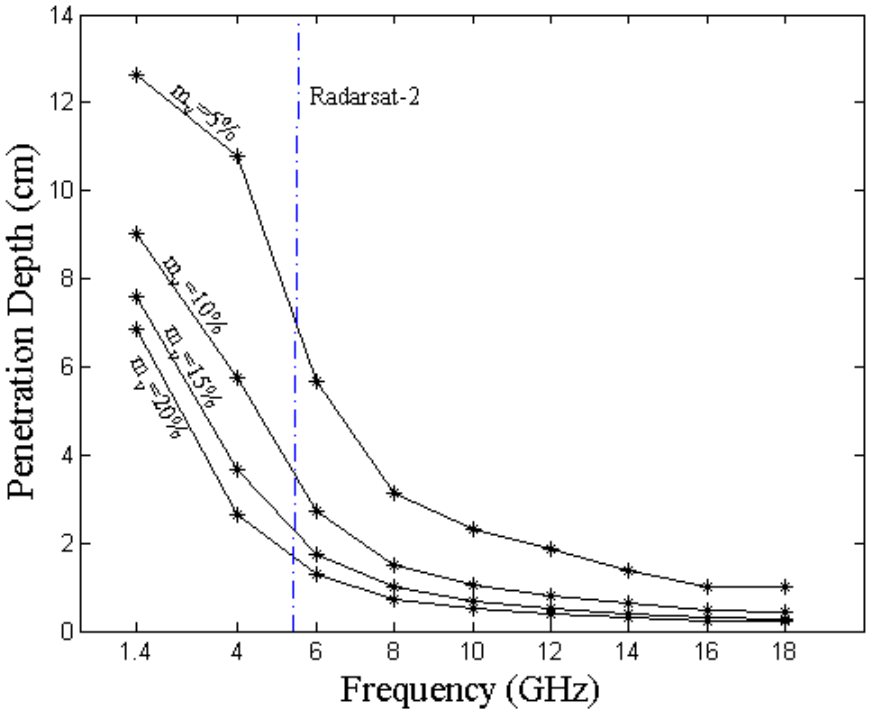

Figure 2.4: Penetration depth of waves with frequencies from 1.4 GHz to 18 GHz into a sandy-loam soil (65% sand, 5% clay and 30% silt) for four different moisture levels (5%, 10%, 15% and 20%). The blue (dash-dot) line shows the location of Radarsat-2 data frequency ($\approx$ 5.4 GHz).

Table 2.1: Coefficients used for ϵ' in the empirical model by Hallikainen et al. (1985)

Frequency (GHz)	a_0	a_1	a_2	b_0	b_1	b_2	c_0	c_1	c_2
1.4	2.862	-0.012	0.001	3.803	0.462	-0.341	119.006	-0.500	0.633
4	2.927	-0.012	-0.001	5.505	0.371	0.062	114.826	-0.389	-0.547
6	1.993	0.002	0.015	38.086	-0.176	-0.633	10.720	1.256	1.522
8	1.997	0.002	0.018	25.579	-0.017	-0.412	39.793	0.723	0.941
10	2.502	-0.003	-0.003	10.101	0.221	-0.004	77.482	-0.061	-0.135
12	2.200	-0.001	0.012	26.473	0.013	-0.523	34.333	0.284	1.062
14	2.301	0.001	0.009	17.918	0.084	-0.282	50.149	0.012	0.387
16	2.237	0.002	0.009	15.505	0.076	-0.217	48.260	0.168	0.289
18	1.912	0.007	0.021	29.123	-0.190	-0.545	6.960	0.822	1.195

Table 2.2: Coefficients used for ϵ'' in the empirical model by Hallikainen et al. (1985)

Frequency (GHz)	a_0	a_1	a_2	b_0	b_1	b_2	c_0	c_1	c_2
1.4	0.356	-0.003	-0.008	5.507	0.044	-0.002	17.753	-0.313	0.206
4	0.004	0.001	0.002	0.951	0.005	-0.010	16.759	0.192	0.290
6	-0.123	0.002	0.003	7.502	-0.058	-0.116	2.942	0.452	0.543
8	-0.201	0.003	0.003	11.266	-0.085	-0.155	0.194	0.584	0.581
10	-0.070	0.000	0.001	6.620	0.015	-0.081	21.578	0.293	0.332
12	-0.142	0.001	0.003	11.868	-0.059	-0.225	7.817	0.570	0.801
14	-0.096	0.001	0.002	8.583	-0.005	-0.153	28.707	0.297	0.357
16	-0.027	-0.001	0.003	6.179	0.074	-0.086	34.126	0.143	0.206
18	-0.071	0.000	0.003	6.938	0.029	-0.128	29.945	0.275	0.377

But, this assumption may not correspond to actual conditions of soil. Indeed, it has been empirically shown that this assumption is only valid for wet soils, while in dry soils SM increases as the depth increases (Le Morvan et al., 2008). Drier soil in upper layers of soil is expected because they are exposed more to air and sunlight, and due to infiltration[2] (Adams et al., 2013).

In order to address this deficiency in the models, researchers have tried to introduce variable SM profiles into the models. For example, Fung et al. (1996) proposed to use an *effective dielectric constant* in the Integral Equation Model (see section 3.2.2.1) which was calculated by an exponential dielectric constant transition model for dry soils. This method was later shown to be only valid for the top 3 mm layer of soil (Walker et al., 1997). A more recent algorithm for improving the Integral Equation Model was presented by Le Morvan et al. (2008) in which the soil medium was modelled as a three-layer dielectric. Their experiments with ground measurements showed that the simulations of backscattering coefficient by their proposed method was not different than the simulations of the Integral Equation Model when the soil was wet. According to (Le Morvan et al., 2008), the studies with the aim of investigating the effect of non-uniform SM profiles on the backscattered signal have made, in general, only slight improvements in SAR backscattering modeling.

[2]Infiltration is the process during which water penetrates into the soil profile (Hillel et al., 1998).

As can be seen in Figure 2.4, the penetration depth of microwave into the soil can be as small as 1 cm or less. However, the devices used for measuring SM for the purpose of calibration or validation of SM estimation by remote sensing methods usually yield an integrated measurement over a much larger depth (e.g., 0-5 cm). The selection of this measurement depth is because of the geometry of the available measurement devices (Escorihuela et al., 2010). In Figure 2.5 a schematic representation of the device used for ground measurements of this study is depicted. This device which is called ThetaProbe has four rods of 6 cm length and 2 mm diameter (Adams et al., 2013). When the rods are inserted into soil, the device can yield the value of SM for the soil between the rods. Although it is also possible to use this device in a horizontal state to measure SM at a smaller depth, this may not be always possible, and may need some digging into the soil to insert the rods into the soil horizontally. Thus, it is easier to use the device in a vertical state as shown in Figure 2.5. In the recent experiments of Adams et al. (2013) for estimating the average SM value for 72 field sites using a ThetaProbe at two depths of 3 cm and 6 cm, a strong linear correlation was found between the average SM of sites calculated at these two depths. However, they found the difference between the distribution of the SM values at these two depths to be statistically significant for 32% of the sites. It has been suggested by different studies that the difference between the operating depth of the SM measurement device and the microwave observation depth may result in systematic errors while evaluating the SM estimation algorithms (Escorihuela et al., 2010)(Bruckler et al., 1988).

The ground measurements used in this study are also carried out for the top 6 cm layer of the soil, and the penetration depth of the C-band radar waves used in this research may be different than the depth at which field SM has been measured. This mismatch may cause inaccuracies in evaluation of the algorithms. However, as we will see in Chapter 6, the calibration model proposed in this study for improving the results of SAR backscattering models is established using a relationship between the ground measurements and variations of

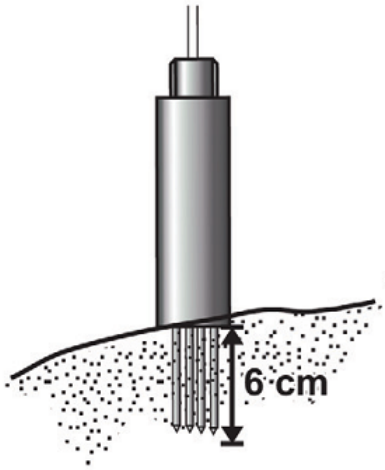

Figure 2.5: Schematic representation of a ThetaProbe (Delta-T Device Ltd., Cambridge, UK) (From (Adams et al., 2013))

the backscattering model outputs. This connection may be able to alleviate the inaccuracies caused by the depth mismatch.

2.5 Ground-Based Methods for SM Estimation

SM may be measured by three methods: direct gravimetric method, dielectric constant usage and neutron scatter detection (Schmugge et al., 1980). In the gravimetric method, soil is first sampled and then dried in an oven, so that we can have its weight before and after drying. The difference between the two weights shows the water content and can be further used to calculate SM percentage as the ratio of water weight to total weight. Given the volume of soil, one can further calculate volumetric SM. This is a direct destructive approach for SM estimation. Indirect non-destructive SM measurement is possible by sensing other properties of the soil, and then computing SM values by relating these properties to SM. Two of these properties are dielectric constant of the soil and hydrogen content.

As mentioned earlier, dielectric constant, also known as relative permittivity, is a parameter describing how a dielectric material acts when exposed to an electrical field. This parameter is measured in two major ways for soil: Time Domain Reflectometry (TDR) and Frequency Domain Reflectometry (FDR). TDR works by transmitting electromagnetic waves

through soil. Wave velocity is calculated by measuring the length of time required for the wave to propagate in soil. The velocity is related to dielectric constant of the soil, which in turn depends on volumetric soil water content (Dalton et al., 1986). Faster transit time means less humidity of soil. FDR is based on calculating the capacitance of soil, which is arranged to be part of a circuit (Dean et al., 1987). Soil capacitance is a property which shows how soil can keep electrical charge and is a function of dielectric constant. Therefore, detecting the amount of capacitance can yield the amount of SM.

Another class of SM sensors exists that is based on neutron scattering phenomenon. High-energy neutrons sent out by special radioactive material, like radium-beryllium (Wormald et al., 1969), are slowed down as a result of collision with hydrogen atoms, and make a neutron cloud. Density of this cloud, which is sensed in the device, is associated with the amount of hydrogen, or water, in soil (Chanasyk et al., 1996).

Although ground-based methods are the most accurate techniques for SM measurement, they are time consuming and their spatial coverage is limited.

2.6 Remote Sensing Methods for SM Estimation

Three different regions of electromagnetic spectrum have been investigated for estimation of SM: visible and near infrared, thermal infrared and microwave wavelengths (Carlson et al., 1995). The models used in these regions will be explained in the following sections.

2.6.1 Optical Sensors

The range of wavelengths covered by optical sensors is from visible to thermal infrared (0.7μm to 13μm). Therefore, they can yield information about the near-surface SM. According to (Haubrock et al., 2008), when dealing with high spectral resolution optical data, SM estimation with these data can also be used in improving the results of classification of these data. Because, SM can affect the background reflectance, and this annoying effect can be

reduced by identifying SM values.

Reflectance from visible and near-infrared (VNIR) is generally not suitable for SM estimation in outdoor applications (Mekonnen, 2009). Haubrock et al. (2008) review a number of approaches under three categories: single-band approaches (e.g., Relative Reflectance (Weidong et al., 2002)), multi-band approaches (e.g., WISOIL index (Whalley et al., 1991)(Bryant et al., 2003)) and spectral modeling approaches (e.g., Soil Moisture Gaussian Model (SMGM) (Whiting et al., 2004)). Most of the these methods have been developed under laboratory conditions where atmospheric errors have been eliminated, but are still sensitive to soil type.

Use of thermal infrared (TIR) data has produced more beneficial results compared to VNIR activities (Mekonnen, 2009). Physical principles are described in (Price, 1982) where it is shown how diurnal soil surface temperature, obtainable from airborne/spaceborne observations, is related to thermal inertia and water content of soil. The limitation of the methods which employ thermal inertia is that they are very sensitive to vegetation cover of the soil, thereby being only applicable on bare lands or lands with little vegetation (Wang et al., 2009).

Another method using both VNIR and TIR wavelengths exists that is based on calculation of surface radiative temperature (T_s) and spectral vegetation indices like Normalized Difference Vegetation Index (NDVI) (Moran et al., 2004). The two factors are dependent on SM via a complex relationship (Chauhan et al., 2003), and for estimating SM, a scatter plot of surface temperature versus the Vegetation Index (VI) for image pixels is created. The method is usually called *Triangle Method*, because the scatter plot, if sufficiently large number of image pixels are considered, will be similar to a triangle, called *universal triangle*, or a truncated trapezoid (Carlson, 2007). Universal triangle is depicted in Figure 2.6. In this figure, horizontal and vertical axes show radiative temperature and NDVI respectively, and O and S indices are for their minimum and maximum values.

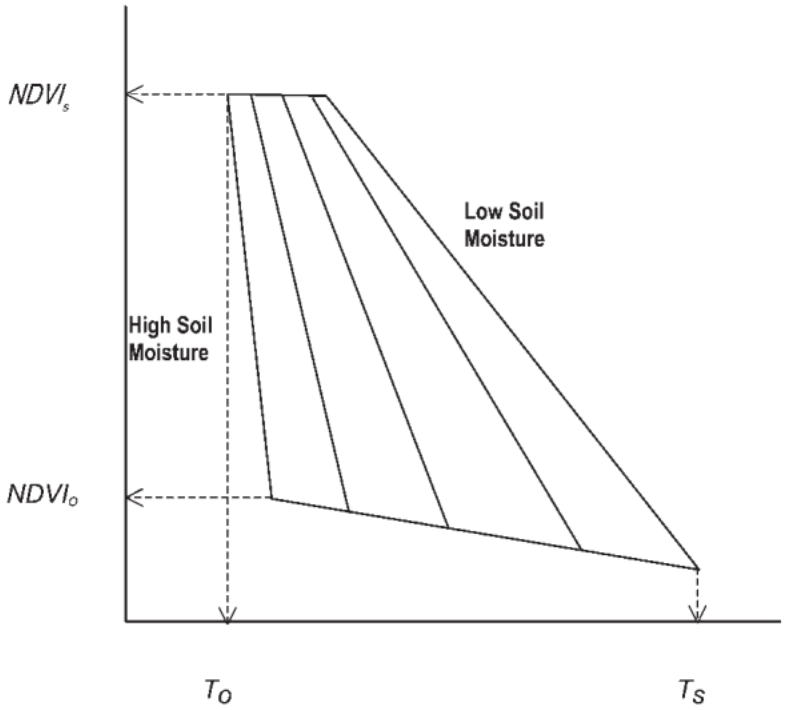

Figure 2.6: Universal triangle (adapted from (Chauhan et al., 2003))

If T and NDVI are scaled by

$$T^* = \frac{T - T_O}{T_S - T_O} \tag{2.12}$$

$$NDVI^* = \frac{NDVI - NDVI_O}{NDVI_S - NDVI_O} \tag{2.13}$$

SM can be written as a third order polynomial (Carlson, 2007)

$$m_v = \sum_{i=0}^{3} \sum_{j=0}^{3} a_{ij} {T^*}^i {NDVI^*}^j \tag{2.14}$$

where a_{ij} needs to be calculated using field measurements. The most important problem with the triangle method is that interpretation of the scatter plot is subjective, it needs a large number of image pixels and it is difficult to identify the shape of the triangle (Carlson, 2007).

Optical RS has seen less improvements in the field of SM estimation in recent years compared to microwave RS (Anderson et al., 2009). Since the final spatial resolution of SM map can be much better than what microwave methods can generate, it seems that more research work is required on this area.

2.6.2 Passive Microwave

Passive microwave has been a greatly successful and progressive part of RS in estimation of SM (Moran et al., 2004). The quantity measured by passive microwave sensors is the intensity of microwave emission that is proportional to brightness temperature T_B (Wang et al., 2009). The brightness temperature, when only related to soil surface, equals the product of soil physical temperature and its emissivity (Bindlish, 2000):

$$T_B = e.T \tag{2.15}$$

where e is emissivity, unity for a blackbody, and T is the true temperature of the soil in Kelvins (Njoku et al., 1996). According to Kirchoff's reciprocity theorem (Njoku et al., 1996):

$$e = 1 - r \tag{2.16}$$

with r being reflectivity of soil. For a smooth unvegetated soil, reflectivity can be related to dielectric constant through Fresnel equations (Engman et al., 1995)(Zheng et al., 2010):

$$R_H = \frac{\cos\theta - \sqrt{\epsilon_r - \sin^2\theta}}{\cos\theta - \sqrt{\epsilon_r + \sin^2\theta}} \tag{2.17}$$

$$R_V = \frac{\epsilon_r\cos\theta - \sqrt{\epsilon_r - \sin^2\theta}}{\epsilon_r\cos\theta - \sqrt{\epsilon_r + \sin^2\theta}} \tag{2.18}$$

where R_H and R_V are reflectivity in horizontal and vertical polarization, ϵ_r is the dielectric constant and θ is incidence angle (Wang, 2008). Although according to these simple equations, given the large signal to noise ratio of passive microwave radiometers and large difference in emissivity of wet and dry soil, SM should be estimated with accuracies better than 2 vol.%, this is not possible in practice (Njoku et al., 1996). The reason is the existence of many disturbing factors like surface roughness, vegetation cover, soil heterogeneity, topography (Mätzler et al., 2000), soil texture and temperature variability. Different ways have been suggested to alleviate the effect of the parameters which contribute to emission

from soil (Wigneron et al., 2003); however, surface roughness and vegetation correction are the only two corrections which are usually applied (Jackson, 1993) (Wang et al., 2009).

The most-widely used model for roughness correction is simple Q/H model (Wang et al., 2009) proposed by Choudhury et al. (1979) using nadir observations and then generalized for any arbitrary incidence angle in (Wang et al., 1981). When working with wavelengths longer than 5 cm (Bindlish, 2000) or in large-scale SM mapping (Wigneron et al., 2003), the magnitude of error caused by roughness is negligible as well and can be left out. But, before reflectivity values from above mentioned model can be used in Fresnel equations, the effect of vegetation should be removed as well, and this in turn needs the vegetation temperature. Obtaining the physical temperatures of soil and/or vegetation layer is possible using concurrent satellite thermal infrared image acquisitions (Jackson, 1993).

Some of the currently-available passive microwave sensors aboard earth observation satellites are listed in Table 2.3. As seen in the table, the spatial resolution of these sensors is usually in the order of a few kilometers and this makes them more useful for global and regional hydrological purposes.

2.6.3 Synthetic Aperture Radar (SAR)

SAR sensors seem suitable for large scale SM estimation, because of their high resolution, independence upon weather conditions, and sensitivity to the SM. As a microwave sensor, SAR is sensitive to the changes in dielectric constant of the soil, and the dielectric constant of a dry soil (about 5) is very different than the dielectric constant of water (about 80). The value of the dielectric constant itself can be converted to the SM value using a *dielectric mixing* model. Thus, quantifying the level of the SM seems to be more accurate by SAR (as a microwave sensor) than an optical sensor.

In SAR remote sensing of SM, differences in the electromagnetic dielectric properties

Table 2.3: Available passive microwave radiometers (Njoku et al., 2003)(Viltard et al., 2006)(Dente et al., 2012)(Hollinger et al., 1990)

Sensor	**Satellite**	**Spatial Resolution (km)**	**Frequencies (GHz)**
AMSR-E (The Advanced Microwave Scanning Radiometer on Earth Observing System)	Aqua	76×44, 49×28, 28×16, 31×18, 14×8 and 6×4	6.92, 10.65, 18.7, 23.8, 36.5 and 89.0
TMI (TRMM Microwave Imager)	TRMM (Tropical Rainfall Measuring Mission)	7×5 (85.5 GHz) to 37×63 (10.7 GHz)	10.65, 19.35, 21.3, 37.0, 85.5
MIRAS (Microwave Imaging Radiometer using Aperture Synthesis)	SMOS (Soil Moisture and Ocean Salinity)	35 to 50	1.4
SSM/I (Special Sensor Microwave/Imager)	DMSP (Defense Meteorological Satellite Program) satellites	69×43, 60×40, 37×28 and 15×13	19.35, 22.235, 37.0 and 85.5

of soil is used for quantifying different levels of moisture. The ground surface affects the signal emitted by sensor depending on the amount of SM. This changes the amplitude of the backscattering coefficient, σ°, and the amount of change is related to, among other parameters, the dielectric properties of the soil. The backscattering coefficient of a surface can be shown as the product of two functions: (Sun et al., 2009)

$$\sigma^\circ(\theta) = f_n(\epsilon_r, \theta)\, f_s(\rho, \theta) \tag{2.19}$$

where θ is the local incidence angle, $f_n(\epsilon_r, \theta)$ is the dielectric function which depends on the relative dielectric constant of the surface, ϵ_r, and $f_s(\rho, \theta)$ is the roughness function which depends on surface roughness ρ. ϵ_r, in turn, depends on the volumetric moisture content of the soil. Thus, having the backscattering coefficient and surface roughness information,

or having the backscattering coefficient in different polarizations, the dielectric constant will be obtainable. The SAR signal can also be attenuated and scattered by the vegetation on the soil. Thus, the vegetation cover can degrade the quality of estimation of SM, and best accuracies in SM estimation can be obtained for bare or thinly-vegetated soils (Behari, 2005). The methods proposed for alleviating the effect of vegetation on SM estimation by SAR include using target decomposition techniques (e.g. (Hajnsek et al., 2009)) and using multi-incidence-angle SAR data (e.g. (Srivastava et al., 2009)) to segregate the contribution of soil and vegetation to the backscattered signal. The data set used in this study has been collected from bare soils. Thus, in this study, we focus on the methods used in estimation of SM for such soils.

Since SAR images are the remotely sensed images used in this study, the exact procedures and different methods of estimating SM by SAR will be the subject of a whole upcoming chapter, and here it is sufficed to the above brief explanation.

2.6.4 Real Aperture Radar (RAR)

RAR sensors are active sensors which work in the microwave region of the electromagnetic spectrum, but unlike SAR sensors, their final observation of a target is not formed by combining multiple observations of the target. These sensors, which are also called scatterometers, have also been used in estimation of near-surface SM. Although, they have not been originally designed for this application.

Since the models proposed for estimation of SM using SAR sensors are based on the operation of radars, theoretically, they should be usable for scatterometers as well. Scatterometer systems generally have weaker spatial resolution than SAR systems, but provide better temporal resolution (Scipal, 2002). This temporal resolution along with specific image acquisition characteristics has been utilized in estimation of SM by these sensors.

In scatterometry researchers have concentrated most of their effort on the use of empirical models (Scipal, 2002). For example, in (Magagi et al., 2001) an algorithm is proposed which

uses a modification of the Oh empirical model (see section 3.2.3.1) to estimate SM with ERS-1[3] wind scatterometer (WSC) data. The ERS-1 WSC was a C-band scatterometer with spatial resolution of about 50 km originally designed for estimating the speed and direction of wind over oceans. The WSC had three antennas (fore-beam, mid-beam and aft-beam) which measured the backscattering coefficient of a target at two different incidence angles[4] and three different azimuth angles. The above-mentioned algorithm first separates the contribution of soil and vegetation to the backscattering coefficient, and then models the contribution of soil to obtain SM value. It is assumed that the total backscattering of a pixel can be written as (Magagi et al., 2001)

$$\sigma^{\circ}(\theta) = (1 - C_v)\sigma^{\circ}_{soil}(\theta) + C_v \left(\sigma^{\circ}_{veg}(\theta) + \gamma^2(\theta)\sigma^{\circ}_{soil}(\theta)\right) \tag{2.20}$$

where θ is the incidence angle, C_v is the proportion of the vegetation in the pixel obtained from NOAA/AVHRR[5] data, γ^2 is the vegetation two-way transmitting factor, and σ°_{veg} is the contribution of vegetation obtained using a separate empirical model. Given the contribution of soil in backscattering coefficient, the algorithm then proceeds to estimating the dielectric constant of soil by coupling the Oh model and a linear relationship.

Another empirical algorithm which has been successfully used for scatterometers aboard ERS-1, ERS-2 and METOP-A satellites is called TU-Wien model(Naeimi et al., 2009). This algorithm, which was originally proposed by Wagner et al. (Wagner et al., 1999), exploits both the multi-incidence angle property of these scatterometers and their high temporal resolution. In TU-Wein model, first, the backscattering coefficients measured for a pixel at different incidence angles are normalized to a reference incidence angle selected as 40° using

$$\sigma^{\circ}(40, t) = \sigma^{\circ}(\theta, t) - \sigma'(40, t)(\theta - 40) - \frac{1}{2}\sigma''(40, t)(\theta - 40)^2 \tag{2.21}$$

[3]European Remote Sensing Satellite 1

[4]The aft and fore antennas had close incidence angles, but their incidence angles were different than the mid antenna.

[5]National Oceanic and Atmospheric Administration/Advanced Very High Resolution Radiometer

where $\sigma^{\circ}(40,t)$ is the normalized backscattering coefficient, $\sigma^{\circ}(\theta,t)$ is the backscattering coefficient measured at time t and incidence angle θ, and σ' and σ'' represent the slope and curvature of σ°, respectively. The values of the slope and the curvature have been calculated for different days of the year using a large database of historical images acquired by the senor. In the next step, the value of the normalized backscattering coefficient is compared to its highest ($\sigma^{\circ}_{wet}(40,t)$) and lowest values ($\sigma^{\circ}_{dry}(40,t)$) ever calculated, and the degree of saturation of soil is obtained by

$$\Theta_s(t) = \frac{\sigma^{\circ}(40,t) - \sigma^{\circ}_{dry}(40,t)}{\sigma^{\circ}_{wet}(40,t) - \sigma^{\circ}_{dry}(40,t)} \tag{2.22}$$

This algorithm has been used in production of the first remotely sensed global SM data set (Naeimi et al., 2009).

We conclude this chapter by presenting Table 2.4 which summarizes the advantages and disadvantages of the methods discussed in this chapter. As shown in this table, SAR has promising properties for large-scale estimation of the SM. Although the algorithms developed for the passive microwave and RAR sensors are more mature than SAR methods, their low spatial resolution is far from sufficient for many field-scale applications, which are the ones considered in this research.

Table 2.4: Comparison of SM estimation methods

Method	**Advantage**	**Disadvantage**
Ground-Based	Very accurate (specially in terms of relative accuracy)	Small measurement volume Time and labour consuming Small area coverage
Optical Data	Large area coverage High spatial resolution Availability of several satellites	Weak physical dependence (for VNIR) Location dependence Requires meteorological and atmospheric information Requires field SM measurements Small penetration in soil
Passive Microwave Data	Large area coverage Less affected by roughness Not affected by atmosphere (Except for rainfall) Less sensitive to topography Mature algorithms Relatively deep penetration in soil	Coarse resolution Needs ancillary information (surface temperature, land cover and vegetation type)
Synthetic Aperture Radar	Strong physical dependence High spatial resolution Relatively deep penetration in soil	Affected by roughness and vegetation Medium data availability Affected by topography Limitation in swath width
Real Aperture Radar	Strong physical dependence Mature algorithms High temporal resolution Relatively deep penetration in soil	Coarse spatial resolution Affected by vegetation Current operational algorithms need historical data

Chapter 3

Soil Moisture Estimation Models for Synthetic Aperture Radar

As mentioned earlier, the data used in this study for estimation of SM is from SAR sensors. The estimation is carried out through a number of surface backscattering models. In this chapter, it is aimed to explain how these models can be utilized for our purpose. Before we can discuss the mathematical details of the models, introducing some fundamental concepts of SAR is necessary.

3.1 Synthetic Aperture Radar (SAR)

An active sensor in RS is a sensor that does not rely on the natural emissions from objects. Instead, it illuminates the objects and then measures the reflected wave. Synthetic aperture radar is an active sensor which emits radio frequency pulses onto the surface of the earth and collects the backscattered signal. It then synthesizes a two-dimensional image by processing the collected signals (Lee et al., 2009). The distinctive characteristic of SAR compared to other radars is that its final observation of a target is formed by combining multiple observations of the target. These observations are made possible by mounting the SAR antenna on a moving platform. SAR works in a side-looking manner as shown in Figure 3.1. The SAR system in this figure is moving along the velocity vector V_{SAR} at height H. The direction of V_{SAR} is called *azimuth direction*, and the direction perpendicular to it in which SAR looks is *range direction*. The *incidence angle* θ_O is the angle that the antenna beam makes with the vertical direction at the sensor. The angle that the antenna beam makes with the local vertical direction at the target (incidence surface) is called *local incidence*

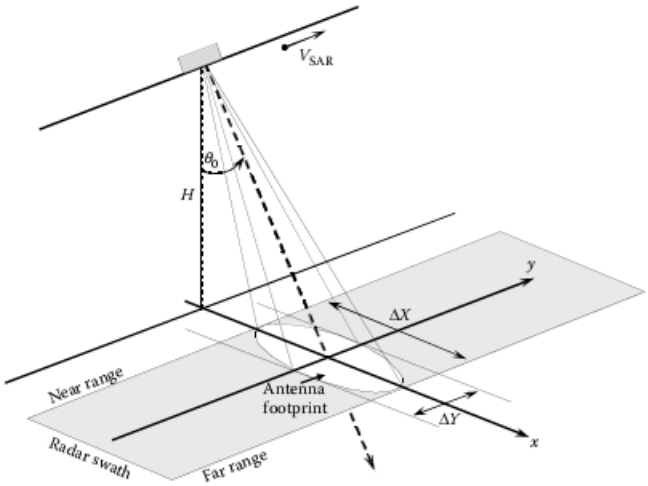

Figure 3.1: SAR geometry (adapted from (Lee et al., 2009))

angle. The area illuminated by the antenna beam is called the *antenna footprint.* ΔX and ΔY are *range swath* and *azimuth swath*, respectively. The notation of equations presented in this section will mainly follow the book by Lee and Pottier (Lee et al., 2009).

The electric field vector of a monochromatic[1] plane electromagnetic wave with constant amplitude $\mathbf{E_0}$ propagating in the direction z of an orthogonal three-dimensional coordinate system can be expressed as

$$\mathbf{E}(z,t) = \begin{bmatrix} E_{0x}cos(\omega t - kz + \delta_x) \\ E_{0y}cos(\omega t - kz + \delta_y) \\ 0 \end{bmatrix} \tag{3.1}$$

where ω is the angular frequency, $k = \frac{2\pi}{\lambda}$ is the wavenumber (λ being the wavelength), and δ_x and δ_y show the phase difference. The locus of the tip of this vector in a plane perpendicular to the direction of propagation is, in general, an ellipse which is called *polarization ellipse*, and is depicted in Figure 3.2. The shape of the polarization ellipse can be fully described by three parameters:

- *Ellipse amplitude* A:

$$A = \sqrt{E_{0x}^2 + E_{0y}^2} \tag{3.2}$$

[1] A monochromatic wave is a wave with constant frequency.

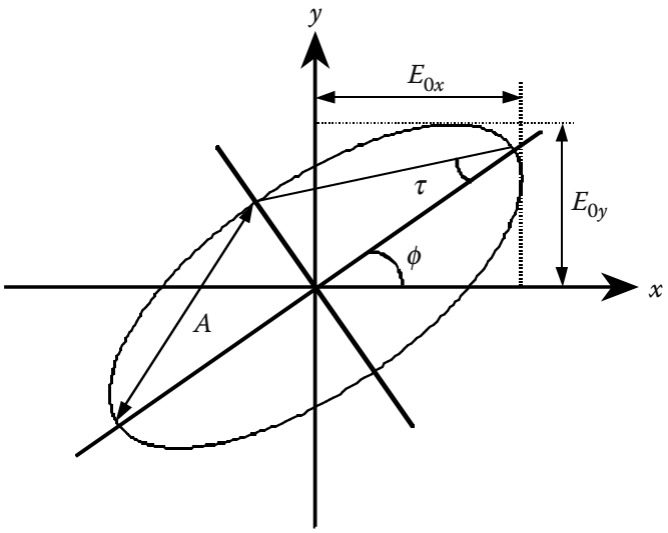

Figure 3.2: Polarization ellipse (from (Lee et al., 2009))

- *Orientation angle* $\phi \in \left[-\frac{\pi}{2}, \frac{\pi}{2}\right]$:

$$\tan(2\phi) = 2\frac{E_{0x}E_{0y}}{E_{0x}^2 - E_{0y}^2}\cos(\delta_y - \delta_x) \tag{3.3}$$

- *Ellipticity angle* $\tau \in \left[-\frac{\pi}{4}, \frac{\pi}{4}\right]$:

$$|\sin 2\tau| = 2\frac{E_{0x}E_{0y}}{E_{0x}^2 + E_{0y}^2}\,|\sin(\delta_y - \delta_x)| \tag{3.4}$$

These parameters are shown in Figure 3.2.

If $\delta_y - \delta_x$ is a multiple of π then the ellipse reduces to a line, and the wave is said to have *linear polarization*. In case $\delta_y - \delta_x = \frac{\pi}{2} + k\pi$ and $E_{0x} = E_{0y}$, the ellipse has equal semi-axes, and the polarization is circular. When the wave has neither linear nor circular polarization, it is said to have *elliptic* polarization. When the polarization is linear, *horizontal* and *vertical* polarization can be defined using the orientation angle. The linear horizontal and linear vertical polarization happen when $\phi = 0$ and $\phi = \frac{\pi}{2}$, respectively. In other words, if the tip of the electric vector field traverses a horizontal line in the plane orthogonal to the direction of wave propagation, the wave has horizontal polarization, and if the tip traverses a vertical line, the state of the polarization is vertical.

The state of the polarization of such an electric field can be equivalently represented

using the so-called *Jones vector*, which is defined as

$$\underline{\mathbf{E}} = \begin{bmatrix} E_x \\ E_y \end{bmatrix} = \begin{bmatrix} E_{0x}e^{j\delta_x} \\ E_{0y}e^{j\delta_y} \end{bmatrix} \tag{3.5}$$

This is a complex vector containing both phase and amplitude information. The Jones vector can only describe the polarization of wave if the wave is *fully-polarized*, i.e. the tip of its electric vector field can be described by parameters of the polarization ellipse. If this is not the case, the Jones vector changes with time. If this changes can be associated with random processes, the wave is called *partially-polarized* (Huynen, 1970).

When a polarized electromagnetic wave reaches a target, the target absorbs part of the energy that the wave carries, and the rest is emitted as another wave. The part of the emitted wave which is backscattered towards the SAR receiving antenna can be depolarized. This can happen because the target can be a *distributed target*. A distributed target is composed of a set of point targets for which the backscattered wave is received by the receiving antenna in different times (Lee et al., 2009). This can happen because of the changes in position of sensor or target (Huynen, 1970). The backscattered waves from a distributed target are generally partially-polarized.

The state of the polarization of a partially-polarize wave can be described by the so-called *Stokes vector*:

$$\underline{\mathbf{g}}_{\underline{\mathbf{E}}} = \begin{bmatrix} g_0 \\ g_1 \\ g_2 \\ g_3 \end{bmatrix} = \begin{bmatrix} |E_x|^2 + |E_y|^2 \\ |E_x|^2 - |E_y|^2 \\ 2\mathrm{Re}\left\{E_x E_y^*\right\} \\ -2\mathrm{Im}\left\{E_x E_y^*\right\} \end{bmatrix} \tag{3.6}$$

where * and $|.|$ show the complex conjugate and the absolute value, respectively. The elements of this vector are real and the vector can be constructed using power measurements alone (Lee et al., 2009). Using this vector, the *degree of polarization* of the wave can be obtained as

$$\mathrm{DoP} = \frac{\sqrt{g_1^2 + g_2^2 + g_3^2}}{g_0} \tag{3.7}$$

For a fully-polarized wave DoP = 1, whereas in case of a partially-polarized wave 0 < DoP < 1. Since the SAR data used in this study are in complex domain, we do not use Stokes vector in this thesis.

When a target is illuminated by SAR signals it changes the polarization properties of the incident wave in return. Using the Jones vectors of the incident and scattered waves, $\underline{\mathbf{E}}_I$ and $\underline{\mathbf{E}}_S$, we can write

$$\underline{\mathbf{E}}_S = \frac{e^{jkr_R}}{r_R} S \underline{\mathbf{E}}_I = \frac{e^{jkr_R}}{r_R} \begin{bmatrix} S_{11} & S_{12} \\ S_{21} & S_{22} \end{bmatrix} \underline{\mathbf{E}}_I \tag{3.8}$$

in which S is called the *scattering matrix*, and shows how the incident wave is affected by a point scatterer . r_R is the distance between the object and the receiver in meters. The SAR data used in this study have been acquired in horizontal and vertical polarizations, i.e. the images contain hh, vv, hv and vh channels. Thus, the scattering matrix can be stated as

$$[S] = \begin{bmatrix} S_{hh} & S_{hv} \\ S_{vh} & S_{vv} \end{bmatrix} \tag{3.9}$$

SAR images are complex images containing both amplitude and phase information, i.e. a complex number is provided for each pixel in each channel of the image. In case of the Radarsat-2 data in this study, a lookup table (LUT) is provided along with the image data by which complex numbers in each image can be converted to the scattering matrix for each pixel.

In case of a distributed target, the statistical properties of the scattering matrix can be analyzed using *polarimetric coherency matrix,* which is a second-order scattering statistic of surface scatterers, and is calculated as

$$[T] = \frac{1}{2} \begin{bmatrix} \left\langle |S_{hh} + S_{vv}|^2 \right\rangle & \langle (S_{hh} + S_{vv})(S_{hh} - S_{vv})^* \rangle & 2 \langle (S_{hh} + S_{vv}) S_{hv}^* \rangle \\ \langle (S_{hh} + S_{vv})(S_{hh} - S_{vv})^* \rangle & \left\langle |S_{hh} - S_{vv}|^2 \right\rangle & 2 \langle (S_{hh} - S_{vv}) S_{hv}^* \rangle \\ 2 \langle (S_{hh} + S_{vv}) S_{hv}^* \rangle & 2 \langle (S_{hh} + S_{vv}) S_{hv}^* \rangle & 4 \left\langle |S_{hv}|^2 \right\rangle \end{bmatrix} \tag{3.10}$$

where $\langle . \rangle$ is the averaging operator. This matrix is obtained from the outer product of *Pauli scattering vector* defined as

$$k_p = \frac{1}{\sqrt{2}} \begin{bmatrix} S_{hh} + S_{vv} \\ S_{hh} - S_{vv} \\ 2S_{hv} \end{bmatrix} \tag{3.11}$$

i.e.

$$[T] = \left\langle k_p k_p^{*^T} \right\rangle \tag{3.12}$$

The coherency matrix is directly used only in one of the scattering models (X-Bragg) introduced in this chapter. The rest of the models use the concept of backscattering coefficient which will be explained in the following.

The properties of the backscattered wave depend not only on the properties of the wave transmitter (frequency, polarization, incidence angle and azimuth angle), but also on the dielectric properties of the object and its geometrical structure (Lee et al., 2009). This interaction for radar is quantified using the *radar equation* expressed as

$$P_R = \frac{P_T G_T}{4\pi r_T^2} \sigma \frac{A_{ER}}{4\pi r_R^2} \tag{3.13}$$

The elements of this equation are as follows:

- P_R: the power received by radar in watts
- P_T : the power transmitted by radar in watts
- G_T: gain of the transmitting antenna
- A_{ER}: the effective aperture of the receiving antenna in squared meters
- r_T: the distance between transmitter and the object in meters
- r_R[2]: the distance between the object and the receiver in meters

[2]In case of a monostatic radar, for which the transmitter and receiver are at the same location, $r_T = r_R$.

- σ: the *Radar Cross Section* (RCS) in squared meters

The RCS is the parameter which determines how the object affects the wave. It is defined as the cross section of an equivalent isotropic scatterer that produces the same amount of power density as the object. Mathematically, it can be defined as the ratio of total power scattered by an equivalent isotropic scatterer to the power density incident on the object (Fung, 1994):

$$\sigma = 4\pi r_R^2 \frac{|\mathbf{E}_S|^2}{|\mathbf{E}_I|^2} \tag{3.14}$$

where $\mathbf{E}_S$ and $\mathbf{E}_I$ are the scattered and incident fields, respectively. The equation 3.13 can be used for a single scatterer; however, if the object is area-extensive, it can be assumed to be composed of multiple scatterers. In this case, the final scattered field is the result of all the single fields summed over the illuminated area A_0:

$$P_R = \iint_{A_0} \frac{P_T G_T}{4\pi r_T^2} \sigma^\circ \frac{A_{ER}}{4\pi r_R^2} ds \tag{3.15}$$

σ° is the *backscattering coefficient* defined as the average radar cross section per unit area:

$$\sigma^\circ = \frac{\langle\sigma\rangle}{A_0} = \frac{4\pi r_R^2 \langle\sigma\rangle}{A_0} \frac{\left\langle |\mathbf{E}_S|^2 \right\rangle}{|\mathbf{E}_I|^2} \tag{3.16}$$

The backscattering coefficient is the quantity employed as the SAR observation in most of the SAR-based scattering models.

As mentioned before, the RCS, and thus, the backscattering coefficient depends on the polarization of the incident and backscattered wave. Therefore, equation (3.16) can be re-written as

$$\sigma^\circ_{qp} = \frac{4\pi r_R^2 \langle\sigma\rangle}{A_0} \frac{\left\langle \left|\mathbf{E}_{S_q}\right|^2 \right\rangle}{\left|\mathbf{E}_{I_p}\right|^2} \tag{3.17}$$

where p and q denote the polarization state of the incident and scattered fields, respectively. The elements of the scattering matrix are related to backscattering coefficient as

$$\sigma^\circ_{qp} = 4\pi \left|S_{qp}\right| \tag{3.18}$$

3.2 Surface Scattering Models

The relationship between the moisture of a typical soil and SAR observations (e.g. σ°) is usually established through a mathematical model. Many models have been used in the literature which have been categorized by different authors by different naming conventions, but the major categories which can be recognized are:

- Statistical models (e.g. (Pultz et al., 2002)(Biftu et al., 1999))
- Physical models (e.g. (Fung et al., 1992)(Fung et al., 1996)(Biftu et al., 1999))
- Empirical (semi-empirical) models (e.g. (Oh et al., 1992)(Dubois et al., 1995))

3.2.1 Statistical Models

These models indeed form the simplest set of methods for inverting the backscattering coefficient to SM or dielectric constant. While statistical methods are relatively easily implemented, they are not reusable for the fields and images other than those for which they were developed (Pietroniro et al., 2005). As an example, Pultz et al. (2002) use the linear equations $\sigma^\circ = -8.49 - 9.46m_v$ and $\sigma^\circ = 15.76 + 7.72m_v - 1.04\theta$ to relate Radarsat-1 backscattering coefficients to moisture and incidence angle.

3.2.2 Physical Models

Physical models are based on theoretical aspects of wave-soil interaction. They predict the radar backscattering coefficient from radar system parameters and soil properties. Although these models have limitations in dielectric constant and roughness range, they are independent of the field they are utilized for.

3.2.2.1 Integral Equation Model (IEM)

The Integral Equation Model is one of the most rigorous models used for estimation of surface parameters from measurements and parameters of a polarimetric SAR system. For the

special case of soil, the IEM is commonly used to retrieve the SM and roughness parameters (RMS height and correlation length). IEM was first proposed by Fung et al. (1992), and then further modified by other researchers and original inventors. Unlike other physical models, e.g. Small Perturbation Model (SPM), Physical Optics Model (POM) and Geometrical Optics Model (GOM), IEM is not limited to either a smooth or rough surface or a specific frequency range and thus, it seems to be suitable for agricultural soils (Alvarez-Mozos et al., 2007).

IEM establishes a relation between radar backscattering coefficients, dielectric constant and roughness parameters of the surface, and the local incidence angle. The co-polarized backscattering coefficient in general form of IEM is expressed as (Fung et al., 2004)

$$\sigma^{\circ}_{pp} = \frac{k^2}{4\pi} exp(-2k^2\sigma^2 cos^2\theta) \sum_{n=1}^{+\infty} \left|I^n_{pp}\right|^2 \frac{W^{(n)}(2k\, sin\theta, 0)}{n!} \tag{3.19}$$

where

$$I^n_{pp} = (2\,k\,\sigma\, cos\theta)\, f_{pp}\, exp(-k^2\sigma^2 cos^2\theta) + (k\,\sigma\, cos\theta)^n\, F_{pp} \tag{3.20}$$

σ°_{pp} is the backscattering coefficient of pp polarization (hh or vv), k is wavenumber ($k = \frac{2\pi}{\lambda}$, λ is the wave length) which is 1.132 cm^{-1} for Radarsat-2, θ is the local incidence angle, σ is surface RMS height, $W^{(n)}$ is the Fourier transform of the n^{th} power of the surface correlation function, which will be described shortly, and f_{hh}, f_{vv}, F_{hh} and F_{vv} are approximated by

$$f_{hh} = \frac{-2R_h}{cos\theta} \tag{3.21}$$

$$f_{vv} = \frac{2R_v}{cos\theta} \tag{3.22}$$

$$F_{hh} = 2\frac{sin^2\theta}{cos\theta}\left[4R_h - \left(1 - \frac{1}{\epsilon_r}\right)(1 + R_h)^2\right] \tag{3.23}$$

$$F_{vv} = 2\frac{sin^2\theta}{cos\theta}\left[\left(1 - \frac{\epsilon_r cos^2\theta}{\epsilon_r - sin^2\theta}\right)(1 - R_v)^2 - \left(1 - \frac{1}{\epsilon_r}\right)(1 + R_v)^2\right] \tag{3.24}$$

Here, R_h and R_v are the horizontally and vertically polarized *Fresnel reflection coefficients*, respectively, defined as

$$R_h = \frac{cos\theta - \sqrt{\epsilon_r - sin^2\theta}}{cos\theta + \sqrt{\epsilon_r - sin^2\theta}} \tag{3.25}$$

$$R_v = \frac{\epsilon_r cos\theta - \sqrt{\epsilon_r - sin^2\theta}}{\epsilon_r cos\theta + \sqrt{\epsilon_r - sin^2\theta}}. \tag{3.26}$$

and ϵ_r is the dielectric constant. A relative magnetic permeability parameter (μ_r) also exists in the original equations which has been deleted here, because we intend to use the IEM to estimate the moisture of soil whose relative magnetic permeability is assumed to be unity. This simplifies the equations to the form mentioned in equations (3.23) to (3.26).

Given the correlation function, $C(\rho)$, the surface power spectrum, $W^{(n)}$ in equation (3.19), can be calculated by taking its Fourier transform or equivalently using (Nesti et al., 1997)

$$W^{(n)}(K) = \int_{\rho=0}^{\rho=+\infty} C^n(\rho) \cdot \rho \cdot J_0(K\rho) d\rho \tag{3.27}$$

where J_0 is the Bessel function of the zeroth order. This can be readily carried out analytically for both Gaussian and exponential functions, but for fractal functions the only solution is to take Fourier transform numerically (Li et al., 2002). Hence, a generalized power law spectrum has been introduced by Li et al. (2002) which generates Gaussian, exponential or an intermediate shape based on the value of its parameter, *power index*. The proposed spectrum is

$$W(K) = \frac{\sigma^2 l}{\sqrt{4\pi}} \cdot \frac{1}{b_p} \left[1 + \left(\frac{a_p}{b_p} \right)^2 \frac{K^2 l^2}{4} \right]^{-p} \tag{3.28}$$

where $a_p = \frac{\Gamma(p-0.5)}{\Gamma(p)}$ and b_p is computed by solving equation

$$\left[\frac{2b_p}{a_p} \right]^{p-0.5} K_{p-0.5} \left(\frac{2b_p}{a_p} \right) = 2^{p-1.5} \Gamma(p - 0.5)\, e^{-1} \tag{3.29}$$

where $K_{p-0.5}(.)$ is modified Bessel function of second kind, $\Gamma(.)$ is gamma function, and p is the power index, which is a real number greater than or equal to 1. The corresponding correlation function of this spectrum is analytically derived as

$$C(\rho) = \frac{\sigma^2}{2^{p-1.5}\Gamma(p-0.5)} \left[\frac{2b_p}{a_p} \cdot \frac{\rho}{l} \right]^{p-0.5} K_{p-0.5} \left(\frac{2b_p}{a_p} \cdot \frac{\rho}{l} \right) \tag{3.30}$$

Here, when power index goes to infinity, we have Gaussian power spectrum, and when power index is equal to 1, we get exponential one. Other values yield intermediate spectra. Given

the spectrum in (3.28), the n^{th} power of the surface power spectrum is approximated by

$$W^{(n)}(K) \simeq 0.5(\frac{l}{n^{f_p}})(p-1)\left(\frac{a_p}{b_p}\right)^2\left[1+\left(\frac{a_p}{b_p}\right)^2\frac{K^2(\frac{l}{n^{f_p}})}{4}\right]^{-p} \tag{3.31}$$

where

$$f_p = 0.5\left[1+\left(\frac{1.5}{p}\right)^2\right] \tag{3.32}$$

The IEM has been modified by other researchers since it was originally introduced by Fung et al. (1992). The changes have been usually applied to remove approximations made in the original IEM. For example, Hsieh et al. (1997) proposed IIEM, in which an assumption about Green's function in the IEM was removed to improve modeling multiple scattering. Álvarez-Pérez (2001) introduced IEM2M to make the IEM reduce to SPM for small roughness values. Advanced IEM (AIEM) was also created to remove some approximations about Green's function (Chen et al., 2003). However, the original version of the model is the one that is used most often (Baghdadi et al., 2006b). Furthermore, the calibration procedure proposed by Baghdadi et al. (2006a), which we use in this study for decreasing the number of unknowns in the IEM, and will be introduced in the few next paragraphs, was developed using the original version of the IEM. Therefore, we have adopted the original version of the IEM in this thesis for the purpose of our study.

Unfortunately, with the IEM, it is not possible to calculate the dielectric constant and roughness parameters separately, as there is no closed form equation for these unknowns. Thus, inversion of the IEM, i.e. solving the IEM equations for soil surface parameters, is not possible using analytical methods as is possible with models such as the Dubois model (see section 3.2.3). When using co-polarized backscattering coefficients in the IEM, we have two equations and three unknowns. In order to solve this under-determined problem, we have to either have a-priori knowledge about an unknown (roughness in case we intend to calculate the dielectric constant), or add some relevant equations to the system of equations.

The surface correlation length of soil is difficult to measure. Furthermore, its field measurements depend on the selected profile length and they are reported to have a large amount

of error with profile lengths usually used (1 m or 2 m) (Baghdadi et al., 2004). Baghdadi et al. (2002) state that although the RMS height and correlation length of the soil are measured independently, correlation length can depend on the RMS height. They present an equation which expresses the correlation length as a function of the RMS height, incidence angle and polarization. The equation is further modified in a series of publications on the topic of calibration of IEM (Baghdadi et al., 2004)(Baghdadi et al., 2006a)(Baghdadi et al., 2011). The final form for use with co-polarized C-band data is (Baghdadi et al., 2006a)

$$L_{opt}(\sigma, \theta, pp) = \delta_{pp}(\sin\theta)^{\mu_{pp}}\, \sigma^{(\eta_{pp}\theta + \xi_{pp})} \tag{3.33}$$

where L_{opt} is the adjusted correlation length, pp is the polarization, and δ, ξ, μ and η are constants:

$$\delta_{hh} = 4.026 \ , \ \delta_{vv} = 3.289 \tag{3.34}$$

$$\xi_{hh} = 1.551 \ , \ \xi_{vv} = 1.222 \tag{3.35}$$

$$\mu_{hh} = \mu_{vv} = -1.744 \tag{3.36}$$

$$\eta_{hh} = \eta_{vv} = -0.0025 \tag{3.37}$$

After using equation (3.33), the correlation length is deleted from equations and one can solve the IEM for the dielectric constant and the RMS height, as there are two equations in these two unknowns. Indeed, the only part of the model which needs to be changed is the definition of the n^{th} power of the surface power spectrum. Since, we use the generalized power law spectrum proposed by Li et al. (2002) in this study, we only need to replace l by L_{opt} in equation (3.31) to obtain

$$W^{(n)}(K) \simeq 0.5(\frac{L_{opt}}{n^{f_p}})(p-1)\left(\frac{a_p}{b_p}\right)^2 \left[1 + \left(\frac{a_p}{b_p}\right)^2 \frac{K^2(\frac{L_{opt}}{n^{f_p}})}{4}\right]^{-p} \tag{3.38}$$

As mentioned earlier, inversion of the IEM is not possible using analytical methods. Thus, a number of methods have been proposed in the literature to invert the equations in order to obtain surface parameters given the the radar imaging parameters and the backscattering coefficient. These include lookup tables, neural networks, Bayesian methods and minimization techniques (Barrett et al., 2009). In particular, dynamic learning neural networks have been successfully applied to invert the IEM with acceptable results with respect to both the time spent on training the network and accuracy (Chen et al., 1995).

3.2.2.2 X-Bragg Model

Another physical model, which is relatively new and is an extension to the Bragg limited model, is X-Bragg. Hajnsek has introduced this in her PhD dissertation which contains comparisons of Oh and Dubois empirical models and her own model (Hajnsek, 2001). The main characteristics of this method is that it

1. makes use of full polarimetric measurements, including both amplitude and phase information.

2. enables us to calculate SM and roughness independently.

The model's task is accomplished by investigation of the coherency matrix and obtaining three parameters from it. Bragg scattering, also used in the SPM, is the base scattering mechanism for X-Bragg. The polarimetric scattering matrix for a Bragg surface is

$$[S] = m_s \begin{bmatrix} R_h(\theta, \epsilon_r) & 0 \\ 0 & R_v(\theta, \epsilon_r) \end{bmatrix} \tag{3.39}$$

where m_s is the backscattering amplitude. SPM has two main limitations: small validity range for surface roughness($ks < 0.3$), and low sensitivity to SM content above 20% (Hajnsek et al., 2003). In order to improve the SPM, use of a rotated Bragg coherency matrix in the form of

$$[T] = \frac{1}{2}\begin{bmatrix} C_1 & C_2\text{sinc}(2\beta_1) & 0 \\ C_2\text{sinc}(2\beta_1) & C_3(1+\text{sinc}(4\beta_1)) & 0 \\ 0 & 0 & C_3(1-\text{sinc}(4\beta_1)) \end{bmatrix} \tag{3.40}$$

is proposed, where

$$C_1 = |R_h + R_v|^2 \tag{3.41}$$

$$C_2 = (R_h + R_v)(R_h^* - R_v^*) \tag{3.42}$$

$$C_3 = \frac{1}{2}|R_h + R_v|^2 \tag{3.43}$$

and β_1 is the rotation angle.

Any coherency matrix can be diagonalized by transformation (Cloude et al., 1996)

$$[T] = [U_3][\Lambda][U_3]^{-1} \tag{3.44}$$

where

$$[\Lambda] = \begin{bmatrix} \lambda_1 & 0 & 0 \\ 0 & \lambda_2 & 0 \\ 0 & 0 & \lambda_3 \end{bmatrix} \tag{3.45}$$

$$[U_3] = \begin{bmatrix} \mathbf{e}_1 & \mathbf{e}_2 & \mathbf{e}_3 \end{bmatrix}^T \tag{3.46}$$

and λ_1, λ_2, λ_3 are eigenvalues, and $\mathbf{e}_1$, $\mathbf{e}_2$, $\mathbf{e}_3$ are eigenvectors of $[T]$. Three physical features are calculated directly from the diagonalization of the coherency matrix. Two of them are

$$H = -\sum p_i \log_3 p_i \tag{3.47}$$

$$A = \frac{p_2 - p_3}{p_2 + p_3} \tag{3.48}$$

respectively polarimetric scattering entropy and the scattering anisotropy. Here p_i is a normalized eigenvalue equal to

$$p_i = \frac{\lambda_i}{\lambda_1 + \lambda_2 + \lambda_3} \tag{3.49}$$

The third physical parameter is calculated by

$$\alpha = p_1\alpha_1 + p_2\alpha_2 + p_3\alpha_3 \tag{3.50}$$

where

$$\alpha_i = arccos((\mathbf{e}_i)_1) \tag{3.51}$$

and $(\mathbf{e}_i)_1$ shows the first element of i^{th} eigenvector of $[T]$. In X-Bragg, soil dielectric constant is calculated by mapping the space of physical parameters H, A and α, to the space of scattering parameters ϵ_r, σ and β_1. This algorithm has been tested using fully polarimetric laboratory measurements as well as airborne L-band SAR. The method is claimed to allow accurate estimations up to moisture level 35%.

For each pixel, or group of pixels with similar incidence angle, a LUT is created using (3.47) and (3.50), which holds values of H and α corresponding to a wide range of ϵ_r and β_1. Thus, given a (H,α) pair, the corresponding (ϵ_r,β_1) pair can be determined by searching for the closest value to (H,α) in the LUT. For the third unknown, the surface roughness RMS height, a simple linear equation

$$\sigma = \frac{1 - A}{k} \tag{3.52}$$

has been proposed (Hajnsek, 2001) in which A is the anisotropy calculated by (3.48). Before starting the inversion process, all the pixels for which $H > 0.5$ or $\alpha > 45°$ need to be filtered out. This filtering is for selecting only surface scatterers, as the model is used for bare surfaces. It has been shown that $H > 0.5$ and $\alpha > 45°$ are related to double-bounce or

volume scattering mechanisms[3] which correspond to vegetation-covered surfaces (Hajnsek, 2001).

3.2.3 Empirical Models

Empirical models have been suggested for SM estimation to handle data acquired from natural surfaces (Dubois et al., 1995), and because more generic models like the IEM are complex. For an empirical model to be developed, it is necessary to gather a large number of experimental measurements to cover various soil parameters and radar configurations. Thus, these models are usually valid only for specific soil conditions (Baghdadi et al., 2006b). The Oh model and the Dubois model are the two empirical models which are widely used for SM estimation in the RS community.

3.2.3.1 Oh Model

The Oh model is proposed based on scatterometer measurements at three frequencies (1.5, 4.5 and 9.5 GHz) at incidence angles from 10° to 70° (Hajnsek, 2001). In this model which has been developed by Oh et al. (Oh et al., 1992), co- and cross-polarized backscatter ratios are written as

$$p = \frac{\sigma^{\circ}_{hh}}{\sigma^{\circ}_{vv}} = \left(1 - \left(\frac{2\theta}{\pi}\right)^{\left[\frac{1}{3\Gamma_0}\right]} exp(-k\sigma)\right)^2 \tag{3.53}$$

$$q = \frac{\sigma^{\circ}_{hv}}{\sigma^{\circ}_{vv}} = 0.23\sqrt{\Gamma_0}(1 - e^{-k\sigma}) \tag{3.54}$$

where θ is the local incidence angle, k is the wavenumber, and σ is the RMS height of the surface. Γ_0 is the Fresnel reflection coefficient at nadir defined as

[3] *Single* (or *surface*) *scattering* is a scattering mechanism during which the radar signal hits a surface and then is reflected back to the sensor, such as the scattering from surface of a bare soil. The mechanism which describes scattering from a canopy-like scatterer is *volume scattering*. The case in which scattered wave from the soil surface hits a vertical part of vegetation, and then scatters back to radar sensor is an instance of *double-bounce* (or *dihedral*) *scattering*.

$$\Gamma_0 = \left| \frac{1 - \sqrt{\epsilon'}}{1 + \sqrt{\epsilon'}} \right|^2 \tag{3.55}$$

where ϵ' is the real part of the surface dielectric constant. It has been shown that large values of the co-polarized ratio and the cross-polarized ratio can represent high soil surface roughness and significant amount of vegetation, respectively (Dubois et al., 1995). For bare soils the Oh model shows good agreement with ground observations when $0.1 \leq k\sigma \leq 6$, $2.5 \leq kl \leq 20$ and $0.09 \leq m_v \leq 0.31$ (m_v being the volumetric moisture content in percents, and l being correlation length of the surface). This model was further revised in (Oh et al., 1994), (Oh et al., 2002) and (Oh, 2004b). In (Oh et al., 2002) the equations directly handle volumetric SM instead of the dielectric constant.

Equations (3.53) and (3.54), can be solved for $exp(-k\sigma)$ and then equated resulting in

$$\left(\frac{2\theta}{\pi}\right)^{\frac{1}{3\Gamma_0}} \left[1 - \frac{q}{0.23\sqrt{\Gamma_0}}\right] + \sqrt{p} - 1 = 0 \tag{3.56}$$

which does not contain the roughness parameter. This equation can not be solved for Γ_0 analytically. Thus, a two-step procedure has been used in our study to find the value of Γ_0 given p and q. After defining the parameters

$$x = \frac{1}{\sqrt{\Gamma_0}},\ a = \frac{2\theta}{\pi},\ b = \frac{q}{0.23},\ c = \sqrt{p} - 1 \tag{3.57}$$

equation (3.56) can be rewritten as

$$f(x) = a^{\frac{x^2}{3}}(1 - bx) + c = 0 \tag{3.58}$$

One can find the solution to this equation using Newton's method of solving equations, although it needs to be initialized by a good approximation. Therefore, in the first step, an approximate solution for x is obtained using a LUT. This LUT is produced so that it contains all possible x values in a certain range, with a pre-defined step, and their corresponding $f(x)$ values. Once we find this approximate value, a more accurate solution is obtained using

Newton's method in the second step. From x, we can have the real part of the dielectric constant and surface roughness by

$$\Gamma_0 = \left(\frac{1}{x}\right)^2 \tag{3.59}$$

$$\epsilon' = \left|\frac{1+\sqrt{\Gamma_0}}{1-\sqrt{\Gamma_0}}\right|^2 \tag{3.60}$$

$$k\sigma = -ln\left(-\frac{\sqrt{\mathrm{p}}-1}{\left(\frac{2\theta}{\pi}\right)^{\frac{1}{3\Gamma_0}}}\right) \tag{3.61}$$

However, this is not the only option for inverting the model. For example, the genetic algorithm has also been used to invert the Oh model using multi-polarized radar observations (Oh, 2004a). LUT-Newton combination has been employed in this study for its simplicity and speed. Note that the Oh model is valid only for pixels with $p < 1$. Thus, before starting the inversion process, pixels which do not satisfy this prerequisite must be filtered out. Also, it has been suggested that, since the model is mainly created for bare soils, the restriction on cross-polarized ratio, which is mentioned for the Dubois model, be applied to the Oh model as well (Hajnsek, 2001).

3.2.3.2 Dubois Model

Dubois et al. (1995) propose to use

$$\sigma^\circ_{hh} = 10^{-2.75}\frac{cos^{1.5}\theta}{sin\theta}10^{0.028\epsilon' tan\theta}(k\sigma\, sin^{1.4}\theta)\lambda^{0.7} \tag{3.62}$$

$$\sigma^\circ_{vv} = 10^{-2.35}\frac{cos^{3}\theta}{sin\theta}10^{0.046\epsilon' tan\theta}(k\sigma\, sin^{3}\theta)^{1.1}\lambda^{0.7} \tag{3.63}$$

with θ being the local incidence angle, σ the RMS height of the surface, k the wavenumber and λ the wavelength. The model was originally developed using scatterometer data, and then further applied to SAR data for demonstrating the robustness (Hajnsek, 2001). The two relationships are claimed by the developers to give best results when $k\sigma < 2.5$, $\theta > 30^\circ$ and

$m_v < 35\%$, and the RMS error in the SM estimate is claimed to be less than 4.2% (Dubois et al., 1995). For C-band data we have used in this study, for which $k = 1.132$ cm^{-1}, the RMS height should be $\sigma < \frac{2.5}{1.132} = 2.21$ cm.

Since the model is not efficient in vegetated areas, such areas are firstly excluded from calculations in (Dubois et al., 1995) using the cross-polarized backscatter ratio, as a vegetation index. For this purpose, all pixels with $q = \frac{\sigma^\circ_{hv}}{\sigma^\circ_{vv}} > -11\,dB$ are masked out before inverting the model. Also, it has been recommended by the creators of the model to apply the model only on data with $p < 1$ to avoid processing the data with surface roughness out of the validity range of the model (Dubois et al., 1995).

Inversion of the Dubois model is straightforward. Using equations (3.62) and (3.63) one can obtain closed form equations for calculation of ϵ' and $k\sigma$ as (Hajnsek, 2001)

$$\epsilon' = \frac{10^{-0.19}\,\lambda^{0.15}\,log_{10}\left(\frac{{\sigma^\circ_{hh}}^{0.7857}}{\sigma^\circ_{vv}}\right)\,cos^{1.82}(\theta)\,sin^{0.93}(\theta)}{-0.024\,tan(\theta)} \tag{3.64}$$

$$k\sigma = \frac{10^{\frac{2.75}{1.4}}\,{\sigma^\circ_{hh}}^{\frac{1}{1.4}}\,sin(\theta)^{2.57}\,\lambda^{-0.5}}{10^{0.02\,\epsilon'\,tan(\theta)}\,cos(\theta)^{1.07}} \tag{3.65}$$

and the unknowns are calculated directly.

3.3 Dielectric Mixing Models

Most of the models mentioned before use dielectric constant as one of their unknown parameters. When volumetric SM is desired, we have to use a dielectric mixing model to convert dielectric constant values to volumetric SM values (Barrett et al., 2009). Two of the most commonly used models are by Topp et al. (1980) and Dobson et al. (1985). The model by Dobson et al. requires some knowledge about soil texture and other parameters, while the model proposed by Topp et al. relates the dielectric constant directly to soil water content

via a third order polynomial:

$$m_v = -5.3 \times 10^{-2} + 2.92 \times 10^{-2}\epsilon' - 5.5 \times 10^{-4}\epsilon'^2 + 4.3 \times 10^{-6}\epsilon'^3 \tag{3.66}$$

in which ϵ' is the real part of the dielectric constant of the soil and m_v is the volumetric SM value. This advantage makes the latter model more widely used, because detailed soil properties are not always available. Since this is also the case with our data, we have adopted the model by Topp et al. in our experiments. The performance of this model has been evaluated for a large set of mineral soils and SM conditions, and the model is believed to have satisfactory accuracy for the majority of applications (Altese et al., 1996).

In this chapter, the three main categories of surface scattering models used for SAR data were explained, and the details of the IEM, X-Bragg, Oh and Dubois models, along with their inversion methods were presented. Our proposed method for improving the quality of SM estimated using these models is based on study of the spatial variability of SM which will be discussed in the next chapter.

Chapter 4

Models for Explaining the Spatial Variability of Soil Moisture

Generally speaking, the methods proposed for refining the results of SM estimated by SAR surface scattering models can be classified, based on the stage of estimation at which the method is used, as follows:

- Manipulation of the mathematical formulation of surface scattering model, e.g. (Fung et al., 2002) and (Wu et al., 2001) which propose corrections to the original IEM
- Processing the data before it is fed into the model, e.g. (Hajnsek, 2001) and (Hajnsek et al., 2009) which decompose the coherency matrix of the data and take single scattering and double-bounce scattering components to be used by the model
- Constraining the process of the inversion of the model by employing additional information, e.g. (Mattia et al., 2009) and (Kim et al., 2012) which make use of multi-temporal images

The method we propose in this study for improving the results of a backscattering model does not fit in any of the above-mentioned categories, in that it tries to calibrate the results of the backscattering model after the inversion is completed. This is carried out by employing a calibration model which transforms the results of the backscattering model in order to increase their agreement with the ground measurements. The calibration model is established by investigating the spatial variability of SM obtained from ground measurements and the backscattering model. In other words, the model tries to make a connection between the

spatial variability of the outputs of the backscattering model with ground measurements of SM. Thus, establishing the model needs at least one epoch of concurrent ground and remotely sensed data. However, as will be shown in Chapter 6, after the parameters of the model are estimated using these data, the model may be generalized to other epochs of data acquisition.

In this chapter we look at the different models proposed in literature for modeling the spatial variability of SM. Then, in Chapter 6 the results from applying this type of modeling on our data set will be presented, which will lead to an empirical calibration model for improving the results of SAR backscattering models.

4.1 Spatial Variability of SM

Physical properties of soil vary considerably (Heuvelink et al., 2001). Their variability is caused by five forming factors of soil: climate, organisms, relief, parent material and time (Mzuku et al., 2005). These factors generate variations in global, regional, field, and even ingredient scale (Adamchuk et al., 2010). Spatial variability of SM and heterogeneity of surface SM patterns have been reported by many researchers (see, for example, (Brocca et al., 2009), (Cantón et al., 2004), (Hébrard et al., 2006) and studies cited therein). According to investigations based on field observations, this variability depends mainly on slope angle, slope orientation (aspect), soil surface cover and vegetation type, soil texture, and organic matter content (Hébrard et al., 2006).

Spatial variability of SM is a key factor in modeling land surface processes and studying soil water dynamics (Giorgi et al., 1997)(Hu et al., 2011). Understanding this spatial variability can, for example, be helpful in planning ground measurement campaigns for evaluation of remote sensing SM products (Famiglietti et al., 2008). The ground measurements are assumed to be point measurements, and to compare the areal image-based SM values with their corresponding ground measurements it is necessary to calculate the average of

ground measurements over a sampling site. The number of the samples required for obtaining a certain level of uncertainty when calculating the average can be determined using an analysis of the spatial variability of SM (Brocca et al., 2010). Due to SM spatio-temporal variations, a limited number of measurements cannot provide a perfect SM map. Therefore, a model is usually used to predict the behavior of soil in space and time.

There has been a large number of studies on the characterization of this variability and identifying a regional or global model to describe the variability by different scientists (Bell et al., 1980)(Owe et al., 1982)(Rodríguez-Iturbe et al., 2006)(Famiglietti et al., 2008). The source of data for these studies is usually remote sensing products or direct ground measurements. In addition to the above-mentioned applications, information about SM spatial variations can assist in improving the accuracy of low-quality SM maps generated using satellite or airborne images. Although this type of information can be fairly easily used to adjust SM values coming out of SAR-based models, to the best knowledge of the author, there has not been any instance of utilizing this information in the SM estimation literature. The feasibility of using SM spatial variability models for our data set, and their actual effect on outputs of the backscattering models will be discussed in Chapter 6. In this chapter, three commonly used models of this type will be reviewed.

Before we move forward in presenting different relationships suggested to explain the spatial variability in SM, we need to define the different types of scale used for this purpose. The variability of SM changes with scale (Western et al., 1999), and we are ultimately going to see if these changes can be used in improving the outputs of SAR backscattering models. The scale at which measurements or modeling are performed can be described by a *scale triplet* including spacing, extent and support (Bloschl et al., 1995). Figure 4.1 depicts a schematic representation of the three scale types. Spacing is the distance between measurements. Extent scale is defined as the overall area covered by the whole set of measurements. Support, which is also called resolution in this context, is used to delineate the measurement

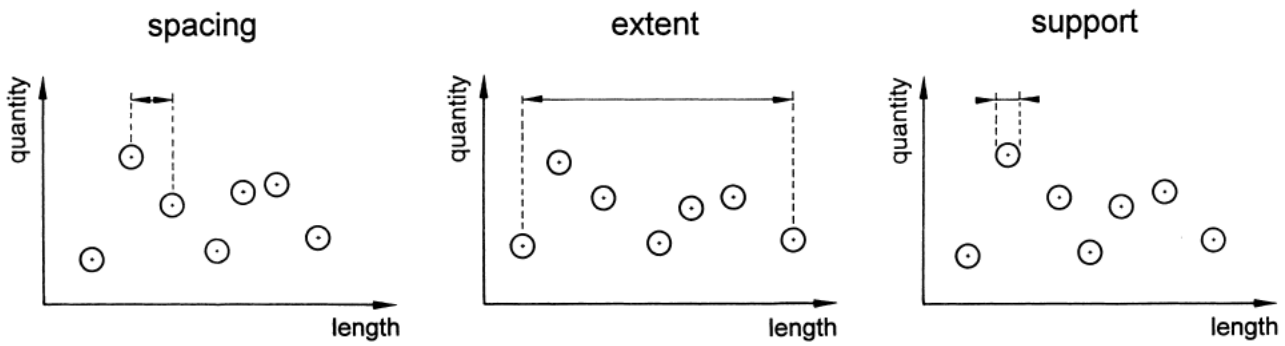

Figure 4.1: Scale triplet (From (Western et al., 1999))

integration area (or volume), i.e. part of space which a measurement represents (Western et al., 1999). For instance, in the case of SM measurements in our study area, the spacing scale is about 30 m, the extent of each site is about 100 m $\times$ 100 m, and the support scale is the volume of a cylinder with a height of 6 cm and radius of a few centimeters.

4.2 Probability Density Function

The spatial variability of SM can be characterized using a probability density function (PDF), and the parameters defining its shape. Different types of probability distributions have been observed, or considered for this purpose, in the literature (Famiglietti et al., 2008):

- Gaussian distribution (Li et al., 1994)(Famiglietti et al., 1999)
- log-normal distribution (Li et al., 1994)
- gamma distribution (Entekhabi et al., 1989)(Famiglietti et al., 1999)
- beta distribution (Li et al., 1994)(Famiglietti et al., 1999)

Since there is no commonly-accepted PDF for the distribution of SM, any result obtained by assuming a specific type of distribution for SM data may be specific to the data set used for running the experiments.

4.3 Exponential Law and Power Law

Information about spatial variation of SM can also be presented in terms of the statistics of the PDF without considering its shape. These statistics may include standard deviation, mean, coefficient of variation and skewness. A widely-accepted empirical formulation is in the form of an exponential law between the SM mean and standard deviation or coefficient of variation (Famiglietti et al., 2008)(Bell et al., 1980)(Jacobs et al., 2004)(Brocca et al., 2007) which has been observed in different regions. Specifically, Famiglietti et al. (2008) reported good fit of ground data for these relationships by analyzing more than 36,000 SM ground measurements collected in SGP97, SGP99, SMEX02 and SMEX03 campaigns. They explored six extent scales ranging from 2.5 m to 1.6 km and obtained similar results for them. Their analysis of extensive ground measurements showed that the standard deviation of SM in a region is dependent on the mean SM in that region. This dependence has been modelled as (Famiglietti et al., 2008)

$$\sigma_\theta = k_1 \cdot \mu_\theta \cdot exp(-k_2 \mu_\theta) \tag{4.1}$$

where σ_θ is the standard deviation of the SM, μ_θ is the average SM in the working region, and k_1 and k_2 are parameters of the model which depend on the region. Equation (4.1) can also be written as

$$CV_\theta = k_1 \cdot exp(-k_2 \mu_\theta) \tag{4.2}$$

where CV_θ is the coefficient of variation defined as

$$CV_\theta = \frac{\sigma_\theta}{\mu_\theta} \tag{4.3}$$

One possibility for improving the output of SAR backscattering models using a spatial variability model, is to force the outputs of the backscattering model to follow the variability model using an optimization procedure. In case the variability model can be empirically calibrated and its parameters (e.g. k_1 and k_2 in the exponential law) calculated from a

reasonable number of ground measurements, then the statistical or physical characteristics of ground measurements may be reproduced in the output of the backscattering model. As a result, the output of backscattering model will be in a better agreement with ground measurements. For the case of the exponential law we need to alter the SM values calculated for pixels of image corresponding to a ground site, so that they ultimately conform to equation (4.1). An issue with this optimization problem is that, in the best case where both k_1 and k_2 are known in advance (for example using ground measurements or modeling) we can construct a weak constraint which is not able to change the original SM values significantly to conform to equation (4.1). Therefore, a stronger constraint consisting a number of equations comparable to the number of unknowns involved in the optimization process is required to improve the original results produced by backscattering models.

Another model which has been suggested for characterizing the variations of SM is a power law between the SM variance and the extent scale (Rodriguez-Iturbe et al., 1995)(Manfreda et al., 2007). Empirical studies of ground measurements and remotely sensed SM have shown that variance of SM values increase as a power of the extent scale of measurements (Famiglietti et al., 2008):

$$\sigma_\theta^2 = C \cdot S^D \tag{4.4}$$

where C and D are parameters, and S is the area covered by the measurements. In other words, log variance changes linearly with log extent scale. This is in fact very similar to fractality attribute of SM which we will discuss shortly in this chapter.

A powerful mathematical tool for analyzing the variations of a complex variable which has received great attention in soil science and other disciplines is *fractal analysis*. In the rest of this chapter we will focus on the materials required for this type of analysis, which is the primary technique used in this study to improve SM estimation by SAR backscattering models. Because of its multi-resolution nature, when dealing with images, the algorithm used for fractal analysis can be better explained using the concept of *image pyramids*. Thus,

we first present a brief review of the idea and theory of image pyramids, and then explain how this can be used in the fractal analysis of a SM image.

4.4 Image Pyramids

An image pyramid is a computationally-efficient coarse-to-fine structure to represent an image at multiple scales (Neskovic et al., 1993), which has found many applications in image processing, computer vision and remote sensing including image registration (Thevenaz et al., 1998), pattern matching (Adelson et al., 1984), surface reconstruction (Samadzadegan et al., 2002) and image classification (Iikura et al., 1995). An image pyramid is generated by consecutive aggregation of blocks of image pixels to create multiple levels of image details. The aggregation is achieved using weighted averaging of the pixels. Weights can be selected so that different types of pyramids, e.g. Gaussian or Laplacian pyramids (Burt et al., 1983), be generated. When all the weights are equal the pyramid is a *mean pyramid*, which is the type used here for analyzing the fractality in SM values. Given an image I_0 of size $2^n \times 2^n$ pixels, each image I_1, I_2, ..., I_N at level 1, 2, ..., N of the pyramid has a lower resolution (larger pixel size) than its ancestors. Usually the pyramid is dyadic, i.e. each image I_k has pixels with sizes twice the size of pixels in image I_{k-1}(see Figure 4.2a). The procedure of creating pixels of an image in a pyramid from pixels of a predecessor (lower) image is called *reduction*. The inverse procedure, i.e. estimating the pixels of an image in pyramid from a higher level image is called *expansion*. Expansion usually requires extra information or assumptions about the distribution or pattern of pixel values.

The value of the pixel at location (i, j) at level l of a mean pyramid can be calculated from the pixel values at level $l-1$ as

$$I_l(i,j) = \frac{1}{4} \sum_{p=-1}^{0} \sum_{q=-1}^{0} I_{l-1}(2i+p, 2j+q) \tag{4.5}$$

This can also be obtained from the original image, I_0, by

$$I_l(i,j) = \frac{1}{2^{2l}} \sum_{r=r_1}^{r_2} \sum_{c=c_1}^{c_2} I_0(r,c) \tag{4.6}$$

where

$$r_1 = (i-1) \times 2^l + 1 \tag{4.7}$$

$$r_2 = r_1 + 2^l - 1 \tag{4.8}$$

$$c_1 = (j-1) \times 2^l + 1 \tag{4.9}$$

$$c_2 = c_1 + 2^l - 1 \tag{4.10}$$

In Figure 4.2b links between pixels of two consecutive layers in a dyadic mean image pyramid is displayed. Blocks of four adjacent pixels in image I_l are reduced to single pixels in image I_{l+1} through an averaging operation.

Figure 4.3 shows five layers of an image pyramid generated from a 16×16 pixel SM grayscale map. The map is created using the SAR backscattering model IEM applied on an image window of our data set. The pixels for which the model has not been able to calculate the dielectric constant of soil have been replaced by the average SM value of the first layer in this representation. This is to avoid displaying missing data in the map. The image at level 0 has a ground resolution of 10 meters, while for the image at the highest level the ground resolution is 160 meters. As seen in this figure, by moving toward the higher levels details of the spatial pattern of SM gradually disappear.

4.5 Fractal Analysis

Fractal analysis has been used in several studies in remote sensing, medical image processing, geophysics, soil science and other disciplines. Interest in fractal techniques in remote sensing is mainly due to the fact that, in addition to spectral and spatial complexity, remotely sensed images show similarities at different spatial scales (Sun et al., 2006). Fractal measures have

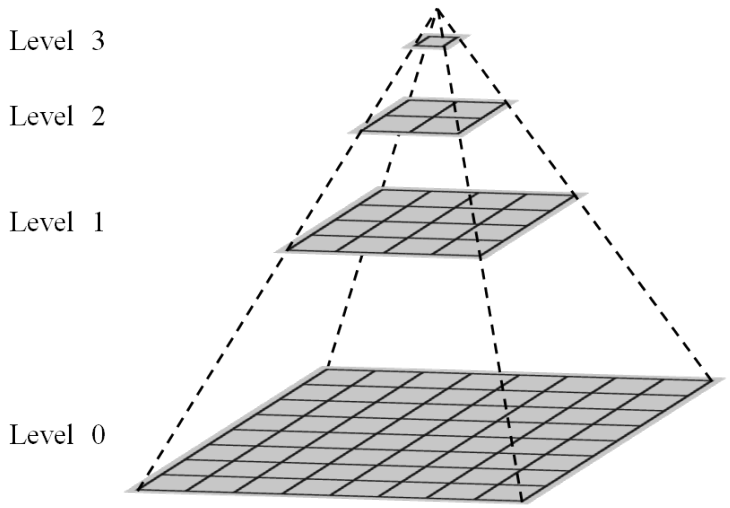

(a) General structure of a four-level image pyramid: The base of the pyramid is the original image (8×8 in this example), and the highest level consists of a single pixel with a value equal to the mean value of pixels in the original image.

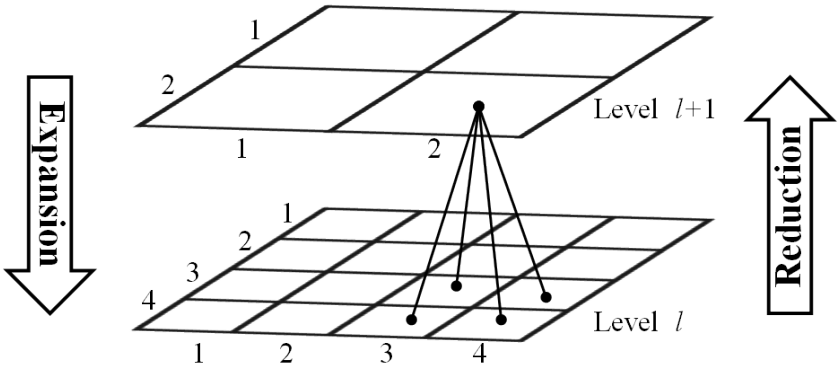

(b) Pixel links in a mean image pyramid: Each pixel in image I_{l+1} is linked to four pixels in image I_l through an averaging operation.

Figure 4.2: Mean image pyramid

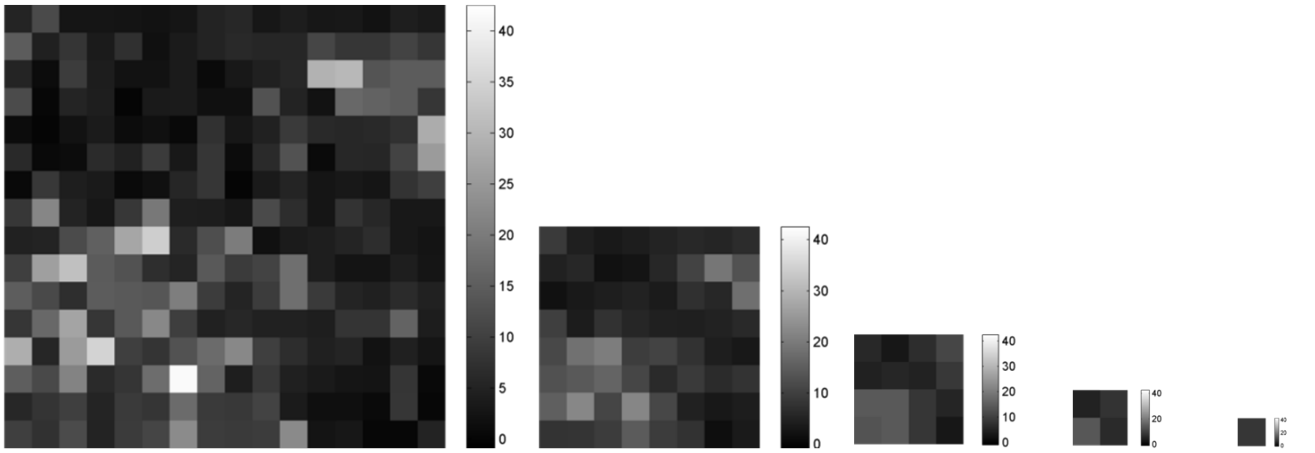

Figure 4.3: Soil moisture image pyramid

usually been utilized for the creation of textural features to identify land surface patterns in remotely sensed imagery. For example, Myint (2003) used three different approaches to extract textural features to distinguish between residential, commercial, woodland, agriculture, and water body land cover classes. Li et al. (2003) proposed a multi-parameter and multi-scale textural feature set based on fractal analysis, and compared its performance with several other fractal-based and wavelet-based features for classification of SPOT images into habitation, field and mixed classes. Fractals have also been employed in data mining and change detection of remotely sensed images. For example, Emerson et al. (2004) introduce a NASA[1] project for indexing the content of images and facilitating searches in imagery databases. Because of their capacity for transferring information over scales and summarizing statistical properties of images, fractals have found applications in satellite image compression as well. It has been shown that a fractal-based compressor can achieve higher compression rates than a JPEG compressor while minimizing information loss (Ghosh et al., 2008). Similar applications have been explored in medical image analysis, for instance, for segmentation, characterization and abnormality detection (Lopes et al., 2009).

Characterization of processes related to atmosphere and terrestrial processes, which are among the geophysical phenomena of interest to geoscientists, needs complex models which

[1]National Aeronautics and Space Administration

usually deal with the scale invariance property of fractals. The relationship between size and frequency of islands, earthquakes, ore deposits and oil fields often exhibit fractal behavior (Turcotte, 1989). Since fractals can also be used for temporal analysis of processes, they can improve the spatial and temporal understanding and the quality of prediction of geophysical phenomena at different scales (Daya Sagar et al., 2004). With the development of remote sensing as a tool for acquiring information about soil at spatial and temporal scales that were not accessible before, understanding the relationship between traditional measurement scales and modern measurement or modeling scales has turned into an important issue in soil science. The objective of studies on upscaling and downscaling[2] soil properties such as soil carbon dioxide efflux (e.g. (Graf et al., 2011)) and soil moisture (e.g. (Merlin et al., 2012)) is usually to satisfy this need. Fractal analysis, with its scaling capabilities, seems to be a suitable means of connecting different levels of measurements and modeling for soil. Fractals have also been used for quantification of soil physical properties such as soil structure. For example, Eghball et al. (1993) utilized fractal analysis to distinguish between different tillage and crop sequences by investigating the values of fractal dimension. (Perfect et al., 1995) includes a detailed review and classification of applications of fractals in soil science.

Fractal behavior of SM has already been reported for both ground measurements and remotely sensed data (Oleschko et al., 2008)(Biswas et al., 2012a). In addition to general analysis of SM variability, fractal theory has been used in downscaling SM obtained from satellite images. For example, Kim et al. (2002) used a fractal-based algorithm for downscaling SM maps produced from ESTAR[3] data at a spatial resolution of 800 m by incorporating ancillary field data. Fractals have even been utilized in estimation of soil water content for ground samples by investigating the relationship between the volume and mass of samples (Jadoski et al., 2009).

[2]Upscaling is predicting coarse resolution data from fine resolution data, and downscaling is the reverse action.

[3]Electronically Scanned Thinned Array Radiometer

In this study, we analyze the fractal properties of the field measurements of SM, and SM values generated by SAR backscattering models, and examine the possibility of using these properties in improving the accuracy of the output of the backscattering models. To the best knowledge of the author, this is the first time fractal theory is being used to improve the results of these models.

The strength of fractal analysis is two-fold:

1. It is a multi-resolution analysis, which means it can be used to study a variable over a range of scales.

2. It is not based on any parametrization or assumption of homogeneity and statistical probability distribution (Schertzer et al., 1997), which makes it a well-suited tool for investigating variables with irregularly high and low values such as SM.

The word "fractal" was first coined by Benoit Mandelbrot, who officially defined a fractal[4] and established a mathematical framework for fractal analysis (Mandelbrot, 1983). The exact definitions and rigorous theory of fractals is beyond the scope of this work, and here we focus more on how the statistical properties of fractals can benefit the study of variability in SM. A fractal shape can be defined as a rough shape which can be partitioned recursively to parts, each of which has statistical properties similar to the original shape (Aouit et al., 2009). Fractals can be fully explained using scaling laws, therefore, their statistical information can be transferred from one scale to another. Associated with each fractal is one or more *fractal dimensions*. Fractal dimension is an index which shows the amount of irregularity and complexity of a fractal. There are different types of fractal dimensions, but the one that is widely used in the literature is *Hausdorff-Besicovitch dimension* (Sun et al., 2013). Different methods have been proposed for calculating the fractal dimension of a fractal (Lopes et al.,

[4]Mandelbrot defined a fractal as "*a set for which the Hausdorff-Besicovitch dimension strictly exceeds the topological dimension*".

2009). Here, we use method of moments (Turiel et al., 2006), which has been successfully used for analyzing SM data (Mascaro et al., 2010).

4.5.1 Method of Moments

Although the algorithms for calculating the fractal dimension are different, they all consist of three main steps (Lopes et al., 2009):

1. Calculate a function of the variable under study using different step sizes
2. Creating a plot of log(function) vs. log(step size) and fitting a straight line through the points in the plot
3. Calculating the fractal dimension using the slope of the straight line

In the method of moments, the above-mentioned function is the moment at different scales. Moments of different orders are standard tools for statistical analysis of variability: mean (first raw moment), variance (second central moment), skewness (third central moment) and kurtosis (fourth central moment). However in fractal analysis by method of moments, the behavior of moments of different orders in different scales are investigated.

Assume that we have a $2^n \times 2^n$ SM image I_0 with a resolution λ_0. Also assume that we create a mean image pyramid from this image which contains images I_0, ..., I_n with resolutions λ_0, ..., λ_n. For each resolution λ a *partition function* $S_q(\lambda)$ is defined as (Mascaro et al., 2010)

$$S_q(\lambda) = \frac{1}{N(\lambda)^2} \sum_{i=1}^{N(\lambda)} \sum_{j=1}^{N(\lambda)} \left[\theta_{(i,j)}(\lambda)\right]^q \tag{4.11}$$

where $\theta_{(i,j)}(\lambda)$ is the value of SM at location (i, j) of the layer in the mean image pyramid which has resolution λ, and $N(\lambda)$ is the number of rows (or columns, as the image forms a square) of that layer in the pyramid. In case SM is not available at some of the locations, these locations are ignored, i.e. they are not considered in calculation of the moments. Thus,

equation (4.11) changes to

$$S_q(\lambda) = \frac{1}{\left(\sum_{i=1}^{N(\lambda)}\sum_{j=1}^{N(\lambda)}\delta_{(i,j)}\right)^2}\sum_{i=1}^{N(\lambda)}\sum_{j=1}^{N(\lambda)}\left[\theta'_{(i,j)}(\lambda)\right]^q \tag{4.12}$$

where

$$\delta_{(i,j)} = \begin{cases} 1 & if\ \theta_{(i,j)}\, is\, available \\ 0 & otherwise \end{cases} \tag{4.13}$$

$$\theta'_{(i,j)} = \begin{cases} \theta_{(i,j)} & if\ \theta_{(i,j)}\, is\, available \\ 0 & otherwise \end{cases} \tag{4.14}$$

SM is said to be *scale invariant* for a range of scales if

$$S_q(\lambda) \sim \lambda^{\tau(q)} \tag{4.15}$$

holds for that range of scales, where $\sim$ shows proportionality, and $\tau(q)$ is called *mass exponent* or *scaling function* of order q. A log transform of the both sides in equation (4.15) yields

$$\log(S_q(\lambda)) \sim \tau(q)\ \log\lambda \tag{4.16}$$

Therefore, scale invariance can be revealed by examining the linearity of $\log(S_q(\lambda))$ vs. $\log\lambda$. if the linearity condition is satisfied, then $\tau(q)$ is the slope of the line. Note that, $\tau(q)$ does not depend on λ, which means the statistical properties of SM can be transferred from one scale to another if $\tau(q)$ is known. The mass exponent spectrum can fully define the fractal, but fractals are sometimes also represented by two alternative spectra called *singularity spectrum* (Telesca et al., 2003):

$$f(\alpha) = q\alpha(q) - \tau(q) \tag{4.17}$$

and *generalized dimension spectrum*:

$$D(q) = \frac{\tau(q)}{1-q} \tag{4.18}$$

where

$$\alpha(q) = \frac{d\tau(q)}{dq} \tag{4.19}$$

is called the *Holder exponent*. In this work we use the mass exponent, $\tau(q)$, to study the fractal behavior of SM data. A fractal is called a *monofractal* when $\tau(q)$ is linear, i.e. a single Holder exponent describes the fractal. When $\tau(q)$ has a nonlinear relationship with q the fractal is a *multifractal*. Positive values of q amplify the effect of large values of the variable under study in the partition function and reduce the effect of small values. On the other hand, negative values of q amplify the effect of small values and reduce the effect of large values (Biswas et al., 2012b). Indeed, the shape of $\tau(q)$ is an indicator of the degree of complexity and irregularity of the variable under study. It has been shown that $\tau(q)$ forms a downward convex curve (Lovejoy et al., 2008); however, if this was the only thing we knew about the mass exponent function, it would be barely applicable in analysis and prediction. Because, in this case, one would need to determine a large number of parameters to link information in different scales (Lovejoy et al., 2008). A two-parameter model called the *Universal Multifractal* has been proposed for $\tau(q)$ (Schertzer et al., 1989) which has found applications in geophysics (Seuront et al., 1999), and is expressed as

$$\begin{cases} \tau(q) = \frac{C_1}{\alpha-1}(q^\alpha - q) & \alpha \neq 1 \\ \tau(q) = C_1 q \log(q) & \alpha = 1 \end{cases} \tag{4.20}$$

where C_1 and α are the parameters of the model.

A similar two-parameter multifractal model called the STRAIN (Space Time RAINfall) model was also proposed by Roberto Deidda in his PhD thesis ((Deidda, 1997) as cited in (Deidda et al., 1999)) in order to understand the scaling properties and statistical characteristics of rainfall and downscaling coarse rainfall data. The model can be expressed as (Mascaro et al., 2010)

$$\tau(q) = -c\frac{q(1-\beta) - (1-\beta^q)}{\log 2}, \;\; q > 1 \tag{4.21}$$

where c and β are parameters of the model which together control the degree of variability of the rainfall field. The parameter c is related to the linearity of $\tau(q)$, and the parameter β causes the nonlinearity in it. Thus, c can be related to monofractality and β can represent the degree of multifractality in the STRAIN model.

As mentioned earlier, SM changes are affected by different factors with complex behaviors. Hence, as already reported in literature (Biswas et al., 2012a)(Kim et al., 2002), its variability cannot be explained by a monofractal. In order to describe the variability of SM values using multifractals, the STRAIN model (equation (4.21)) was applied in some studies on SM images generated from remotely sensed data in regions with different climates. In all of the study areas the parameter β found to exhibit the same behavior, i.e. it was rather constant. Mascaro et al. (2010) used the model for the data from SGP97 campaign (humid subtropical and subhumid climate), and calculated mean β as 0.85 for the region, while Mascaro et al. (2011) found mean β to be 0.89 and 0.71 for SMEX02 (subhumid climate) and SMEX04 (semiarid climate) campaigns, respectively. As we will see in Chapter 6, our experiments with ground measurements in our study area show moderately small variations in β.

4.5.2 Multifractal Analysis Procedure

The algorithm used in this research for multifractal analysis of a SM image can be summarized as below:

1. Create a mean image pyramid from the SM image under analysis
2. Calculate partition function $S_q(\lambda)$ for all layers of the pyramid for a range of moments of order q_1, ..., q_m using equation (4.12)
3. Examine the scale invariance in the SM image by examining the linearity of $\log(S_q(\lambda))$ vs. $\log(\lambda)$ for every $q \in \{q_1, ..., q_m\}$
4. Calculate $\tau(q)$ the slope of each line obtained in previous step for $q \in \{q_1, ..., q_m\}$

5. Fit the STRAIN model to the pairs of (q,$\tau(q)$) for $q \in \{q_1, ..., q_m\}$, and calculate β and c parameters

In this study, we use the multifractal model (4.21) to analyze both the ground measurements of SM and SM estimated from output of a SAR backscattering model to examine the feasibility of improving the backscattering model output using the multifractal analysis. As mentioned above, in multifractal analysis using the STRAIN model, estimation of the two parameters of the model, β and c, is necessary. This is done by fitting the STRAIN model to values of mass exponent, $\tau(q)$, obtained from a SM image.

Assume that we have a SM image of size $2^n \times 2^n$ pixels which has fractal properties and obeys the model (4.21). In order to calculate β and c for this image, we first estimate the values of τ_i, the slopes obtained from fitting a line to $\log(S_q(\lambda))$-$\log(\lambda)$ plot, for q_i where $i \in \{1, 2, ..., m\}$. Then, we create the pairs (q_1, τ_1), (q_2, τ_2), ..., (q_m, τ_m) and minimize the norm of residuals of the fit of the STRAIN model to (q, τ) pairs. Thus, the minimization problem can be defined as

$$\underset{\beta,c}{Minimize} \sqrt{\sum_{i=1}^{m} \left(\tau(q_i) - \tau_i\right)^2} \tag{4.22}$$

This minimization problem can be solved using a nonlinear optimization algorithm. The algorithm we have used in this study is the sequential quadratic programming. This algorithm along with some necessary prerequisite material will be covered in the next section. A Matlab function for the calculation of β and c parameters of the STRAIN model, given the data and resolution, is presented in Appendix B.

4.6 Mathematical Optimization

Optimization is the process of making a decision about the parameters of a system in an optimal manner. The three steps required for making this decision are (Wilde et al., 1967) (as cited in (Diwekar, 2008)) :

1. Identifying the system

2. Developing a suitable measure of performance

3. Minimizing or maximizing the measure of performance

Identifying the system consists of modeling the relationship between elements of the system and translating them into constraints. The measure of performance demonstrates the quality of the modeling in terms of closeness to real phenomenon being analyzed. For the minimization/maximization step above, first, possible solutions are sought, and the most desirable solution is selected. Then, we try to find a better solution, and the procedure is repeated until no better solution is encountered (Deb, 2001). Since minimization and maximization operations can be easily converted to each other, an optimization problem, in general form, can be expressed as

$$\begin{aligned} &\underset{\mathbf{x}}{Minimize}\ f(\mathbf{x}) \\ &subject\,to \quad c_i(\mathbf{x}) = 0\ \forall i \in \mathcal{E} \\ &\qquad\qquad c_i(\mathbf{x}) \geq 0\ \forall i \in \mathcal{I} \end{aligned} \tag{4.23}$$

Here, $\mathbf{x}$ is the vector of parameters (decision variables) we are trying to estimate. $f(\mathbf{x})$, which is the measure of performance, is called an *objective function.* $c_i(\mathbf{x})$ are the equality constraints when $i \in \mathcal{E}$, and is used to introduce inequality constraints into the optimization process when $i \in \mathcal{I}$. $\mathcal{E}$ and $\mathcal{I}$ are the sets containing indices of equality and inequality constraints. If $c_i(\mathbf{x})$ is not defined, i.e. $\mathcal{E}$ and $\mathcal{I}$ are empty sets, the problem is called an *unconstrained optimization*; otherwise it is a *constrained optimization* problem. If $f(\mathbf{x})$ and all $c_i(\mathbf{x})$ constraints are linear functions, the problem is called a *linear optimization* (*linear programming*) problem, otherwise it is called a *non-linear optimization* problem. The parameter domain can be continuous or integer. In the case of integer decision variables,

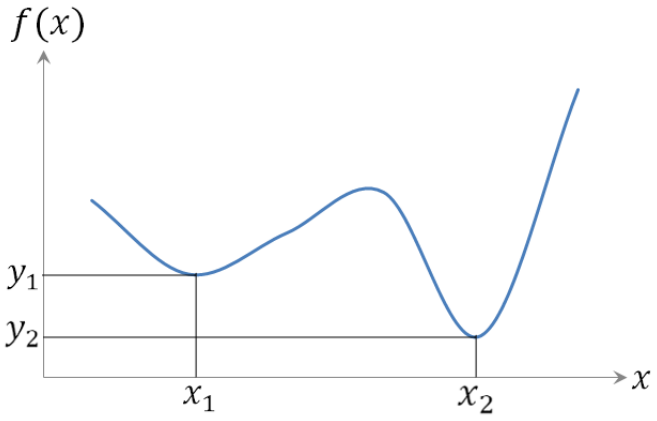

Figure 4.4: Typical one-dimensional optimization

the problem will be an *integer programming* problem. A special case happens when $f(\mathbf{x})$ is a vector, i.e. there are more than a single objective. In such a situation we will have a *multi-objective optimization* problem.

Optimization algorithms have also been categorized based on their range of operation. Figure 4.4 includes a typical representation of a one-dimensional optimization problem. As demonstrated, function $f(x)$ has a local minimum at x_1. If the optimization algorithm gets stuck in the valley around this point, it will not be able to yield the correct minimum value of the function over its whole domain, as the correct one occurs at x_2. The optimization algorithms designed to search for the optimum value of the objective function over its whole domain are called *global optimization* algorithms, and the algorithms which may not be able to locate the global optimum are known as *local optimization* algorithms. Local optimization methods need to be provided with an initial value of the decision variable that is close to the optimum. In other words, if we can execute a local algorithm by a sufficiently large number of set of initial values, we should be able to select the optimum among the answers obtained.

Several algorithms have been proposed to solve global optimization problems, for example multi-start algorithm (Oldenhuis, 2010), simulated annealing (Kirkpatrick et al., 1983), evolutionary algorithms (such as genetic algorithm (Whitley, 1994) and differential evolution (Storn et al., 1997)), and swarm-based algorithms (such as particle swarm optimization (PSO) (Kennedy et al., 1995) and ant colony optimization (ACO) (Dorigo et al., 1996)).

The general approach in global optimization algorithms is to start from an initial population of candidates as the best values of decision variables, selecting new candidates in the neighborhood of the initial ones, replacing the initial candidates by the new ones if the new ones are better (in terms of minimizing the cost function), and repeating the selection of new candidates and replacement until no better candidate can be found.

Global algorithms are time consuming algorithms, and the processing time increases as the number of decision variables increases. The emphasis in these type of algorithms is more on investigating the whole range of decision variable values which may lead to a global solution of the problem, not on finding the answer quickly. In order to improve the SM estimated from the SAR backscattering models by means of multifractal analysis, the parameters of the STRAIN model, β and c, must be estimated using an optimization procedure. For creating a full SM map with dimensions of a satellite image, the optimization process has to be performed many times. For example, for a SAR image of 2048x2048 pixels if we use 16x16 windows[5] in multifractal analysis, then the optimization procedure needs to be performed 16,384 times, which can take a long time if a global optimization algorithm is used. Thus, in this study, we have used an algorithm called *sequential quadratic programming (SQP)* which is a local algorithm, but can achieve global convergence[6] by using a suitable *merit function* (Boggs et al., 1995). The SQP was originally designed for constrained nonlinear optimization, but can also be used for unconstrained optimization if we simply define a range for unknowns, which converts the problem to a constrained optimization problem. Sequential quadratic programming is one of the most powerful methods for constrained nonlinear programming (Nocedal et al., 2006). The main idea behind SQP is to replace the Lagrangian function (see Definition 4.3) with a quadratic approximation, and the

[5]This is the smallest $2^n \times 2^n$ window which covers a ground measurement site (10×10 pixels) in our data set.

[6]A global convergent algorithm is an algorithm which can find the global optimum from any starting point.

constraints by a linearized version of theirs. In this study, we used the Matlab Optimization Toolbox implementation of the SQP to estimate parameters β and c of the STRAIN model for ground measurements and SM images.

The SQP tries to solve a constrained nonlinear optimization problem by generating a sequence of *quadratic programming (QP)* sub-problems, and that is where its name comes from. Before we can discuss the QP and the SQP, we need to present some definitions and theorems from Nocedal et al. (2006).

Definition 4.1 *Given the optimization problem (4.23), at a point* $\mathbf{x}$ *within the feasible region, a constraint* $c_i(\mathbf{x})$ *with index* $i \in \mathcal{E} \cup \mathcal{I}$ *is called* active *if* $c_i(\mathbf{x}) = 0$. *Otherwise it is called an* inactive *constraint. Clearly all the equality constraints are active.*

The active set *for any point in the feasible region is defined as the the set of indices of all of active constraints:*

$$\mathcal{A}(\mathbf{x}) = \mathcal{E} \cup \{i \in \mathcal{I} \,|\, c_i(\mathbf{x}) = 0\} \tag{4.24}$$

Definition 4.2 *Given the optimization problem (4.23), point* $\mathbf{x}$ *and the active set* $\mathcal{A}(\mathbf{x})$, *it is said that the* linear independence constraint qualification (LICQ) *holds if at the point* $\mathbf{x}$ *the gradients of active constraints,* $\nabla c_i(\mathbf{x})$, $i \in \mathcal{A}(\mathbf{x})$, *are linearly independent.*

Definition 4.3 *The* Lagrangian *function for the optimization problem (4.23) is defined as*

$$\mathcal{L}(\mathbf{x}, \lambda) = f(\mathbf{x}) + \sum_{i \in \mathcal{E} \cup \mathcal{I}} \lambda_i c_i(\mathbf{x}) \tag{4.25}$$

Theorem 4.1 *If we assume that* $\mathbf{x}^*$ *is a local minimizer of the problem (4.23), and* f *and* c_i *are continuously differentiable, and the LICQ applies to* $\mathbf{x}^*$, *then there is a vector of*

Lagrangian multipliers, λ^* made up of members λ_i^*, $i \in \mathcal{E} \cup \mathcal{I}$, so that we have

$$\begin{aligned} \nabla_x \mathcal{L}(\mathbf{x}^*, \lambda^*) &= 0 \\ c_i(\mathbf{x}^*) &= 0 \quad \forall i \in \mathcal{E} \\ c_i(\mathbf{x}^*) &\geq 0 \quad \forall i \in \mathcal{I} \\ \lambda_i^* &\geq 0 \quad \forall i \in \mathcal{I} \\ \lambda_i^* c_i(\mathbf{x}^*) &= 0 \quad \forall i \in \mathcal{E} \cup \mathcal{I} \end{aligned} \tag{4.26}$$

This set of conditions is known as the *first-order necessary conditions* for optimality, or *Karush-Kuhn-Tucker (KKT)* conditions (Nocedal et al., 2006) for the names of its inventors (Karush, 1939)(Kuhn et al., 1950) (as cited in (Kjeldsen, 2000)). KKT conditions are the basis for solving many of the constrained nonlinear optimization problems.

4.6.1 Quadratic Programming (QP)

The general structure of a QP problem can be expressed as

$$\begin{aligned} \underset{\mathbf{x}}{Minimize}\ & q(\mathbf{x}) = \frac{1}{2}\mathbf{x}^T G\mathbf{x} + \mathbf{x}^T c \\ subject\ to\ & \mathbf{a}_i^T \mathbf{x} = \mathbf{b}_i,\ i \in \mathcal{E} \\ & \mathbf{a}_i^T \mathbf{x} \geq \mathbf{b}_i,\ i \in \mathcal{I} \end{aligned} \tag{4.27}$$

where G is a symmetric square matrix, and $\mathbf{a}_i$ and $\mathbf{b}_i$ are vectors (Nocedal et al., 2006). If we assume the special case that the problem includes only equality constraints, then (4.27) reduces to

$$\begin{aligned} \underset{\mathbf{p}}{Minimize}\ & q(\mathbf{x}) = \frac{1}{2}\mathbf{x}^T G\mathbf{x} + \mathbf{x}^T \mathbf{c} \\ subject\ to\ & A\mathbf{x} = \mathbf{b} \end{aligned} \tag{4.28}$$

The KKT conditions state that, if $\mathbf{x}^*$ is a solution to the latter problem, there must be a λ^* vector such that

$$\begin{bmatrix} G & -A^T \\ A & 0 \end{bmatrix} \begin{bmatrix} \mathbf{x}^* \\ \lambda^* \end{bmatrix} = \begin{bmatrix} -\mathbf{c} \\ \mathbf{b} \end{bmatrix} \tag{4.29}$$

This equation results in the minimizer of the problem (4.27) (Nocedal et al., 2006). For the general case of the problems including both equality and inequality constraints, the MATLAB Optimization Toolbox uses an active-set method. This algorithm tries to find the optimal active set, which is the active set for the optimal point $\mathbf{x}^*$, by starting from an initial active set and improving it iteratively. In each iteration, some of the inequality constraints plus all equality constraints are considered, all as equalities. This way the problem (4.27) is converted to a series of less complex problems with format (4.28), which can be solved using KKT conditions. The interested reader can refer to (Gill et al., 1984) and (MathWorks, n.d.) for the details of this specific implementation of the algorithm.

4.6.2 Sequential Quadratic Programming (SQP)

Optimization techniques are iterative procedures. Starting from initial values for the decision variables, which are usually provided by the user, the algorithm tries to improve it step by step. In each step the current value of the decision variable $\mathbf{x}_k$ is updated to $\mathbf{x}_{k+1}$ using information from the objective function, and steps are repeated until a satisfactory optimum is reached or no more progress has been observed for a while.

The SQP tries to solve a constrained nonlinear optimization problem by generating a sequence of QP sub-problems, and that is where its name comes from. The SQP contains two loops, an outer loop and an inner one. The outer loop makes the QP sub-problem, and, based on the results from the sub-problem, moves the current point $\mathbf{x}_k$ to an improved position $\mathbf{x}_{k+1}$. The main duty of the inner loop is to solve the QP sub-problem provided by the outer loop. The specific version of the SQP implemented by the library used in our research can be stated in the following processing steps (MathWorks, n.d.):

1. Select an initial value for $(\mathbf{x}_0,\lambda_0)$. Set k to zero.

2. Convert the original optimization problem in (4.23) to a QP sub-problem by Taylor-series expansion of the Lagrangian function (4.25), and linearizing the

constraints. Taylor-series expansion of $f(\mathbf{x})$ around $\mathbf{x}_k$ is

$$f(\mathbf{x}_k + \mathbf{p}) = f_k + \nabla f_k^T \mathbf{p} + \frac{1}{2}\mathbf{p}^T B_k \mathbf{p} \tag{4.30}$$

where f_k is the objective function assessed at $\mathbf{x}_k$ and ∇ is the gradient operator defined as

$$\nabla f = \begin{bmatrix} \frac{\partial f}{\partial x_1} & \frac{\partial f}{\partial x_2} & \cdots & \frac{\partial f}{\partial x_n} \end{bmatrix}^T \tag{4.31}$$

B_k can be the *Hessian* of f at $\mathbf{x}_k$ or an approximate value for the Hessian. The Hessian matrix is the matrix of second order partial derivatives of a function:

$$\nabla^2 f = \begin{bmatrix} \frac{\partial^2 f}{\partial x_1^2} & \frac{\partial^2 f}{\partial x_1 \partial x_2} & \cdots & \frac{\partial^2 f}{\partial x_1 \partial x_n} \\ \frac{\partial^2 f}{\partial x_2 \partial x_1} & \frac{\partial^2 f}{\partial x_2^2} & \cdots & \frac{\partial^2 f}{\partial x_2 \partial x_n} \\ \vdots & \vdots & \ddots & \vdots \\ \frac{\partial^2 f}{\partial x_n \partial x_1} & \frac{\partial^2 f}{\partial x_n \partial x_2} & \cdots & \frac{\partial^2 f}{\partial x_n^2} \end{bmatrix} \tag{4.32}$$

The QP sub-problem in the SQP can be expressed as

$$\begin{aligned} \underset{\mathbf{p}}{Minimize}\ & f(\mathbf{x})\nabla f_k^T \mathbf{p} + \frac{1}{2}\mathbf{p}^T \nabla_{xx}^2 \mathcal{L}_k \mathbf{p} \\ subject\,to\ & \nabla c_i^T(\mathbf{x}_k)\mathbf{p} + c_i(\mathbf{x}_k) = 0,\ i \in \mathcal{E} \\ & \nabla c_i^T(\mathbf{x}_k)\mathbf{p} + c_i(\mathbf{x}_k) \geq 0,\ i \in \mathcal{I} \end{aligned} \tag{4.33}$$

3. Solve the QP sub-problem using the method explained in section 4.6.1 to obtain the best $\mathbf{p}$, which shows the direction of search.

4. Update $\mathbf{x}$ using $\mathbf{x}_{k+1} = \mathbf{x}_k + \alpha\mathbf{p}$, where α shows the distance we can proceed along the direction $\mathbf{p}$. A merit function

$$\Psi(\mathbf{x}) = f(\mathbf{x}) + \sum_{i \in \mathcal{E}} r_i\, c_i(\mathbf{x}) + \sum_{i \in \mathcal{I}} r_i\, max\left\{0, c_i(\mathbf{x})\right\} \tag{4.34}$$

where

$$(r_{k+1})_i = \underset{i}{max}\left\{\lambda_i, \frac{(r_k)_i + \lambda_i}{2}\right\},\ i \in \mathcal{E} \cup \mathcal{I} \tag{4.35}$$

$$(r_0)_i = \frac{\|\nabla f(\mathbf{x})\|}{\|\nabla c_i(\mathbf{x})\|} \tag{4.36}$$

is used in determining α. α should be calculated in a way that makes sufficient decrease in the merit function. The merit function (4.34) has been adopted from (Powell, 1978).

5. If a sufficient change in $\mathbf{x}$ has not happened, or a pre-set number of function calls has reached, quit. Otherwise continue from step 2.

The Hessian matrix $H_k = \nabla^2_{xx}\mathcal{L}_k$, containing the second-order partial derivatives of the Lagrangian function, can be evaluated directly, but its calculation in all iterations is time consuming. To alleviate this problem, a class of methods called *quasi-Newton* methods have been proposed, which use only the first-order derivatives (gradient). In this implementation of the SQP, a quasi-Newton algorithm called BFGS, named after its inventors Broyden, Fletcher, Goldfarb and Shanno, has been used, which updates the Hessian matrix by (MathWorks, n.d.)

$$H_{k+1} = H_k + \frac{q_k q_k^T}{q_k^T \mathbf{s}_k} - \frac{H_k^T \mathbf{s}_k^T \mathbf{s}_k H_k}{\mathbf{s}_k^T H_k \mathbf{s}_k} \tag{4.37}$$

where

$$\mathbf{s}_k = \mathbf{x}_{k+1} - \mathbf{x}_k \tag{4.38}$$

$$q_k = \left(\nabla f(\mathbf{x}_{k+1}) + \sum_{i \in \mathcal{E} \cup \mathcal{I}} \lambda_i \nabla c_i(\mathbf{x}_{k+1})\right) - \left(\nabla f(\mathbf{x}_k) + \sum_{i \in \mathcal{E} \cup \mathcal{I}} \lambda_i \nabla c_i(\mathbf{x}_k)\right) \tag{4.39}$$

In this chapter, commonly-used models proposed to explain and model the variations of SM were reviewed. In Chapter 6, the applicability of these models to the ground measurements of SM in our study area will be discussed, and the results of the analysis of the spatial variability in ground measurements and outputs of SAR backscattering models will be presented.

Chapter 5

Implementation

In this chapter we will explain the data and methods used for evaluation of the models and analyzing the spatial variability of SM. The parameters used and the criteria by which the performance of models are measured will be described in the following sections.

5.1 Study Area and Data

The area under study in this research is a bare agricultural area located in Carman, about 50 km southwest of Winnipeg, Manitoba, Canada. It has a level topography which helps in processing SAR images without using a digital elevation model (DEM). According to the slope maps of Canadian Digital Surface Model (CDSM) from Natural Resources Canada, the region has an average slope of 0.56 degrees. The climate of the area is classified as subhumid to humid continental, and most of the precipitation happens in summer in this area (Merzouki et al., 2010). The models were implemented using three single look complex (SLC) Radarsat-2 images of the area acquired in fine quad-polarization mode from 22 April 2008 to 16 May 2008. Acquisition parameters of each image are mentioned in Table 5.1. The temporal differences between the images are 17 and 7 days. As presented in the table, the second image has a different incidence angle than the other two, which causes a difference in the original pixel size.

Figure 5.1 shows the location of the study area and the measurement sites covered by the SAR image of Epoch 1. Concurrent with every epoch of image acquisition SM measurements were carried out in the field for the top 6 cm of soil using ThetaProbe (Delta-T Device Ltd., Cambridge, UK) sensors by Agriculture and Agri-Food Canada (AAFC). In order to remove the effect of vegetation cover, only bare fields were selected for ground measurements. In

Table 5.1: Satellite images used in this study: Dates and times are local.

Epoch	Date of Acquisition	Time of Acquisition	Beam Mode	Incidence Angle	Orbit	Nominal Pixel Size (m×m)
Epoch 1	22 April 2008	19:15:41	FQ11	31°	Ascending	9×6
Epoch 2	9 May 2008	19:19:51	FQ15	35°	Ascending	8×5
Epoch 3	16 May 2008	19:15:41	FQ11	31°	Ascending	9×6

addition, the selected sites were homogeneous with respect to soil type, slope and soil surface roughness. For each test field, data were collected in an approximately 150 m×150 m site over a grid of 16 sampling points, and each point was sampled 4 times, resulting in 64 measurements in each site. In addition to SM, surface roughness RMS height and correlation length were estimated for selected fields using the measurements of a one-meter needle profiler which consisted of a camera to take ground profile photographs. The photographs were processed by AAFC to extract RMS height and correlation length. For each site, five sampling points, representative of the sampling site, were selected which were at least 5 m apart, and the roughness measurements were carried out in the look direction of Radarsat-2 sensor (Merzouki et al., 2010).

Figure 5.2 shows a typical site of field measurements carried out by AAFC. The boundaries of each site in AAFC maps are defined by four points which are shown by circles in this figure. For the site displayed in the figure, this makes an area consisting of 272 SAR image pixels. The dimensions of each pixel are 10 m × 10 m, as we will describe later in section 5.3. However, as mentioned above, the SM data in each site was collected on a grid of 16×16 points, which are displayed by triangles in the grey area. Thus, no ground measurement of SM is available for the white pixels in Figure 5.2. Measuring SM for each pixel in the field is not practical, and, the average SM for each site needs to be compared to the average SM values estimated by the scattering model in the same site when evaluating the models. However, given the high spatial variability of SM, it does not seem reasonable to assume that the average SM value calculated for the grey area, which covers only 100 pixels, can

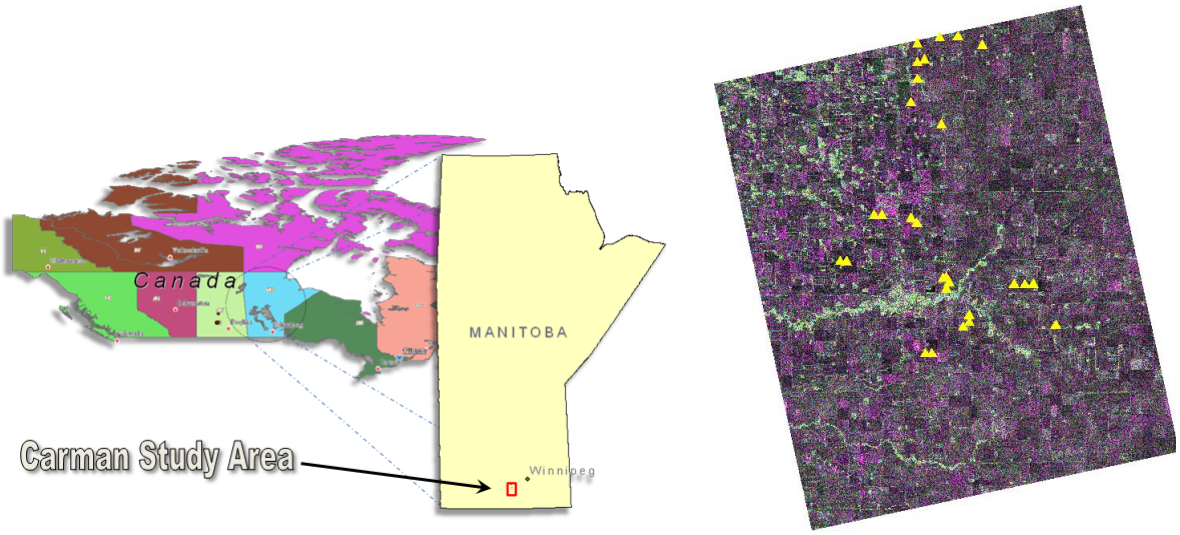

(a) Map of Carman Site

(b) Radarsat-2 image of the study area acquired in Epoch 1, and location of fields used for ground measurement of SM and roughness covered by this image.

Figure 5.1: Study area near Carman, Manitoba, Canada

represent the status of SM for the whole area defined by circles in Figure 5.2. Therefore, in this study, for the purpose of evaluation of the backscattering models, we compare the average SM value of the pixels covering the measurement grid in each site, i.e. only pixels in the grey area, with the average value of ground measurements of SM in that site.

Using Monte Carlo simulations, it has been shown that in order to have a 10% precision in measuring RMS height and correlation length of the surface roughness, it is necessary to have surface profiles of length at least $40\,\bar{l}$ and $200\,\bar{l}$, respectively (Oh et al., 1998), where $\bar{l}$ is the average correlation length. The average correlation length measured in the Carman experiment has been 10.58 cm. Therefore, the length of the profiles needed to be, at least, 4 m to have a 10% precision in RMS height measurements. Furthermore, for natural surfaces, it has been shown that in order to extract valuable roughness information (5%-13% precision for RMS height and 10%-40% precision for correlation length) the length of the profiles used for calculations should be at least 10 m (Baghdadi et al., 2000). Since the ground measurements of surface roughness for Carman area have been carried out using a 1 m profiler, these measurements do not seem to be reliable and suitable for comparison

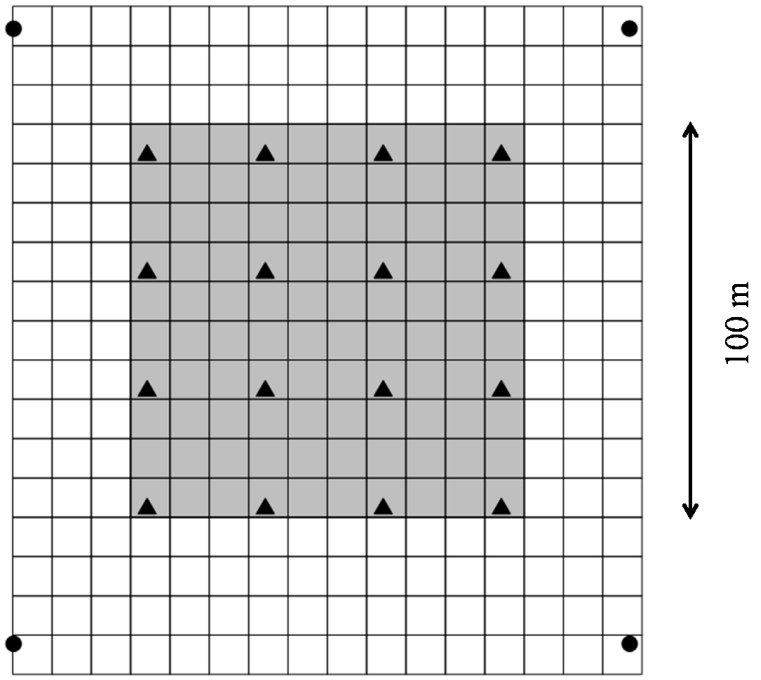

Figure 5.2: A typical ground measurement grid in Carman study area: Triangles show the location of ground measurements of SM. The circles represent the four points which have been used in AAFC maps to define site boundaries. Each small square depicts a pixel of size 10 m $\times$ 10 m.

with RMS height estimations from the models. Moreover, in this study, we intended to estimate SM without using any ancillary field measurements. Thus, the information about soil surface roughness are not used in the inversion process in our study. Furthermore, the calibration process that will be proposed for SM is not related to and does not produce roughness parameters.

According to AAFC publications that have used these data for estimation of SM, meteorological constraints were considered so that ground measurements and satellite image acquisitions were not carried out during extreme rainfall or long freezing periods (Merzouki et al., 2010). Table 5.2a and Table 5.2b show temperature and precipitation data for Carman study area during April and May 2008 (Environment Canada, 2013). According to these tables, for Epoch 1 and Epoch 2 of data collection the minimum temperature has been below zero, which may have caused freezing of SM. This may result in errors in SM estimation using SAR backscattering models. The dielectric mixing model does not take into account

the change in the dielectric constant because of freezing when estimating SM values from the dielectric constant of soil. Furthermore, there was some precipitation on the day the data for Epoch 1 was collected and a few days before that. This may also affect the performance of SM estimation by backscattering models.

In tables 5.3 to 5.5 a summary of the SM information provided by AAFC for the three epochs of data collection in Carman study area is presented. In these tables, mean value of 64 ground measurements for each site, 95% confidence interval for the mean value, and the range of SM values around the mean value covered by the 95% confidence interval are presented. The 95% range is calculated by subtracting the mean SM value of each site from the lower and upper bounds of the confidence interval of the mean for that site. Averaging the 95% range values suggests that, on average, the mean SM value has been measured with about 1.27 vol.% precision. This precision will later be used in Chapter 6 to help in assessing the performance of the models. The confidence intervals are estimated using a nonparametric method called *bootstrapping* (using 1000 iterations) which is explained in Appendix A. Note that, the SAR images do not cover all of the sites.

5.2 Pre-processing

As the very first step, the original Radarsat-2 SLC images were converted[1] to coherency matrix format (using σ° LUT). The rest of operations were carried out using this format. This is mainly because we intend to compare the results of the four scattering models before analyzing the spatial variability of SM. The X-Bragg model needs the coherency matrix for calculating $H/A/\alpha$ parameters in order to invert the soil surface parameters. Thus, for the sake of consistency in data used with all models, speckle filtering was performed on the coherency matrix, and backscattering coefficients for the Oh, the Dubois and the IEM models were calculated using the coherency matrix elements:

[1] using PolSARpro v4.2 (European Space Agency, 2011) software

Table 5.2: Daily climate data for Carman study area for April and May 2008: The rows corresponding to dates of data collection for the three epochs of the data are marked in the tables.

(a) April 2008

Day	Max Temp. (°C)	Min Temp. (°C)	Mean Temp. (°C)	Total Precip. (mm)
01	4.1	-6.8	-1.4	0
02	7.6	-3.9	1.9	0.7
03	11	-2.2	4.4	0
04	5.2	-4.3	0.5	1.3
05	-0.3	-15.1	-7.7	0
06	2.8	-7.6	-2.4	0
07	7.4	-6.3	0.6	0.6
08	10.5	-4.8	2.9	0
09	6.5	-3.3	1.6	0
10	10.9	-1.7	4.6	0
11	8	-0.4	3.8	0
12	8.8	-5.6	1.6	0
13	14.1	-7.6	3.3	0.7
14	19.2	0.6	9.9	0.7
15	15.7	4.2	10	0
16	14.8	2.8	8.8	0
17	15.6	-2.8	6.4	0.6
18	20.5	-1.1	9.7	0.8
19	19.9	-0.9	9.5	0.6
20	16.9	2.2	9.6	0.6
21	9.3	-4.1	2.6	4.3
22	13	-5.8	3.6	0.7
23	8.1	-3	2.6	2.4
24	0.4	-2.2	-0.9	7.5
25	1.5	-4.3	-1.4	0
26	4.4	-2.1	1.2	0.6
27	6.4	-5.3	0.6	0
28	9.6	-7.2	1.2	0
29	16.4	-1.7	7.4	0
30	16.9	-1.4	7.8	0

(b) May 2008

Day	Max Temp. (°C)	Min Temp. (°C)	Mean Temp. (°C)	Total Precip. (mm)
01	14	2.1	8.1	0
02	8.6	-1.6	3.5	0
03	11.4	-4.3	3.6	0
04	5.9	-5.9	0	0
05	16.8	-7.3	4.8	0
06	16.1	2	9.1	0
07	11.3	-1.2	5.1	0
08	13.1	-5.8	3.7	0
09	8.9	-1	4	0
10	9.4	-3.6	2.9	0
11	17.3	-5.7	5.8	0
12	11.1	4.2	7.7	15.4
13	13.8	3.6	8.7	2.6
14	19.5	3.3	11.4	0.8
15	21.1	3.1	12.1	0
16	23.2	6.6	14.9	0
17	19	5.3	12.2	0
18	16.9	1.7	9.3	0
19	12.3	4.8	8.6	6.4
20	14.2	2.1	8.2	0
21	17.3	1.8	9.6	0
22	17.9	4.1	11	0
23	22.6	6.1	14.4	0
24	25.7	5.1	15.4	0.2
25	17.4	3.8	10.6	4.4
26	12.7	3	7.9	1.6
27	17.8	-1.2	8.3	0
28	21.9	2.7	12.3	M
29	20.8	4.9	12.9	0
30	18.7	8.9	13.8	2.2
31	21.7	8.8	15.3	0

Table 5.3: Ground measurements of Epoch 1 in Carman study area: Mean value of 64 ground measurements, 95% confidence interval for the mean value, and the range of SM values around the mean value covered by the 95% confidence interval are presented for each site.

Site	Mean SM (vol.%)	95% Confidence Interval (vol.%)	95% Range (vol.%)
1	17.36	(16.01,18.72)	(-1.35,1.36)
2	20.08	(18.56,21.56)	(-1.51,1.49)
3	19.34	(17.96,20.73)	(-1.38,1.39)
8	19.56	(18.43,20.81)	(-1.13,1.24)
9	8.45	(8.02,8.88)	(-0.43,0.42)
10	10.82	(10.05,11.50)	(-0.77,0.68)
11	10.79	(10.16,11.44)	(-0.63,0.65)
12	7.26	(6.84,7.75)	(-0.43,0.48)
13	10.11	(9.02,11.37)	(-1.09,1.26)
14	17.79	(16.18,19.33)	(-1.61,1.54)
15	9.13	(8.61,9.68)	(-0.51,0.56)
16	16.15	(15.07,17.18)	(-1.07,1.03)
17	12.71	(11.54,13.99)	(-1.17,1.28)
18	11.66	(11.07,12.30)	(-0.59,0.64)
19	13.67	(11.84,15.51)	(-1.82,1.85)
22	13.56	(12.41,14.75)	(-1.15,1.19)
23	11.39	(10.06,12.92)	(-1.33,1.54)
24	10.97	(9.70,12.46)	(-1.27,1.49)
25	9.50	(8.55,10.44)	(-0.95,0.94)
26	7.16	(6.38,7.95)	(-0.78,0.79)
27	12.21	(11.38,13.15)	(-0.83,0.94)
28	14.78	(12.81,16.60)	(-1.98,1.81)
29	8.92	(7.60,10.35)	(-1.32,1.43)
30	7.94	(6.70,9.18)	(-1.24,1.24)
31	8.32	(7.32,9.42)	(-1.01,1.10)
32	12.17	(11.46,13.01)	(-0.71,0.84)
33	13.10	(12.08,14.26)	(-1.02,1.15)
34	16.63	(15.48,17.85)	(-1.16,1.22)
35	20.45	(19.29,21.67)	(-1.16,1.22)
36	19.25	(18.14,20.36)	(-1.12,1.10)
37	16.69	(14.88,18.50)	(-1.81,1.81)
38	15.96	(14.97,17.01)	(-0.99,1.05)
39	15.00	(14.23,15.88)	(-0.78,0.88)
40	16.08	(15.04,17.13)	(-1.04,1.05)
43	13.55	(12.39,14.63)	(-1.16,1.08)
44	20.32	(17.83,22.83)	(-2.49,2.51)
45	13.01	(12.02,14.02)	(-0.99,1.01)
46	12.76	(11.85,13.65)	(-0.91,0.89)

Table 5.4: Ground measurements of Epoch 2 in Carman study area: See Table 5.3 for an explanation of the columns.

Site	Mean SM (vol.%)	95% Confidence Interval (vol.%)	95% Range (vol.%)
1	14.91	(13.18,16.55)	(-1.73,1.64)
2	18.67	(16.88,20.43)	(-1.79,1.76)
4	20.60	(18.47,22.76)	(-2.13,2.16)
5	25.15	(23.49,26.88)	(-1.66,1.73)
6	24.32	(22.67,26.07)	(-1.65,1.76)
7	19.74	(17.66,21.89)	(-2.08,2.15)
8	17.47	(15.56,19.25)	(-1.91,1.78)
9	1.46	(1.16,1.77)	(-0.29,0.31)
10	11.55	(10.33,12.71)	(-1.22,1.16)
11	7.60	(6.77,8.48)	(-0.83,0.88)
12	1.21	(0.98,1.47)	(-0.23,0.26)
13	2.68	(2.21,3.22)	(-0.47,0.54)
14	7.51	(6.32,8.72)	(-1.20,1.21)
15	2.40	(1.89,2.98)	(-0.51,0.58)
16	10.00	(9.10,10.94)	(-0.90,0.94)
17	12.61	(10.93,14.41)	(-1.67,1.80)
18	18.65	(16.75,20.57)	(-1.91,1.92)
19	14.13	(12.57,15.72)	(-1.56,1.59)
20	16.85	(14.82,19.02)	(-2.03,2.16)
21	14.96	(13.22,16.81)	(-1.74,1.85)
22	14.65	(12.87,16.52)	(-1.78,1.87)
23	14.20	(12.70,15.82)	(-1.50,1.62)
24	11.12	(9.84,12.52)	(-1.28,1.40)
25	4.69	(3.72,5.71)	(-0.96,1.02)
26	2.73	(2.27,3.20)	(-0.46,0.47)
27	8.36	(7.26,9.49)	(-1.10,1.13)
28	13.62	(11.70,15.36)	(-1.92,1.75)
29	8.29	(6.86,9.63)	(-1.42,1.35)
30	8.97	(7.52,10.49)	(-1.46,1.51)
31	9.61	(8.30,11.03)	(-1.31,1.42)
33	7.97	(7.14,8.83)	(-0.84,0.86)
34	10.76	(9.48,12.11)	(-1.28,1.35)
38	7.89	(6.43,9.51)	(-1.46,1.62)
39	9.50	(7.72,11.20)	(-1.78,1.71)
40	11.72	(9.40,13.78)	(-2.32,2.06)
42	11.92	(10.32,13.57)	(-1.60,1.65)
43	8.76	(7.64,9.93)	(-1.12,1.16)
44	15.96	(13.68,18.18)	(-2.28,2.22)
45	7.91	(7.02,8.79)	(-0.89,0.88)
46	6.54	(5.80,7.35)	(-0.75,0.81)

Table 5.5: Ground measurements of Epoch 3 in Carman study area: See Table 5.3 for an explanation of the columns.

Site	Mean SM (vol.%)	95% Confidence Interval (vol.%)	95% Range (vol.%)	Site	Mean SM (vol.%)	95% Confidence Interval (vol.%)	95% Range (vol.%)
1	20.35	(18.96,21.79)	(-1.39,1.43)	23	23.83	(22.26,25.43)	(-1.58,1.60)
2	22.15	(20.86,23.56)	(-1.29,1.41)	24	18.15	(16.87,19.47)	(-1.28,1.31)
3	21.75	(20.20,23.25)	(-1.55,1.50)	25	14.95	(13.69,16.19)	(-1.26,1.24)
4	27.72	(26.00,29.76)	(-1.72,2.03)	26	8.89	(8.16,9.60)	(-0.73,0.71)
5	34.07	(32.78,35.48)	(-1.29,1.41)	27	16.60	(15.50,17.77)	(-1.10,1.17)
6	31.30	(29.69,32.96)	(-1.61,1.66)	28	21.50	(19.89,23.03)	(-1.61,1.53)
7	24.09	(21.85,26.41)	(-2.24,2.32)	29	13.02	(12.24,13.86)	(-0.78,0.84)
8	19.02	(17.72,20.29)	(-1.30,1.27)	30	17.89	(16.75,19.23)	(-1.14,1.34)
9	10.02	(9.38,10.67)	(-0.64,0.66)	31	14.47	(13.52,15.37)	(-0.95,0.90)
10	20.70	(19.80,21.56)	(-0.91,0.85)	33	10.12	(9.41,10.84)	(-0.71,0.72)
11	12.60	(12.11,13.17)	(-0.49,0.56)	34	17.15	(15.74,18.52)	(-1.41,1.37)
12	7.19	(6.79,7.65)	(-0.41,0.46)	35	16.54	(15.64,17.46)	(-0.90,0.92)
13	11.23	(10.71,11.72)	(-0.52,0.49)	36	15.92	(14.83,17.06)	(-1.09,1.14)
14	16.25	(15.03,17.46)	(-1.22,1.21)	37	17.08	(15.88,18.41)	(-1.20,1.33)
15	9.01	(8.47,9.51)	(-0.54,0.50)	38	17.37	(15.54,19.11)	(-1.83,1.75)
16	14.32	(13.32,15.32)	(-1.01,1.00)	39	17.33	(15.64,19.18)	(-1.68,1.86)
17	20.38	(19.03,21.84)	(-1.35,1.46)	40	16.92	(15.16,18.81)	(-1.75,1.89)
18	22.94	(21.60,24.23)	(-1.34,1.29)	42	21.94	(20.09,23.76)	(-1.85,1.82)
19	20.29	(18.77,21.95)	(-1.51,1.66)	43	13.64	(12.55,14.60)	(-1.09,0.96)
20	22.80	(21.16,24.48)	(-1.64,1.68)	44	25.45	(23.51,27.34)	(-1.93,1.90)
21	25.91	(24.16,27.63)	(-1.75,1.72)	45	10.84	(10.14,11.63)	(-0.70,0.79)
22	22.11	(20.39,23.62)	(-1.73,1.51)	46	7.97	(7.34,8.58)	(-0.63,0.61)

$$\sigma^{\circ}_{hh} = \frac{|T_{11} + T_{12} - \Im(T_{12})\ 2\mathrm{i}|^2}{2\,|\mathrm{T}_{11}|} \tag{5.1}$$

$$\sigma^{\circ}_{vv} = \frac{|T_{11} - T_{12} - \Im(T_{12})\ 2\mathrm{i}|^2}{2\,|T_{11}|} \tag{5.2}$$

$$\sigma^{\circ}_{hv} = \frac{T_{33}}{2} \tag{5.3}$$

where T_{ij} shows the element at row i and column j of the coherency matrix.

Given the level topography of the study area, the incidence angle for each pixel was calculated as

$$\theta = \arcsin\left\{\frac{(\beta^{\circ})^2}{(\sigma^{\circ})^2}\right\} \tag{5.4}$$

where β° and σ° can be obtained from the two LUTs in the meta-data delivered with Radarsat-2 images. In an experiment with the purpose of assessing the effect of changes of incidence angle in estimated SM value by the IEM, it was revealed that changing the local incidence angle from 30.2572° (the minimum incidence angle of the image in Epoch 1) to 31.9678° (the maximum incidence angle of the image in Epoch 1), when considering the average backscattering coefficients of the image in Epoch 1, could change the estimated SM value by 1.96 vol.%. This change is slightly bigger than the precision of mean SM from the ground measurements with which the model estimates should be compared. Therefore, the local incidence angle could not be assumed constant for the whole image, and it was assumed constant only within each site. Also, it was revealed that a change in the local incidence angle equal to the average slope of the study area can cause about 0.49 vol.% change in estimated SM value. Thus, as mentioned before, the slope was neglected in processing of the SAR images.

In order to reduce the effect of speckle, the coherency matrix image was filtered with a Lee refined filter (Lee, 1981) with a 7×7 sliding window, which has been reported to yield good results (Lee et al., 1994).

5.3 Geo-referencing

Since our ground measurements are provided in the ground coordinate system (NAD 1983 UTM Zone 14N), in order for them to be compared with output of a model, it was necessary to either geo-reference the original image and do the calculations in geo-referenced image domain, or transfer the ground measurements to image domain and compare them to model outputs after doing calculations in the raw image domain. Processing in raw image domain can be faster if we need to calculate the local incidence angles for each pixel. Because the local incidence angles in flat areas are constant along the azimuth direction, which is usually the vertical direction (along columns) on the raw image. Therefore, by working on the original image domain, one can probably use the same local incidence angle values for a large subset of model input calculations when generating full SM maps. However, in this study, we have assumed that local incidence angle is constant within each site, because its changes is very small for the small dimensions of a site. Furthermore, only pixels within sites (not all of the pixels in the image) have been processed to speed up the algorithms.

Since working in the geo-referenced image domain makes implementing the models easier, in this study we performed our calculations in this domain. The images were geo-referenced using a second order polynomial transformation

$$\begin{cases} x &= a_1X^2 + b_1Y^2 + c_1XY + d_1X + e_1Y + f_1 \\ y &= a_2X^2 + b_2Y^2 + c_2XY + d_2X + e_2Y + f_2 \end{cases} \tag{5.5}$$

where x and y are the coordinates in image system, and X and Y are the coordinates in ground system. The coefficients in the above equations are calculated using a number of ground control points acquired from previously geo-referenced SPOT images, i.e. an image-to-image registration was performed. The RMSE values for the transformation of images of the three epochs were 0.69, 0.77 and 0.68 pixels, respectively. In order not to change the original values of backscattering coefficient and coherency matrix, a nearest neighbor resampling was used for geo-referencing, and the resampled pixels were 10 m $\times$ 10 m.

5.4 Inversion of the Models and Multifractal Analysis

The Oh model and the Dubois model can be easily inverted analytically according to equations (3.58) to (3.61) and (3.64) to (3.65). For inverting the IEM and the X-Bragg models, a LUT has been utilized in this study, because it is fast and easy to implement. The LUT is, indeed, a rectangular grid of regularly-spaced values of the two unknown parameters of the model over a reasonable domain of theses parameters. For each node in the grid, the surface scattering model is executed to simulate the backscattering coefficients, in case of the IEM, and H and α, in case of the X-Bragg.

For the IEM, the unknown parameters are the dielectric constant of the soil and the surface RMS height. For the ranges of the parameters Loew et al. (2006) and Kim et al. (2012) suggest to use $5 < \epsilon_r < 35$ for the dielectric constant, and 0.5 cm $< \sigma <$ 5 cm for the RMS height. In this study, we decreased the lower bound of the dielectric constant to cover even some negative numbers of SM values, i.e. we selected $0.1 < \epsilon_r < 35$. The purpose was to check if the model estimates any negative SM values. Although the negative SM values estimated by the model were rare, they were deleted from the outputs of the model, i.e. they were assumed as missing data. It should be mentioned that, according to the Topp dielectric mixing model, $\epsilon_r = 35$ is equivalent to $m_v = 48$ vol.%, and the maximum SM value measured in the field in our study area is 43.6 vol.%. Thus, the selected upper bound of ϵ_r is consistent with the ground measurements. Also, the minimum and maximum RMS height observed in the field for our study area are 0.52 cm and 3.81 cm, respectively, which both are within the range 0.5 cm $< \sigma <$ 5 cm selected in this study. For the X-Bragg, the unknown parameters are the dielectric constant of the soil and the β_1 angle. The possible range of values for the angle is $0^\circ < \beta_1 < 90^\circ$ (Hajnsek, 2001). Sample spacing for ϵ_r, σ and β_1 were 0.1, 0.01 cm and 0.1°, respectively.

Before the IEM can simulate the backscattering coefficients, it is also necessary to set the value of the power index parameter for constructing the n^{th} power of the surface power

spectrum, i.e. equation (3.31). In order to find the best value for power index, p , multiple values were used in the IEM simulation module. The results of this experiment will be presented in Chapter 6. It is worth mentioning that, in the process of the IEM simulation, b_p parameter in (3.28) was approximated by

$$b_p = 0.9993\, p\, (0.1083 + p)^{-1} \tag{5.6}$$

suggested by Loew et al. (2006). As mentioned earlier, the models were only executed for pixels inside the ground measurement sites, and the incidence angle for all pixels inside a single site was assumed constant and equal to the average of the incidence angle values inside the site for the sake of speeding the inversion process up. In figure 5.3 a flowchart of the steps for implementing the IEM is displayed. As we will see in the next chapter, the IEM is the model selected for multifractal analysis of SM values because of its high inversion rates. It should be mentioned that, after obtaining the dielectric constant values form the SAR backscattering models, they were converted to volumetric SM values using the Topp dielectric mixing model.

In the optimization procedure for fitting the STRAIN model to data, the range of parameter β was set to $0 < \beta < 1$ as this is the possible range in the model (Deidda et al., 1999). There is not a predefined range for parameter c, thus, in this study it was set to $0 < c < 50$ to cover a wide range. In producing the final results and estimating the parameters of the calibration model, as we will see in Chapter 6, all the estimated values for the parameter c are less than 20 when β is fixed. The initial values for these two parameters were set to 0 in the SQP optimization procedure. The moment order, q, was changed in the range 2-6 (integer numbers) following (Mascaro et al., 2010).

All the processing steps except for reading the raw SLC images, speckle filtering, and producing $H/A/\alpha$ images (which were carried out using PolSARpro) were executed in the Matlab R2012a programming environment. PolSARpro software includes modules for executing the same version of the Oh and the Dubois model implemented in this study. In

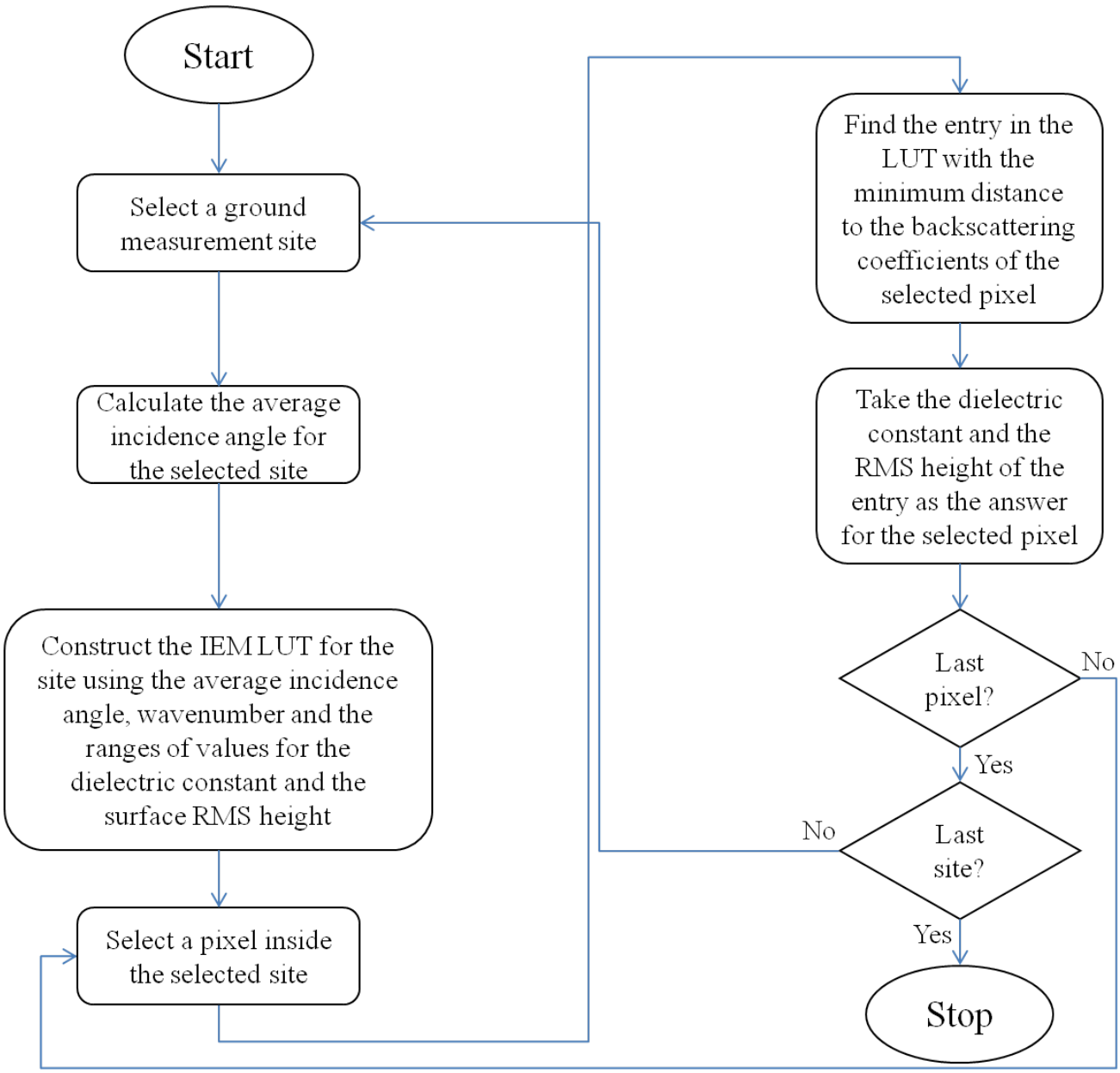

Figure 5.3: Flowchart of the IEM

order to validate the outputs of our implementation of these two models against the outputs of PolSARpro, average of SM values calculated for the field sites of Epoch 1 using our implementation and PolSARpro implementation where compared. The correlation coefficient between the two sets of SM values were 0.98 and 0.97 for the Oh and Dubois models, respectively. Since the exact same equations have been used for both implementations, the slight difference in the results may be associated with rounding and difference in programming languages. There is also a module in PolSARpro for executing a model called X-Bragg2008. Unfortunately, no documentation of this model was found in the package. Thus, it could not be used for validation of our implementation of X-Bragg. However, as mentioned in section 6.2.1, the results of X-Bragg2008 in PolSARpro exhibited very low inversion rates similar to what obtained from the results of our implementation of X-Bragg.

5.5 Evaluation of the Algorithms

Validation of the results of the SM estimation algorithms against ground measurements of SM is difficult. The reason is that, while output of such algorithms is a continuous areal estimate for the average SM over a pixel or group of pixels, the ground measurements are discontinuous point or areal measurements with a limited spatial domain (Sharma, 2009). Therefore, it is necessary to compare the average value of SM values from model estimations and ground measurements over the same geographical extent. The extent can be the area of a pixel (in case ground measurements within every pixel can be identified), a field, a catchment, or even a larger area depending on the resolution of the data used and the number and sparsity of SM measurements. An issue with comparing the averages is that, as we will see in Chapter 6, some of the models generate patchy outputs with large connected inverted and uninverted pixels. In this case, the average SM value estimated by the model may not be a good representative for the selected geographic extent for which it is calculated. Therefore, comparing the average value of the ground measurements and the average value of

the model outputs may not be reasonable. However, unless there is plenty of images obtained in different dates, there is not much one can do about filling the large gaps in estimated SM values.

There has not been much research work on performance metrics for SM estimation using RS (Entekhabi et al., 2010). Researchers often use the two well-known measures namely the *correlation coefficient* (or its square, *coefficient of determination*) and the *Root Mean Square Error* (RMSE) (Hajnsek, 2001)(Alvarez-Mozos et al., 2007)(Oh et al., 1992)(Dubois et al., 1995). In this study, for evaluating the agreement of the SM estimated from the models and ground measurements, we use these two measures along with the average value of the residuals, $\bar{r}$, as an indicator of bias in the model.

For evaluation of linear fits, in this study, the correlation coefficient and p-value of F-test is considered. The p-value can show the significance of the fit. For example a p-value less than 0.05 shows that the fit is significant at a 95% significance level. Since the F-test can only be performed when residuals of the fit are normally distributed, the p-value is reported only when Kolmogorov-Smirnov test (Massey, 1951) fails to reject the null hypothesis (that the distribution of the residuals is normal) at 5% significance level.

Kvalseth (1985) compares 8 different versions of the correlation coefficient used in literature, and concludes that if the correlation coefficient is defined as

$$R = \sqrt{1 - \frac{\sum_{i=1}^{N}(O_i - P_i)^2}{\sum_{i=1}^{N}(O_i - \bar{O})^2}} \tag{5.7}$$

it can be used for both linear and nonlinear fits. In this equation, O_i is the i^{th} observed value for the dependent variable, P_i is the fitted value corresponding to O_i, $\bar{O}$ is the average of O_i's, and N is the number of data points. Kvalseth (1985) also suggests that in addition to the correlation coefficient, RMSE be reported for the fit. Following (Kvalseth, 1985), in this thesis, we report the correlation coefficient defined in (5.7) and the RMSE when assessing

nonlinear fits.

Chapter 6

Experimental Results

The backscattering models introduced in Chapter 3 were implemented and applied in estimation of surface SM using three Radarsat-2 images. In order to assess the performance of these models, the outputs of the models (after converting to volumetric SM values using the Topp model) were then compared to three epochs of ground measurements concurrent with image acquisitions explained in Chapter 5. As will be shown in the following sections, the RMSE obtained by comparing the outputs of the models with field measurements are large in comparison to the confidence intervals calculated for mean ground-measured SM of field sites. This suggests that the RMSE values are significant, and the models need improvement.

Because of its dense pattern of inversion, the IEM was selected for exploring the feasibility of using the spatial variability analysis introduced in Chapter 4 for improving the outputs of this backscattering model. On the other hand, examining the field measurements by these analysis tools shows that the fractal analysis is more suitable for our data set. Thus, both ground measurements and output of the IEM were studied for scale invariance and multifractality according to the STRAIN model. The results of this investigation along with our findings about improving the quality of SM estimation using the fractal analysis are presented in this chapter. We first start by examining the performance of the backscattering models, and then look at the results of spatial variability analysis.

6.1 Power Index Experiment for the IEM

The shape of the power law spectrum in equation (3.28) has to be selected when using this generalized form in the IEM. To select the shape, it is needed to determine the best value for the power index parameter p for our data set. For this purpose, the IEM was run on

Table 6.1: Summary of the performance of the IEM in all epochs using different values of power index

		$p = 1.5$	$p = 2$	$p = 3$	$p = 5$	$p = 10$	$p = 20$
Epoch 1	RMSE (vol.%)	17.45	5.83	9.57	7.83	8.16	9.48
	R	-0.13	-0.11	-0.37	-0.32	-0.32	-0.32
Epoch 2	RMSE (vol.%)	24.13	7.88	9.8	12.85	14.81	13.40
	R	-0.05	0.19	0.07	0.03	0.00	0.05
Epoch 3	RMSE (vol.%)	15.83	9.57	14.14	12.23	12.15	13.06
	R	-0.35	-0.23	-0.19	-0.13	-0.21	-0.24

SAR images of all epochs using multiple values of the power index. The scatter plots of the results for Epoch 1 are presented in Figure 6.1. In this figure each point (black circle) in a graph depicts a field site for which the model has calculated SM values. The abscissa and ordinate of each site represents the average of SM values measured on the ground and the average of SM values estimated by the model in that field, respectively. The 1:1 line is also displayed on each graph to show the location were perfect matches between ground-measured and model-calculated SM could happen.

For $p = 1$, which corresponds to an exponential correlation function, the model did not generate any results. According to scatter plots in Figure 6.1, the model almost constantly overestimates SM when power index is set to 1.5. In contrast, $p = 3$ makes the model underestimate SM for most of the sites. It should be mentioned that negative correlation coefficients calculated for all p values in Epoch 1 show a weak performance of the IEM for all cases in this epoch. However, $p = 2$ seems to generate better results than other cases according to both RMSE (5.83 vol.%) and correlation coefficient (-0.11) measures. The values of p have been selected so that they cover a wide range of power index values from 1 to 20. The reason for selecting $p = 3$ and $p = 1.5$ is to check the results for values around $p = 2$, for which the IEM performs usually better for our data.

Table 6.1 summarizes the values of performance measures for the IEM when applied on

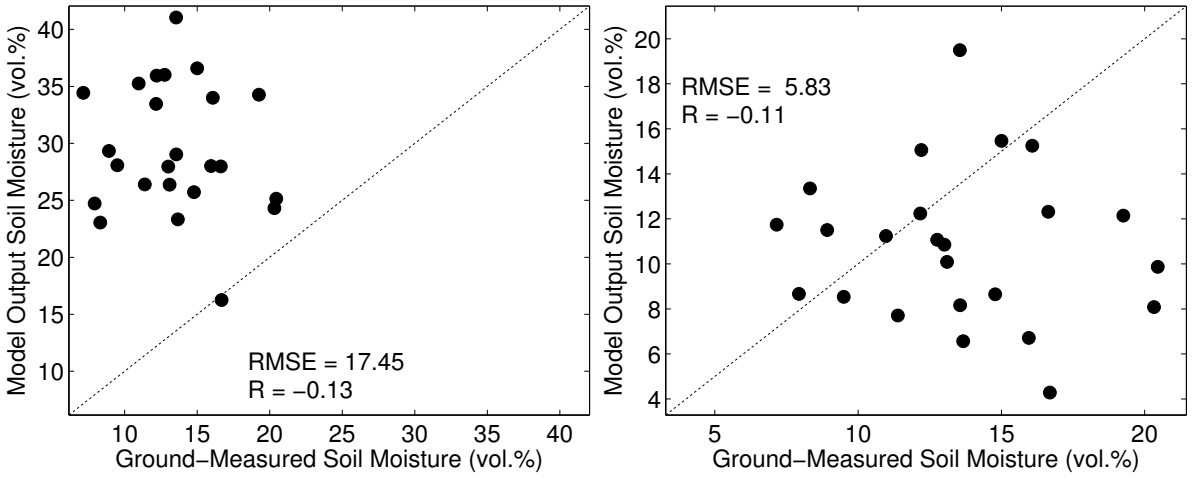

(a) p=1.5

(b) p=2

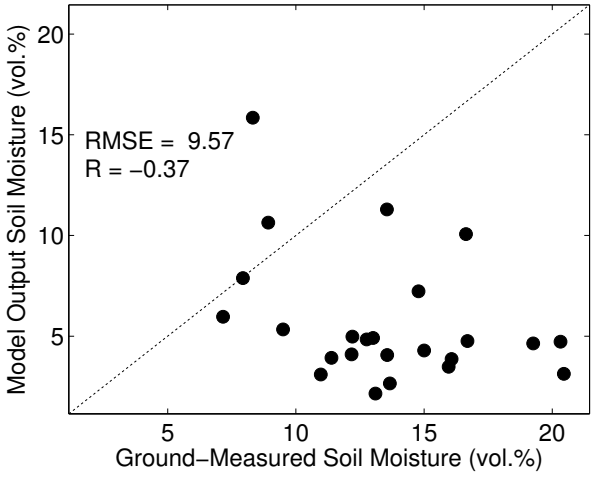

(c) p=3

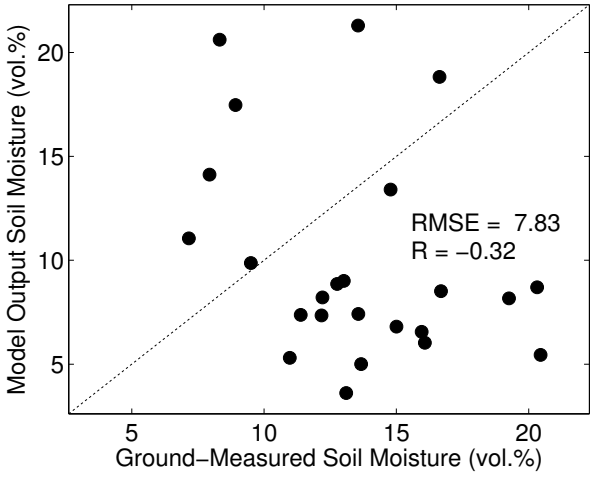

(d) p=5

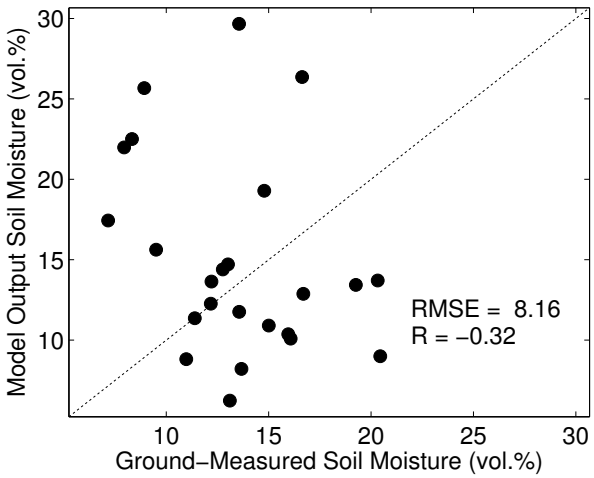

(e) p=10

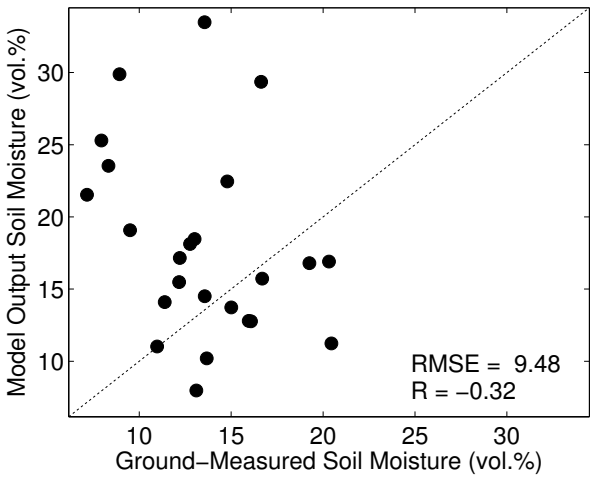

(f) p=20

Figure 6.1: Performance of the IEM for Epoch 1 using different values of power index

all epochs of data using the same set of p values. For Epoch 2, $p = 2$ again yields the highest correlation coefficient and lowest RMSE. This epoch is indeed the only epoch for which the IEM has positive correlation coefficients for some of the power index values. For data in Epoch 3 the best correlation coefficient is not associated with $p = 2$, but selecting this power index results again in the lowest RMSE for this epoch. As per the results of this experiment, a surface correlation function close to exponential, i.e. a generalized correlation function with $p = 2$ (see equation (3.30)), was selected as the most suitable one among the tested surface correlation functions for our data set to be used in this research.

6.2 Comparison of SAR Backscattering Models

6.2.1 X-Bragg

The X-Bragg model was able to invert a very limited number of pixels in the whole area, i.e. its inversion rate was negligible. For example, for the Radarsat-2 image of Epoch 1 it could only invert 9 pixels (out of 100 pixels) in Site 29 and 4 pixels in Site 31. By comparing the site-based average value of these pixels to the average ground measurements of SM in the sites, the RMSE for this inversion process was calculated as 26.68 vol.% which is a very high value compared to other models.

The problem of X-Bragg in inversion of the surface parameters for our data may be illustrated using scatter plots of entropy (H) vs. α parameter simulated by X-Bragg for a few ranges of the dielectric constant (ϵ), β_1 parameter of the model, and incidence angle (θ), which are shown in Figure 6.2. In all of the plots of this figure the value of the dielectric constant is constant along each curve, i.e. each curve is an iso-ϵ contour. But the value of β_1 angle changes from 0° to 30° along each contour. Contours start with the one generated for $\epsilon = 2$, and go up to the one with $\epsilon = 40$. The arrows in Figure 6.2a show the direction of increase in ϵ and β_1. If all the above-mentioned contours are plotted in Figure 6.2a, the area formed between the vertical axis of the plot and the arrows is the area for which the model

can invert pixels. In other words, if we create a lookup table by X-Bragg for $2 < \epsilon < 40$, $0° < \beta_1 < 10°$ and $\theta = 31°$, only pixels whose H and α values fall within the bounds of the above-mentioned area can be inverted using the lookup table. For example, if the values of H and α are calculated as 0.05 and 0.15, respectively, for a specific pixel of the SAR image, its ϵ and β_1 values can be obtained using a lookup table created with the above ranges of ϵ and β_1 parameters. But a pixel with $H = 0.1$ and $\alpha = 0.15$ cannot be inverted using this configuration of lookup table, because the pixel is located outside of the area.

Increasing the upper limit of β_1 can expand the area, as shown in Figure 6.2b, which enables the lookup table to invert pixels with higher H values. However, as it is clear from comparing Figure 6.2a and Figure 6.2b, increasing the upper boundary of β_1 also increases the slope of iso-ϵ contours. The rate of this increase in the slope is related to the incidence angle of the SAR image as can be observed by comparing figures 6.2b, 6.2c, and 6.2d. For smaller incidence angle values the slope increases faster. Therefore, a narrower range of H values can be covered by the lookup table when processing images with smaller incidence angles.

As for the dielectric constant, the range of ϵ values should be selected in a way that it reflects the range of possible SM values. The range considered in Figure 6.2 corresponds to SM values between 0.32 vol.% and 51.02 vol.% (according to Topp dielectric mixing model, see section 3.3), which cover a wider range than that of our data set. In addition, increasing the values of ϵ beyond 40 does not increase the maximum values of H and α much, because as ϵ grows, the contours become denser.

As a result, the maximum value of H which can be covered by a lookup table with configuration of Figure 6.2b, which has similar conditions to data of Epoch 1 and Epoch 3, is less than 0.25, i.e. the pixels with H values greater than 0.25 cannot be inverted by a lookup table created using X-Bragg for $\theta = 31°$ for our data. Figure 6.2c corresponds to a lookup table generated by X-Bragg for $\theta = 35°$ which is the incidence angle of the SAR

image in Epoch 2. Larger values of H can be covered by the model in this case; however, even with this incidence angle, pixels with $H > 0.35$ cannot be inverted. For the sake of comparison, the results of X-Bragg simulation with the same settings but for a much larger incidence angle ($\theta = 50°$) is presented in 6.2d. In this case, the model can handle entropy values of up to about 0.6.

Figure 6.3 shows the histograms of entropy values calculated for images of the three epochs used in this study. Considering the pixels which have to be filtered out to satisfy the original $H < 0.5$ condition of the model (see section 3.2.2.2), from the histograms it can be concluded that only a very small portion of pixels in each image of our data set can be inverted using X-Bragg. A similar behavior was observed in the outputs of the X-Bragg2008 model generated by PolSARpro software. Because of this very low inversion rate, the outputs from the X-Bragg model are not presented here.

6.2.2 Oh and Dubois Models

The Oh and Dubois models were also executed using the images of the three epochs. The scatter plots generated for comparing the ground measurements and estimation by these two models are shown in Figure 6.4, and summary statistics are presented in Table 6.2. This table also contains is a copy of the statistics for the IEM with $p = 2$ from Table 6.1, to make the comparison of the three models easier.

The Dubois model exhibits overestimation of SM for all of the sites of the first two epochs, and for most of the sites of the third epoch. This behavior is identical to what was reported in (Hajnsek, 2001) for part of their data. The RMSE values for the Dubois model are better than the average RMSE reported by Hajnsek (2001), i.e. 25 vol.%, but much higher than the overall RMSE (4.2 vol.%) reported in the original paper by Dubois (Dubois et al., 1995). Other studies such as (Neusch et al., 1999) have also reported similar weak performance for the Dubois model (RMSE = 7.4 vol.% in C-band, RMSE=14 vol.% in L-band). The overall performance of the model can be assessed as weak for the data used in this study, as the

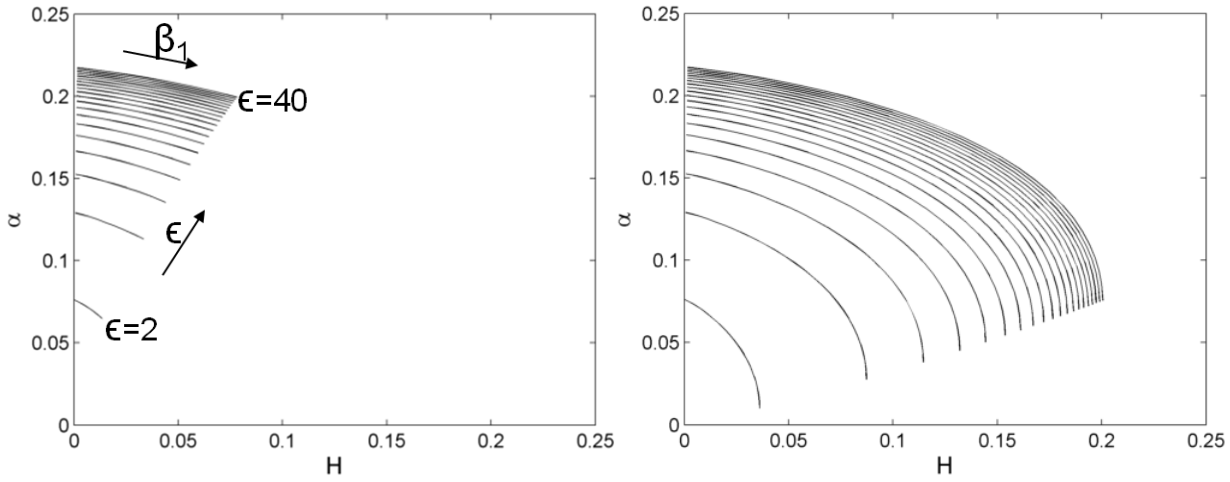

(a) $2 < \epsilon < 40$, $0° < \beta_1 < 10°$, $\theta = 31°$

(b) $2 < \epsilon < 40$, $0° < \beta_1 < 30°$, $\theta = 31°$

(c) $2 < \epsilon < 40$, $0° < \beta_1 < 30°$, $\theta = 35°$

(d) $2 < \epsilon < 40$, $0° < \beta_1 < 30°$, $\theta = 50°$

Figure 6.2: Corresponding H and α values simulated by the X-Bragg model for dielectric constants (ϵ) between 2 and 40, β_1 angle between 0° and 30°, and incidence angles (θ) of 31°, 35° and 50°. α is in radians.: In the inversion process of X-Bragg ϵ and β_1 are calculated given the values of H and α for each pixel. In case the incidence angle be low and H and α be large for a pixel, the model cannot cover those H and α values, and hence, it cannot yield the dielectric constant for that specific pixel.

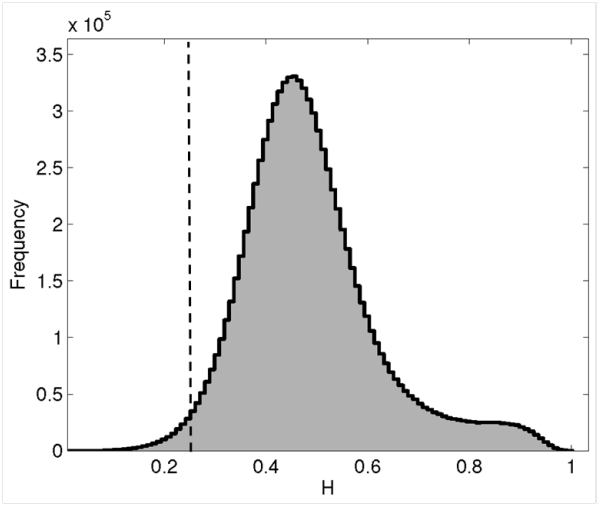

(a) Epoch 1

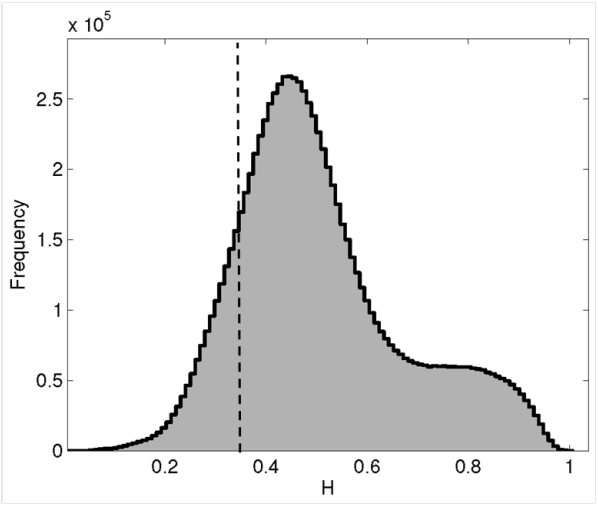

(b) Epoch 2

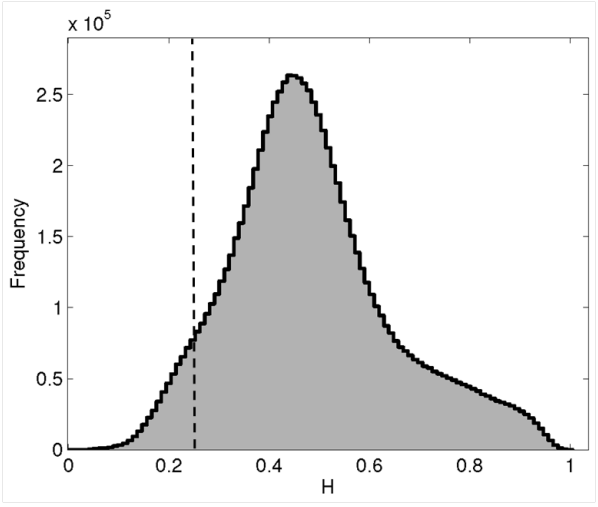

(c) Epoch 3

Figure 6.3: Histogram of entropy for the images of all three epochs: The dashed lines in (a) and (c) correspond to the largest H value shown on the horizontal axis in Figure 6.2b, i.e. 0.25 . The line in (b) corresponds to the largest H value shown on the horizontal axis in Figure 6.2c, i.e. 0.35. For each of the figures above, if we show the area of the grey region to the left of the dashed line by A_L, and the area of the grey region to the right of the dashed line by A_R, then the inversion rate of X-Bragg for that figure is less than $\frac{A_L}{A_L+A_R} \times 100$.

Table 6.2: The results of execution of the Oh and the Dubois models for all epochs of data

	Epoch 1			Epoch 2			Epoch 3		
	Oh	Dubois	IEM	Oh	Dubois	IEM	Oh	Dubois	IEM
RMSE (vol.%)	4.34	15.71	5.83	5.11	16.15	7.88	8.74	15.60	9.57
R	0.28	-0.23	-0.11	-0.09	-0.05	0.19	-0.10	-0.33	-0.23

correlation coefficients are always negative for this model and the RMSE values are at least twice the RMSE values for the Oh model.

The Oh model has the most accurate SM estimations among the models indicated by the highest correlation coefficient, 0.28, and the lowest RMSE of 4.34 vol.%, obtained using the image of Epoch 1. For other images, the performance is not as strong, but its RMSE is always better than the Dubois and the IEM models. In Epoch 3 the correlation coefficient of the Oh model is also the highest one. The results for the Oh model are considerably more accurate than those reported by Hajnsek (2001) (18 vol.% for the 0-4 cm soil depth and about 25 vol.% for the 4-8 cm soil depth), and, for Epoch 1, have about the same RMSE (4.0 vol.%) reported by Oh in his original paper (Oh et al., 1992).

6.2.3 IEM

The IEM performance is weaker than the Oh model in Epoch 1 and Epoch 3, but its correlation coefficient is about 28% better than that of the Oh model in Epoch 2. The IEM always outperforms the Dubois model for our data according to both the RMSE and the correlation coefficient measures. The RMSE of the IEM in this study is higher than the RMSE (5.37 vol.%) reported by McNairn et al. (2010) who studied the same area. This may be because they made averaging according to soil texture classes, not based on sites. Another recent study (Lievens et al., 2011) has also reported about the same accuracy (RMSE= 4 vol.% - 6.5 vol.%) when using "effective roughness parameters" with a large data set consisting of L-band (ALOS and airborne E-SAR) and C-band (ENVISAT, Radarsat-1 and ERS-1/2) data.

An important aspect of the inversion process which, to the best knowledge of the author,

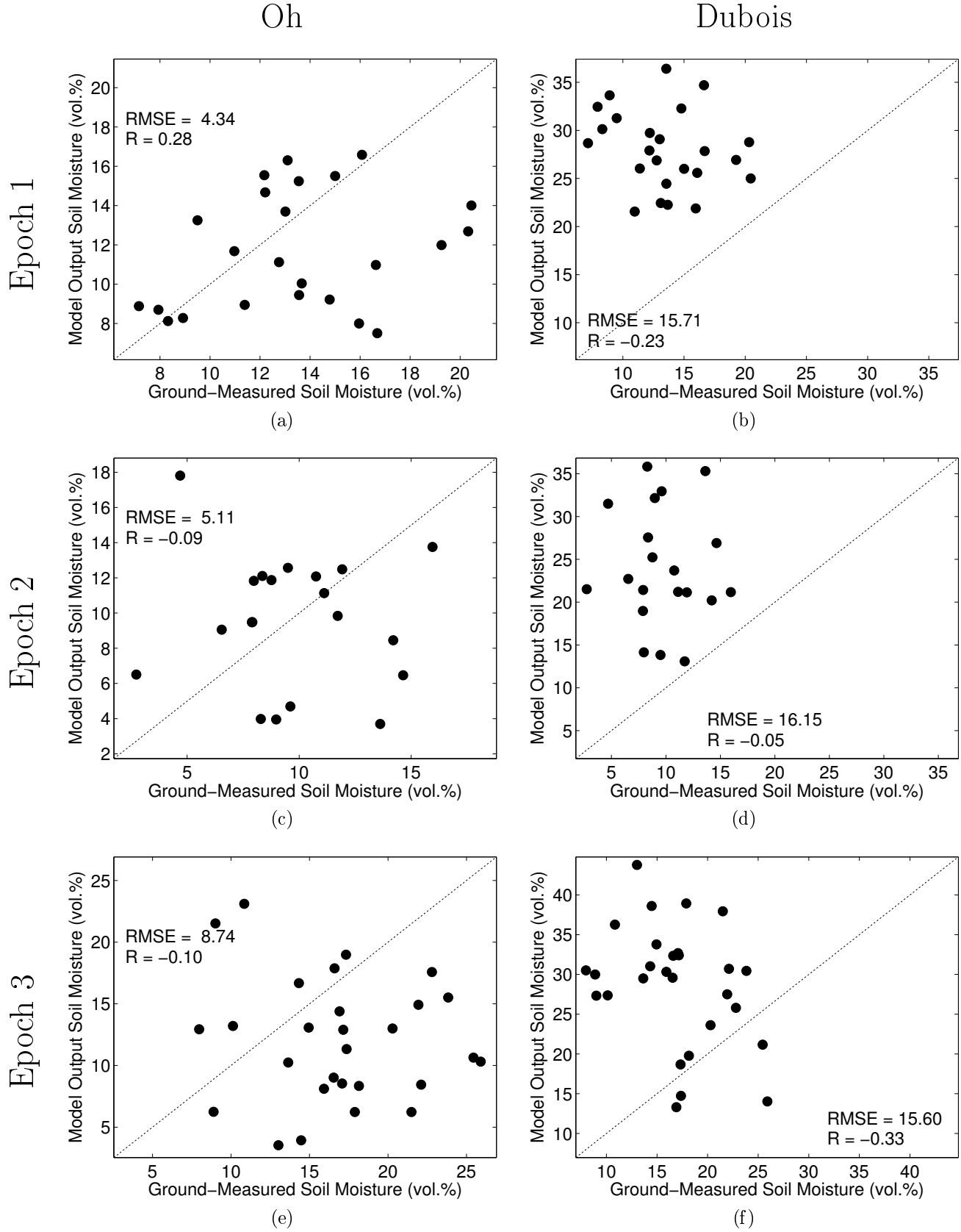

Figure 6.4: The results of execution of the Oh and the Dubois models for all epochs of data: Rows from top to bottom show Epoch 1, Epoch 2 and Epoch 3

has never been considered in any other similar study before, is the spatial pattern of inversion. The importance of the inversion pattern is because of the special method usually used for evaluation of the results of a SAR backscattering model using field measurements. As already discussed, since the ground measurements of SM are point measurements, the output of the models are areal estimations, and these two may have different sampling characteristics, usually the averages of them over a common geographic extent (site) are compared to evaluate the performance of the models. Field measurements of SM for the purpose of validation or calibration of the remote sensing products are generally carried out in regular grids which cover the ground site with a reasonable sample spacing. Thus, assuming that their average value can approximately represent the conditions of SM in the whole site is not unreasonable. However, in case the number of pixels inverted by the model is small compared to the total number of the pixels which cover a ground site, i.e. the inversion rate of the model is low, the pattern of inversion should be investigated as well. In this case, randomly scattered inverted pixels over the field can still be acceptable for making the averages. But, an uneven distribution of pixels over the field may make the average value biased, and such an average value may not represent the SM conditions of the whole site to be compared with ground measurements.

Table 6.3 contains the inversion rates for the three models discussed above for each site in three epochs of data. The inversion rates of the Oh and the Dubois model are identical because the same filtering conditions are applied to them prior to inversion, and this filtering is the main source of changes in their inversion rates. For the IEM, no filtering is used prior to inversion, but some pixels may be masked out because either the lookup table cannot find an answer for the inversion problem, or the dielectric constant calculated by the lookup table is so low that the dielectric mixing model yields negative values of SM for those pixels, which is not physically possible. According to the tables, the IEM clearly inverts many more pixels than the other two models. Low inversion rates for the Oh and the Dubois models

have already been reported in other studies (Wang et al., 1997)(Hajnsek, 2001).

Figures 6.5 to 6.7 are schematic representations of the inversion pattern of the Oh and the Dubois models for each field site for each of the three epochs. Each small square in each site represents a 10 m x 10 m image pixel, and each site is consisted of 10x10 pixels. The black squares represent the inverted pixels and the white ones are the pixels for which these two models cannot generate an output. As clearly seen in these figures, the inversion patterns are patchy and the sites exhibit large connected groups of inverted or uninverted pixels. In order to estimate the value of uninverted pixels, some "*spatio-temporal gap filling*" algorithms, including *Data INterpolating Empirical Orthogonal Functions (DINEOF)* (Alvera-Azcárate et al., 2005) and *Robust Spline Smoothing* (Garcia, 2010) were applied on the outputs of the models, but they were not successful in reconstructing the data.

6.3 Probability Density Function of the Field Measurements

The histograms of SM values measured for each site for the three epochs of ground measurements in our study area are shown in figures 6.8 to 6.10. Each histogram represents a single site, and is created using the complete set of measurements (64 measurements) for that site. In Figure 6.11 four PDF types proposed by other studies for SM values (see section 4.2) are presented for reference and comparison with the histograms of ground SM values in our study area. Each PDF has been generated using three sets of parameters to cover some different possible shapes of the PDF type. The parameters can be seen in the legend of each graph. Visual inspection can easily reveal that, although a number of the histograms roughly resemble Gaussian (e.g., site 30 in Epoch 3) or beta (e.g., site 25 in Epoch 2) distribution, the ground measurements of SM (each site considered separately) in the data set used for this study do not seem to conform to a single particular probability distribution from the distributions mentioned in section 4.2. For many of the sites shown in figures 6.8 to 6.10 the histograms are bimodal or multimodal, for example sites 2 and 44 in Epoch 1, sites 28 and

Table 6.3: Inversion rates of the Oh, Dubois and IEM models for three epochs: The right column in each table contains the inversion rates of field measurement sites for the IEM, and the middle column contains the inversion rates of the sites for the Oh and the Dubois models. The last row in each table shows the average inversion rates for the epoch.

Epoch 1		
Site	Oh & Dubois (%)	IEM (%)
19	34	97
22	38	100
23	45	98
24	62	98
25	15	100
26	65	100
27	20	97
28	30	100
29	49	96
30	30	100
31	24	100
32	58	100
33	51	95
34	42	100
35	43	98
36	66	97
37	7	100
38	33	100
39	69	98
40	73	95
43	62	99
44	27	100
45	49	99
46	68	100
Average:	44.2	98.6

Epoch 2		
Site	Oh & Dubois (%)	IEM (%)
22	61	99
23	52	100
24	70	100
25	9	98
26	58	98
27	17	96
28	33	99
29	21	99
30	44	100
31	57	99
33	64	98
34	22	99
38	35	97
39	19	96
40	29	95
42	31	98
43	36	99
44	42	98
45	34	99
46	69	98
Average:	40.2	98.3

Epoch 3		
Site	Oh & Dubois (%)	IEM (%)
15	56	97
16	38	97
19	40	93
20	52	96
21	35	100
22	66	100
23	48	99
24	35	100
25	22	100
26	49	99
27	40	98
28	46	100
29	7	78
30	30	99
31	32	99
33	31	100
34	58	98
35	47	99
36	45	100
37	24	100
38	28	100
39	50	95
40	31	97
42	35	98
43	39	100
44	29	100
45	35	91
46	26	100
Average:	38.4	97.6

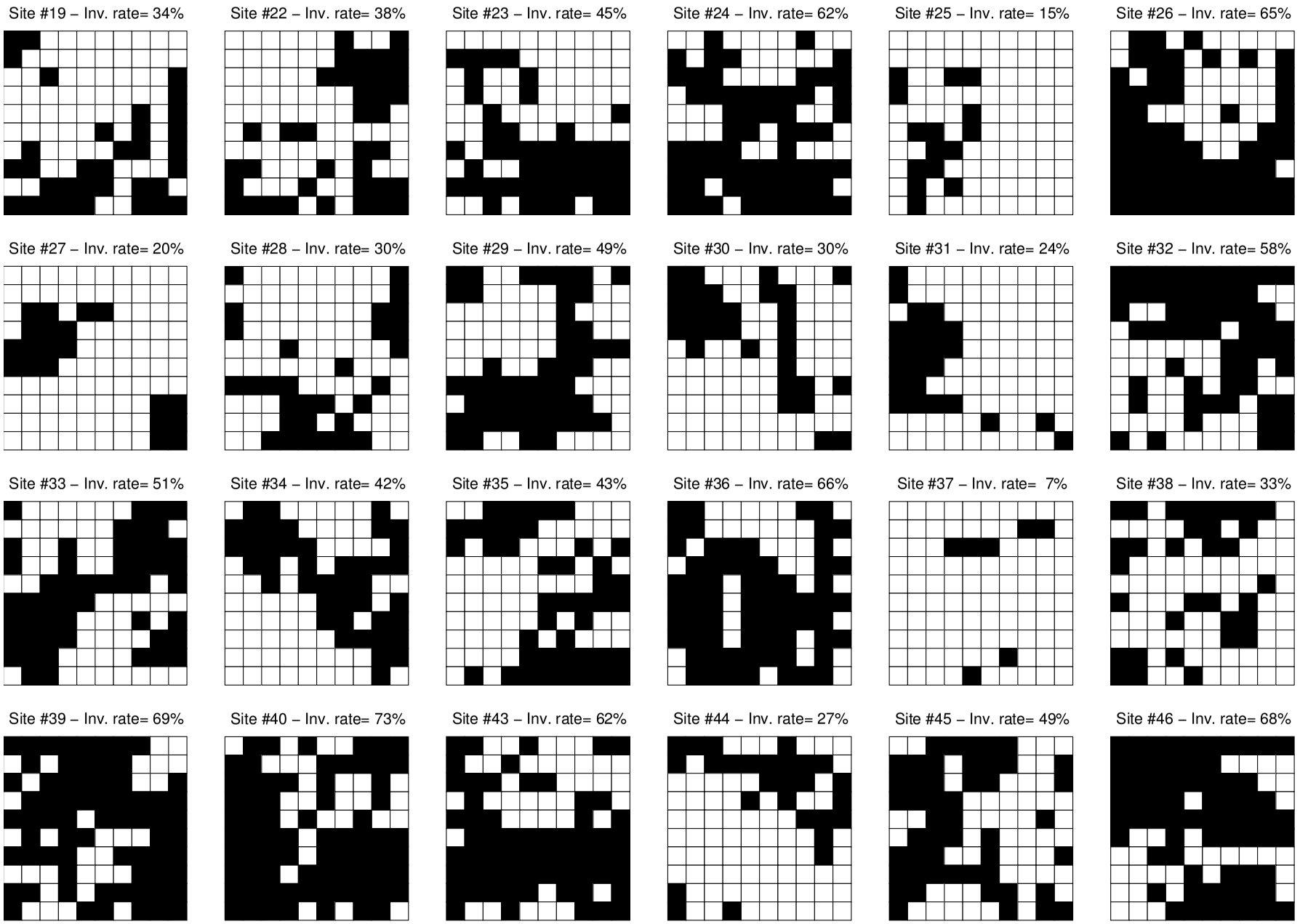

Figure 6.5: Inversion pattern for the Oh and the Dubois models for Epoch 1 of data set

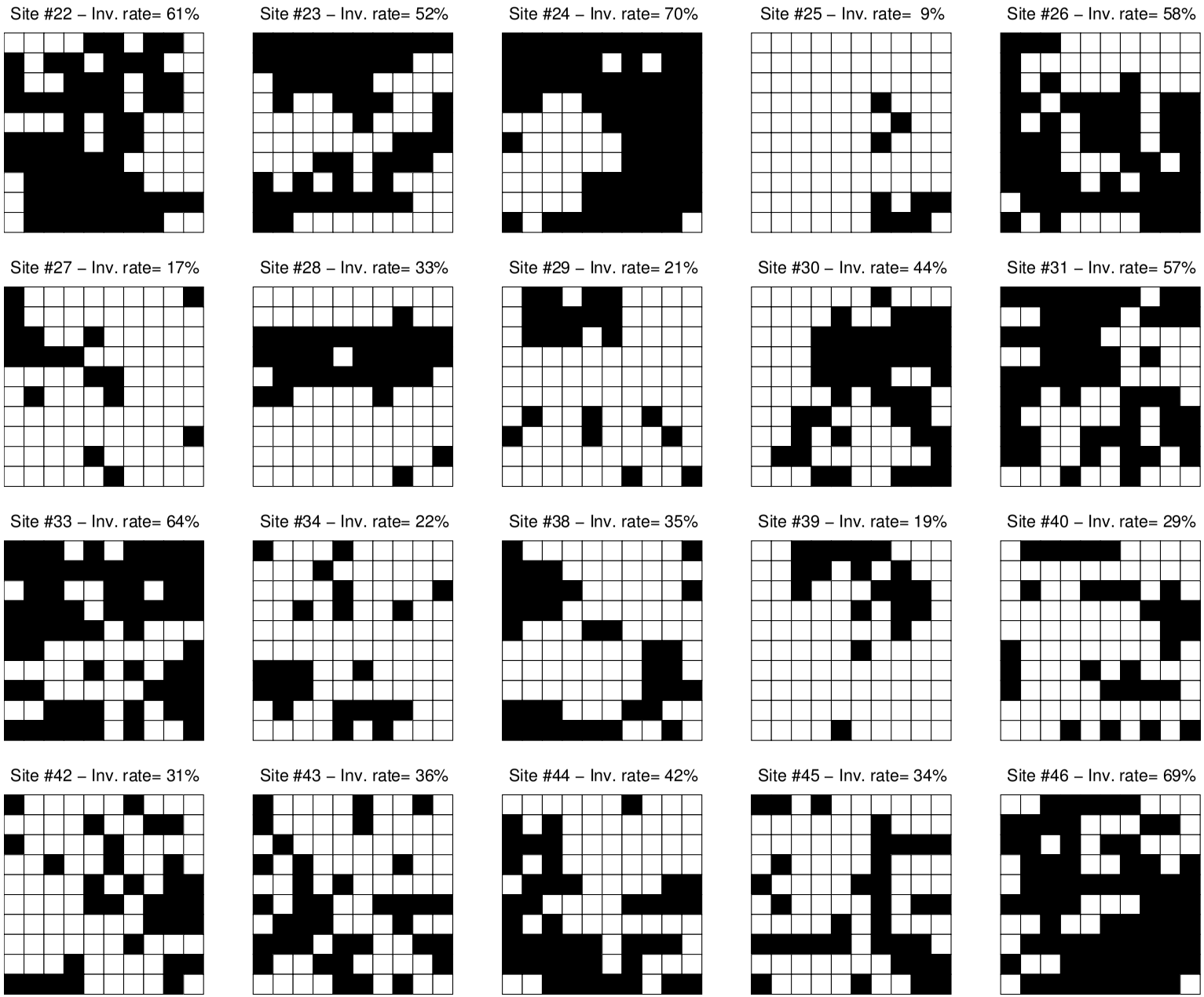

Figure 6.6: Inversion pattern for the Oh and the Dubois models for Epoch 2 of data set

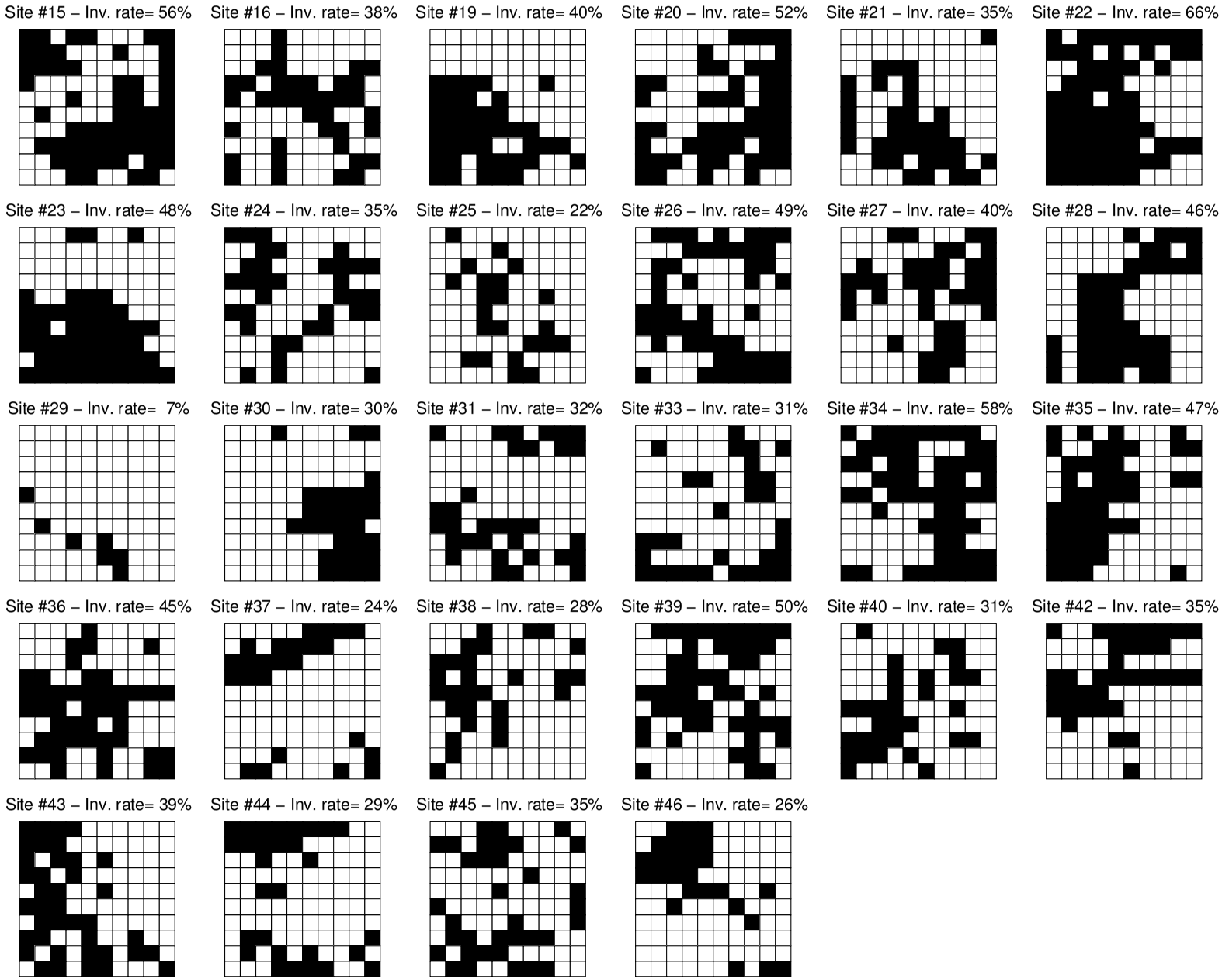

Figure 6.7: Inversion pattern for the Oh and the Dubois models for Epoch 3 of data set

31 in Epoch 2, and sites 22 and 43 in Epoch 3. As a result, a fixed PDF of one of the types mentioned in section 4.2 does not seem to be useful in explaining the spatial variability of ground measurements of our data set.

6.4 Exponential Law in the Field Measurements

Figure 6.12a contains a scatter plot of SM mean vs. standard deviation of each site for the ground measurements of the first epoch in our study area. Each point in the plot represents a single site. As mentioned in section 5.1, each node in the 4×4 grid of field measurements in each site has 4 replicates. One way to get a single SM value for each node is to average the 4 replicates. The mean and standard deviation values in Figure 6.12a are calculated using this method for each site. However, the difference between the replicates is usually large compared to the measurement values, and averaging smooths the values of standard deviations. Thus, Famiglietti et al. (2008) suggest a random selection scheme for calculation of the standard deviation of SM in each grid (site). In this scheme, for each node of a ground measurement grid, first, one of the 4 replicates of the node is selected randomly. By this selection, we obtain 16 measurements for the site. Assume that we call the standard deviation of these 16 measurements σ_1. The procedure of random selection of replicates and calculation of the standard deviations is repeated N times, so that we obtain σ_1 to σ_N. The average value of σ_1 to σ_N is considered as the final standard deviation of the site, and the whole procedure is repeated for all ground measurement sites. Figure 6.12b contains a scatter plot created using the random selection scheme with $N = 1000$. Another possibility is to use all of the 64 measurements of a site to calculate the standard deviation of SM in that site. The result of this type of calculation of standard deviation can be seen in Figure 6.12c.

In Figure 6.12 the curves are generated by fitting equation (4.1) to the points, and calculating the parameters k_1 and k_2. Values of the parameters along with RMSE and

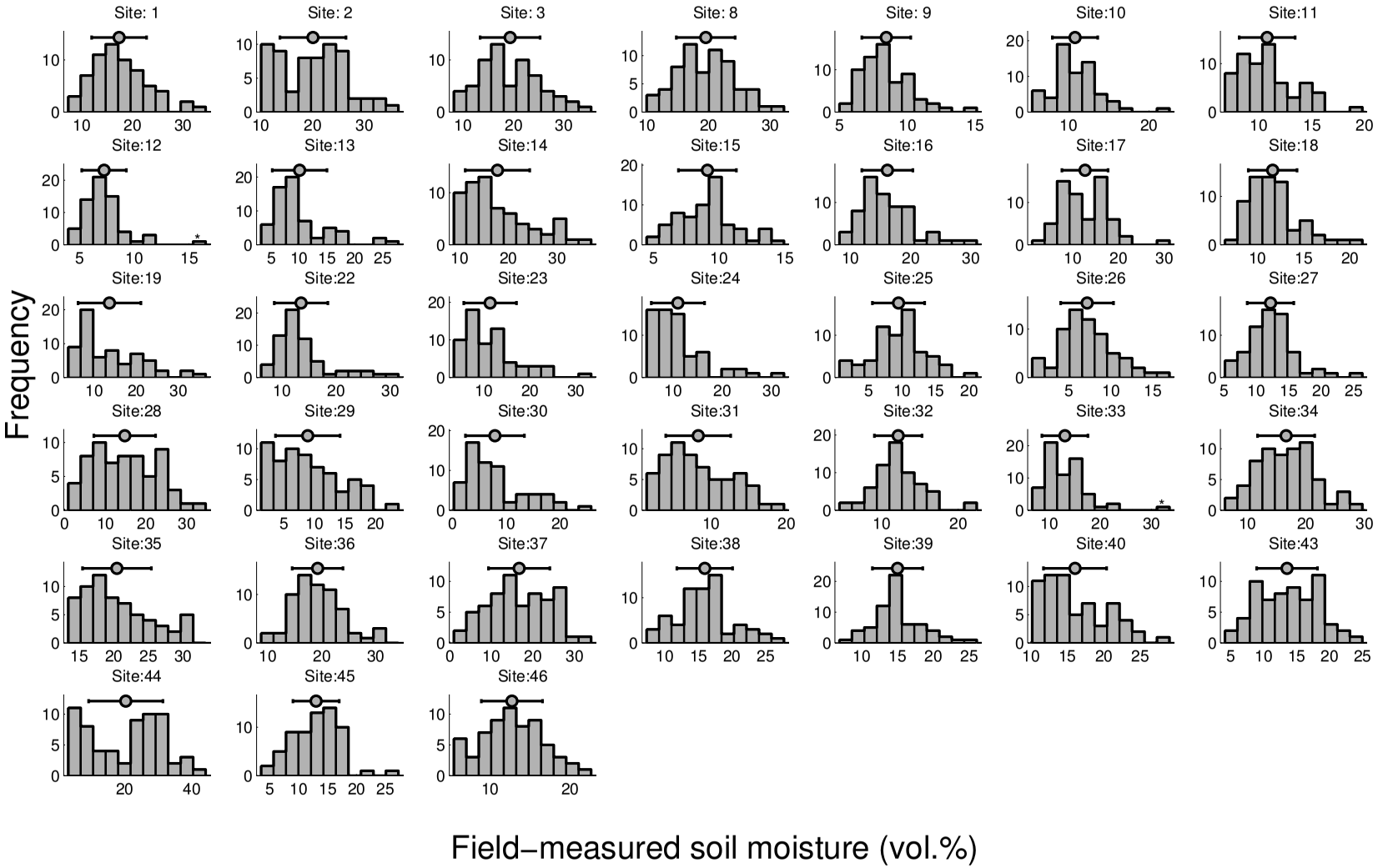

Figure 6.8: Histogram of SM ground measurements for each site observed in Epoch 1: The bar on top of the histogram of each site shows the standard deviation of SM values within the site, and the circle on the bar depicts the location of mean SM value of the site.

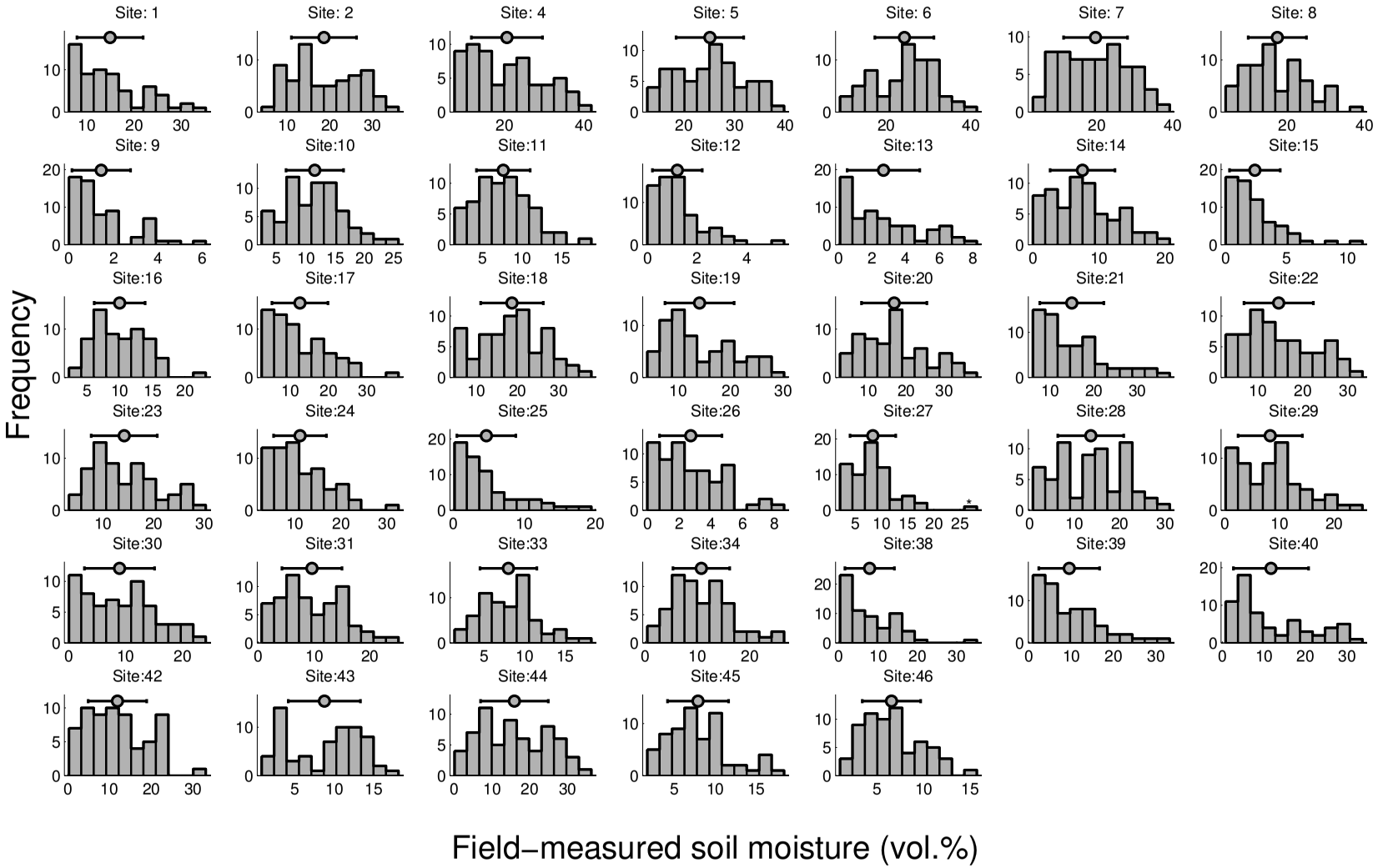

Figure 6.9: Histogram of SM ground measurements for each site observed in Epoch 2: The bar on top of the histogram of each site shows the standard deviation of SM values within the site, and the circle on the bar depicts the location of mean SM value of the site.

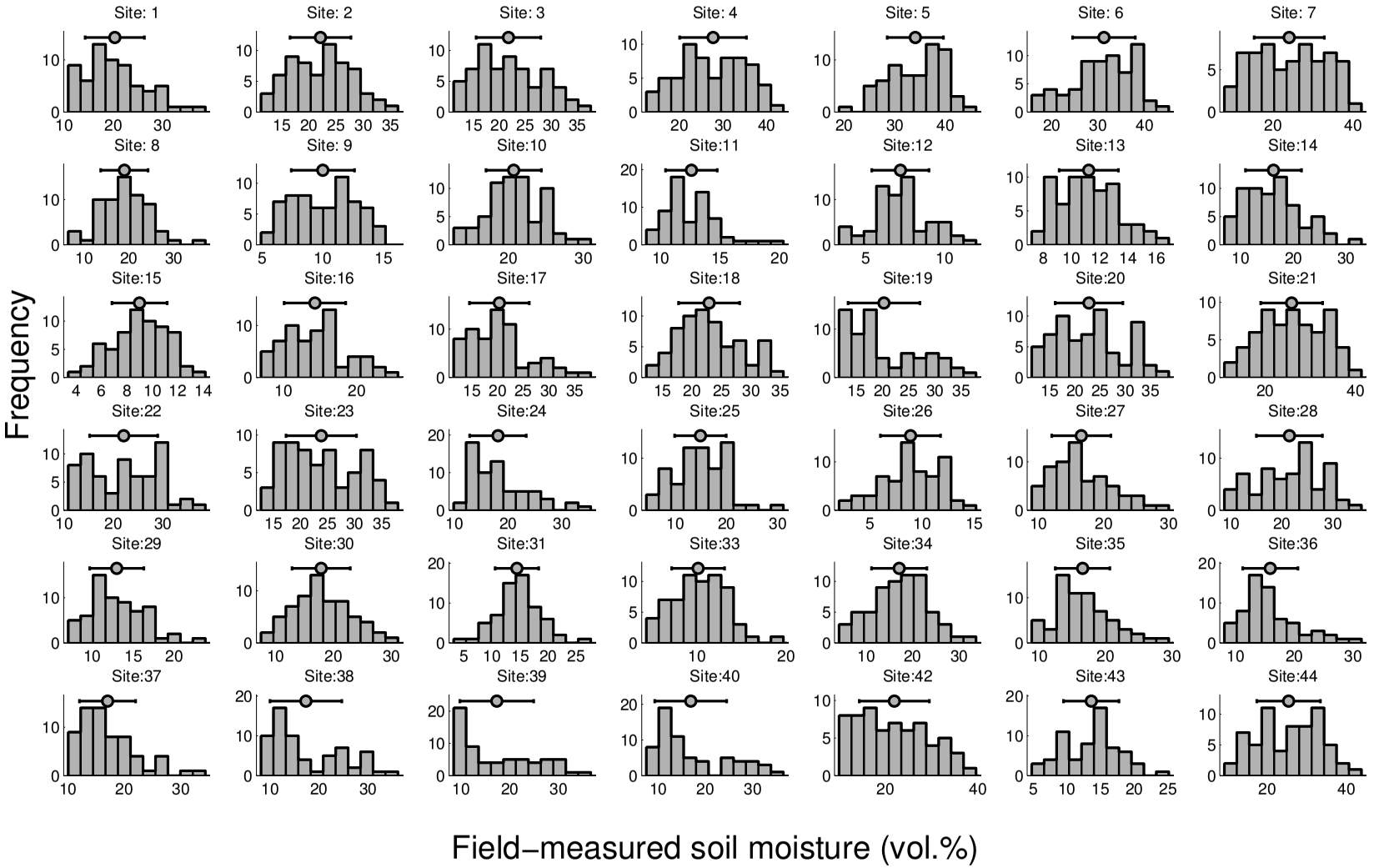

Figure 6.10: Histogram of SM ground measurements for each site observed in Epoch 3: The bar on top of the histogram of each site shows the standard deviation of SM values within the site, and the circle on the bar depicts the location of mean SM value of the site. The last two sites, sites 45 and 46, were skipped in order to better fit the histograms in the figure.

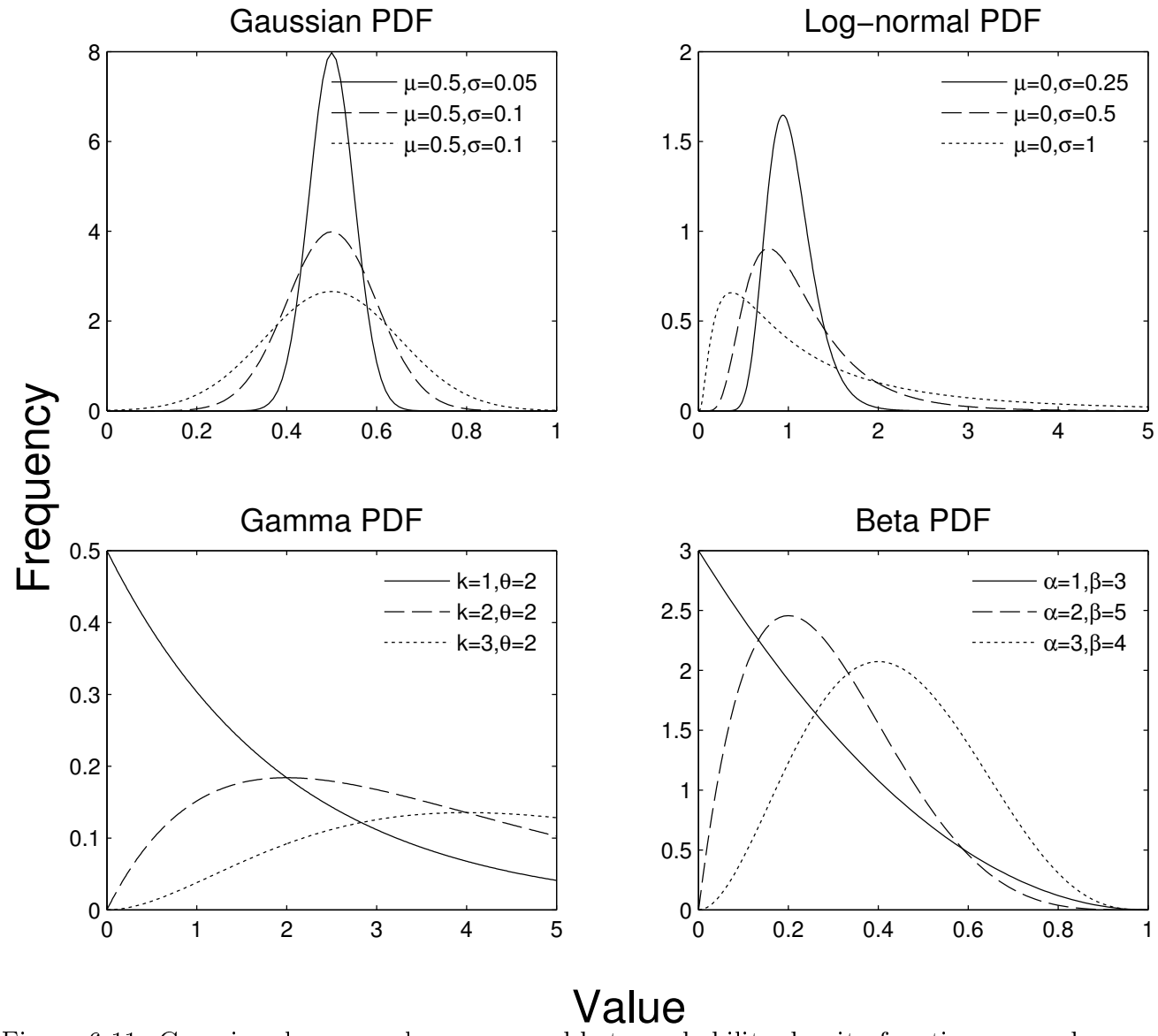

Figure 6.11: Gaussian, log-normal, gamma and beta probability density functions: μ and σ are mean and standard deviation of Gaussian and log-normal distributions, k and θ are shape parameter and scale parameter of gamma distribution, and α and β are shape parameters of beta distribution.

correlation coefficient of the fit are presented beneath each graph. Random selection seems to improve the fit in terms of correlation coefficient, but the fit has about the same quality when using random selection and full measurements. k_1 and k_2 are close in all of the cases, but they are different than that reported in (Famiglietti et al., 2008). They have reported $k_1 = 0.8941$ and $k_2 = 8.0774$ for the extent scale of 100 m in their study area, which is close to the extent scale of the measurements in each site in our study area. The RMSE calculated by them is also about half of the RMSE obtained here. Indeed, for the ground measurements in our study area the curves are close to being straight lines. This happens because as k_2 decreases, the term $exp(-k_2\mu_\theta)$ tends to unity, and (4.1) tends to a linear equation of the form $\sigma_\theta = k_1 \cdot \mu_\theta$.

In Figure 6.13 the results of using the same model for ground measurements of Epoch 2 and Epoch 3 with standard deviations calculated from all measurements of each site are presented. According to correlation coefficients, the quality of fit is better for these epochs. However, the values of parameters in the three epochs are not compatible. Because of the observed differences in the shape of the model in three epochs of our data and the one reported by Famiglietti et al. (2008), which has used extensive field work in estimation of the parameters of the model, and because of the difficulties, explained in section 4.3, in implementing a spatial constraint using this model, we did not find this model very useful in improving the results of SAR backscattering models. In order to obtain a more informative model to describe the variability of SM, the rest of this chapter will focus on multifractal analysis.

6.5 Multifractal Analysis of the Field Measurements

To perform the multifractal analysis on field measurements of our data set using the procedure explained in section 4.5.2, SM ground measurements in each field site need to be treated as a SM image. Thus, the 4 point by 4 point grid of ground measurements in each site was

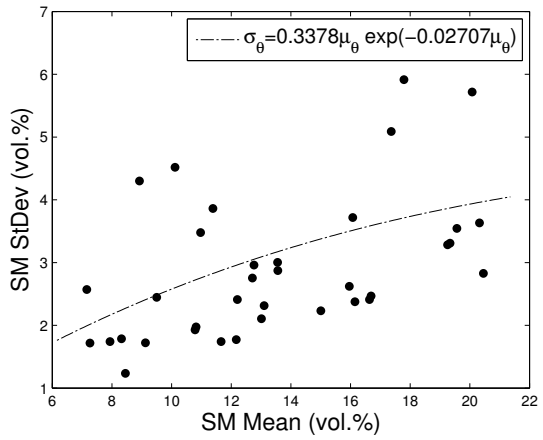

(a) Using average of replicates for calculation of standard deviation: $k_1 = 0.3378$, $k_2 = 0.02707$, RMSE=1.23(vol.%), R=0.43

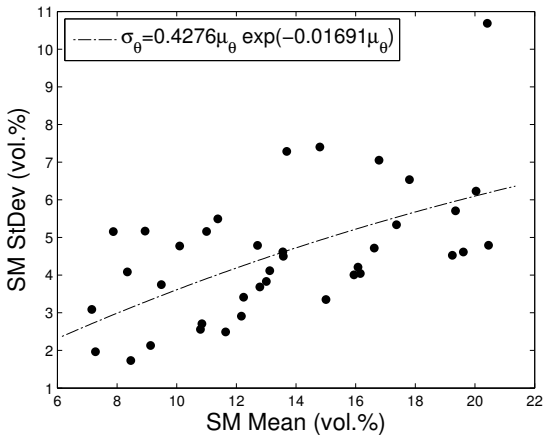

(b) Using random selection of replicates for calculation of standard deviation: $k_1 = 0.4276$, $k_2 = 0.01691$, RMSE=1.43(vol.%), R=0.56

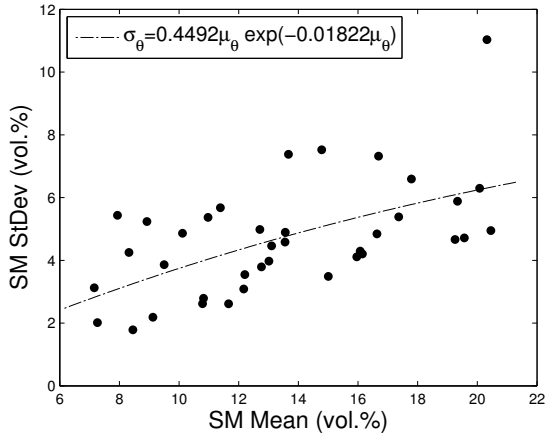

(c) Using all measurements of each site for calculation of standard deviation: $k_1 = 0.4492$, $k_2 = 0.01822$, RMSE=1.47(vol.%), R=0.56

Figure 6.12: Investigating exponential law in ground measurements of Epoch 1: Each point represents a field site.

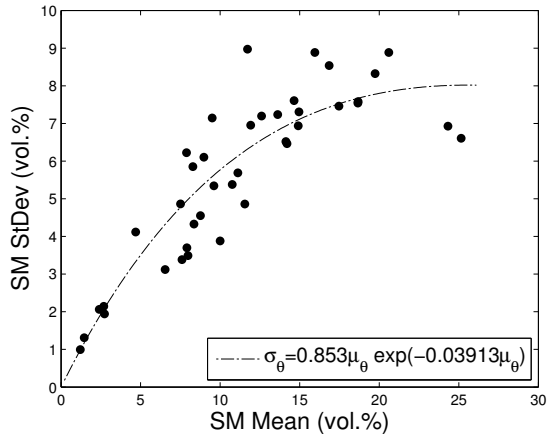

(a) Epoch 2: $k_1 = 0.8530$, $k_2 = 0.03913$, RMSE=0.97(vol.%), R=0.89

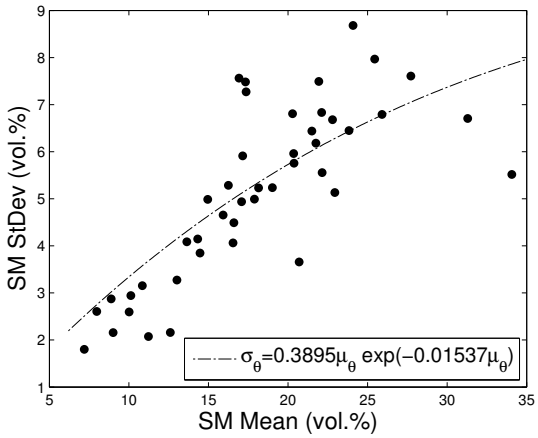

(b) Epoch 3: $k_1 = 0.3895$, $k_2 = 0.01537$, RMSE=1.08(vol.%), R=0.80

Figure 6.13: Investigating exponential law in ground measurements of Epoch 2 and Epoch 3 using all measurements of each site for calculation of standard deviation: Each point represents a field site.

assumed as a 4 pixel by 4 pixel image of resolution 30 m, which is the approximate distance between two neighboring measurements in the field. The value of each pixel was set to the average value of the 4 replicates on each node of the measurement grid.

For each 4x4 image, i.e. for each site, then, an image pyramid was produced as per the instructions in section 4.4. Unfortunately, using a base 4x4 image only 3 levels of details for the image pyramid can be generated. This small number can result in poor estimation of multifractal parameters, but as we will see later in the estimation of STRAIN parameters, even using this small number of scales the parameters obtained from our ground measurements are consistent with what other studies have obtained from passive microwave SM images using more scales.

In order to examine the scale invariance in ground measurements, partition functions ($S_q(\lambda)$) were calculated for λ =30 m, 60 m and 120 m, and q =2, 3, 4, 5 and 6 for each field site. The resolution values (λ) are associated with three levels of the image pyramid, and the exponent values (q) are selected following Mascaro et al. (2010). The scale invariance can be revealed by examining the linearity of $\log\lambda - \log S_q(\lambda)$ plots. Two of these plots are presented in Figure 6.14a and Figure 6.14c for Site 1 and Site 23 in Epoch 1, respectively. Site 1 was

selected for comparatively low correlation (R=-0.901) between $\log \lambda$ and $\log S_q(\lambda)$, and Site 23 is selected for a high correlation (R=-1.000). The negative correlation coefficients show negative slopes of the fitted line. The $\log \lambda - \log S_q(\lambda)$ plots for the same sites in Epoch 2 and Epoch 3 are also presented in figures 6.15a, 6.15c, 6.16a and 6.16c.

There is no specific threshold for correlation coefficient for accepting or rejecting the scale invariance in data, and different studies have used different numbers as threshold. For example Mascaro et al. (2010) set 0.9 as the threshold for absolute value of the correlation coefficient, but in (Deidda et al., 1999) a more stringent threshold of 0.995 is considered. The reason for selection of a specific threshold is not mentioned. This can be because probably scale invariance is not an absolute property of data, i.e. different levels of linearity of the $\log \lambda - \log S_q(\lambda)$ plot can show different degrees of scale invariance; the higher the linear correlation between $\log \lambda$ and $\log S_q(\lambda)$, the higher the degree of scale invariance in data.

In this study, in addition to the correlation coefficient of fit, we report the p-value of the F-test which can be used to find the confidence level at which the linear fit is statistically significant. The correlation coefficients and p-values for all sites are reported in tables 6.4 to 6.6 for the highest exponent, $q = 6$, in Epoch 1, Epoch 2 and Epoch 3, respectively. The correlation coefficients for different exponent values for the same site are close, as shown for the first 10 sites of Epoch 1 in Table 6.7. According to tables 6.4 to 6.6, the maximum p-value is 0.32 and the worst correlation coefficient is -0.880. The maximum p-value shows that the linear fits are statistically significant at at least a 68% confidence interval. This may suggest that at least a weak scale invariance is observed in the ground measurements. As mentioned above, the small number of scales does not allow to execute a more rigorous analysis of scale invariance, however, since multiple other studies, e.g. (Biswas et al., 2012a)(Kim et al., 2002)(Mascaro et al., 2010)(Mascaro et al., 2011), have reported the scale invariance behavior in SM values, and given that our ground measurements exhibit at least a weak scale invariance, we proceed to analyzing the variability in ground measurements using the

Table 6.4: Results of fitting a line to $\log\lambda - \log S_q(\lambda)$ plots for $q = 6$ for ground measurements of all sites in Epoch 1 for examining the scale invariance: For each site the correlation coefficient and the p-value of F-test of the fit are reported. Sites with R values closer to -1 exhibit stronger scale invariance.

Epoch 1					
Site ID	R	p-value	Site ID	R	p-value
1	-0.901	0.29	26	-0.950	0.20
2	-0.908	0.28	27	-0.897	0.29
3	-0.991	0.08	28	-0.983	0.12
8	-0.909	0.27	29	-0.959	0.18
9	-0.993	0.07	30	-0.891	0.30
10	-0.945	0.21	31	-0.907	0.28
11	-0.890	0.30	32	-0.970	0.16
12	-0.901	0.29	33	-0.959	0.18
13	-0.926	0.25	34	-0.957	0.19
14	-0.916	0.26	35	-0.934	0.23
15	-0.964	0.17	36	-0.961	0.18
16	-0.908	0.28	37	-0.900	0.29
17	-0.969	0.16	38	-0.944	0.21
18	-0.891	0.30	39	-0.924	0.25
19	-0.996	0.06	40	-0.953	0.20
22	-0.944	0.21	43	-0.976	0.14
23	-1.000	0.01	44	-0.884	0.31
24	-0.960	0.18	45	-0.980	0.13
25	-0.998	0.04	46	-0.898	0.29

STRAIN model.

The slope of the line in each of the $\log\lambda - \log S_q(\lambda)$ plots, that can be created for a fixed q, is called $\tau(q)$, which can be modeled using the STRAIN model. Thus, the STRAIN model was fitted to the pairs of (q,$\tau(q)$), obtained in previous stage of the analysis, for each field site using the SQP optimization algorithm explained in section 4.6. In other words, we, first, determined the slope of a straight line which can describe the relationship between $\log\lambda$ and $\log S_q(\lambda)$ when we keep q constant, and change λ from 30 m to 120 m. Then, we changed q from 2 to 6 and calculated the slope, $\tau(q)$, for each q to obtain pairs of (q,$\tau(q)$). Then, we used these pairs to find parameters β and c of the STRAIN model by fitting the model to the pairs as data points. Therefore, for each site one β and one c is obtained which together describe the multifractal properties of the ground measurements in that site. In other words,

Table 6.5: Results of fitting a line to $\log \lambda - \log S_q(\lambda)$ plots for $q = 6$ for ground measurements of all sites in Epoch 2 for examining the scale invariance: For each site the correlation coefficient and the p-value of F-test of the fit are reported. Sites with R values closer to -1 exhibit stronger scale invariance.

Epoch 2					
Site ID	R	p-value	Site ID	R	p-value
1	-0.954	0.19	22	-0.928	0.24
2	-0.914	0.27	23	-0.940	0.22
4	-0.995	0.06	24	-0.896	0.29
5	-0.902	0.28	25	-0.970	0.16
6	-0.885	0.31	26	-0.934	0.23
7	-0.979	0.13	27	-0.903	0.28
8	-0.904	0.28	28	-0.999	0.02
9	-0.935	0.23	29	-0.897	0.29
10	-0.996	0.05	30	-0.910	0.27
11	-0.989	0.09	31	-1.000	0.00
12	-0.994	0.07	33	-0.914	0.27
13	-0.917	0.26	34	-1.000	0.01
14	-0.943	0.22	38	-0.963	0.17
15	-0.971	0.15	39	-0.976	0.14
16	-0.889	0.30	40	-0.911	0.27
17	-0.971	0.15	42	-1.000	0.00
18	-0.930	0.24	43	-1.000	0.01
19	-0.943	0.22	44	-0.943	0.22
20	-0.968	0.16	45	-0.924	0.25
21	-0.925	0.25	46	-0.920	0.26

Table 6.6: Results of fitting a line to $\log\lambda - \log S_q(\lambda)$ plots for $q = 6$ for ground measurements of all sites in Epoch 3 for examining the scale invariance: For each site the correlation coefficient and the p-value of F-test of the fit are reported. Sites with R values closer to -1 exhibit stronger scale invariance.

Epoch 3					
Site ID	R	p-value	Site ID	R	p-value
1	-0.916	0.26	23	-0.998	0.04
2	-0.929	0.24	24	-0.915	0.26
3	-1.000	0.01	25	-0.975	0.14
4	-0.921	0.25	26	-0.992	0.08
5	-0.998	0.04	27	-0.997	0.05
6	-0.999	0.03	28	-0.999	0.03
7	-0.999	0.02	29	-0.957	0.19
8	-1.000	0.00	30	-0.936	0.23
9	-0.888	0.30	31	-0.993	0.08
10	-0.998	0.04	33	-0.984	0.12
11	-0.922	0.25	34	-0.984	0.11
12	-0.933	0.24	35	-0.973	0.15
13	-0.973	0.15	36	-0.988	0.10
14	-0.941	0.22	37	-0.884	0.31
15	-0.999	0.03	38	-0.985	0.11
16	-0.904	0.28	39	-0.922	0.25
17	-0.985	0.11	40	-0.880	0.32
18	-0.917	0.26	42	-0.987	0.10
19	-0.973	0.15	43	-0.945	0.21
20	-0.963	0.17	44	-0.952	0.20
21	-0.968	0.16	45	-0.910	0.27
22	-0.888	0.30	46	-0.999	0.03

Table 6.7: The correlation coefficients of fitting a line to $\log\lambda - \log S_q(\lambda)$ plots for q=2 to 6 for ground measurements of the first 10 sites in Epoch 1 for examining the scale invariance: The values of the correlation coefficient are close for different q's in each site.

Site ID	q=2	q=3	q=4	q=5	q=6
1	-0.898	-0.899	-0.900	-0.900	-0.901
2	-0.900	-0.902	-0.904	-0.906	-0.908
3	-0.994	-0.994	-0.993	-0.992	-0.991
8	-0.907	-0.908	-0.908	-0.909	-0.909
9	-0.990	-0.990	-0.991	-0.992	-0.993
10	-0.942	-0.943	-0.944	-0.944	-0.945
11	-0.892	-0.891	-0.891	-0.890	-0.890
12	-0.908	-0.905	-0.903	-0.902	-0.901
13	-0.935	-0.931	-0.928	-0.927	-0.926
14	-0.907	-0.909	-0.911	-0.913	-0.916

Table 6.8: Parameters and accuracy of fitting the STRAIN model to ground measurements of Epoch 1

Epoch 1					Epoch 1				
Site	β	c	R	RMSE	Site	β	c	R	RMSE
1	0.8979	4.0033	1.00000	0.00068	26	0.8122	1.7014	1.00000	0.00043
2	0.8180	1.1853	1.00000	0.00025	27	0.8946	1.7516	1.00000	0.00037
3	0.8794	0.9846	1.00000	0.00012	28	0.6042	0.6233	0.99999	0.00164
8	0.9452	5.4288	1.00000	0.00016	29	0.7285	1.4843	0.99996	0.00478
9	0.9328	2.3666	1.00000	0.00014	30	0.9780	49.9979	0.99999	0.00088
10	0.9816	50.0000	0.99995	0.00120	31	0.9773	44.6018	0.99999	0.00058
11	0.9816	50.0000	0.99982	0.00228	32	0.9091	1.2759	1.00000	0.00005
12	0.9743	50.0000	0.99876	0.01187	33	0.9820	50.0000	0.99993	0.00140
13	0.8473	4.2071	0.99991	0.00770	34	0.9827	35.9291	0.99995	0.00075
14	0.8736	3.4355	0.99996	0.00284	35	0.9076	1.1175	1.00000	0.00009
15	0.8673	1.0006	1.00000	0.00013	36	0.9768	27.2982	0.99999	0.00047
16	0.9843	50.0000	0.99894	0.00415	37	0.9079	1.2835	1.00000	0.00008
17	0.9781	50.0000	0.99994	0.00189	38	0.9827	50.0000	0.99913	0.00452
18	0.9491	4.2749	1.00000	0.00008	39	0.9843	46.2875	0.99993	0.00097
19	0.6757	0.9453	0.99998	0.00268	40	0.9062	3.0869	0.99997	0.00130
22	0.9258	4.0846	0.99999	0.00064	43	0.8167	0.7249	1.00000	0.00042
23	0.8742	3.6178	0.99996	0.00320	44	0.9812	46.0703	0.99997	0.00083
24	0.8766	3.2783	0.99997	0.00238	45	0.8801	0.9095	1.00000	0.00016
25	0.9144	4.4919	0.99999	0.00096	46	0.9390	7.1232	1.00000	0.00038

the spatial variability of SM within each field site is described by values of β and c for that site.

In figures 6.14b, 6.14d, 6.15b, 6.15d, 6.16b, and 6.16d the fitted curves are presented for Site 1 and Site 23 of Epoch 1, Epoch 2 and Epoch 3. In these figures, each point represents a $(q,\tau(q))$ pair, and the curve shows the fitted STRAIN model to the data points. In the legend of each plot the parameters of the fit, β and c, are shown. The values of parameters β and c for these sites along with other sites in the three epochs are presented in tables 6.8 to 6.10. Also presented in these tables are the correlation coefficient and RMSE of the fit for each site.

The correlation coefficients of the fits are very high and the RMSE values are usually low compared to the typical values of $\tau(q)$ shown in Figure 6.14 to Figure 6.16. This suggests that the STRAIN model has been successful in modeling the SM variations in the three

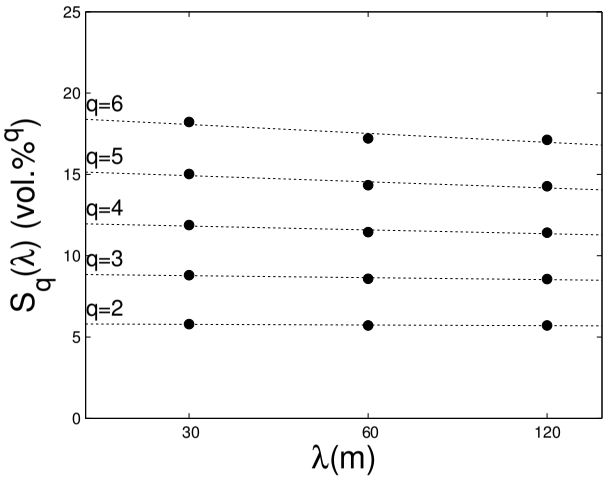

(a) Site 1

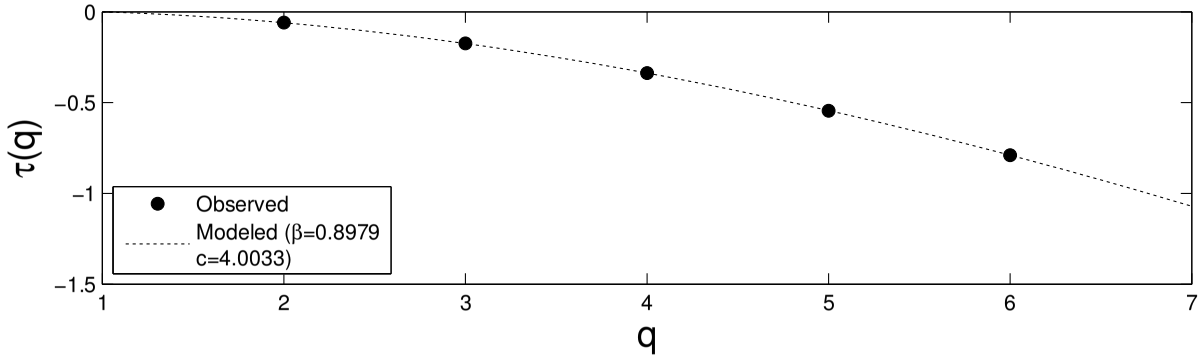

(b) Site 1

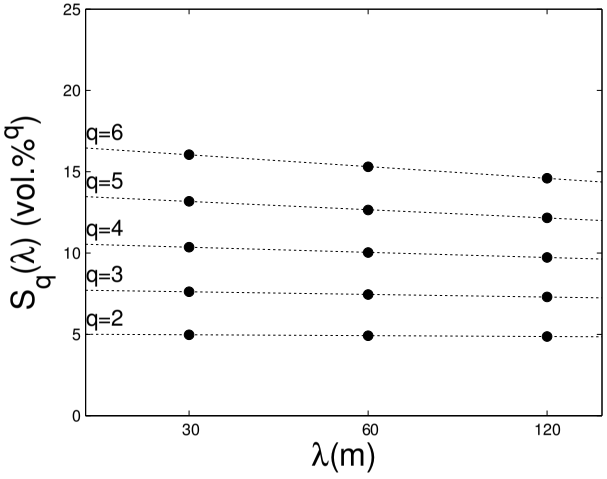

(c) Site 23

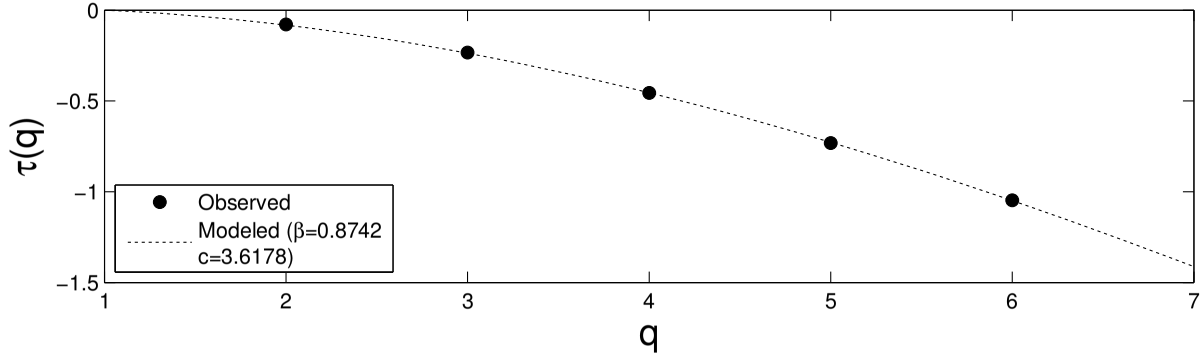

(d) Site 23

Figure 6.14: Multifractal analysis for Site 1 and Site 23 in Epoch 1: (a) and (c): Plot of resolution, λ, vs. partition function, $S_q(\lambda)$, for q=2 to 6, and λ=30 m, 60 m and 120 m in log-log axes. (b) and (d): Plot of q vs. $\tau(q)$, the slope of lines in (a) and (c). The curves show the fitted STRAIN model. The parameters of the fit, β and c, are shown in the legend of the plot.

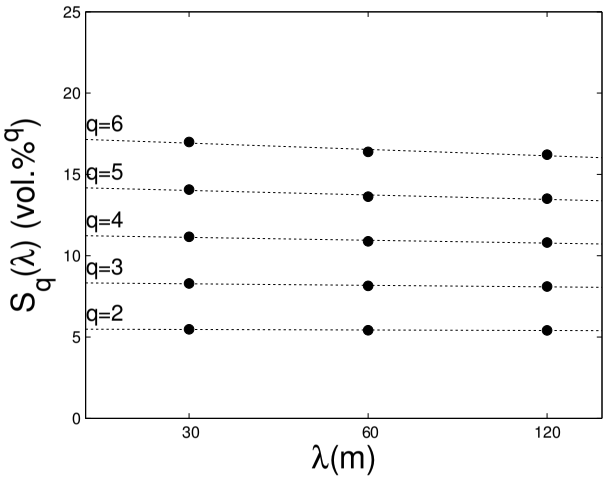

(a) Site 1

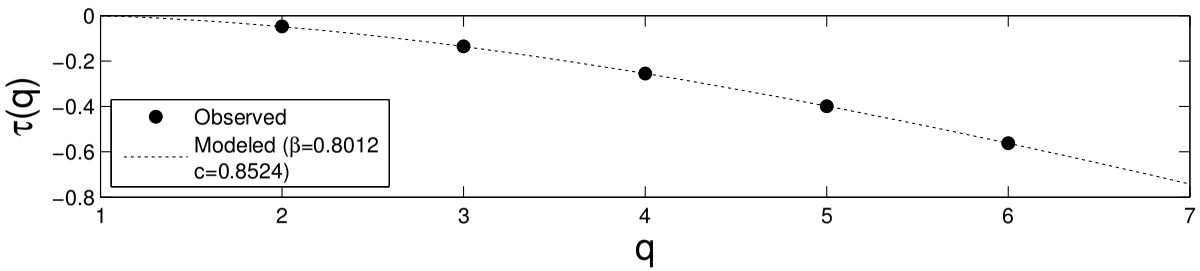

(b) Site 1

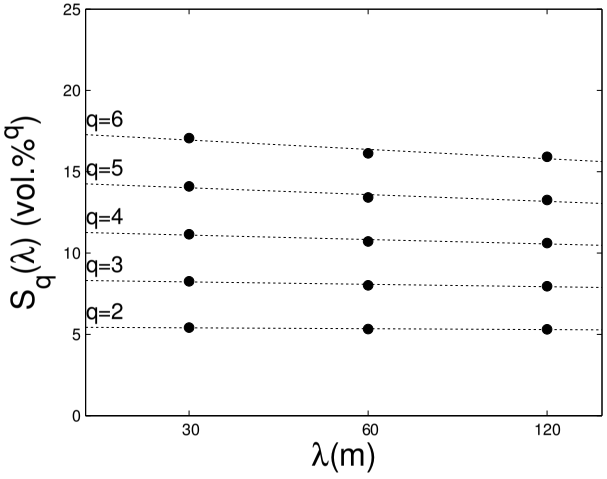

(c) Site 23

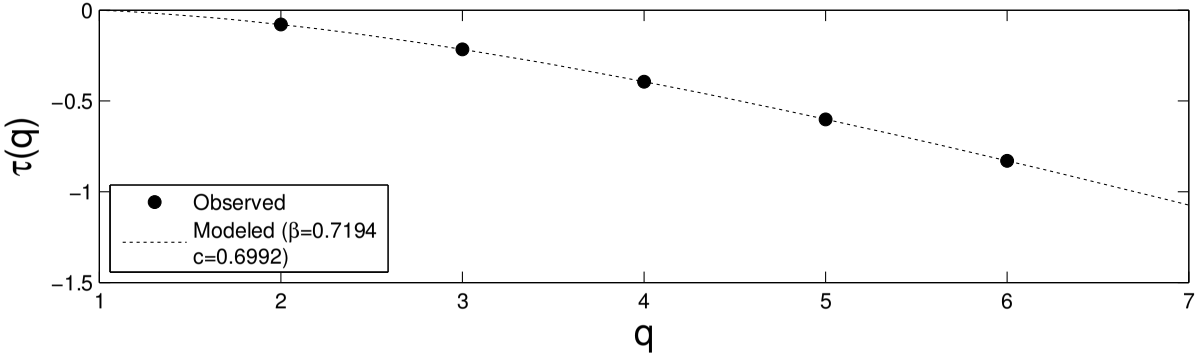

(d) Site 23

Figure 6.15: Multifractal analysis for Site 1 and Site 23 in Epoch 2: (a) and (c): Plot of resolution, λ, vs. partition function, $S_q(\lambda)$, for q=2 to 6, and λ=30 m, 60 m and 120 m in log-log axes. (b) and (d): Plot of q vs. $\tau(q)$, the slope of lines in (a) and (c). The curves show the fitted STRAIN model. The parameters of the fit, β and c, are shown in the legend of the plot.

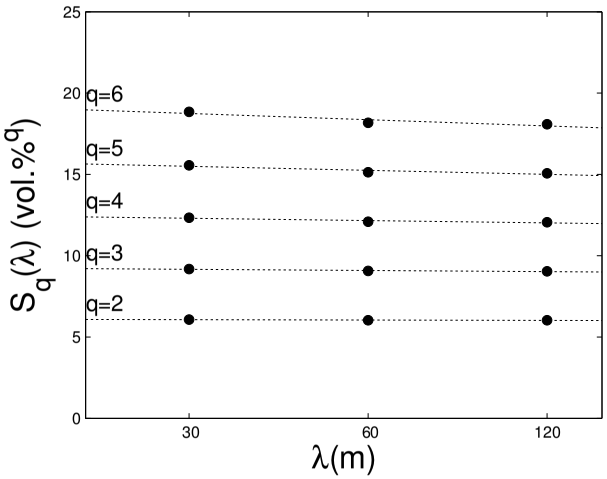

(a) Site 1

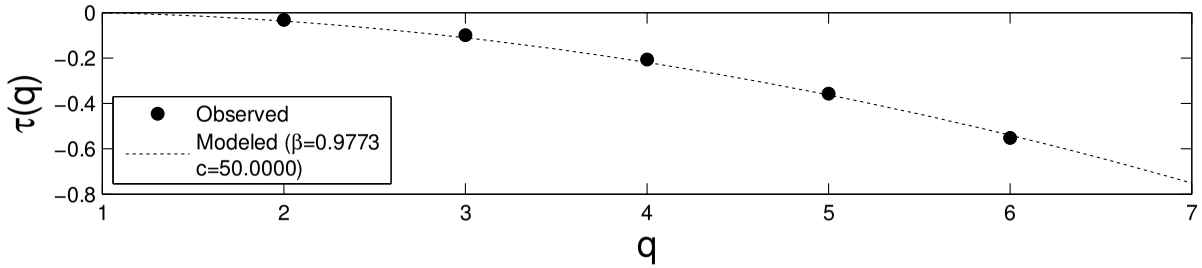

(b) Site 1

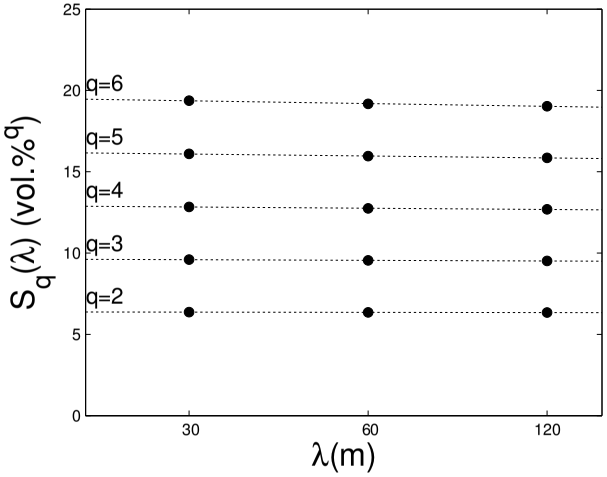

(c) Site 23

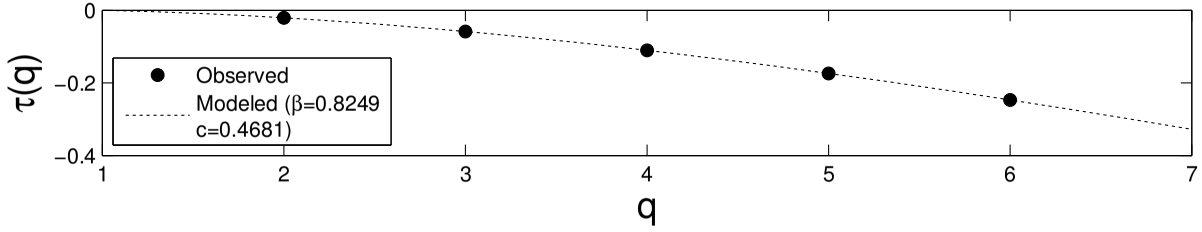

(d) Site 23

Figure 6.16: Multifractal analysis for Site 1 and Site 23 in Epoch 3: (a) and (c): Plot of resolution, λ, vs. partition function, $S_q(\lambda)$, for q=2 to 6, and λ=30 m, 60 m and 120 m in log-log axes. (b) and (d): Plot of q vs. $\tau(q)$, the slope of lines in (a) and (c). The curves show the fitted STRAIN model. The parameters of the fit, β and c, are shown in the legend of the plot.

Table 6.9: Parameters and accuracy of fitting the STRAIN model to ground measurements of Epoch 2

Epoch 2					Epoch 2				
Site	β	c	R	RMSE	Site	β	c	R	RMSE
1	0.8012	0.8524	0.99999	0.00068	22	0.9226	3.4034	0.99999	0.00054
2	0.9045	2.7769	1.00000	0.00039	23	0.7194	0.6992	1.00000	0.00030
4	0.9797	50.0000	0.99993	0.00177	24	0.8868	5.1007	0.99996	0.00379
5	0.9802	7.0979	0.99998	0.00012	25	0.8135	2.1078	1.00000	0.00090
6	0.8314	0.1840	1.00000	0.00001	26	0.7309	0.6376	1.00000	0.00029
7	0.9202	1.7020	1.00000	0.00014	27	0.9288	11.2249	0.99994	0.00425
8	0.8522	0.9326	1.00000	0.00009	28	0.8271	1.1242	1.00000	0.00031
9	0.6261	0.7387	1.00000	0.00072	29	0.7468	1.2309	0.99998	0.00276
10	0.8076	0.6019	1.00000	0.00003	30	0.8788	2.5144	0.99997	0.00165
11	0.8306	2.3868	1.00000	0.00122	31	0.8990	2.0137	1.00000	0.00035
12	0.8058	2.8350	1.00000	0.00146	33	0.9349	6.2263	0.99999	0.00056
13	0.5774	0.8399	0.99998	0.00351	34	0.9430	13.6848	0.99999	0.00104
14	0.5908	0.6817	1.00000	0.00102	38	0.7810	0.6236	1.00000	0.00038
15	0.7575	1.6095	1.00000	0.00023	39	0.8703	2.2758	0.99999	0.00113
16	0.9809	33.1879	0.99998	0.00056	40	0.9696	50.0000	0.99953	0.01006
17	0.7999	1.5299	0.99999	0.00180	42	0.7427	0.5961	1.00000	0.00036
18	0.8952	1.6988	1.00000	0.00020	43	0.4926	0.3488	0.99999	0.00139
19	0.9089	3.3471	1.00000	0.00031	44	0.8826	2.3199	0.99999	0.00103
20	0.6918	0.5756	1.00000	0.00023	45	0.9677	50.0000	0.99990	0.00528
21	0.8628	3.3682	0.99991	0.00502	46	0.9099	6.3580	0.99999	0.00134

Table 6.10: Parameters and accuracy of fitting the STRAIN model to ground measurements of Epoch 3

Epoch 3					Epoch 3				
Site	β	c	R	RMSE	Site	β	c	R	RMSE
1	0.9773	50.0000	0.99861	0.00986	23	0.8249	0.4681	1.00000	0.00003
2	0.9534	4.0282	1.00000	0.00008	24	0.9723	28.2158	0.99998	0.00092
3	0.8804	0.4943	1.00000	0.00003	25	0.8751	1.4002	1.00000	0.00024
4	0.9817	36.5965	0.99996	0.00077	26	0.8805	1.8058	0.99999	0.00052
5	0.9527	1.2264	1.00000	0.00000	27	0.9478	3.8966	1.00000	0.00006
6	0.9774	8.3400	0.99999	0.00012	28	0.8736	1.1207	1.00000	0.00015
7	0.9806	18.7854	0.99998	0.00034	29	0.9670	6.5683	1.00000	0.00005
8	0.9812	27.4378	0.99996	0.00063	30	0.9375	1.9284	1.00000	0.00005
9	0.9850	13.0059	0.99989	0.00031	31	0.9835	50.0000	0.99985	0.00169
10	0.8756	0.5463	1.00000	0.00009	33	0.9312	1.1222	1.00000	0.00002
11	0.9836	50.0000	0.99834	0.00569	34	0.7931	0.7600	1.00000	0.00009
12	0.9832	50.0000	0.99969	0.00254	35	0.9779	26.6877	1.00000	0.00028
13	0.9418	2.6879	1.00000	0.00010	36	0.8859	0.9347	1.00000	0.00015
14	0.8353	1.3410	1.00000	0.00064	37	0.9314	1.4624	1.00000	0.00000
15	0.9112	1.6641	1.00000	0.00006	38	0.9262	5.3960	1.00000	0.00051
16	0.9757	26.7654	1.00000	0.00029	39	0.8277	0.7710	1.00000	0.00029
17	0.9808	50.0000	0.99991	0.00177	40	0.8022	0.7501	1.00000	0.00048
18	0.9393	3.2991	0.99999	0.00029	42	0.9803	43.5142	0.99998	0.00077
19	0.9318	6.0249	1.00000	0.00054	43	0.8344	0.9256	1.00000	0.00014
20	0.9695	15.9035	0.99999	0.00041	44	0.9701	12.9425	1.00000	0.00022
21	0.8222	0.3459	1.00000	0.00008	45	0.9850	40.9245	0.99990	0.00094
22	0.9605	6.4124	1.00000	0.00018	46	0.8641	0.5905	1.00000	0.00007

scales of ground measurements studied here.

In Table 6.11 the average value of β and c for each epoch can be seen. These values are calculated by averaging β and c over all sites in an epoch of measurements. The standard deviation of the two parameters are also presented in the table. The average and standard deviation values discussed here are presented in the table under "Free β".

Obviously, the values of parameter c have a large spread, and in all cases their standard deviation is larger than their mean. This can be better observed in the histograms of c values for each epoch plotted in Figure 6.17. In this figure, the bar on top of each histogram shows the standard deviation of c, and the circle on the bar shows the location of mean c.

In contrast, the distribution of β for each epoch is characterized by small standard deviation compared to its mean. Interestingly, the values of mean β and its standard deviation are close to what Mascaro et al. (2010) and Mascaro et al. (2011) reported for some different regions. Considering the range of standard deviations of β in the three epochs, even the values of mean β in the three epochs are not very different. Therefore, it seems reasonable to try to use a uniform β, as a regional value, for the whole data set. This means assuming a constant β in the process of fitting the STRAIN model to $(q,\tau(q))$ pairs. Working with a fixed β gives us the opportunity to study the behavior of a single parameter, c, with changes of SM around the study area. Thus, following what Mascaro et al. (2010) and Mascaro et al. (2011) suggested, we assume that β is constant and equal to the mean β value for Epoch 1.

Indeed, a more appropriate value for a regional β would be the average of β over all epochs of data. However, because of two reasons, for now, we set the constant β to the average of β in Epoch 1. First, we are trying to use as little ancillary information as possible for improving the results of SAR backscattering models. Second, the values of mean β in the three epochs are not very different. When presenting the final results, we will consider selecting the regional value of β from other two epochs.

In tables 6.12 to 6.14 the results of using the STRAIN model with fixed β=0.9034 is

Table 6.11: Summary statistics for the parameters of the STRAIN model in three epochs using free β, and after setting β=0.9034, which is the average β of Epoch 1

	Free β				Fixed β=0.9034	
	Mean β	StDev β	Mean c	StDev c	Mean c	StDev c
Epoch 1	0.9034	0.0881	17.4887	21.3758	3.2191	2.4026
Epoch 2	0.8313	0.1175	6.9859	13.6047	4.6096	2.6423
Epoch 3	0.9262	0.0594	13.7975	17.5502	1.6029	0.8428

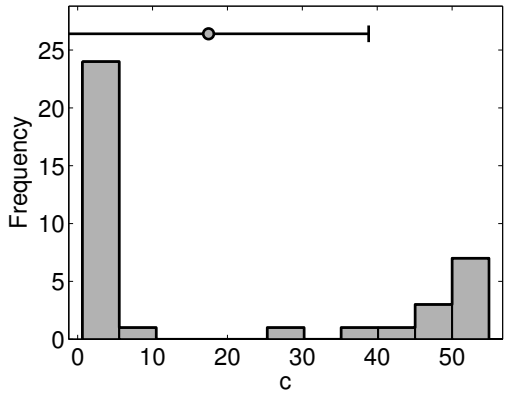

(a) Epoch 1

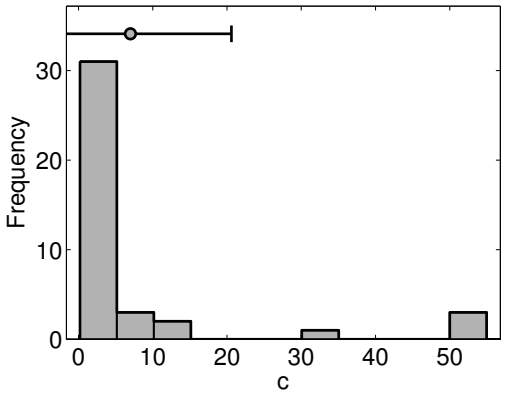

(b) Epoch 2

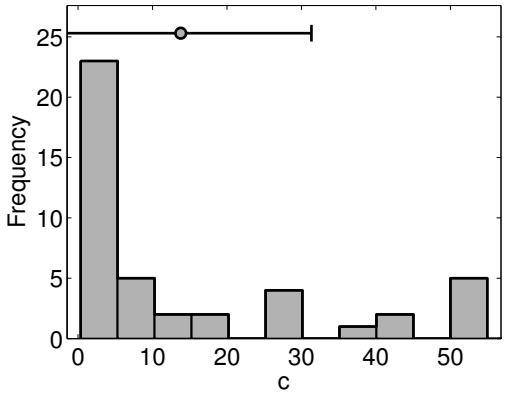

(c) Epoch 3

Figure 6.17: Distribution of parameter c when the STRAIN model is used with free β for three epochs of ground measurements

Table 6.12: Accuracy of fitting the STRAIN model to ground measurements of Epoch 1, and calculated values for parameter c by assuming a fixed β=0.9034

Epoch 1			
Site	c	R	RMSE
1	4.4447	0.99999	0.00094
2	3.8252	0.99921	0.00869
3	1.4934	0.99994	0.00097
8	1.8280	0.99982	0.00208
9	1.1835	0.99991	0.00095
10	1.9876	0.99900	0.00540
11	1.9748	0.99858	0.00643
12	3.8278	0.99678	0.01915
13	9.8679	0.99957	0.01675
14	5.6873	0.99987	0.00537
15	1.8118	0.99986	0.00175
16	1.4484	0.99671	0.00732
17	2.7977	0.99903	0.00750
18	1.2512	0.99978	0.00155
19	8.3053	0.99417	0.04923
22	2.4696	0.99994	0.00163
23	5.9312	0.99987	0.00565
24	5.1894	0.99989	0.00443
25	3.5696	0.99998	0.00144

Epoch 1			
Site	c	R	RMSE
26	5.8089	0.99910	0.01407
27	2.0643	0.99999	0.00061
28	7.5727	0.98982	0.05789
29	9.6709	0.99657	0.04479
30	2.8209	0.99934	0.00620
31	2.6780	0.99936	0.00577
32	1.1365	1.00000	0.00018
33	1.8982	0.99892	0.00537
34	1.2589	0.99898	0.00345
35	1.0277	1.00000	0.00015
36	1.7158	0.99936	0.00370
37	1.1718	1.00000	0.00016
38	1.7498	0.99708	0.00828
39	1.3405	0.99886	0.00389
40	2.9182	0.99997	0.00132
43	2.3690	0.99919	0.00548
44	1.9128	0.99917	0.00471
45	1.3634	0.99994	0.00086
46	2.9524	0.99987	0.00288

presented. According to values of correlation coefficient and RMSE, the model can still explain the changes of $\tau(q)$ with q accurately. The histogram of the values of parameter c in each epoch is shown in Figure 6.18. Also, the summary statistics of c for each epoch can be found in Table 6.11 under "Fixed β=0.9034" columns. Obviously, parameter c is spread over a much narrower range than what it was before setting β to a constant value. The standard deviation of c for each epoch is also less than its mean, and large gaps do not exist in the histograms.

It has been suggested by other studies (Mascaro et al., 2010)(Mascaro et al., 2011) that the new value of parameter c for each site is related to the mean SM in that site through an exponential relationship of the form

$$c = c_{\infty} + ae^{-\gamma\langle\theta\rangle} \tag{6.1}$$

where $\langle\theta\rangle$ is the mean SM value of the site, and c_{∞}, a and γ are parameters. The same

Table 6.13: Accuracy of fitting the STRAIN model to ground measurements of Epoch 2, and calculated values for parameter c by assuming a fixed β=0.9034

Epoch 2			
Site	c	R	RMSE
1	3.2215	0.99886	0.00877
2	2.7138	1.00000	0.00040
4	2.4141	0.99896	0.00669
5	0.3239	0.99919	0.00079
6	0.5170	0.99945	0.00099
7	1.1823	0.99997	0.00056
8	2.0603	0.99972	0.00281
9	8.1941	0.99130	0.05827
10	2.1445	0.99901	0.00545
11	6.7633	0.99943	0.01318
12	10.2727	0.99897	0.02666
13	11.3207	0.98793	0.09306
14	8.7306	0.98891	0.06919
15	8.6314	0.99767	0.03314
16	1.4158	0.99917	0.00350
17	5.8505	0.99882	0.01620
18	1.9799	0.99999	0.00048
19	2.9950	1.00000	0.00055
20	4.6474	0.99501	0.02557
21	6.4856	0.99974	0.00868

Epoch 2			
Site	c	R	RMSE
22	2.2303	0.99995	0.00128
23	4.8189	0.99625	0.02319
24	6.8699	0.99993	0.00488
25	7.1059	0.99913	0.01696
26	4.0913	0.99672	0.01847
27	6.2798	0.99987	0.00607
28	3.3069	0.99937	0.00673
29	7.1108	0.99727	0.02950
30	3.8458	0.99991	0.00303
31	2.1879	0.99999	0.00043
33	2.9281	0.99989	0.00256
34	4.9755	0.99983	0.00545
38	2.7973	0.99837	0.00907
39	3.9484	0.99987	0.00368
40	5.3224	0.99829	0.01916
42	3.5401	0.99716	0.01495
43	6.2268	0.98067	0.06301
44	3.3449	0.99994	0.00213
45	6.0253	0.99919	0.01475
46	5.5632	0.99999	0.00167

Table 6.14: Accuracy of fitting the STRAIN model to ground measurements of Epoch 3, and calculated values for parameter c by assuming a fixed β=0.9034

Epoch 3			
Site	c	R	RMSE
1	2.9948	0.99640	0.01585
2	0.9896	0.99974	0.00135
3	0.7384	0.99994	0.00046
4	1.4362	0.99905	0.00379
5	0.3111	0.99975	0.00042
6	0.4946	0.99932	0.00110
7	0.8291	0.99915	0.00207
8	1.1336	0.99904	0.00302
9	0.3431	0.99869	0.00107
10	0.8773	0.99992	0.00066
11	1.5718	0.99574	0.00910
12	1.6508	0.99818	0.00611
13	1.0199	0.99985	0.00107
14	3.6103	0.99950	0.00659
15	1.4171	0.99999	0.00031
16	1.8396	0.99939	0.00387
17	2.1631	0.99887	0.00625
18	1.3575	0.99986	0.00135
19	3.1004	0.99991	0.00245
20	1.7053	0.99954	0.00311
21	1.0698	0.99929	0.00231
22	1.1451	0.99966	0.00179

Epoch 3			
Site	c	R	RMSE
23	1.4084	0.99934	0.00294
24	2.5060	0.99949	0.00481
25	2.2664	0.99991	0.00173
26	2.6934	0.99994	0.00174
27	1.1949	0.99980	0.00144
28	1.8544	0.99991	0.00149
29	0.8229	0.99958	0.00143
30	0.8378	0.99988	0.00078
31	1.5922	0.99860	0.00514
33	0.5870	0.99992	0.00044
34	3.0836	0.99868	0.00900
35	1.5203	0.99937	0.00325
36	1.2780	0.99997	0.00062
37	0.7603	0.99992	0.00058
38	3.2289	0.99994	0.00206
39	2.2537	0.99938	0.00455
40	2.8091	0.99889	0.00756
42	1.9817	0.99923	0.00472
43	2.5183	0.99949	0.00463
44	1.3363	0.99954	0.00244
45	1.0772	0.99872	0.00332
46	1.1173	0.99984	0.00117

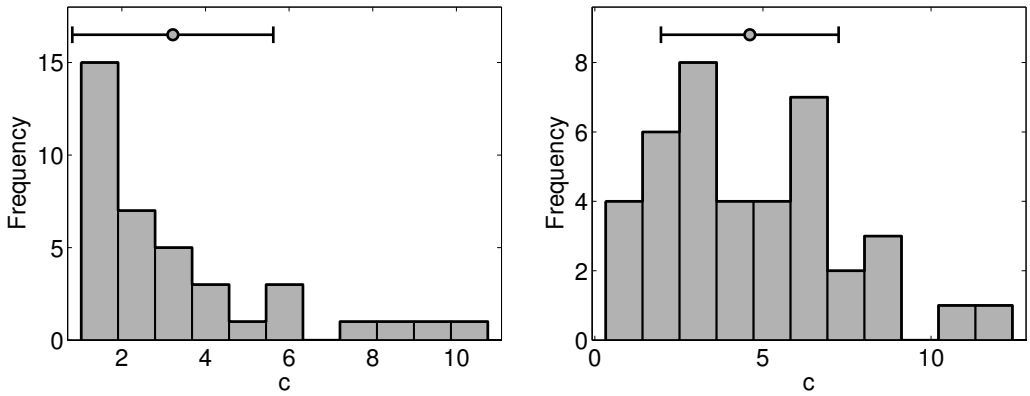

(a) Epoch 1

(b) Epoch 2

(c) Epoch 3

Figure 6.18: Distribution of parameter c when the STRAIN model is used with fixed β=0.9034 for three epochs of ground measurements

relationship has also been observed when studying rain rates using the STRAIN model (Deidda, 2000)(Deidda et al., 2004). In order to examine this relationship in our study area, scatter plots of mean SM of the sites vs. their estimated c were created for the three epochs. These scatter plots are presented in 6.19. In contrast to what other studies have reported, an exponential equation of type 6.1 does not seem to be always able to explain the relationship between $\langle\theta\rangle$ and c. Indeed, in case of the data in Epoch 2, a simple linear relationship seems to be able to model most of the changes of c with respect to $\langle\theta\rangle$.

Several features were examined in an attempt to find a relationship between the parameter c and a predictable quantity in our study area. The features included:

- several moments of field measurements
- coefficient of variation of field measurements
- descriptors for the shape of the distribution of field measurements (e.g. Hartigan descriptor of unimodality (Hartigan et al., 1985))
- Haralick's image texture features based on Grey Level Co-occurrence Matrix (contrast, correlation, energy, homogeneity) (Haralick et al., 1973) applied on field measurements

Interestingly, the coefficient of variation (CV) of the SM values of the base layer of the image pyramid used in the initial stage of the multifractal analysis found to be strongly related to the parameter c. As mentioned before, the base layer is obtained by averaging the four replicates at each node of a ground measurement grid. The scatter plots of CV vs. c for the three epochs are displayed in Figure 6.20 along with a line fitted to data points in each plot. The equation for each epoch is shown in the legend of the scatter plot. The correlation coefficient of fits demonstrate very high correlation between c and CV. It can be seen that the fitted lines in Epoch 1 and Epoch 2 have closer slopes and intercepts.

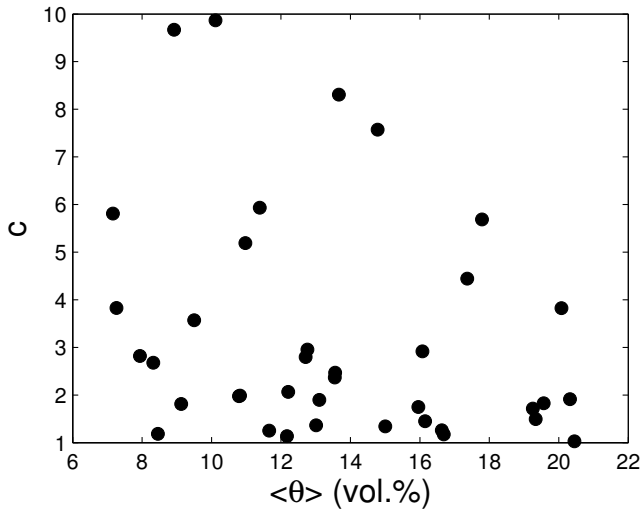

(a) Epoch 1

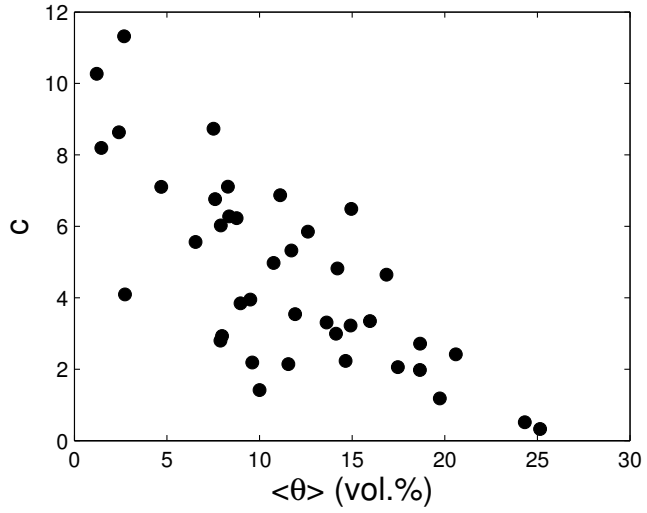

(b) Epoch 2

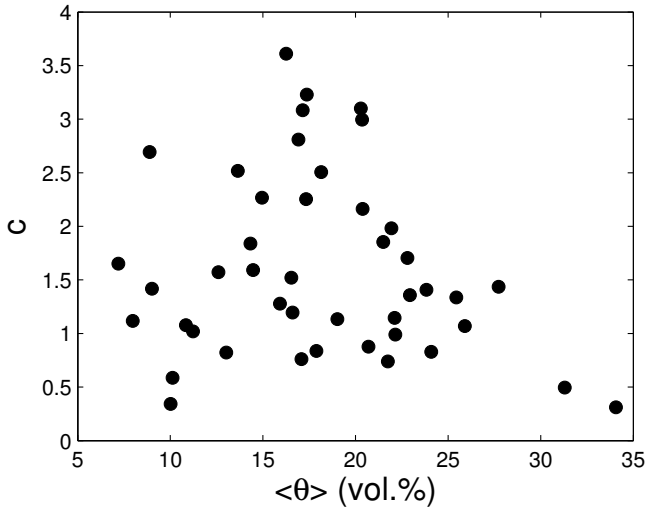

(c) Epoch 3

Figure 6.19: Scatter plot of mean SM vs. c of each site for field measurements of Epoch 1, Epoch 2 and Epoch 3

Although it is beyond the scope of this thesis, given that SM values in the ground measurements of each epoch cover a wide range of moisture conditions, a linear model for CV-c can be useful in downscaling the ground measurements to better resolutions than the original resolution of field campaign as per the algorithm described in (Mascaro et al., 2010). To the best knowledge of the author, this type of relationship between CV and c has not been reported by other studies, thus, it may be specific to the conditions of soil and climate in our study area.

Even though a relationship between statistical properties of ground measurements in different scales can be useful in downscaling the ground measurements, it does not seem to be useful in optimizing the SM values estimated by the SAR backscattering models. Instead, a relationship between ground measurements and remotely-measured SM is required to make SM estimates from backscattering models correspond more closely to field measurements. In order to examine this relationship we need to execute a multifractal analysis on outputs of the backscattering models. One issue in applying multifractal analysis on the outputs of these models is that, accurate calculation of mass exponent, $\tau(q)$, needs a dense initial SM image. Using a simulation with the purpose of quantifying the effect of missing data on the accuracy of $\tau(q)$, Mascaro et al. (2010) showed that 3% of missing pixels caused an error of about 1% in estimation of $\tau(q)$. Obviously, the low inversion rate of the Oh and the Dubois models, with, on average, at least 55% of the pixels missing for sites in our data set, can result in high levels of error in the multifractal analysis procedure. Therefore, we will perform multifractal analysis only on the outputs of the IEM.

6.6 Multifractal Analysis of the IEM Outputs

The dielectric constants of soil were first estimated by the IEM, and then converted to SM values using the Topp dielectric mixing model for every pixel in a 16x16 window (256 pixels) covering each field site. Each site in the study area corresponds to a 10x10 image window

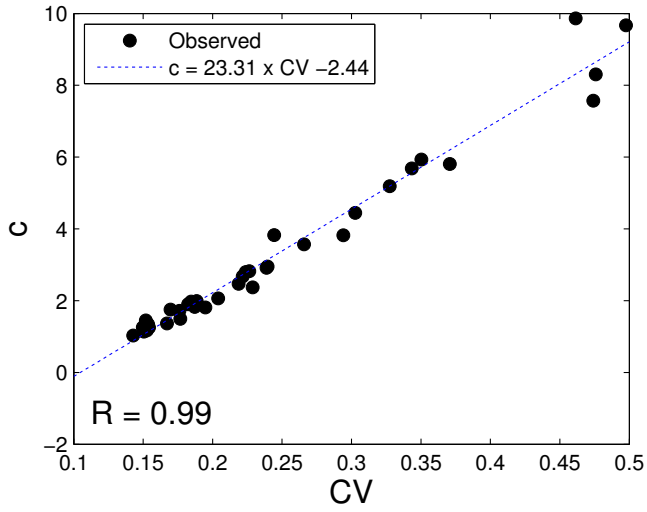

(a) Epoch 1

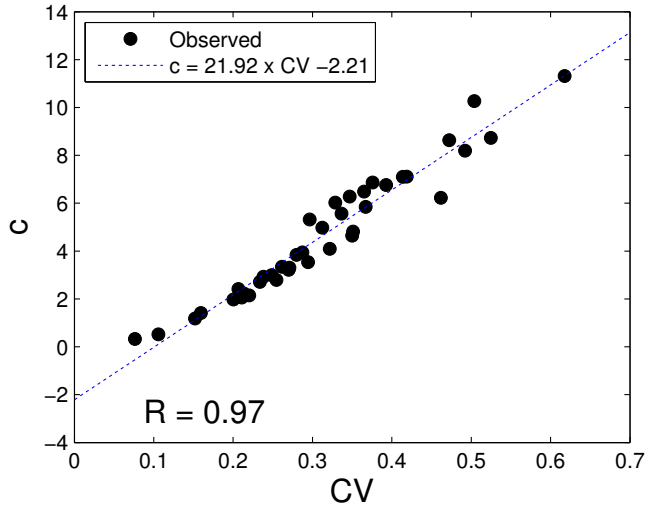

(b) Epoch 2

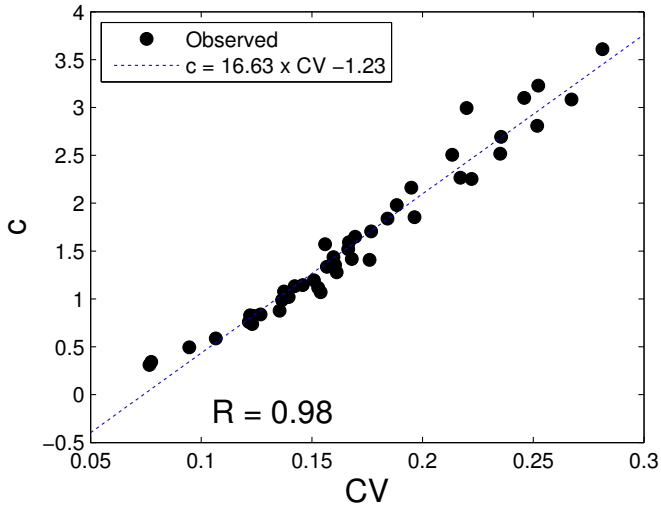

(c) Epoch 3

Figure 6.20: Coefficient of variation of SM vs. c in field measurements of Epoch 1, Epoch2 and Epoch 3: Coefficient of variation is calculated by averaging the four replicates at each node of a ground measurement grid. A high correlation can be seen in each plot. The equation of the line for each plot is displayed in the legend of the plot.

(100 pixels) on the georeferenced Radarsat-2 images. However, since multifractal analysis needs a $2^n \times 2^n$ image, a 16x16 window covering each site was selected for the analysis. Similar to what explained for the ground measurements, an image pyramid was constructed for each of the 16x16 images. This image size will produce 5 levels in each pyramid, resulting in a better analysis than performed for the ground measurements with 3 level pyramids. The scale invariance was again examined by investigating the linearity in log-log plots of λ vs. $S_q(\lambda)$. The values of moment order, q, were set to 2, 3, 4, 5 and 6, and the resolution, λ, was set to 10 m, 20 m, 40 m, 80 m and 160 m, as enforced by the dyadic structure of the image pyramid. The results of this procedure in presented in Table 6.15 for q=6. The values of correlation coefficients and p-values for other moment orders are close to the values mentioned in this table for q=6. The SM values estimated by IEM seem to exhibit more scale invariance than what we observed for the ground measurements, as the correlation coefficients are high, and according to the F-test p-values, the linear fits are almost always statistically significant at a 99% level.

As the next step in multifractal analysis, the STRAIN model was fitted to the data points $(q, \tau(q))$ for each site, where $\tau(q)$ was calculated in the previous step for q =2 to 6. This was done by keeping β constant and equal to the value calculated from ground measurements of Epoch 1, β=0.9034. This resulted in estimation of the c parameter for each site in each epoch. The c values for each site along with the correlation coefficient and the RMSE of the fit are shown in Table 6.16 to Table 6.18. The minimum and maximum values of $\tau(q)$ for each site is also mentioned in the tables for the sake of comparison with the magnitude of the RMSE values. The minimum values of $\tau(q)$ are associated with $q = 6$, and the maximum values are associated with $q = 2$. The performance of the STRAIN model is not identical in different sites. For example, in Site 44 of Epoch 3, the RMSE is about 6% of $|\tau(6)|$, whereas in Site 31 of the same epoch the RMSE is as small as about 0.7% of $|\tau(6)|$.

In Figure 6.21, the histograms of calculated c values for the three epochs of SAR image

Table 6.15: Scale invariance analysis (for q=6) for 16x16 image windows of Radarsat-2 data covering each site in Carman study area: Note that, only the sites covered by the Radarsat-2 image in each epoch can be analyzed, and are presented in the table.

Epoch1			Epoch 2			Epoch 3		
Site	R	p-value	Site	R	p-value	Site	R	p-value
19	-0.9688	0.00659	22	-0.9847	0.00227	15	-0.9815	0.00302
22	-0.9788	0.00371	23	-0.9903	0.00114	16	-0.9798	0.00344
23	-0.9806	0.00324	24	-0.9941	0.00054	19	-0.9834	0.00255
24	-0.9632	0.00844	25	-0.9965	0.00025	20	-0.9884	0.00149
25	-0.9293	0.02231	26	-0.9722	0.00553	21	-0.976	0.00445
26	-0.9871	0.00175	27	-0.9693	0.00643	22	-0.9976	0.00014
27	-0.9793	0.00356	28	-0.9253	0.02421	23	-0.9794	0.00355
28	-0.977	0.00417	29	-0.9926	0.00077	24	-0.9653	0.00773
29	-0.9563	0.01091	30	-0.9908	0.00105	25	-0.9859	0.00201
30	-0.9886	0.00145	31	-0.9757	0.00453	26	-0.9553	0.01126
31	-0.9979	0.00012	33	-0.9485	0.01394	27	-0.9817	0.00296
32	-0.9854	0.00211	34	-0.9944	0.0005	28	-0.9863	0.00193
33	-0.9909	0.00104	38	-0.9887	0.00145	29	-0.8859	0.04548
34	-0.9964	0.00026	39	-0.9842	0.00238	30	-0.9874	0.0017
35	-0.9803	0.00331	40	-0.9597	0.00966	31	-0.9871	0.00175
36	-0.9918	0.0009	42	-0.9794	0.00355	33	-0.9396	0.01764
37	-0.9764	0.00434	43	-0.9485	0.01391	34	-0.9865	0.00189
38	-0.9528	0.01222	44	-0.9879	0.0016	35	-0.9569	0.01067
39	-0.9738	0.00506	45	-0.9569	0.01067	36	-0.9895	0.0013
40	-0.9618	0.00891	46	-0.9684	0.00672	37	-0.9951	0.00041
43	-0.9782	0.00384				38	-0.9894	0.0013
44	-0.9811	0.0031				39	-0.9499	0.01337
45	-0.9938	0.00058				40	-0.9873	0.00172
46	-0.9925	0.00078				42	-0.973	0.00531
						43	-0.9619	0.00887
						44	-0.977	0.00417
						45	-0.9818	0.00294
						46	-0.9725	0.00547

Table 6.16: Accuracy of fitting the STRAIN model to SM calculated from outputs of the IEM in Epoch 1, and calculated values for parameter c by assuming a fixed β=0.9034

Epoch 1					
Site	c	R	Min $\tau(q)$	Max $\tau(q)$	RMSE
19	10.8450	0.9938	-1.9287	-0.1461	0.0662
22	10.3989	0.9933	-1.8493	-0.1401	0.0656
23	8.6579	0.9998	-1.5397	-0.1166	0.0090
24	9.7070	0.9953	-1.7263	-0.1308	0.0522
25	10.6284	0.9933	-1.8901	-0.1432	0.0671
26	10.2535	0.9956	-1.8235	-0.1381	0.0536
27	9.8049	0.9887	-1.7437	-0.1321	0.0786
28	12.2951	0.9918	-2.1865	-0.1656	0.0852
29	10.3343	0.9996	-1.8378	-0.1392	0.0180
30	11.3322	0.9994	-2.0153	-0.1526	0.0222
31	6.4716	0.9981	-1.1509	-0.0872	0.0224
32	11.0821	0.9847	-1.9708	-0.1493	0.1016
33	12.6312	0.9785	-2.2463	-0.1701	0.1343
34	12.4967	0.9856	-2.2224	-0.1683	0.1115
35	10.9676	0.9807	-1.9505	-0.1477	0.1107
36	11.7408	0.9894	-2.0880	-0.1582	0.0915
37	10.7020	0.9932	-1.9032	-0.1442	0.0683
38	14.4089	0.9936	-2.5625	-0.1941	0.0899
39	10.4737	0.9904	-1.8626	-0.1411	0.0779
40	9.3154	0.9921	-1.6566	-0.1255	0.0632
43	6.9814	0.9929	-1.2416	-0.0940	0.0455
44	9.9954	0.9887	-1.7776	-0.1346	0.0800
45	11.9105	0.9925	-2.1182	-0.1604	0.0794
46	7.3584	0.9962	-1.3086	-0.0991	0.0355

Table 6.17: Accuracy of fitting the STRAIN model to SM calculated from outputs of the IEM in Epoch 2, and calculated values for parameter c by assuming a fixed β=0.9034

Epoch 2					
Site	c	R	Min $\tau(q)$	Max $\tau(q)$	RMSE
22	7.0463	0.9958	-1.2531	-0.0949	0.0357
23	10.1647	0.9944	-1.8077	-0.1369	0.0595
24	8.2724	0.9877	-1.4712	-0.1114	0.0689
25	8.3277	0.9937	-1.4810	-0.1122	0.0512
26	7.8096	0.9971	-1.3888	-0.1052	0.0334
27	11.5405	0.9917	-2.0523	-0.1555	0.0804
28	4.6917	0.9884	-0.8344	-0.0632	0.0380
29	4.4254	0.9945	-0.7870	-0.0596	0.0254
30	3.2172	0.9975	-0.5721	-0.0433	0.0129
31	3.0939	0.9999	-0.5502	-0.0417	0.0019
33	8.8540	0.9934	-1.5746	-0.1193	0.0556
34	5.9880	0.9905	-1.0649	-0.0807	0.0444
38	8.3882	0.9931	-1.4917	-0.1130	0.0535
39	12.1936	0.9868	-2.1685	-0.1643	0.1048
40	8.2003	0.9980	-1.4583	-0.1105	0.0293
42	9.0164	0.9940	-1.6035	-0.1215	0.0543
43	7.8624	0.9974	-1.3982	-0.1059	0.0321
44	9.5862	0.9947	-1.7048	-0.1291	0.0547
45	8.6414	0.9983	-1.5368	-0.1164	0.0288
46	6.6061	0.9959	-1.1748	-0.0890	0.0332

Table 6.18: Accuracy of fitting the STRAIN model to SM calculated from outputs of the IEM in Epoch 3, and calculated values for parameter c by assuming a fixed β=0.9034

Epoch 3					
Site	c	R	Min τ(q)	Max $\tau(q)$	RMSE
15	11.2617	0.9837	-2.0028	-0.1517	0.1060
16	11.8762	0.9913	-2.1120	-0.1600	0.0845
19	17.8554	0.9785	-3.1754	-0.2405	0.1902
20	13.5207	0.9793	-2.4045	-0.1821	0.1415
21	14.7636	0.9960	-2.6255	-0.1989	0.0733
22	11.8575	0.9943	-2.1087	-0.1597	0.0695
23	13.3875	0.9851	-2.3808	-0.1803	0.1214
24	13.2625	0.9961	-2.3586	-0.1787	0.0649
25	11.6577	0.9978	-2.0732	-0.1570	0.0439
26	5.4186	0.9989	-0.9636	-0.0730	0.0143
27	9.9299	0.9889	-1.7659	-0.1338	0.0790
28	7.4075	0.9952	-1.3173	-0.0998	0.0400
29	4.8081	0.9869	-0.8551	-0.0648	0.0414
30	4.0146	0.9949	-0.7139	-0.0541	0.0222
31	4.4411	0.9998	-0.7898	-0.0598	0.0057
33	10.9649	0.9954	-1.9500	-0.1477	0.0585
34	10.5784	0.9882	-1.8813	-0.1425	0.0865
35	9.0740	0.9976	-1.6137	-0.1222	0.0350
36	9.4900	0.9953	-1.6877	-0.1278	0.0508
37	10.1346	0.9947	-1.8023	-0.1365	0.0575
38	12.9980	0.9907	-2.3116	-0.1751	0.0956
39	12.9301	0.9847	-2.2995	-0.1742	0.1188
40	15.1507	0.9911	-2.6944	-0.2041	0.1093
42	13.0388	0.9782	-2.3188	-0.1756	0.1395
43	7.6218	0.9999	-1.3554	-0.1027	0.0071
44	16.0964	0.9750	-2.8626	-0.2168	0.1824
45	10.5649	0.9886	-1.8788	-0.1423	0.0850
46	12.7291	0.9898	-2.2637	-0.1715	0.0977

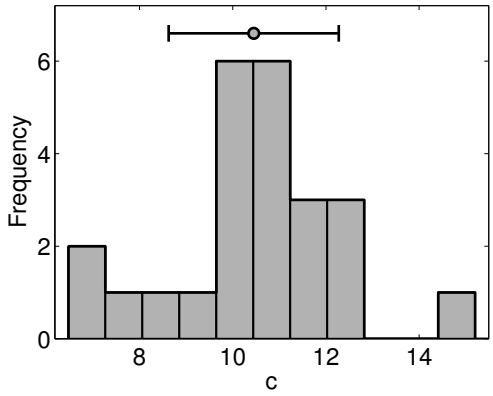

(a) Epoch 1: Averag c=10.4497, StDev c=1.8257

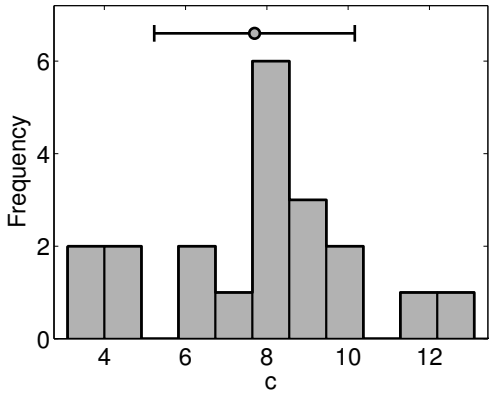

(b) Epoch 2:Averag c=7.6963, StDev c=2.4671

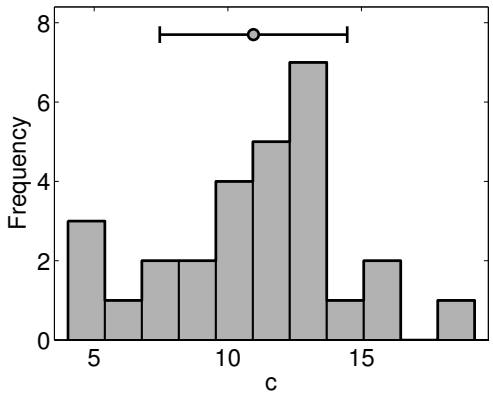

(c) Epoch 3:Averag c=10.9584, StDev c=3.5078

Figure 6.21: Distribution of parameter c when the STRAIN model is used with fixed β=0.9034 for three epochs of SM values calculated from outputs of the IEM

acquisition are displayed. Similar to what observed in fractal analysis of ground measurements with fixed β, the standard deviation of parameter c is small compared to its mean, and large gaps do not exist in the histograms.

As mentioned before, if parameter c can be predicted without using the STRAIN model, then the STRAIN model can be used in transferring statistical properties of SM over scales and downscaling the SM information as per the algorithm explained in (Mascaro et al., 2010). The strong linear relationship between the coefficient of variation and c was demonstrated in Figure 6.20 for ground measurements of all epochs. Obviously, downscaling SM images obtained from remotely sensed data is also valuable, as usually the pixel sizes of such images

are larger than needed. Therefore, we examined the relationship between c and the coefficient of variation calculated for the field sites on our SAR images. In Figure 6.22 three scatter plots of values of the parameter c vs. the coefficient of variation of SM calculated from the outputs of the IEM are depicted. Each point in a plot corresponds to a site in the study area. According to these plots, the correlation of c and CV are not as strong as what observed for ground measurements, but changes in c can still describe a good amount of the changes of CV. The linear relationship is stronger in Epoch 2 and Epoch 3 than Epoch 1. This may be because of the precipitation which has possibly happened concurrent with the acquisition of the SAR image of Epoch 1, which may have caused irregularities in the output of the IEM. But, a linear relationship with R=0.7 (Epoch 1) may still be useful in predicting the values of the parameter c from the values of the coefficient of variation, and assist in transferring the statistical properties of SM images over scales.

As mentioned earlier, in order to improve the outputs of the IEM, we need to establish a connection between the parameter c and a quantity estimated from ground measurements. In an attempt to find such a connection, it was observed that, quite interestingly, the value of c for a site is correlated with the value of the residual, r, calculated as

$$r = \bar{\theta}_{model} - \bar{\theta}_{ground} \tag{6.2}$$

where $\bar{\theta}_{model}$ is the average of SM estimated by the IEM output in the site, and $\bar{\theta}_{ground}$ is the average of ground measurements of SM for the site. The relationship between c and r is demonstrated in Figure 6.23 for the three epochs of data using a regional value of 0.9034 for β. As seen in the plots of this figure, as c increases, usually r decreases. The smallest residuals are usually obtained for the sites that their c is about 10. However, this is not true for all the sites, as, for example, there are sites which their c values are close to 10 in Figure 6.23a, but are located close to the horizontal axis, and the absolute value of their residuals are as large as 10 vol.% or more. However the fitted lines in all three plots have fairly good correlation coefficients.

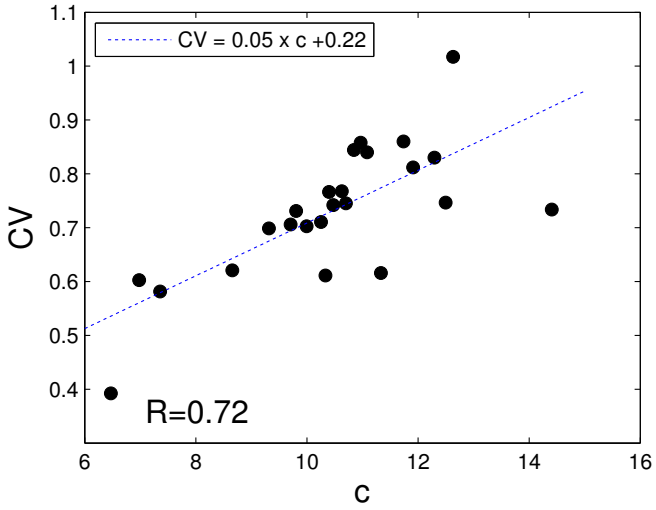

(a) Epoch 1

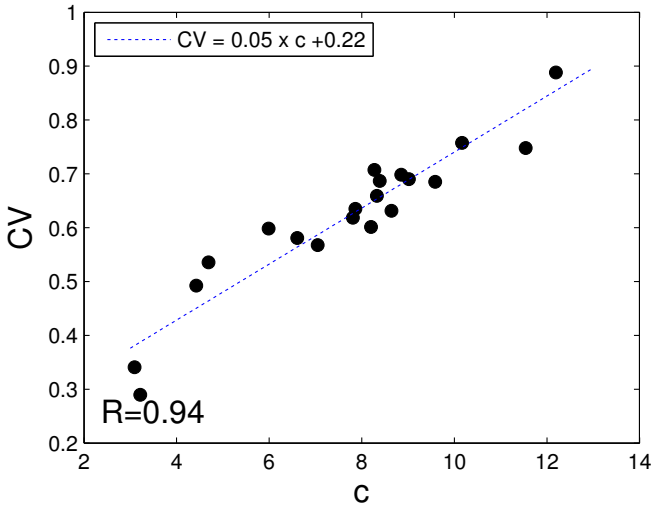

(b) Epoch 2

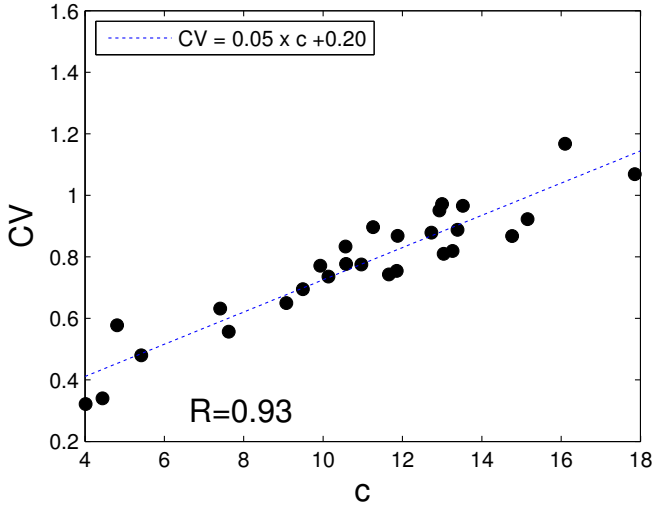

(c) Epoch 3

Figure 6.22: Relationship between c and CV for SM values obtained from IEM outputs. β=0.9034.

An important aspect of the linear relationship between c and residuals obtained here is that the slope of the fitted lines in all epochs are close. This suggests the possibility of calculating the parameters of the line using a single epoch of data, and then using the parameters as approximate values of the parameters for other epochs. In Figure 6.24 the three sets of data points and fitted lines for the three epochs are plotted together for the sake of comparison of the lines. The slope and intercept of each line is mentioned in the legend of the plot. The equation of the line corresponding to each epoch is under the item showing the data points of the epoch in the legend. The regional β is calculated from the ground measurements of Epoch 1 and is equal to 0.9034.

Another important aspect is that, although changing the regional value of β changes the range of values of c, it has little effect on the relative location of the fitted lines. In other words, the fitted lines are fairly stable with respect to each other when β is changed. This gives us the opportunity to use the ground measurements in any of the epochs to estimate the parameters of the fitted line; hence, using only information from a single epoch of measurements and image acquisition. This can be seen in Figure 6.25 and Figure 6.26 which present the same information as Figure 6.24, but by setting the regional β to the average of β calculated from fitting the STRAIN model to ground measurements of Epoch 2 and Epoch 3, respectively.

The linear relationship between the parameter c and the residuals can be used as a calibration model to improve the quality of SM estimation using the IEM at site level. Assume that the relationship between c and a residual, r, for each site can be approximately modeled as

$$r = \bar{\theta}_{IEM} - \bar{\theta}_{ground} = A \times c + B \tag{6.3}$$

where $\bar{\theta}_{IEM}$ is the average SM of a site estimated by the IEM, and $\bar{\theta}_{ground}$ is the average SM value measured on the ground for the same site. Thus a calibrated SM value can be

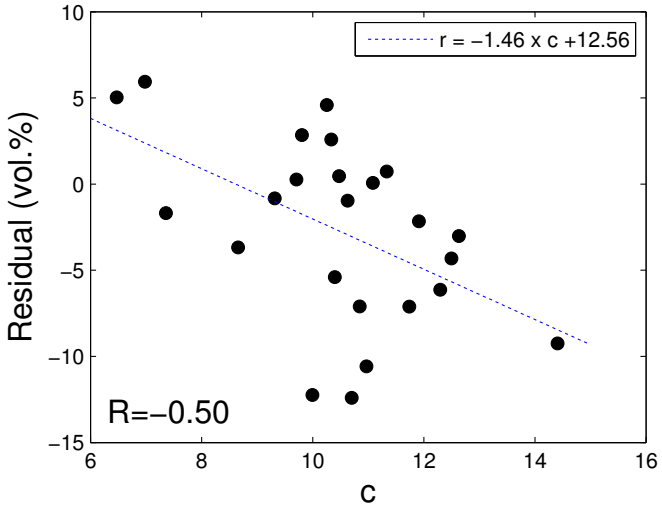

(a) Epoch 1

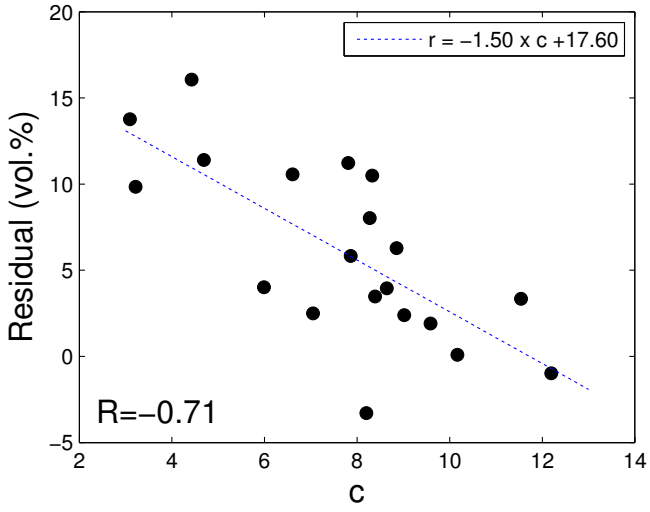

(b) Epoch 2

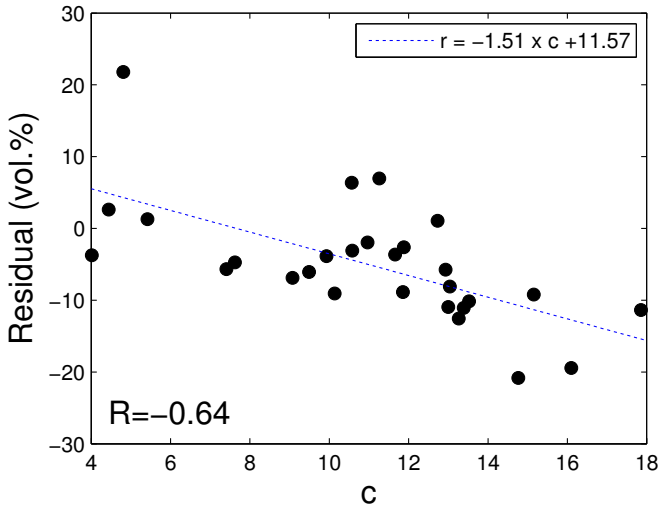

(c) Epoch 3

Figure 6.23: The relationship between parameter c of the STRAIN model and the residuals: The residual for each site is calculated as the difference between the average of SM estimated by the IEM output in the site and the average of ground measurements of SM for the site. β=0.9034.

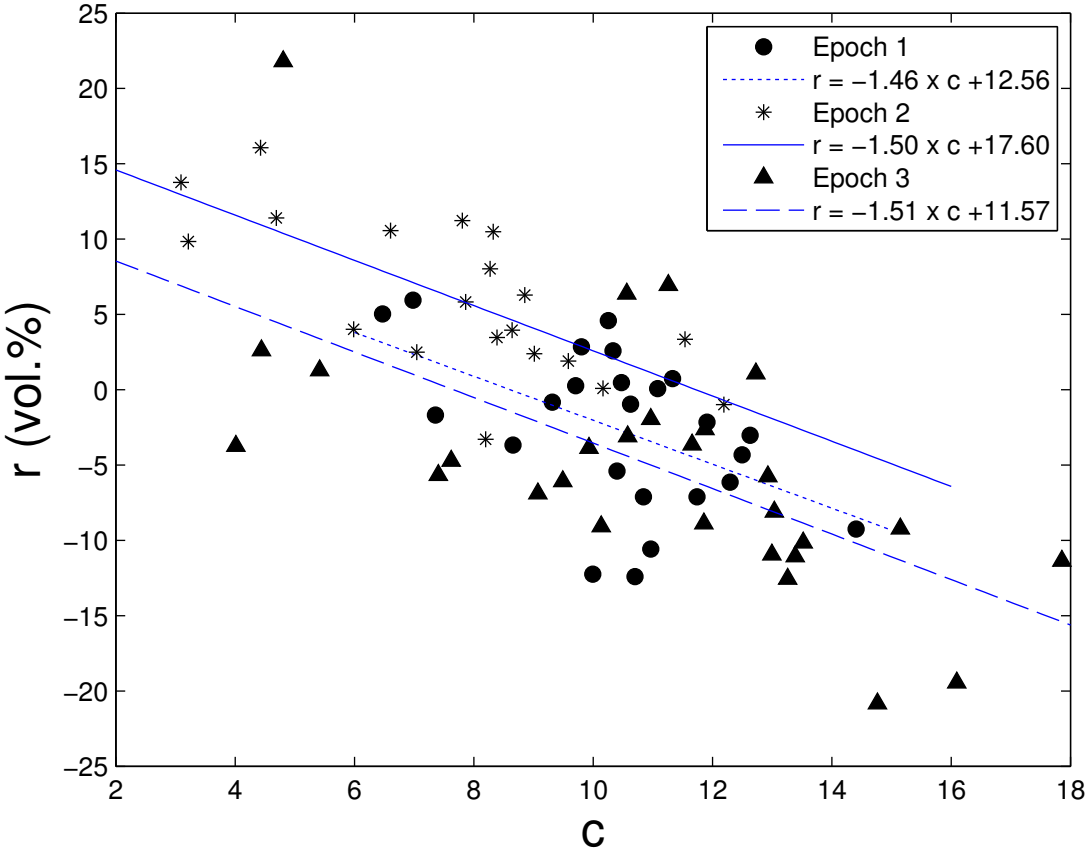

Figure 6.24: The relationship between parameter c of the STRAIN model and the residuals for the three epochs of data in our study area: β=0.9034 is calculated using the ground measurements of Epoch 1. The equation of the line corresponding to each epoch is under the item showing the data points of the epoch in the legend.

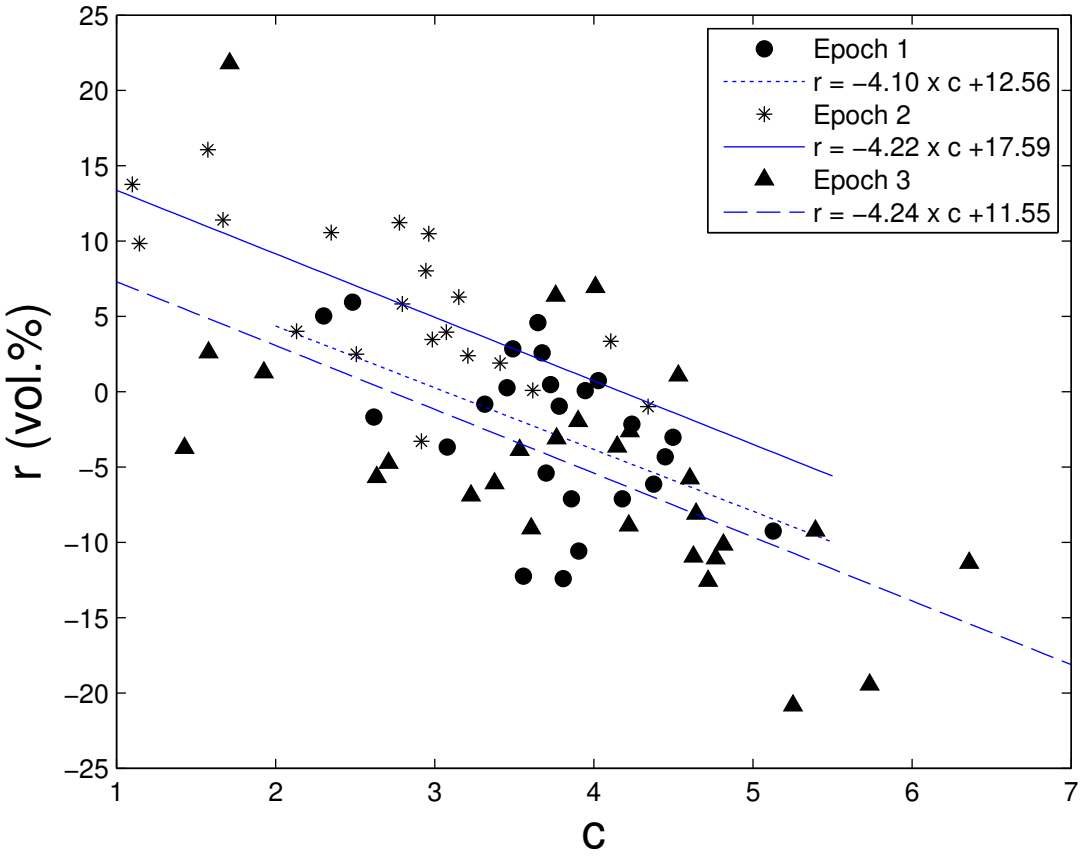

Figure 6.25: The relationship between parameter c of the STRAIN model and the residuals for the three epochs of data in our study area: β=0.8313 is calculated using the ground measurements of Epoch 2. The equation of the line corresponding to each epoch is under the item showing the data points of the epoch in the legend.

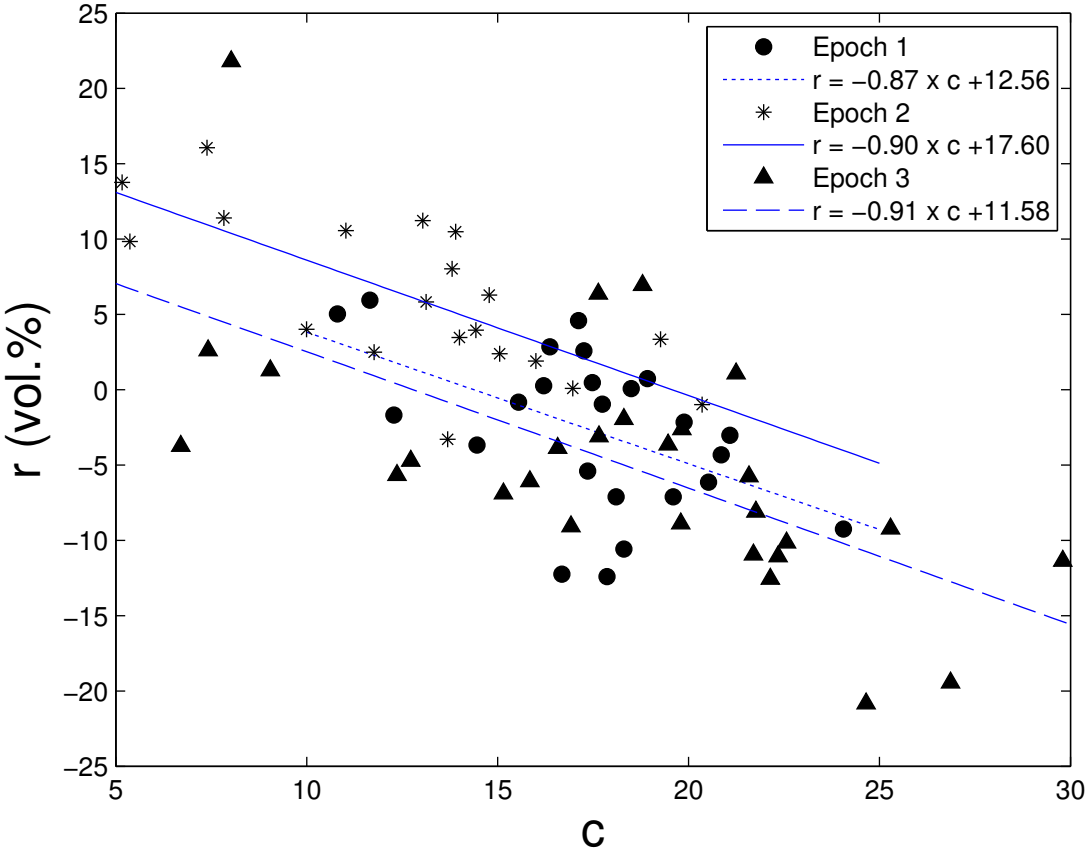

Figure 6.26: The relationship between parameter c of the STRAIN model and the residuals for the three epochs of data in our study area: β=0.9262 is calculated using the ground measurements of Epoch 3. The equation of the line corresponding to each epoch is under the item showing the data points of the epoch in the legend.

calculated for the site by

$$\hat{\theta} = \bar{\theta}_{IEM} - (A \times c + B) \tag{6.4}$$

In this equation, the values of c and $\bar{\theta}_{IEM}$ are calculated from the SM values obtained from outputs of the IEM. The parameters of the calibration model, A and B can be estimated by fitting a line to values of c and r obtained from an epoch of concurrent image and ground measurements. If the calibration model could completely explain the relationship between c and r, then (6.4) could convert $\bar{\theta}_{IEM}$ to $\bar{\theta}_{ground}$. The correlation coefficients show that the calibration model cannot completely describe the changes in r using c. However, because of the fairly high correlation coefficients between c and r, it seems reasonable to expect that calibrating the SM estimated using the IEM for a site, $\bar{\theta}_{IEM}$, using equation (6.4) can on average improve $\bar{\theta}_{IEM}$.

In order to examine the effect of calibrating the SM estimated by the IEM using the above-mentioned calibration model, these SM values were transformed using equation 6.4 and then compared to the ground measurements. For this purpose, Epoch 1 was selected as the reference epoch, and the parameters A, and B were calculated using the ground measurements and SAR image in this epoch. The results of this calibration are presented in Figure 6.27. In this figure the left column shows the performance of the IEM, i.e. agreement of SM values estimated by the IEM outputs with the ground measurements, before applying the calibration model. The right column shows the agreement of the calibrated SM values with ground measurements. According to the plots in this figure, the calibration model obtained using Epoch 1 as the reference epoch always decreases the RMSE and increases the correlation coefficient of SM estimation.

The calibration model is expected to have the most influence on the results of Epoch 1. Because the calibration parameters have been calculated using the information from this Epoch. Since we are assuming that the ground measurements are available for this epoch to estimate the parameters of the calibration model, the data in this epoch cannot be used to

assess the improvement that the calibration model can make. The results of applying the calibration model in Epoch 1 are presented to see the changes it makes on data points. For this epoch, the calibration model increases the correlation coefficient by 0.25 and decreases the RMSE by 1.35 vol.%. For Epoch 2, the calibration model almost doubles the correlation coefficient and decreases the RMSE by 1.99 vol.%. For the data in Epoch 3, the calibration model makes 0.42 increase in R and 3.08 vol.% improvement in the RMSE. For Epoch 2 and Epoch 3, the IEM has a strong overestimation and underestimation of SM before calibration. Although the calibration model improves the distribution of the data points along the 1:1 line for Epoch 2 and Epoch 3, but it has a slight effect on the overestimation and underestimation problems. The effect of applying the calibration model in the three epochs can also be seen in Figure 6.28 where histograms of residuals are presented before and after calibration. According to the values of $\bar{r}$, the average of residuals, the calibration model removes almost all of the systematic error in Epoch 1, as expected. For the other two epochs, although the calibration model alleviates the systematic error of the SM estimation by the IEM, systematic error still exists after the calibration.

It should be mentioned that, the calibration model tries to calibrate the average SM value estimated using the IEM for each site. Thus, it can not operate on individual pixels of the SM image generated by the IEM. This results in increasing the pixel size of the final SM map to 160 m if we use 16×16 pixel windows in multifractal analysis. However, the resolution is still better than the resolution considered as field-scale resolution which is the target resolution in this study.

In figures 6.29 to 6.32 the results of the calibration procedure for the three epochs of data, when using data in Epoch 2 and Epoch 3 for estimation of the calibration parameters, are presented. A summary of the results of different combinations of calibration-evaluation is shown in Table 6.19. In this table, reference epoch is the epoch that using its ground measurements and SAR image the calibration coefficients, A and B in equation (6.4), are

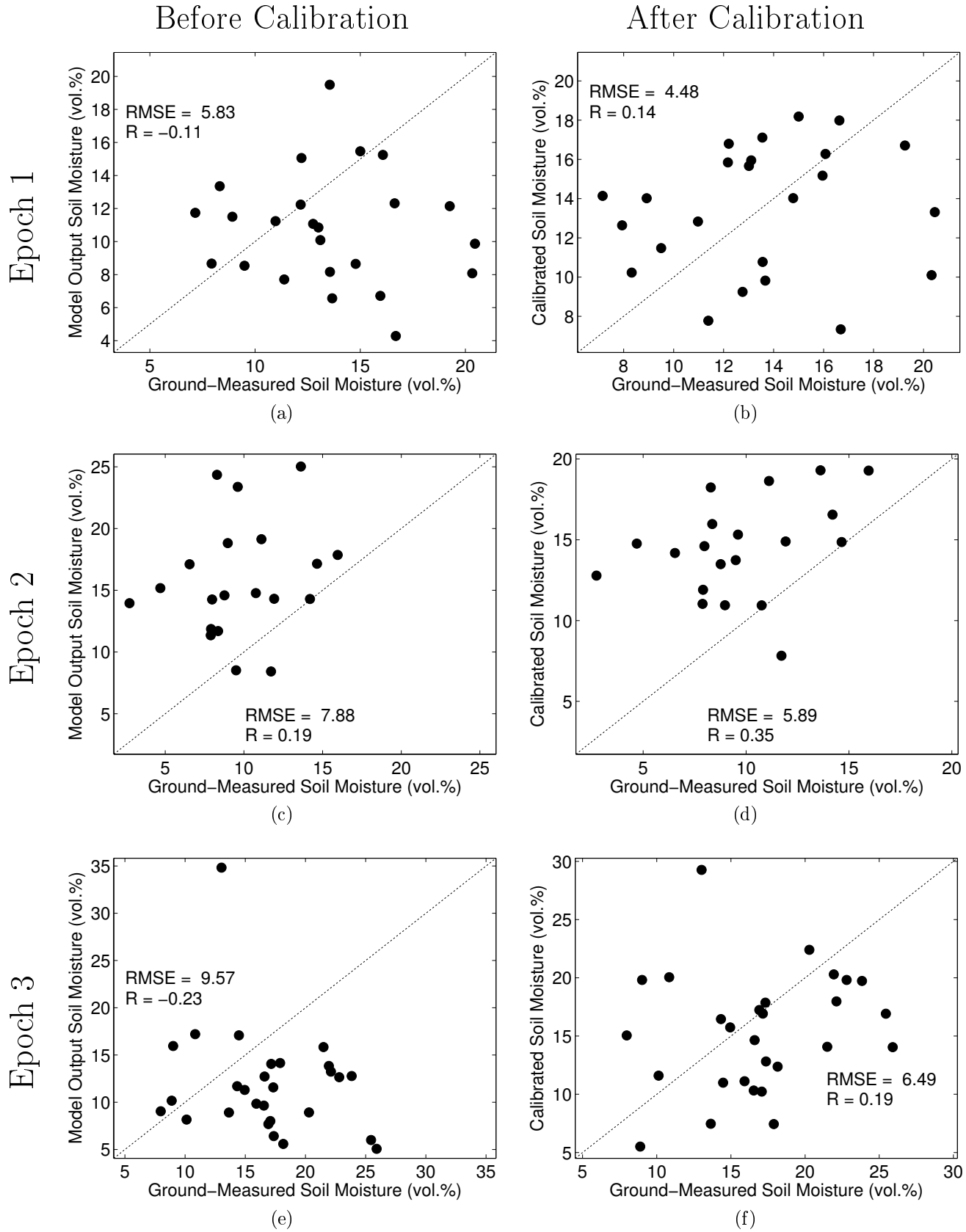

Figure 6.27: Comparison of the agreement of the SM estimated by the IEM and the ground measurements before and after calibration using the proposed calibration model. Data in Epoch 1 is used to estimate the calibration parameters. RMSE is in vol.%.

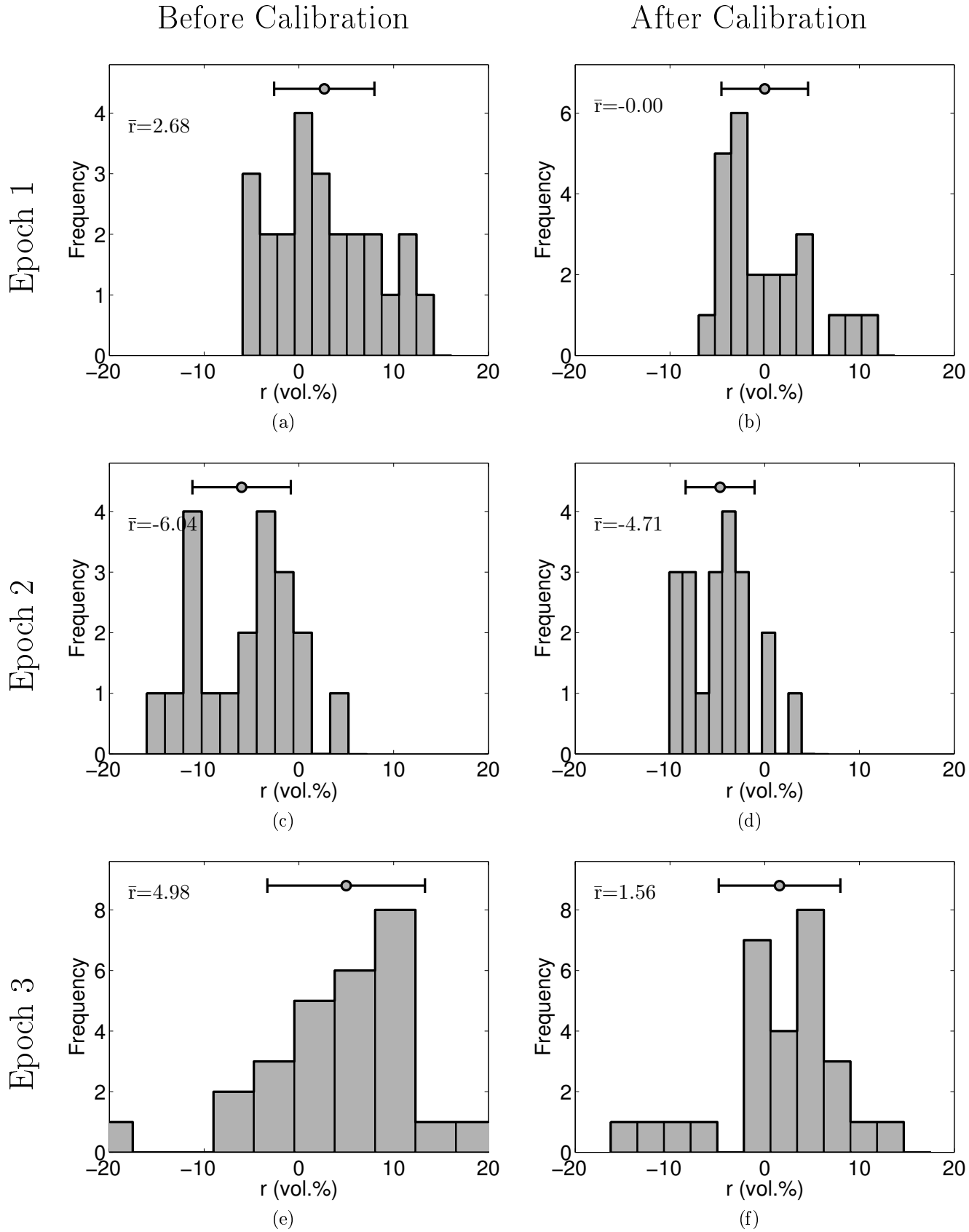

Figure 6.28: Comparison of the histograms of residuals before and after calibration using the proposed calibration model. Data in Epoch 1 is used to estimate the calibration parameters. $\bar{r}$ is the average residual in vol.%.

calculated. Evaluation epoch shows the epoch that the SM values calculated by the IEM for it have been calibrated using the reference epoch. $\bar{r}$ is the average residual, which represents the systematic error in prediction.

According to figures 6.29 to 6.32, and Table 6.19, the calibration model always improves the correlation coefficient by at least 0.16. When Epoch 3 is the reference epoch, similar results to what explained for Epoch 1 as reference is observed, i.e. RMSE is always improved. However, $\bar{r}$ is increased for Epoch 2 when Epoch 3 is the reference epoch.

The weakest performance of the calibration model is observed when the ground measurements and SAR image of Epoch 2 are used for establishing the model. In this case, the RMSE for Epoch1 is increased after calibration, and the bias is increased for Epoch 3 after calibration. This suggests that the calibration model established by data in Epoch 2 is not performing as well as the calibration models established using data in other two epochs. However, this may not be because of the difference in dates of data collection and image acquisition, as the temporal distance between Epoch 1 and Epoch 3 is more than that of Epoch 2 and the other two epochs. This can suggest that the calibration procedure is robust in time. The weak performance of the calibration model established by Epoch 2 data may be because the IEM has not been able to model the effect of incidence angle. In this case, the difference in incidence angle of Epoch 2 image with the other two images may affect the outputs of IEM and calculation of c.

When Epoch 1 is used as reference, the improvements in RMSEs for other two epochs are larger than the precision of the average ground-measured SM values. This suggests that observing the improvement made by the calibration model in this case is not because of the uncertainty in ground measurements, and the improvement is meaningful.

The calibration model proposed above is an empirical model which seems useful in improving the outputs of the IEM for our study area. The physical or mathematical reason behind the correlation between the parameter c and the residuals of the IEM does not seem

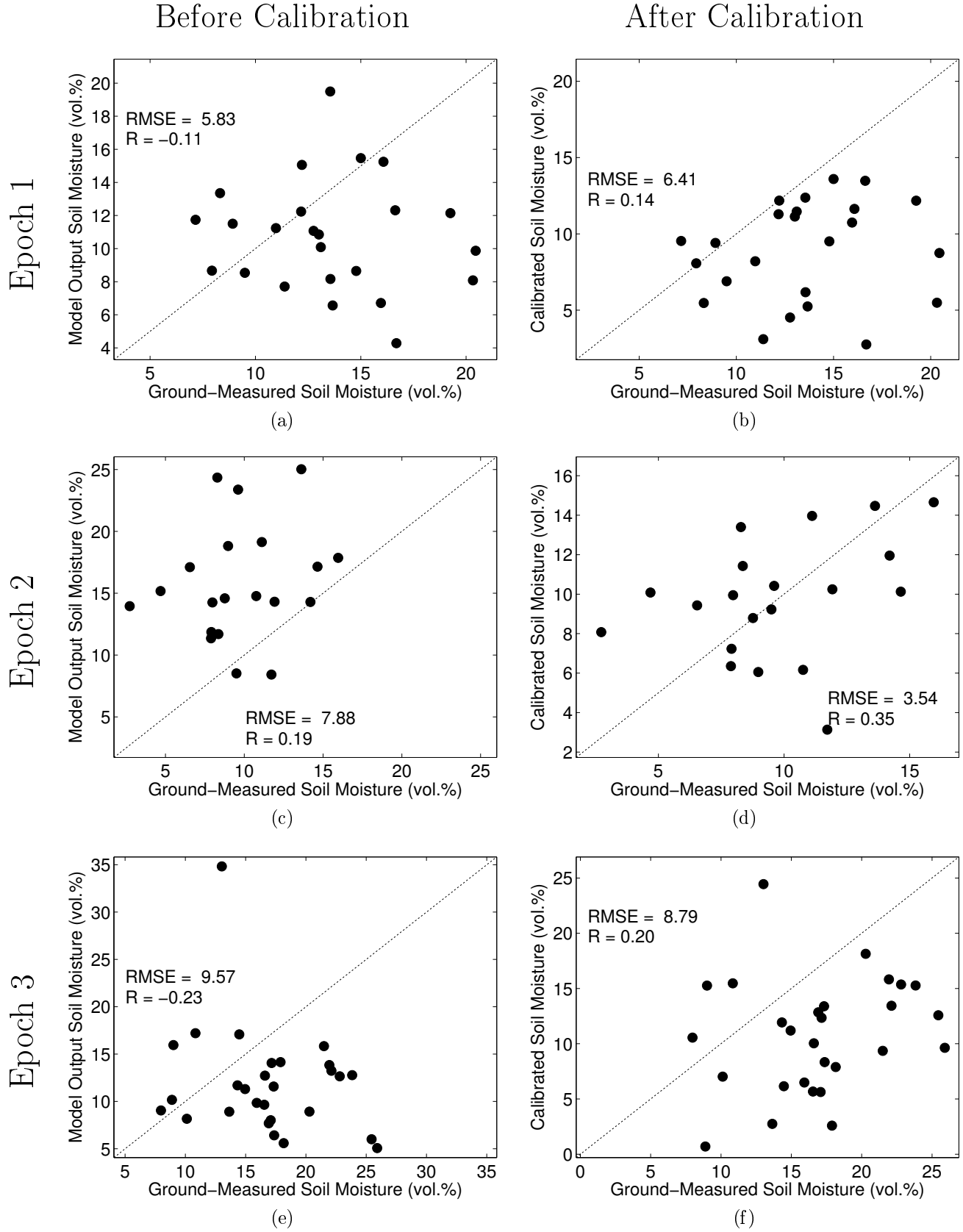

Figure 6.29: Comparison of the agreement of the SM estimated by the IEM and the ground measurements before and after calibration using the proposed calibration model. Data in Epoch 2 is used to estimate the calibration parameters. RMSE is in vol.%.

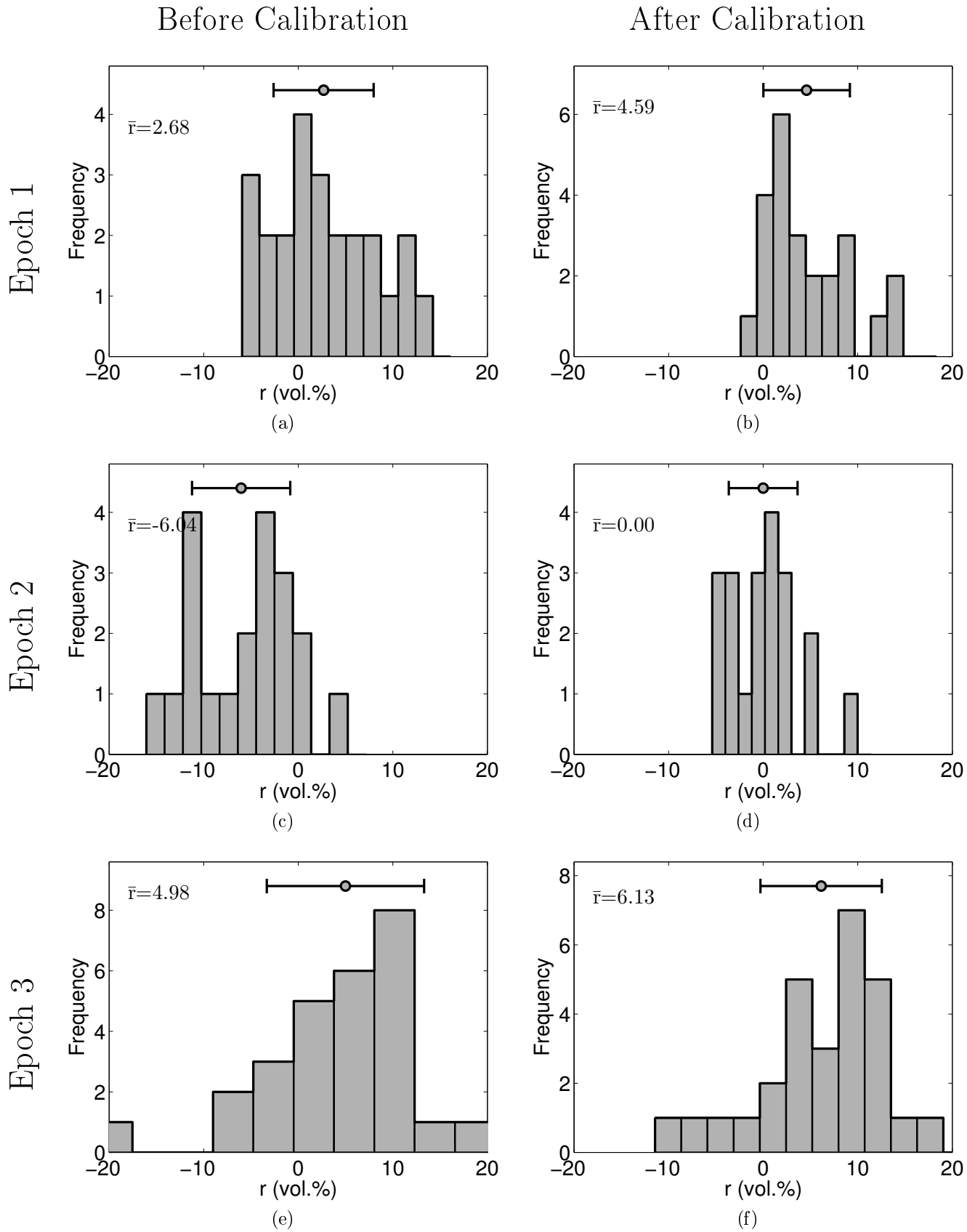

Figure 6.30: Comparison of the histograms of residuals before and after calibration using the proposed calibration model. Data in Epoch 2 is used to estimate the calibration parameters. $\bar{r}$ is the average residual in vol.%.

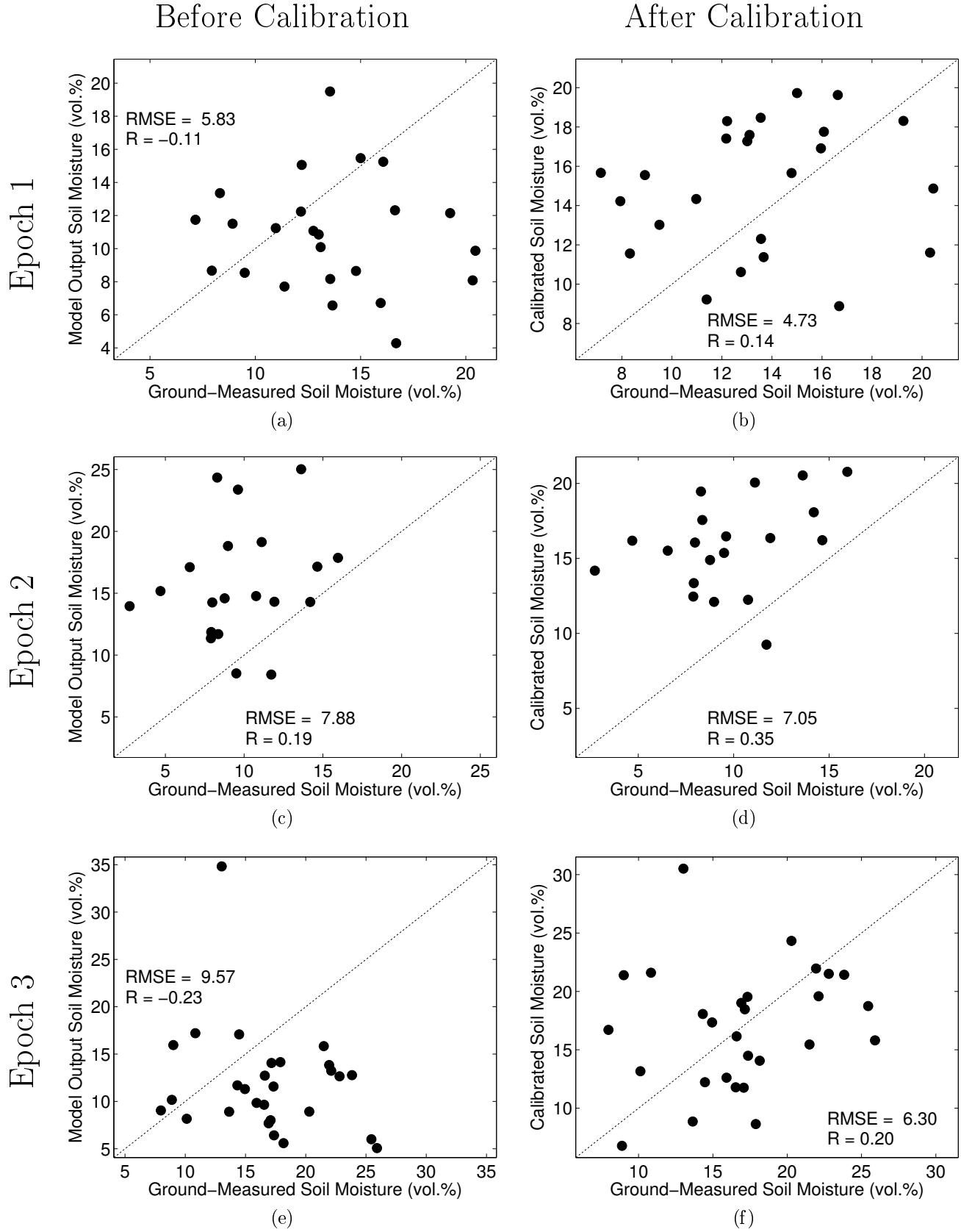

Figure 6.31: Comparison of the agreement of the SM estimated by the IEM and the ground measurements before and after calibration using the proposed calibration model. Data in Epoch 3 is used to estimate the calibration parameters. RMSE is in vol.%.

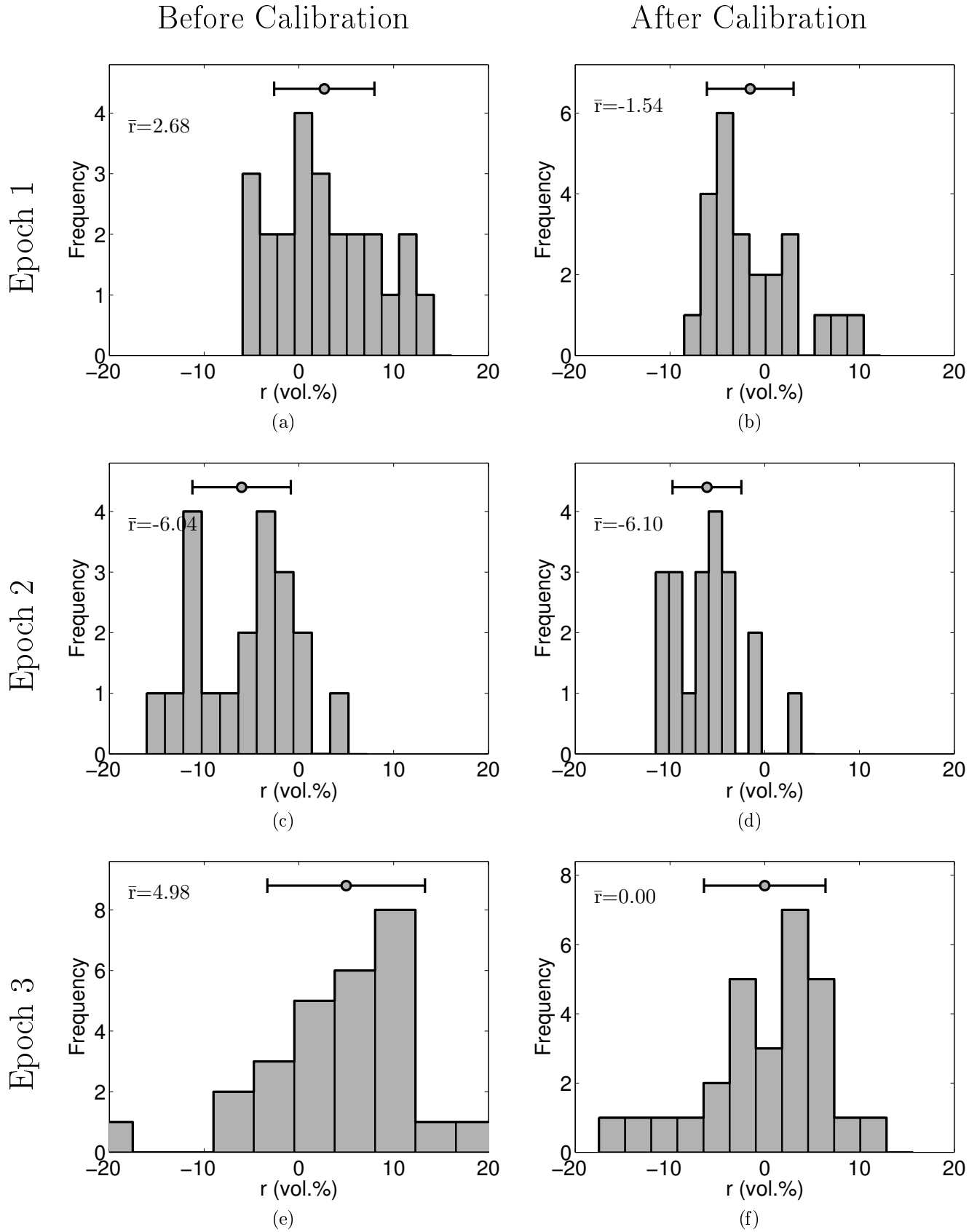

Figure 6.32: Comparison of the histograms of residuals before and after calibration using the proposed calibration model. Data in Epoch 3 is used to estimate the calibration parameters. $\bar{r}$ is the average residual in vol.%.

Table 6.19: The effect of applying the calibration model on different epochs of data: RMSE and $\bar{r}$ are in vol.%.

Reference Epoch	Parameters	Evaluation Epoch	Before Calibration	After Calibration
Epoch 1	Reference β=0.9034 Calib. Eq.: $r = -1.4589c + 12.5639$ R=-0.50	Epoch 1	RMSE= 5.83	RMSE= 4.48
			R= -0.11	R= 0.14
			$\bar{r}$= -2.68	$\bar{r}$= 0.00
		Epoch 2	RMSE= 7.88	RMSE= 5.89
			R= 0.19	R= 0.35
			$\bar{r}$= 6.04	$\bar{r}$= 4.71
		Epoch 3	RMSE= 9.57	RMSE= 6.49
			R= -0.23	R= 0.19
			$\bar{r}$= -4.98	$\bar{r}$= -1.56
Epoch 2	Reference β=0.8313 Calib. Eq.: $r =: -4.2155c + 17.5887$ R=-0.71	Epoch 1	RMSE= 5.83	RMSE= 6.41
			R= -0.11	R= 0.14
			$\bar{r}$= -2.68	$\bar{r}$= -4.59
		Epoch 2	RMSE= 7.88	RMSE= 3.54
			R= 0.19	R= 0.35
			$\bar{r}$= 6.04	$\bar{r}$= -0.00
		Epoch 3	RMSE= 9.57	RMSE= 8.79
			R= -0.23	R= 0.20
			$\bar{r}$= -4.98	$\bar{r}$= -6.13
Epoch 3	Reference β=0.9262 Calib. Eq.: $r = -0.9054c + 11.5761$ R=-0.64	Epoch 1	RMSE= 5.83	RMSE= 4.73
			R= -0.11	R= 0.14
			$\bar{r}$= -2.68	$\bar{r}$= 1.54
		Epoch 2	RMSE= 7.88	RMSE= 7.05
			R= 0.19	R= 0.35
			$\bar{r}$= 6.04	$\bar{r}$= 6.10
		Epoch 3	RMSE= 9.57	RMSE= 6.30
			R= -0.23	R= 0.20
			$\bar{r}$= -4.98	$\bar{r}$= -0.00

clear. Our experiments with different regional β values reveal that the improvements made by the calibration model in final results do not depend on the value of the regional β. Even for $\beta = 0$, which is the lower bound of β, very similar results to what presented in Table 6.19 are obtained. For $\beta = 0$, the STRAIN model converts to a monofractal model. We already saw that c was related to the coefficient of variation. Since for a fixed β the lines fitted to the values of c and residuals are moderately close (see figures 6.24 to 6.26), it seems that a fixed level of variability, i.e. a fixed c, may be expected for all the sites in the area. So that, as c calculated from the outputs of the IEM approaches this fixed c, the difference between the SM estimated by the IEM and the one observed in the field vanishes. However, determining the physical or mathematical bases for the relationship between the values of c and the residuals needs more investigation, and can be the subject of a future study.

It should be noted that filtering the images for decreasing speckle affects the variability of the backscattering coefficient. Thus, the variability observed for the outputs of the IEM are connected to both the variability of SM and the effect of speckle filtering. In other words, the parameter c calculated for each site reflects the combined fractal properties of SM values and speckle filtering. Therefore, changing the size of the window used in speckle filtering can, in general, change the parameters of the calibration model proposed here. Separating the effect of variations in SM and speckle filtering, and investigating the effect of size of speckle filter window on the parameters of the calibration model does not seem trivial, and can be the subject of a future study.

We conclude this chapter by mentioning some of the factors that can cause inaccuracies in the performance of the calibration model:

- The size of the image windows used for multifractal analysis in this study was 16×16 pixels. The dimensions of the windows were selected based on the fact that a 16×16 pixel window is the smallest window of size $2^n \times 2^n$ which can cover a 10×10 pixel field site. Thus, the values of parameter c were estimated

for the 16×16 pixel windows, whereas the size of field sites was 10×10 pixels. The difference in the size of the analysis windows and field sites was inevitable in our study, as the analysis window has to be $2^n \times 2^n$ pixels for our multifractal analysis. Since the c values calculated for the 16×16 pixel windows are then used to calibrate the SM values of 10×10 pixel sites, this can cause inaccuracies in the calibration model.

- Any environmental factor affecting the estimation of SM by the IEM, such as freeze and precipitation at the time of image acquisition, can result in changes in parameter c, and, thus, in estimation of the parameters of the calibration model.

- Possible low inversion rate of the IEM for some of the sites can affect the accuracy of estimation of the parameters of the STRAIN model. Because, as already mentioned, 3% of missing pixels can cause an error of about 1% in estimation of the mass exponent function in the fractal analysis, and this function is later used in estimation of the parameter c.

- Differences in the times of ground measurements and image acquisition can cause inaccuracies in comparison of the ground measurements to SM estimated by the IEM. This can result in errors in fitting a line to values of c and residuals.

Chapter 7

Conclusions

Four SAR surface scattering models (X-Bragg, Oh, Dubois and IEM) were implemented using three epochs of Radarsat-2 C-band data for estimation of SM, and their outputs were compared with field measurements of SM over bare soil surfaces in Manitoba, Canada, collected concurrent with the image acquisitions. We compared the site averaged model predictions with site averaged measurements and assessed the performance of the models using correlation coefficient and RMSE measures which show the prediction-observation agreement. The percentage of pixels inverted by the X-Bragg, Oh and Dubois models were low compared to the IEM. Because of the very low inversion rate of the X-Bragg model for our data set, it was difficult to compare its outputs with the ground measurements. The Oh model had the best performance in terms of the RMSE measure. However, both the Oh and the Dubois models produce patchy outputs with large gaps, which makes it difficult to interpret performance measures for them. The IEM could, on average, invert more than 97% of pixels in each site. A power index of 2, among the power indices examined, was also determined to generate the best surface correlation function for using with the IEM in our study area.

Our main objective was to study the feasibility of using the spatial variability analysis of ground measurements and SAR backscattering model outputs to improve the quality of the outputs of these models. Multifractal analysis, which is a multi-scale method, was found useful for investigating the spatial variability of the data. However, since this type of analysis does not perform well in presence of missing data, it could only be used for analyzing the outputs of the IEM.

Multifractal analysis of the ground measurements using the STRAIN model yielded two

parameters, β and c, for each site. Parameter β had less variations compared to the parameter c. Thus, a regional fixed value was assumed for β which gave us the opportunity to characterize the variability of SM in each site using a single parameter c.

Analyzing the output of the IEM by the STRAIN model using the regional value of β revealed that there was good correlation between the values estimated for the parameter c for SM estimated by the IEM in each site, and the residuals of the model calculated by comparing the IEM outputs with ground measurements of that site. This correlation was used to establish a linear calibration model to alleviate the error in the outputs of the IEM for each site.

The proposed model is an empirical model which can be used in a post-processing step for increasing the agreement between model-estimated and ground-measured SM, i.e. it can be used after the inversion procedure of the IEM is complete and average values of SM for $2^n \times 2^n$ image windows are calculated. The two parameters of the linear calibration model has to be estimated using a comparison of SAR backscattering model outputs for a SAR image and ground measurements coincident with the acquisition of the SAR image. Therefore, it needs at least one epoch of concurrent image acquisition and field data collection. However, according to our experiments, the calibration model is, to some degree, independent of the data used for estimating its parameters.

Comparing the performance measures before and after calibration showed that the proposed calibration model could always improve the correlation coefficient for our data set. The RMSE and bias were not always improved, but when Epoch 1 was used as the reference epoch for estimating the parameters of calibration model, improvements in RMSE were larger than the precision of field-measured SM averages, suggesting that the improvement was meaningful. The data in Epoch 2 were found to establish the least useful calibration model.

One disadvantage of using the proposed calibration model is that, it increases the pixel

size of the outputs of the IEM. For example, if a 16×16 pixel window is used in the multifractal analysis of the outputs of the IEM, the outputs of the calibration model will have pixel dimensions 16 times the original pixel dimensions of the SAR image. However, using a fairly strong correlation observed between the parameter c and the coefficient of variation of SM estimated by the IEM in each site, the SM values upscaled by the calibration model may be downscaled by the algorithms available in the literature such as the one explained in (Mascaro et al., 2010). Processing the image using overlapping $2^n \times 2^n$ windows and applying constraints based on the relative location of these windows may also help in improving the results of the calibration model.

Unfortunately, the data used in this study were limited to three epochs of data for a single study area. Thus, a comprehensive analysis of the calibration model for different dates, locations and soil conditions was not possible. The calibration model may be extensible to other study areas, but, much more concurrent ground measurements and SAR images are needed to examine the reliability of the proposed calibration model and its extensibility to other regions of the world. Also, speckle filtering and change of incidence angle are two factors which may affect the calibration parameters, and quantifying their effect on the calibration model needs more investigation.

The calibration model proposed in this study is a simple linear model which was fit to a small number of data points. More complex models established by, for example, Support Vector Machines may be used for this purpose if more data is available.

Appendix A

Bootstrapping for Estimation of Confidence Interval of Mean

Bootstrapping is a method for estimation of the sampling distribution of a statistic defined on a random sample (Efron, 1979). Bootstrapping is a nonparametric method which makes it applicable for samples from unknown probability distributions. The method can be used to estimate the confidence interval of, for example, mean value of measurements of a random variable (Efron, 1981). There are several types of bootstrapping techniques for estimating a confidence interval (Efron et al., 1994), but the one used in this study is the basic *percentile method*, which is easy to implement and fast to run.

Assume that we have N samples, X_1, X_2, ..., X_N, of a random variable R with an unknown probability distribution. Also, assume that we calculate $\hat{\theta}$ the sample statistic of statistic θ, and that estimating the $100(1-2\alpha)\%$ confidence interval for $\hat{\theta}$ is desired. According to basic percentile bootstrapping method, the steps for calculation of the confidence interval are (Efron, 1981):

1. Sample with replacement N of X_i's:

$$\theta^* = (X_1^*, X_2^*, ..., X_N^*) \tag{A.1}$$

   This is called a *bootstrap sample*.

2. Calculate $\hat{\theta}^*$ using the bootstrap sample created in previous step:

$$\hat{\theta}^* = \hat{\theta}(X_1^*, X_2^*, ..., X_N^*) \tag{A.2}$$

3. Repeat the previous steps B times independently to obtain $\hat{\theta}_1^*$, $\hat{\theta}_2^*$, ..., $\hat{\theta}_B^*$.

4. Let $\widehat{CDF}(t)$ be the cumulative distribution function of $\hat{\theta}_b^*$'s, formed by B bootstrap samples:

$$\widehat{CDF}(t) = \text{Prob}\{\hat{\theta}^* < t\} = \frac{\#\{\hat{\theta}_b^* < t\}}{B} \tag{A.3}$$

where $\#\{\hat{\theta}_b^* < t\}$ is the number of all $\hat{\theta}_b^*$'s that are less than t. Then the $100(1-2\alpha)\%$ confidence interval for $\hat{\theta}$ is calculated as

$$\hat{\theta} \in \left[\widehat{CDF}^{-1}(\alpha), \widehat{CDF}^{-1}(1-\alpha)\right] \tag{A.4}$$

B is set to a large number, for example 1000. As mentioned above, this is a basic bootstraping technique for estimation of confidence intervals. For other types of bootstrapping techniques proposed for this purpose, for example *bias-corrected percentile method*, reader can refer to (Efron et al., 1994).

Appendix B

Matlab Code for Calculation of the Parameters of The STRAIN Multifractal Model

STRAIN two-parameter multifractal model is the primary tool used in this study to analyze SM field measurements and outputs of SAR backscattering models. Function `STRAIN` in Listing B.1 shows how parameters β and c of this model can be estimated using Matlab. The function accepts two parameters, `Data` and `Resolution`, which are the working image and it's resolution, and outputs the parameters of the STRAIN model fitted to `Data`.

Listing B.1: The function used to calculate parameters β and c in the STRAIN multifractal model for soil moisture

```
1
2  function [Beta, c] = STRAIN(Data, Resolution)
3      WinSize = size(Data, 1);
4      NoLevels = log2(WinSize)+1;
5      CurveData = [];
6
7      for q = 2 : 6  % Loop over all exponents
8          LineData = [];
9          for Level = 1 : NoLevels % Loop over all pyramid levels
10             Scale = 2^(Level-1);
11             MaxCoord = WinSize / Scale;
12             Lambda = Resolution * Scale;
13             LogLambda = log(Lambda);
14             Sq = 0;
15             cnt = 0;
```

```
16
17              % Create partition function
18              for r=1:MaxCoord
19                  for c=1:MaxCoord
20                      r1 = (r-1)*Scale+1; r2 = r1+Scale-1;
21                      c1 = (c-1)*Scale+1; c2 = c1+Scale-1;
22
23                      % Create pixel (r,c) in current pyramid level
24                      CoarsePix = Data(r1:r2,c1:c2);
25                      aux = mean(CoarsePix(~isnan(CoarsePix)));
26                      if isnan(aux)
27                          continue;
28                      end
29                      Sq = Sq + aux ^ q;
30                      cnt = cnt+1;
31                  end
32              end
33              Sq = Sq / cnt;
34              LineData = [LineData; LogLambda , log(Sq)];
35          end
36          p = polyfit(LineData(:,1), LineData(:,2), 1);
37          CurveData = [CurveData; q, p(1), p(2)];
38      end
39
40      % Run SQP to fit STRAIN model to data
41      options = optimset('Display', 'off', ...
42                         'MaxFunEvals', 1000, ...
43                         'Algorithm', 'sqp');
```

```
44
45      [OptimX, fval] = fmincon(@Cost_Func, [0 0], ...
46                               [], [], [], [], ...
47                               [0 0], [1 50], [], options);
48
49      Beta = OptimX(1); c = OptimX(2);
50  return
51
52  function Cost = Cost_Func(X)
53      Cost=[];
54      for ii=1:size(CurveData,1)
55          Cost = [Cost;
56                  abs((-X(2) * (CurveData(ii,1)*(1-X(1))- ...
57                  (1-X(1)^CurveData(ii,1))), ...
58                  / log(2)) - CurveData(ii,2))];
59      end
60      Cost = norm(Cost);
61  end % End of Cost_Func
62
63  end % End of main function
```

Bibliography

Adamchuk, V. I., R. B. Ferguson, and G. W. Hergert (2010). "Soil heterogeneity and crop growth". In: *Precision Crop Protection - the Challenge and Use of Heterogeneity*. Ed. by E.-C. Oerke, R. Gerhards, G. Menz, and R. A. Sikora. Dordrecht, Netherlands: Springer Netherlands, pp. 3–16.

Adams, J. R., A. A. Berg, and H. McNairn (2013). "Field level soil moisture variability at 6- and 3-cm sampling depths: implications for microwave sensor validation". In: *Vadose Zone Journal* 12.3.

Adelson, E. H., C. H. Anderson, J. R. Bergen, P. J. Burt, and J. M. Ogden (1984). "Pyramid methods in image processing". In: *RCA Engineer* 29.6, pp. 33–41.

Altese, E., O. Bolognani, M. Mancini, and P. A. Troch (1996). "Retrieving soil moisture over bare soil from ERS 1 synthetic aperture radar data: sensitivity analysis based on a theoretical surface scattering model and field data". In: *Water Resources Research* 32.3, pp. 653–661.

Alvarez-Mozos, J., M. Gonzalez-Audícana, and J. Casalí (2007). "Evaluation of empirical and semi-empirical backscattering models for surface soil moisture estimation". In: *Canadian Journal of Remote Sensing* 33.3, pp. 176–188.

Álvarez-Pérez, J. L. (2001). "An extension of the IEM/IEMM surface scattering model". In: *Waves in Random Media* 11.3, pp. 307–329.

Alvera-Azcárate, A., A. Barth, M. Rixen, and J. Beckers (2005). "Reconstruction of incomplete oceanographic data sets using empirical orthogonal functions: application to the Adriatic Sea surface temperature". In: *Ocean Modelling* 9.4, pp. 325–346.

Anantharaj, A., G. Mostovoy, and P. J. Fitzpatrick (2008). "Impact of soil moisture initialization on numerical weather forecasting over the Mississippi Delta region". In: *88th Annual Meeting of the American Meteorological Society*. (New Orleans, LA, USA).

Anderson, K. and H. Croft (2009). "Remote sensing of soil surface properties". In: *Progress in Physical Geography* 33.4, pp. 457–473.

Aouit, D. A. and A. Ouahabi (2009). "Wavelet-based multifractal identification of fracture stages". In: *Damage and Fracture Mechanics*. Ed. by T. Boukharouba, M. Elboujdaini, and G. Pluvinage. Dordrecht, Netherlands: Springer Netherlands, pp. 513–522.

Atkins, P. W. and J. De Paula (2006). *Atkins' Physical Chemistry*. Oxford, UK; New York, NY, USA: Oxford University Press.

Baghdadi, N., P. Paillou, G. Grandjean, P. Dubois, and M Davidson (2000). "Relationship between profile length and roughness variables for natural surfaces". In: *International Journal of Remote Sensing* 21.17, pp. 3375–3381.

Baghdadi, N., C. King, A. Chanzy, and J. P. Wigneron (2002). "An empirical calibration of the integral equation model based on SAR data, soil moisture and surface roughness measurement over bare soils". In: *International Journal of Remote Sensing* 23.20, pp. 4325–4340.

Baghdadi, N., I. Gherboudj, M. Zribi, M. Sahebi, C. King, and F. Bonn (2004). "Semi-empirical calibration of the IEM backscattering model using radar images and moisture and roughness field measurements". In: *International Journal of Remote Sensing* 25.18, pp. 3593–3623.

Baghdadi, N., N. Holah, and M. Zribi (2006a). "Calibration of the Integral Equation Model for SAR data in C-band and HH and VV polarizations". In: *International Journal of Remote Sensing* 27.4, pp. 805–816.

Baghdadi, N. and M. Zribi (2006b). "Evaluation of radar backscatter models IEM, Oh and Dubois using experimental observations". In: *International Journal of Remote Sensing* 27.18, pp. 3831–3852.

Baghdadi, N., J. Chaaya, and M. Zribi (2011). "Semiempirical calibration of the Integral Equation Model for SAR data in C-band and cross polarization using radar images and field measurements". In: *IEEE Geoscience and Remote Sensing Letters* 8.1, pp. 14–18.

Barrett, B., E. Dwyer, and P. Whelan (2009). "Soil moisture retrieval from active spaceborne microwave observations: an evaluation of current techniques". In: *Remote Sensing* 1.3, pp. 210–242.

Behari, J. (2005). *Microwave Dielectric Behavior of Wet Soils*. New York, NY, USA: Springer.

Bell, K. R., B. J. Blanchard, T. J. Schmugge, and M. W. Witczak (1980). "Analysis of surface moisture variations within large-field sites". In: *Water Resources Research* 16.4, pp. 796–810.

Biftu, G. and T. Gan (1999). "Retrieving near-surface soil moisture from Radarsat SAR data". In: *Water Resources Research* 35.5, pp. 1569–1579.

Bindlish, R. (2000). "Active and passive microwave remote sensing of soil moisture". PhD thesis. The Pennsylvania State University, State College, PA, USA.

Biswas, A., T. B. Zeleke, and B. C. Si (2012a). "Multifractal detrended fluctuation analysis in examining scaling properties of the spatial patterns of soil water storage". In: *Nonlinear Processes in Geophysics* 19.2, pp. 227–238.

Biswas, A., H. P. Cresswell, and C. S. Bing (2012b). "Application of multifractal and joint multifractal analysis in examining soil spatial variation: a review". In: *Fractal Analysis and Chaos in Geosciences*. Ed. by S.-A. Ouadfeul. InTech. Chap. 6.

Bloschl, G. and M. Sivapalan (1995). "Scale issues in hydrological modeling: a review". In: *Hydrological Processes* 9.3-4, pp. 251–290.

Boggs, P. T. and J. W. Tolle (1995). "Sequential quadratic programming". In: *Acta Numerica* 4.2, pp. 1–51.

Brocca, L., R. Morbidelli, F. Melone, and T. Moramarco (2007). "Soil moisture spatial variability in experimental areas of central Italy". In: *Journal of Hydrology* 333.2, pp. 356–373.

Brocca, L., F. Melone, T. Moramarco, and R. Morbidelli (2009). "Soil moisture temporal stability over experimental areas in central Italy". In: *Geoderma* 148.3, pp. 364–374.

Brocca, L., F. Melone, T. Moramarco, and R. Morbidelli (2010). "Spatial-temporal variability of soil moisture and its estimation across scales". In: *Water Resources Research* 46.2, W02516.

Bruckler, L., H. Witono, and P. Stengel (1988). "Near surface soil moisture estimation from microwave measurements". In: *Remote Sensing of Environment* 26.2, pp. 101–121.

Bryant, R., D. Thoma, S. Moran, C. Holifield, D. Goodrich, T. Keefer, G. Paige, D. Williams, and S. Skirvin (2003). "Evaluation of hyperspectral, infrared temperature and radar measurements for monitoring surface soil moisture". In: *Proceedings of the First Interagency Conference on Research in the Watersheds*. (Benson, AZ, USA). Ed. by K. G. Renard, S. A. McElroy, W. J. Gburek, H. E. Canfield, and R. L. Scott. U.S. Department of Agriculture, Agricultural Research Service, pp. 27–30.

Burt, P. and E. Adelson (1983). "The Laplacian pyramid as a compact image code". In: *IEEE Transactions on Communications* 31.4, pp. 532–540.

Cantón, Y., A. Solé-Benet, and F. Domingo (2004). "Temporal and spatial patterns of soil moisture in semiarid badlands of SE spain". In: *Journal of Hydrology* 285.1, pp. 199–214.

Carlson, T. (2007). "An overview of the "triangle method" for estimating surface evapotranspiration and soil moisture from satellite imagery". In: *Sensors* 7.8, pp. 1612–1629.

Carlson, T. N., R. R. Gillies, and T. J. Schmugge (1995). "An interpretation of methodologies for indirect measurement of soil water content". In: *Agricultural and Forest Meteorology* 77.3, pp. 191–205.

Chanasyk, D. S. and M. A Naeth (1996). "Field measurement of soil moisture using neutron probes". In: *Canadian Journal of Soil Science* 76.3, pp. 317–323.

Chauhan, N. S., S. Miller, and P. Ardanuy (2003). "Spaceborne soil moisture estimation at high resolution: a microwave-optical/IR synergistic approach". In: *International Journal of Remote Sensing* 24.22, pp. 4599–4622.

Chen, K., W. Kao, and Y. Tzeng (1995). "Retrieval of surface parameters using dynamic learning neural network". In: *International Journal of Remote Sensing* 16.5, pp. 801–809.

Chen, K., T.-D. Wu, L. Tsang, Q. Li, J. Shi, and A. Fung (2003). "Emission of rough surfaces calculated by the integral equation method with comparison to three-dimensional moment method simulations". In: *IEEE Transactions on Geoscience and Remote Sensing* 41.1, pp. 90–101.

Choudhury, B. J., T. J. Schmugge, A. Chang, and R. W. Newton (1979). "Effect of surface roughness on the microwave emission from soils". In: *Journal of Geophysical Research* 84.C9, pp. 5699–5706.

Chudinova, S. M. (2009). "Dielectric characteristics of soils and categories of soil water". In: *Eurasian Soil Science* 42.4, pp. 405–414.

Cloude, S. and E. Pottier (1996). "A review of target decomposition theorems in radar polarimetry". In: *IEEE Transactions on Geoscience and Remote Sensing* 34.2, pp. 498–518.

Dalton, F. N. and M. T. V. Genuchten (1986). "The time-domain reflectometry method for measuring soil water content and salinity". In: *Geoderma* 38.1-4, pp. 237–250.

Daya Sagar, B., G. Rangarajan, and D. Veneziano (2004). "Fractals in geophysics". In: *Chaos, Solitons & Fractals* 19.2, pp. 237–239.

Dean, T., J. Bell, and A. Baty (1987). "Soil moisture measurement by an improved capacitance technique, part i. sensor design and performance". In: *Journal of Hydrology* 93.1, pp. 67–78.

Deb, K. (2001). *Multi-Objective Optimization using Evolutionary Algorithms*. Chichester, UK; New York, NY, USA: John Wiley & Sons.

Deidda, R (1997). "Simulazione numerica delle proprieta' statistiche dei campi di precipitazione". PhD thesis. University of Padua, Padua, Italy.

Deidda, R. (2000). "Rainfall downscaling in a space-time multifractal framework". In: *Water Resources Research* 36.7, pp. 1779–1794.

Deidda, R., R. Benzi, and F. Siccardi (1999). "Multifractal modeling of anomalous scaling laws in rainfall". In: *Water Resources Research* 35.6, pp. 1853–1867.

Deidda, R., M. G. Badas, and E. Piga (2004). "Space-time scaling in high-intensity Tropical Ocean Global Atmosphere Coupled Ocean-Atmosphere Response Experiment (TOGA-COARE) storms". In: *Water Resources Research* 40.2, W02056.

Dente, L., Z. Su, and J. Wen (2012). "Validation of SMOS soil moisture products over the Maqu and Twente regions". In: *Sensors* 12.8, pp. 9965–9986.

Diwekar, U. M. (2008). *Introduction to Applied Optimization*. New York, NY, USA: Springer.

Dobson, M., F. Ulaby, M. Hallikainen, and M. El-Rayes (1985). "Microwave dielectric behavior of wet soil-part II: dielectric mixing models". In: *IEEE Transactions on Geoscience and Remote Sensing* GE-23.1, pp. 35–46.

Dorigo, M., V. Maniezzo, and A. Colorni (1996). "Ant system: optimization by a colony of cooperating agents." In: *IEEE Transactions on Systems, Man, and Cybernetics. Part B, Cybernetics* 26.1, pp. 29–41.

Dubois, P., J. van Zyl, and T. Engman (1995). "Measuring soil moisture with imaging radars". In: *IEEE Transactions on Geoscience and Remote Sensing* 33.4, pp. 915–926.

Efron, B. (1979). "Bootstrap methods: another look at the jackknife". In: *The Annals of Statistics* 7.1, pp. 1–26.

Efron, B. (1981). "Nonparametric standard errors and confidence intervals". In: *The Canadian Journal of Statistics / La Revue Canadienne de Statistique* 9.2, pp. 139–158.

Efron, B. and R. Tibshirani (1994). *An Introduction to the Bootstrap*. New York, NY, USA: Chapman & Hall.

Eghball, B., L. N. Mielke, G. A. Calvo, and W. W. Wilhelm (1993). "Fractal description of soil fragmentation for various tillage methods and crop sequences". In: *Soil Science Society of America Journal* 57.5, pp. 1337–1341.

Emerson, C. W., D. A. Quattrochi, and N. S.-N. Lam (2004). "Spatial metadata for remote sensing imagery". In: *NASA's Earth Science Technology Conference*. (Palo Alto, CA, USA). NASA.

Engman, E. T. and N. Chauhan (1995). "Status of microwave soil moisture measurements with remote sensing". In: *Remote Sensing of Environment* 51.1, pp. 189–198.

Entekhabi, D. and P. S. Eagleson (1989). "Land surface hydrology parameterization for atmospheric general circulation models including subgrid scale spatial variability". In: *Journal of Climate* 2.8, pp. 816–831.

Entekhabi, D., R. H. Reichle, R. D. Koster, and C. W. T. (2010). "Performance metrics for soil moisture retrievals and application requirements". In: *Journal of Hydrometeorology* 11.3, pp. 832–840.

Environment Canada (2013). *National Climate Data and Information Archive*. Last accessed Jan. 3, 2013. URL: `http://climate.weatheroffice.gc.ca/climateData/canada_e.html`.

Escorihuela, M. J., A. Chanzy, J. P. Wigneron, and K. Y.H. (2010). "Effective soil moisture sampling depth of L-band radiometry: a case study". In: *Remote Sensing of Environment* 114.5, pp. 995–1001.

European Space Agency (2011). *The Polarimetric SAR Data Processing and Educational Tool*. Last accessed Oct. 22, 2013. URL: `http://earth.eo.esa.int/polsarpro`.

Famiglietti, J. S., J. A. Devereaux, C. A. Laymon, T. Tsegaye, P. R. Houser, T. J. Jackson, S. T. Graham, M. Rodell, and P. J. van Oevelen (1999). "Ground-based investigation of soil

moisture variability within remote sensing footprints during the southern Great Plains 1997 (SGP97) hydrology experiment". In: *Water Resources Research* 35.6, pp. 1839–1851.

Famiglietti, J. S., D. Ryu, A. A. Berg, M. Rodell, and T. J. Jackson (2008). "Field observations of soil moisture variability across scales". In: *Water Resources Research* 44.1, W01423.

Fannin, P., S. Charles, D. Vincent, and A. Giannitsis (2002). "Measurement of the high-frequency complex permittivity and conductivity of magnetic fluids". In: *Journal of Magnetism and Magnetic Materials* 252.1, pp. 80–82.

Fung, A. K. (1994). *Microwave Scattering and Emission Models and Their Applications*. Boston, MA, USA: Artech House.

Fung, A., Z. Li, and K. Chen (1992). "Backscattering from a randomly rough dielectric surface". In: *IEEE Transactions on Geoscience and Remote Sensing* 30.2, pp. 356–369.

Fung, A., K. Chen, A. Hsu, E. Engman, P. O'Neill, and J. Wang (1996). "A modified IEM model for scattering from soil surfaces with application to soil moisture sensing". In: *Proceedings of the IEEE International Geoscience and Remote Sensing Symposium (IGARSS)*. (Lincoln, NE, USA). Vol. 2. IEEE, pp. 1297–1299.

Fung, A., W. Liu, K. Chen, and M. Tsay (2002). "An improved IEM model for bistatic scattering from rough surfaces". In: *Journal of Electromagnetic Waves and Applications* 16.5, pp. 689–702.

Fung, A. and K. Chen (2004). "An update on the IEM surface backscattering model". In: *IEEE Geoscience and Remote Sensing Letters* 1.2, pp. 75–77.

Garcia, D. (2010). "Robust smoothing of gridded data in one and higher dimensions with missing values". In: *Computational Statistics & Data Analysis* 54.4, pp. 1167–1178.

Ghosh, J. and A. Singh (2008). "Fractal compression of satellite images". In: *Journal of the Indian Society of Remote Sensing* 36.4, pp. 299–311.

Gill, P. E., W. Murray, M. A. Saunders, and M. H. Wright (1984). "Procedures for optimization problems with a mixture of bounds and general linear constraints". In: *ACM Transactions on Mathematical Software* 10.3, pp. 282–298.

Giorgi, F. and R. Avissar (1997). "Representation of heterogeneity effects in earth system modeling: experience from land surface modeling". In: *Reviews of Geophysics* 35.4, pp. 413–437.

Goward, S. N., Y. Xue, and K. P. Czajkowski (2002). "Evaluating land surface moisture conditions from the remotely sensed temperature/vegetation index measurements: an exploration with the simplified simple biosphere model". In: *Remote Sensing of Environment* 79.2, pp. 225–242.

Graf, A., N. Prolingheuer, A. Schickling, M. Schmidt, K. Schneider, D. Schüttemeyer, M. Herbst, J. A. Huisman, L. Weihermüller, B. Scharnagl, C. Steenpass, R. Harms, and H. Vereecken (2011). "Temporal downscaling of soil carbon dioxide efflux measurements based on time-stable spatial patterns". In: *Vadose Zone Journal* 10.1, pp. 239–251.

Hajnsek, I., E. Pottier, and S. Cloude (2003). "Inversion of surface parameters from polarimetric SAR". In: *IEEE Transactions on Geoscience and Remote Sensing* 41.4, pp. 727–744.

Hajnsek, I., T. Jagdhuber, H. Schon, and K. Papathanassiou (2009). "Potential of estimating soil moisture under vegetation cover by means of PolSAR". In: *IEEE Transactions on Geoscience and Remote Sensing* 47.2, pp. 442–454.

Hajnsek, I. (2001). "Inversion of Surface Parameters using Polarimetric SAR". PhD thesis. Friedrich-Schiller University, Jena, Germany.

Hallikainen, M., F. Ulaby, M. Dobson, M. El-rayes, and L.-K. Wu (1985). "Microwave dielectric behavior of wet soil-Part 1: empirical models and experimental observations". In: *IEEE Transactions on Geoscience and Remote Sensing* 23.1, pp. 25–34.

Haralick, R., K. Shanmugam, and I. Dinstein (1973). "Textural features for image classification". In: *IEEE Transactions on Systems, Man and Cybernetics* SMC-3.6, pp. 610–621.

Hartigan, J. A. and P. M. Hartigan (1985). "The dip test of unimodality". In: *The Annals of Statistics* 13.1, pp. 70–84.

Haubrock, S. N., S. Chabrillat, C. Lemmnitz, and H. Kaufmann (2008). "Surface soil moisture quantification models from reflectance data under field conditions". In: *International Journal of Remote Sensing* 29.1, pp. 3–29.

Hébrard, O., M. Voltz, P. Andrieux, and R. Moussa (2006). "Spatio-temporal distribution of soil surface moisture in a heterogeneously farmed Mediterranean catchment". In: *Journal of Hydrology* 329.1, pp. 110–121.

Heathman, G. C., P. J. Starks, L. R. Ahuja, and T. Jackson (2003). "Assimilation of surface soil moisture to estimate profile soil water content". In: *Journal of Hydrology* 279.1-4, pp. 1–17.

Heuvelink, G. B. M. and R. Webster (2001). "Modelling soil variation: past, present, and future". In: *Geoderma* 100.3, pp. 269–301.

Hillel, D., A. W. Warrick, R. S. Baker, and C. Rosenzweig (1998). *Environmental soil physics.* San Diego, CA: Academic Press.

Hollinger, J., J. Peirce, and G. Poe (1990). "SSM/I instrument evaluation". In: *IEEE Transactions on Geoscience and Remote Sensing* 28.5, pp. 781–790.

Houser, P. R., W. J. Shuttleworth, J. S. Famiglietti, H. V. Gupta, K. H. Syed, and D. C. Goodrich (1998). "Integration of soil moisture remote sensing and hydrologic modeling using data assimilation". In: *Water Resources Research* 34.12, pp. 3405–3420.

Hsieh, C.-Y., A. K. Fung, G. Nesti, A. J. Sieber, and P. Coppo (1997). "A further study of the IEM surface scattering model". In: *IEEE Transactions on Geoscience and Remote Sensing* 35.4, pp. 901–909.

Hu, W., M. Shao, F. Han, and K. Reichardt (2011). "Spatio-temporal variability behavior of land surface soil water content in shrub- and grass-land". In: *Geoderma* 162.3, pp. 260–272.

Huynen, J. R. (1970). "Phenomenological theory of radar targets." PhD thesis. Technical University of Delft, Delft, Netherlands.

Iikura, Y. and K. Sakuma (1995). "Pyramid linking for satellite image classification". In: *Proceedings of the IEEE International Geoscience and Remote Sensing Symposium (IGARSS)*. (Firenze, Italy). Vol. 3. IEEE, pp. 1693–1695.

Jackson, T. J. (1993). "Measuring surface soil moisture using passive microwave remote sensing". In: *Hydrological Processes* 7.2, pp. 139–152.

Jacobs, J. M., B. P. Mohanty, E.-C. Hsu, and D. Miller (2004). "SMEX02: field scale variability, time stability and similarity of soil moisture". In: *Remote Sensing of Environment* 92.4, pp. 436–446.

Jadoski, S. O., L. C. Sander, and A. Suchoronczek (2009). "Methodology for determining the soil water content based on fractal dimension". In: *Pesquisa Aplicada & Agrotecnologia* 1.1, pp. 150–168.

Jeyaseelan, A. (2003). "Droughts & floods assessment and monitoring using remote sensing and GIS". In: *Proceedings of Satellite Remote Sensing and GIS Applications in Agricultural Meteorology*. (Dehra Dun, India). Ed. by M. Sivakumar, P. Roy, K. Harmsen, and S. Saha. World Meteorological Organization (WMO), pp. 291–313.

Karush, W. (1939). "Minima of Functions of Several Variables with Inequalities as Side Conditions". MA thesis. University of Chicago, Chicago, IL, USA.

Katra, I., D. G. Blumberg, H. Lavee, and P. Sarah (2006). "A method for estimating the spatial distribution of soil moisture of arid microenvironments by close range thermal infrared imaging". In: *International Journal of Remote Sensing* 27.12, pp. 2599–2611.

Kennedy, J. and R. Eberhart (1995). "Particle swarm optimization". In: *Proceedings of the IEEE International Conference on Neural Networks*. (Perth, WA, Australia). Vol. 4. IEEE, pp. 1942–1948.

Kim, G. and A. P. Barros (2002). "Downscaling of remotely sensed soil moisture with a modified fractal interpolation method using contraction mapping and ancillary data". In: *Remote Sensing of Environment* 83.3, pp. 400–413.

Kim, S.-B., L. Tsang, J. Johnson, S. Huang, J. van Zyl, and E. Njoku (2012). "Soil moisture retrieval using time-series radar observations over bare surfaces". In: *IEEE Transactions on Geoscience and Remote Sensing* 50.5, pp. 1853–1863.

Kirkpatrick, S., C. D. Gelatt, and M. P. Vecchi (1983). "Optimization by simulated annealing." In: *Science* 220.4598, pp. 671–680.

Kjeldsen, T. H. (2000). "A contextualized historical analysis of the Kuhn-Tucker theorem in nonlinear programming: the impact of world war II". In: *Historia Mathematica* 27.4, pp. 331–361.

Kuhn, H. W. and A. W. Tucker (1950). "Nonlinear programming". In: *Proceedings of the Second Berkeley Symposium on Mathematical Statistics and Probability*. Ed. by J. Neyman. Berkeley, CA, USA: University of California Press, pp. 481–492.

Kvalseth, T. O. (1985). "Cautionary note about R^2". In: *The American Statistician* 39.4, pp. 279–285.

Laymon, C., W. Crosson, T. Jackson, A. Manu, and T. Tsegaye (2001). "Ground-based passive microwave remote sensing observations of soil moisture at S-band and L-band with insight into measurement accuracy". In: *IEEE Transactions on Geoscience and Remote Sensing* 39.9, pp. 1844–1858.

Le Morvan, A., M. Zribi, N. Baghdadi, and A. Chanzy (2008). "Soil moisture profile effect on radar signal measurement". In: *Sensors* 8.1, pp. 256–270.

Lee, J. S., L. Jurkevich, P. Dewaele, P. Wambacq, and A. Oosterlinck (1994). "Speckle filtering of synthetic aperture radar images: a review". In: *Remote Sensing Reviews* 8.4, pp. 313–340.

Lee, J.-S. (1981). "Refined filtering of image noise using local statistics". In: *Computer Graphics and Image Processing* 15.4, pp. 380–389.

Lee, J.-S. and E. Pottier (2009). *Polarimetric Radar Imaging: From Basics to Applications*. Bocca Raton, FL, USA: CRC Press.

Li, B. and R. Avissar (1994). "The impact of spatial variability of land-surface characteristics on land-surface heat fluxes". In: *Journal of Climate* 7.4, pp. 527–537.

Li, Q., J. Shi, and K. Chen (2002). "A generalized power law spectrum and its applications to the backscattering of soil surfaces based on the integral equation model". In: *IEEE Transactions on Geoscience and Remote Sensing* 40.2, pp. 271–280.

Li, Y. and J.-X. Peng (2003). "Remote sensing texture analysis using multi-parameter and multi-scale features". In: *Photogrammetric Engineering and Remote Sensing* 69.4, pp. 351–356.

Lievens, H., N. Verhoest, E. D. Keyser, H. Vernieuwe, B. D. Baets, P. Matgen, and J. Alvarez-Mozos (2011). "Effective roughness modelling as a tool for soil moisture retrieval from C- and L-band SAR". In: *Hydrology and Earth System Sciences* 15.1, pp. 151–162.

Loew, A. and W. Mauser (2006). "A semi-empirical surface backscattering model for bare soil surfaces based on a generalized power law spectrum approach". In: *IEEE Transactions on Geoscience and Remote Sensing* 44.4, pp. 1022–1035.

Lopes, R. and N. Betrouni (2009). "Fractal and multifractal analysis: a review". In: *Medical Image Analysis* 13.4, pp. 634–649.

Lovejoy, S., A. Tarquis, H. Gaonac'h, and D. Schertzer (2008). "Single- and multiscale remote sensing techniques, multifractals, and MODIS-derived vegetation and soil moisture". In: *Vadose Zone Journal* 7.2, pp. 533–546.

Magagi, R. and Y. Kerr (2001). "Estimating surface soil moisture and soil roughness over semiarid areas from the use of the copolarization ratio". In: *Remote Sensing of Environment* 75.3, pp. 432–445.

Mandelbrot, B. B. (1983). *The Fractal Geometry of Nature*. New York, NY, USA: W.H. Freeman.

Manfreda, S., M. F. McCabe, M. Fiorentino, I. Rodríguez-Iturbe, and E. F. Wood (2007). "Scaling characteristics of spatial patterns of soil moisture from distributed modelling". In: *Advances in Water Resources* 30.10, pp. 2145–2150.

Mascaro, G., E. Vivoni, and R. Deidda (2011). "Soil moisture downscaling across climate regions and its emergent properties". In: *Journal of Geophysical Research* 116.D22, p. D22114.

Mascaro, G., E. R. Vivoni, and R. Deidda (2010). "Downscaling soil moisture in the southern Great Plains through a calibrated multifractal model for land surface modeling applications". In: *Water Resources Research* 46.8, W08546.

Massey, F. J. (1951). "The Kolmogorov-Smirnov test for goodness of fit". In: *Journal of the American Statistical Association* 46.253, pp. 68–78.

MathWorks (n.d.). *Constrained Nonlinear Optimization Algorithms*. Last accessed Oct. 11, 2012. URL: `http://www.mathworks.com/help/optim/ug/constrained-nonlinear-optimization-algorithms.html`.

Mattia, F., G. Satalino, L. Dente, and G. Pasquariello (2006). "Using a priori information to improve soil moisture retrieval from ENVISAT ASAR AP data in semiarid regions". In: *IEEE Transactions on Geoscience and Remote Sensing* 44.4, pp. 900–912.

Mattia, F., G. Satalino, V. R. N. Pauwels, and A. Loew (2009). "Soil moisture retrieval through a merging of multi-temporal L-band SAR data and hydrologic modelling". In: *Hydrology and Earth System Sciences* 13.3, pp. 343–356.

McNairn, H., A. Merzouki, and A. Pacheco (2010). "Estimating surface soil moisture using Radarsat-2". In: *International Archives of the Photogrammetry, Remote Sensing and Spatial Information Science* 38.8, pp. 576–579.

Mekonnen, D. (2009). "Satellite remote sensing for soil moisture estimation : Gumara Catchment, Ethiopia". MA thesis. International Institute for Geo-Information Science and Earth Observation (ITC), Enschede, Netherlands.

Merlin, O., C. Rudiger, A. Al Bitar, P. Richaume, J. P. Walker, and Y. H. Kerr (2012). "Disaggregation of SMOS soil moisture in southeastern Australia". In: *IEEE Transactions on Geoscience and Remote Sensing* 50.5, pp. 1556–1571.

Merzouki, A., H. McNairn, and A. Pacheco (2010). "Evaluation of the Dubois, Oh, and IEM radar backscatter models over agricultural fields using C-band Radarsat-2 SAR image data". In: *Canadian Journal of Remote Sensing* 36.SUPPL. 2, S274–S286.

Moran, M. S., C. D. Peters-Lidard, J. M. Watts, and S. McElroy (2004). "Estimating soil moisture at the watershed scale with satellite-based radar and land surface models". In: *Canadian Journal of Remote Sensing* 30.5, pp. 805–826.

Mätzler, C. and A. Standley (2000). "Technical note: relief effects for passive microwave remote sensing". In: *International Journal of Remote Sensing* 21.12, pp. 2403–2412.

Myint, S. W. (2003). "Fractal approaches in texture analysis and classification of remotely sensed data: comparisons with spatial autocorrelation techniques and simple descriptive statistics". In: *International Journal of Remote Sensing* 24.9, pp. 1925–1947.

Mzuku, M., R. Khosla, R. Reich, D. Inman, F. Smith, and L. MacDonald (2005). "Spatial variability of measured soil properties across site-specific management zones". In: *Soil Science Society of America Journal* 69.5, pp. 1572–1579.

Naeimi, V., K. Scipal, Z. Bartalis, S. Hasenauer, and W. Wagner (2009). "An improved soil moisture retrieval algorithm for ERS and METOP scatterometer observations". In: *IEEE Transactions on Geoscience and Remote Sensing* 47.7, pp. 1999–2013.

Neskovic, M. and D. Brzakovic (1993). "Mammogram screening using multiresolution-based image segmentation". In: *International Journal of Pattern Recognition and Artificial Intelligence* 7.6, pp. 1437–1460.

Nesti, G., R. Estevan de Quesada, J. Lopez, and A. Sieber (1997). "Implementation of the integral equation model for rough surfaces with generic isotropic autocorrelation functions". In: *Proceedings of the IEEE International Geoscience and Remote Sensing Symposium (IGARSS)*. (Singapore). Vol. 3. IEEE, pp. 1361–1364.

Neusch, T. and M. Sties (1999). "Application of the Dubois model using experimental synthetic aperture radar data for the determination of soil moisture and surface roughness". In: *ISPRS Journal of Photogrammetry and Remote Sensing* 54.4, pp. 273–278.

Ni-Meister, W., J. P. Walker, and P. R. Houser (2005). "Soil moisture initialization for climate prediction: characterization of model and observation errors". In: *Journal of Geophysical Research* 110.D13, p. D13111.

Njoku, E. G. and D. Entekhabi (1996). "Passive microwave remote sensing of soil moisture". In: *Journal of Hydrology* 184.1, pp. 101–129.

Njoku, E., T. Jackson, V. Lakshmi, T. Chan, and S. Nghiem (2003). "Soil moisture retrieval from AMSR-E". In: *IEEE Transactions on Geoscience and Remote Sensing* 41.2, pp. 215–229.

Nocedal, J. and S. J. Wright (2006). *Numerical Optimization*. New York, NY, USA: Springer.

Notarnicola, C. and F. Posa (2001). "Bayesian fusion of active and passive microwave data for estimating bare soil water content". In: *Proceedings of the IEEE International Geoscience and Remote Sensing Symposium (IGARSS)*. (Sydney, NSW, Australia). Vol. 3. IEEE, pp. 1167–1169.

Oh, Y. (2004a). "Comparison of two inversion methods for retrieval of soil moisture and surface roughness from polarimetric radar observation of soil surfaces". In: *Proceedings of the*

IEEE International Geoscience and Remote Sensing Symposium (IGARSS). (Anchorage, AK, USA). Vol. 2. IEEE, pp. 807–810.

Oh, Y. (2004b). "Quantitative retrieval of soil moisture content and surface roughness from multipolarized radar observations of bare soil surfaces". In: *IEEE Transactions on Geoscience and Remote Sensing* 42.3, pp. 596–601.

Oh, Y., K. Sarabandi, and F. Ulaby (1992). "An empirical model and an inversion technique for radar scattering from bare soil surfaces". In: *IEEE Transactions on Geoscience and Remote Sensing* 30.2, pp. 370–382.

Oh, Y., K. Sarabandi, and F. Ulaby (1994). "An inversion algorithm for retrieving soil moisture and surface roughness from polarimetric radar observation". In: *Proceedings of the IEEE International Geoscience and Remote Sensing Symposium (IGARSS)*. (Pasadena, CA, USA). Vol. 3. IEEE, pp. 1582–1584.

Oh, Y and Y. C. Kay (1998). "Condition for precise measurement of soil surface roughness". In: *IEEE Transactions on Geoscience and Remote Sensing* 36.2, pp. 691–695.

Oh, Y., K. Sarabandi, and F. Ulaby (2002). "Semi-empirical model of the ensemble averaged differential Mueller matrix for microwave backscattering from bare soil surfaces". In: *IEEE Transactions on Geoscience and Remote Sensing* 40.6, pp. 1348–1355.

Oldenhuis, R. P. (2010). "Trajectory Optimization of a Mission to the Solar Bow Shock and Minor Planets". MA thesis. Delft University of Technology, Delft, Netherlands.

Oleschko, K., G. Korvin, A. Munoz, J. Velazquez, M. E. Miranda, D. Carreon, L. Flores, M. Martínez, M. Velásquez-Valle, and F. Brambila (2008). "Mapping soil fractal dimension in agricultural fields with GPR". In: *Nonlinear Processes in Geophysics* 15.5, pp. 711–725.

Owe, M., E. B. Jones, and T. J. Schmugge (1982). "Soil moisture variation patterns observed in Hand County, South Dakota". In: *Journal of the American Water Resources Association* 18.6, pp. 949–954.

Perfect, E. and B. D. Kay (1995). "Applications of fractals in soil and tillage research: a review". In: *Soil and Tillage Research* 36.1, pp. 1–20.

Pietroniro, A. and R. Leconte (2005). "A review of Canadian remote sensing and hydrology, 1999-2003". In: *Hydrological Processes* 19.1, pp. 285–301.

Pinel, N., C. Bourlier, and J. Saillard (2010). "Degree of roughness of rough layers: extensions of the Rayleigh roughness criterion and some applications". In: *Progress In Electromagnetics Research B* 19, pp. 41–63.

Powell, M. (1978). "A fast algorithm for nonlinearly constrained optimization calculations". In: *Numerical Analysis*. Ed. by G. Watson. Vol. 630. Springer Berlin Heidelberg, pp. 144–157.

Prakash, R., D. Singh, and N. Pathak (2012). "A fusion approach to retrieve soil moisture with SAR and optical data". In: *IEEE Journal of Selected Topics in Applied Earth Observations and Remote Sensing* 5.1, pp. 196–206.

Price, J. C. (1982). "On the use of satellite data to infer surface fluxes at meteorological scales". In: *Journal of Applied Meteorology* 21.8, pp. 1111–1122.

Pultz, T., J. Sokol, A. Deschamps, and D. Jobin (2002). "Temporal soil moisture estimation of pastures from Radarsat data for applications in watershed modelling". In: *Proceedings of the IEEE International Geoscience and Remote Sensing Symposium (IGARSS)*. (Toronto, ON, Canada). IEEE, pp. 1402–1404.

Quattrochi, D. A. and J. C. Luvall (2004). *Thermal Remote Sensing in Land Surface Processes*. Boca Raton, FL, USA: CRC Press.

Reddy, M. A. (2008). *Textbook of Remote Sensing and Geographical Information Systems*. Hyderabad, India: BS Publications.

Rees, W. G. (2001). *Physical Principles of Remote Sensing*. Cambridge, UK: Cambridge University Press.

Rodríguez-Iturbe, I., V. Isham, D. R. Cox, S. Manfreda, and A. Porporato (2006). "Space-time modeling of soil moisture: stochastic rainfall forcing with heterogeneous vegetation". In: *Water Resources Research* 42.6, W06D05.

Rodriguez-Iturbe, I., G. K. Vogel, R. Rigon, D. Entekhabi, F. Castelli, and A. Rinaldo (1995). "On the spatial organization of soil moisture fields". In: *Geophysical Research Letters* 22.20, pp. 2757–2760.

Samadzadegan, F., A. Azizi, C. Lucas, and M. Hahn (2002). "Automatic surface reconstruction based on the fusion of fuzzy logic and robust estimation techniques". In: *The Photogrammetric Record* 17.100, pp. 651–674.

Schertzer, D and S. Lovejoy (1989). "Nonlinear variability in geophysics: multifractal analysis and simulation". In: *Fractals: Physical Origin and Consequences*. Ed. by L. Pietronero. New York, NY, USA: Plenum, pp. 49–79.

Schertzer, D. and S. Lovejoy (1997). "Universal multifractals do exist!: comments on "A statistical analysis of mesoscale rainfall as a random cascade"". In: *Journal of Applied Meteorology* 36.9, pp. 1296–1303.

Schmugge, T. (1985). *Hydrological Forecasting*. New York, NY, USA: John Wiley.

Schmugge, T., P. Gloersen, T. Wilheit, and F. Geiger (1974). "Remote sensing of soil moisture with microwave radiometers". In: *Journal of Geophysical Research* 79.2, pp. 317–323.

Schmugge, T. J., T. J. Jackson, and H. L. McKim (1980). "Survey of methods for soil moisture determination". In: *Water Resources Research* 16.6, pp. 961–979.

Scipal, K. (2002). "Global soil moisture retrieval from ERS scatterometer data". PhD thesis. Vienna University of Technology, Vienna, Austria.

Seuront, L., F. Schmitt, Y. Lagadeuc, D. Schertzer, and S. Lovejoy (1999). "Universal multifractal analysis as a tool to characterize multiscale intermittent patterns: example of phytoplankton distribution in turbulent coastal waters". In: *Journal of Plankton Research* 21.5, pp. 877–822.

Shang, K. Z., S. G. Wang, Y. X. Ma, Z. J. Zhou, J. Y. Wang, H. L. Liu, and Y. Q. Wang (2007). "A scheme for calculating soil moisture content by using routine weather data". In: *Atmospheric Chemistry and Physics Discussions* 7.3, pp. 7451–7472.

Shao-E, Y. and W. Bing-fang (2010). "Agricultural drought monitoring using web-serviced remote sensing data". In: *Proceedings of the International Conference on e-Education, e-Business, e-Management, and e-Learning (IC4E)*. (Sanya, Hainan, China). IEEE, pp. 532–535.

Sharma, P. (2009). "Disaggregation of soil moisture measurements using SAR and optical remotely sensed data". PhD thesis. International Institute for Geo-Information Science and Earth Observation (ITC), Enschede, Netherlands.

Sikdar, M. and I. Cumming (2004). "A modified empirical model for soil moisture estimation in vegetated areas using SAR data". In: *Proceedings of the IEEE International Geoscience and Remote Sensing Symposium (IGARSS)*. (Anchorage, AK, USA). Vol. 2. IEEE, pp. 803–806.

Soil Survey Division Staff (1993). *Soil survey manual, U.S. Department of Agriculture Handbook 18*. WA, USA: USDA.

Srivastava, H., P. Patel, Y. Sharma, and R. Navalgund (2009). "Large-area soil moisture estimation using multi-incidence-angle Radarsat-1 SAR data". In: *IEEE Transactions on Geoscience and Remote Sensing* 47.8, pp. 2528–2535.

Storn, R. and K. Price (1997). "Differential evolution - a simple and efficient heuristic for global optimization over continuous spaces". In: *Journal of Global Optimization* 11.4, pp. 341–359.

Sun, J. and J. Southworth (2013). "Remote sensing-based fractal analysis and scale dependence associated with forest fragmentation in an Amazon Tri-National frontier". In: *Remote Sensing* 5.2, pp. 454–472.

Sun, R., J. Shi, T. Jackson, K. Chen, and Y. Oh (2009). "Improvement of bare surface soil moisture estimation with L-band dual-polarization radar". In: *Proceedings of the IEEE International Geoscience and Remote Sensing Symposium (IGARSS)*. (Cape Town, South Africa). Vol. 4. IEEE, pp. 971–974.

Sun, W., G. Xu, P. Gong, and S. Liang (2006). "Fractal analysis of remotely sensed images: a review of methods and applications". In: *International Journal of Remote Sensing* 27.22, pp. 4963–4990.

Telesca, L., G. Colangelo, V. Lapenna, and M. Macchiato (2003). "Monofractal and multifractal characterization of geoelectrical signals measured in southern Italy". In: *Chaos, Solitons & Fractals* 18.2, pp. 385–399.

Thevenaz, P., U. E. Ruttimann, and M. Unser (1998). "A pyramid approach to subpixel registration based on intensity". In: *IEEE Transactions on Image Processing* 7.1, pp. 27–41.

Topp, G., J. Davis, and A. Annan (1980). "Electromagnetic determination of soil water content: measurements in coaxial transmission lines". In: *Water Resources Research* 16.2, pp. 574–582.

Turcotte, D. L. (1989). "Fractals in geology and geophysics". In: *Pure and applied Geophysics* 131.1, pp. 171–196.

Turiel, A., C. J. Pérez-Vicente, and J. Grazzini (2006). "Numerical methods for the estimation of multifractal singularity spectra on sampled data: a comparative study". In: *Journal of Computational Physics* 216.1, pp. 362–390.

Ulaby, F. T., R. K. Moore, and A. K. Fung (1982). *Microwave Remote Sensing: Active and Passive. Vol. 2, Radar Remote Sensing and Surface Scattering and Emission Theory*. Reading, MA, USA: Addison-Wesley.

Ulaby, F. T., R. K. Moore, and A. K. Fung (1986). *Microwave Remote Sensing: Active and Passive. Vol. 3, From Theory to Applications*. Norwood, MA, USA: Artech House.

Verhoest, N. E., H. Lievens, W. Wagner, J. Álvarez Mozos, M. S. Moran, and F. Mattia (2008). "On the soil roughness parameterization problem in soil moisture retrieval of bare surfaces from synthetic aperture radar". In: *Sensors* 8.7, pp. 4213–4248.

Viltard, N., C. Burlaud, and C. D. Kummerow (2006). "Rain retrieval from TMI brightness temperature measurements using a TRMM PR-based database". In: *Journal of Applied Meteorology and Climatology* 45.3, pp. 455–466.

Wagner, W., G. Lemoine, and H. Rott (1999). "A method for estimating soil moisture from ERS scatterometer and soil data". In: *Remote Sensing of Environment* 70.2, pp. 191–207.

Walker, J. P. (1999). "Estimating soil moisture profile dynamics from near-surface soil moisture measurements and standard meteorological data". PhD thesis. The University of Newcastle, New South Wales, Australia.

Walker, J., P. Troch, M. Mancini, G. Willgoose, and J. Kalma (1997). "Profile soil moisture estimation using the modified IEM". In: *Proceedings of the IEEE International Geoscience and Remote Sensing Symposium (IGARSS)*. (Singapore). Vol. 3. IEEE, pp. 1263–1265.

Wang, J. R. and B. J. Choudhury (1981). "Remote sensing of soil moisture content over bare field at 1.4 GHz frequency". In: *Journal of Geophysical Research* 86.C6, pp. 5277–5282.

Wang, J. R. and T. J. Schmugge (1980). "An empirical model for the complex dielectric permittivity of soils as a function of water content". In: *IEEE Transactions on Geoscience and Remote Sensing* GE-18.4, pp. 288 –295.

Wang, J., A. Hsu, J. Shi, P. O'Neill, and E. Engman (1997). "A comparison of soil moisture retrieval models using SIR-C measurements over the Little Washita River watershed". In: *Remote Sensing of Environment* 59.2, pp. 308–320.

Wang, L. (2008). "Remote sensing techniques for soil moisture and agricultural drought monitoring". PhD thesis. George Mason University, Fairfax, VA, USA.

Wang, L. and J. Qu (2009). "Satellite remote sensing applications for surface soil moisture monitoring: a review". In: *Frontiers of Earth Science in China* 3.2, pp. 237–247.

Weidong, L., F. Baret, G. Xingfa, T. Qingxi, Z. Lanfen, and Z. Bing (2002). "Relating soil surface moisture to reflectance". In: *Remote Sensing of Environment* 81.2-3, pp. 238–246.

Western, A. W. and G. Blöschl (1999). "On the spatial scaling of soil moisture". In: *Journal of Hydrology* 217.3, pp. 203–224.

Whalley, W. R., P. B. Leeds-Harrison, and G. E. Bowman (1991). "Estimation of soil moisture status using near infrared reflectance". In: *Hydrological Processes* 5.3, pp. 321–327.

Whiting, M. L., L. Li, and S. L. Ustin (2004). "Predicting water content using Gaussian model on soil spectra". In: *Remote Sensing of Environment* 89.4, pp. 535–552.

Whitley, D. (1994). "A genetic algorithm tutorial". In: *Statistics and Computing* 4.2, pp. 65–85.

Wigneron, J. P., J. C. Calvet, T. Pellarin, A. A. V. de Griend, M. Berger, and P. Ferrazzoli (2003). "Retrieving near-surface soil moisture from microwave radiometric observations: current status and future plans". In: *Remote Sensing of Environment* 85.4, pp. 489–506.

Wilde, D. and C. Beightler (1967). *Foundations of Optimization*. Englewood Cliffs, NJ, USA: Prentice-Hall.

Wormald, R. and A. Britch (1969). "Methods of measuring moisture content applicable to building materials". In: *Building Science* 3.3, pp. 135–145.

Wu, T.-D., K. Chen, J. Shi, and A. Fung (2001). "A transition model for the reflection coefficient in surface scattering". In: *IEEE Transactions on Geoscience and Remote Sensing* 39.9, pp. 2040–2050.

Zheng, X. and K. Zhao (2010). "A method for surface roughness parameter estimation in passive microwave remote sensing". In: *Chinese Geographical Science* 20.4, pp. 345–352.